Kunsági-Máté Sándor

10 db válogatott Q1 publikáció

A pályázat benyújtásának időpontjáig a tudományos pálya egészére vonatkozóan legfontosabbnak ítélt öt publikáció, valamint a pályázat benyújtását megelőző öt évben megjelent művek közül a legfontosabbnak ítélt további öt publikáció:

Sor-szám	Cím	Szerző(k)	A pályázó szerzői szerepe (egyedüli/első/utolsó/levelező)	Szakfolyóirat	
				neve	besorolása a publikálás évében (pl. Q1)
1.	Anodic Polymerization of Phenylphenols in Methyl Isobutyl Ketone and Mesityl Oxide: Incorporation of a Cavitand into the Layers Formed for Sensing Phenols in Organic Media	Kiss, László ; Nagymihály, Zoltán ; Szabó, Péter ; Kollár, László ; Kunsági-Máté, Sándor	**utolsó és levelező**	MOLECULES 27 (2022) 5366	Q1 (2021)
2.	Weak Interactions of the Isomers of Phototrexate and Two Cavitand Derivatives	Preisz, Zsolt ; Nagymihály, Zoltán ; Kollár, László ; Kálai, Tamás ; Kunsági-Máté, Sándor	**utolsó és levelező**	INTERNATIONAL JOURNAL OF MOLECULAR SCIENCES 22:19 (2021) 10764	Q1(D1)
3.	Comparative EPR Study on the Scavenging Effect of Methotrexate with the Isomers of Its Photoswitchable Derivative	Preisz, Zsolt ; Hartvig, Nóra ; Bognár, Balázs ; Kálai, Tamás ; Kunsági-Máté, Sándor	**utolsó és levelező**	PHARMACEUTIC ALS 14:7 (2021) 665	Q1(D1)
4.	Weak Interaction of the Antimetabolite Drug Methotrexate with a Cavitand Derivative	Preisz, Zsolt ; Nagymihály, Zoltán ; Lemli, Beáta ; Kollár, László ; Kunsági-Máté, Sándor	**utolsó és levelező**	INTERNATIONAL JOURNAL OF MOLECULAR SCIENCES 21:12 (2020) 4345	Q1(D1)
5.	Effect of exposure time and pre-heating on the conversion degree of conventional, bulk-fill, fiber reinforced and polyacid-modified resin composites	Lempel, Edina ; Őri, Zsuzsanna ; Szalma, József ; Lovász, Bálint Viktor ; Kiss, Adél ; Tóth, Ákos ; Kunsági-Máté, Sándor	**utolsó**	DENTAL MATERIALS 35 (2019) 217	Q1(D1)
6.	Structural properties of methanol - water binary mixtures within the quantum cluster equilibrium model	Gergely, Matisz ; Anne-Marie, Kelterer; Walter, Fabian ; Sándor, Kunsági-Máté	**utolsó**	PHYSICAL CHEMISTRY CHEMICAL PHYSICS 17 (2015) 8467	Q1(D1)

7.	Some Unexpected Behavior of the Adsorption of Alkali Metal Ions onto the Graphene Surface under the Effect of External Electric Field	Beáta, Peles-Lemli ; Dániel, Kánnár ; Jia, Cai Nie ; Heng, Li ; Sándor, Kunsági-Máté	**utolsó és levelező**	JOURNAL OF PHYSICAL CHEMISTRY C 117 (2013) 21509	Q1(D1)
8.	Host-guest interaction between water-soluble calix[6]arene hexasulfonate and p-nitrophenol	Kunsagi, Mate S; Szabo, K ; Lemli, B ; Bitter, I ; Nagy, G ; Kollar, L	**első és levelező**	THERMOCHIMIC A ACTA 425 (2005) 121	Q1
9.	Host-guest interaction of calixarene molecules with neutral benzotrifluorides: Comparison of luminescence spectral data with results of model calculations relating to complex formation	Kunsagi, Mate S ; Nagy, G; Kollar, L	**első**	ANALYTICA CHIMICA ACTA 428 (2001) 301	Q1
10	Coordination of Methanol Clusters to Benzene: A Computational Study	Matisz, G ; Kelterer, AM ; Fabian, WMF ; Kunsagi-Mate, S	**utolsó és levelező**	JOURNAL OF PHYSICAL CHEMISTRY A 115 (2011) 10556	Q1(D1)
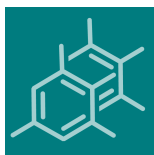
Article

Anodic Polymerization of Phenylphenols in Methyl Isobutyl Ketone and Mesityl Oxide: Incorporation of a Cavitand into the Layers Formed for Sensing Phenols in Organic Media

László Kiss, Zoltán Nagymihály, Péter Szabó, László Kollár and Sándor Kunsági-Máté

Article

Anodic Polymerization of Phenylphenols in Methyl Isobutyl Ketone and Mesityl Oxide: Incorporation of a Cavitand into the Layers Formed for Sensing Phenols in Organic Media

László Kiss [1,2], **Zoltán Nagymihály** [2], **Péter Szabó** [3], **László Kollár** [2] **and Sándor Kunsági-Máté** [1,2,*]

1 Department of Organic and Medicinal Chemistry, University of Pécs, Honvéd Street 1, H 7624 Pécs, Hungary
2 János Szentágothai Research Center, Ifjúság útja 20, H 7624 Pécs, Hungary
3 Environmental Analytical and Geoanalytical Research Group, Szentágothai Research Center, Ifjúság útja 20, H 7624 Pécs, Hungary
* Correspondence: sandor.kunsagi-mate@gytk.pte.hu

Abstract: The electropolymerization of three phenylphenol isomers was studied in methyl isobutyl ketone and mesityl oxide, and the remarkable differences highlighted the importance of the carbon–carbon double bond in mesityl oxide. In the case of each substrate, a brownish deposit formed during the electrooxidation. The obvious difference between the polymers formed from the two solvents was recognized via voltammetric signal enhancement of 4-methoxyphenol and 4-chlorophenol, and it was only observed in the case of mesityl oxide. The experiments highlighted that incorporation of a cavitand with biphenyl groups on the upper rim of the polymers of phenylphenols improved the results to a small extent. The cavitand was, itself, electroactive without any fouling effect. As 2-phenylphenol is by far the cheapest of the three isomers, a cavitand was incorporated into its polymer, which was exploited to solve analytical problems while mesityl oxide was used as solvent. Useful quantifications were achieved in organic solvents; however, it failed under aqueous conditions due to the high hydrophobicity of the deposit. Application of differential pulse voltammetry for 4-methoxyphenol and 4-chlorophenol gave detection limits of 9.28 and 50.8 μM in acetonitrile, respectively. This procedure resulted in the immobilization of cavitand derivatives onto the electrode's surface, and the layer formed offered selective sensing of phenols by electrochemical methods.

Keywords: phenylphenols; methyl isobutyl ketone; mesityl oxide; cavitand

1. Introduction

Phenylphenols are very attractive phenol derivatives, especially 2-phenylphenol due to the fact of its outgoing practical importance in the food industry (detection in citrus fruits) [1–3]. On the other hand, they are important intermediates for organic synthesis, and they are susceptible to oxidative polymerization as is usually characteristic of phenols. Thus, electrochemical study of them in uncommon solvents was the topic of this work. Phenols usually undergo formation of a radical during anodic polymerization, and the prepared deposits have favorable properties exploited in many areas. Herein, the analytical usefulness of poly(phenylphenols) was estimated.

Cavitands are an important class of macromolecules with excellent binding properties, especially in their cavity. As a matter of fact, they are cyclic oligomers of aromatic monomers predominantly consisting of four members interconnected by methylene bridges. This cavity is usually substituted with organic substituents on each member on the lower and/or upper rim, making their binding capabilities more selective. The interaction of organic molecules with molecular capsules is a hot topic of research, as selective binding of certain molecules is possible in their cavity. In the cavity of larger host molecules of cavitands, not only can neutral guest molecules be accommodated but organic ions [4,5] and, moreover, metal ions [6] as well. Predominantly, weak π–π interactions are responsible for their

binding capability, originating from the delocalized electron system of the aromatic moieties which can surround the guest species. This is the reason why the skeleton of all cavitands also show high affinity to electron-poor aromatics. Therefore, sensing methods based on photoluminescence and electrochemical techniques have widespread application [7–11].

Numerous cavitands have promising properties in electrochemical applications, whether they are electroinactive or if they are electroactive. The favorable binding properties of redox inactive resorcinarenes can be utilized by their incorporation into carbon paste electrodes due to the fact of their accumulation close to the electrode's surface [12]. In the majority of examples, the cavity skeleton of resorcinarenes is electrochemically inactive and the side chains on their rims have redox properties. Usually, weak electronic communication occurs among them, especially if they remain neutral. In contrast, reports can be found where the appearance of more voltammetric peaks were observed [13].

Earlier studies have pointed out that such remarkable differences come from the fact that either methyl isobutyl ketone (MIBK) or mesityl oxide (MO) are used as a solvent in electropolymerization reactions of organic compounds susceptible to this process [14,15]. However, these solvents differ from each other only in a carbon–carbon double bond; therefore, copolymerization takes place when mesityl oxide is used as a solvent, as the electrochemically generated radicals can undergo saturation reactions, thus altering the structural properties of the formed polymer. Therefore, in the present study, this was one of the selected solvents used to investigate anodic polymerization reactions of phenylphenol monomers and to prepare modifying layers on an electrode. This procedure resulted in the immobilization of cavitand derivatives onto the electrode's surface, and the layer formed offered selective sensing of phenols by electrochemical methods.

2. Materials and Methods

The solutes investigated in this study were obtained from Merck, and analytical reagent grade solvents were used to prepare the solutions. The cavitand possessing 2-phenylphenoxy moieties on the upper rim (Figure 1) was prepared as described for similar host compounds [16]. The supporting electrolyte in the organic solvents was tetrabutylammonium perchlorate (TBAP), and in aqueous solvents 0.1 M at pH = 7 in phosphate buffer was used.
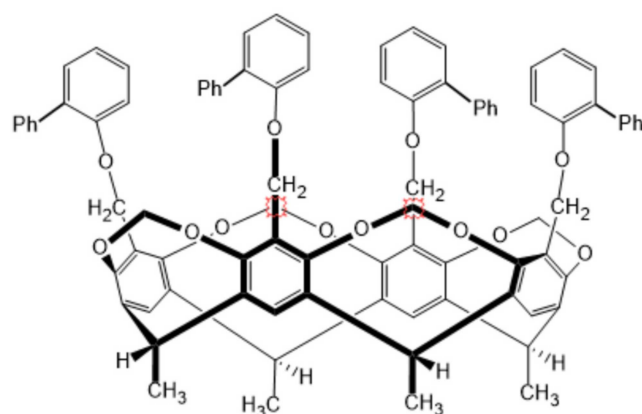

Figure 1. Structural formula of the studied cavitand (**1**).

All voltammetric measurements were carried out with a Dropsens Potentiostat (Spain) connecting to it a three-electrode cell. For the working electrode, a 1 mm diameter platinum disc electrode was used to seal in the polyether ether ketone (PEEK). A platinum rod served as the counter and a silver wire as the reference electrode. A saturated calomel electrode was used as the reference in the aqueous solutions. Before all experiments, the surface of the platinum disc was cleaned by polishing with alumina using a polishing cloth. This was followed by thorough washing with deionized water and, finally, dried by rinsing with dry acetone.

Surface images of the samples were captured with a Jeol JSM-IT500HR (Jeol, Tokyo, Japan) scanning electron microscope (SEM) using the secondary electron mode and a 30 kV acceleration voltage. The samples were coated with gold with a Jeol JFC-1300 auto fine coater (Jeol, Tokyo, Japan). The indium–tin oxide (ITO)-coated glass slides used for the microscopic experiments had an 8–12 Ω/sq surface resistance. Their surfaces were cleaned before use in an ultrasonic bath by immersion in ultrapure water to remove the physically adsorbed particles and then thoroughly washed with dry acetone.

*Synthesis of the Cavitand (**1**)*

First, 3.00 mmol (511 mg) of 2-phenylphenol and 6.00 mmol of K_2CO_3 (830 mg) were dissolved in 15 mL of dimethyl sulfoxide in a 50 mL Schlenk flask under an argon stream. The mixture was stirred with a magnetic stirrer and allowed to stir for one hour at room temperature. Then, 0.375 mmol (362 mg) of tetrakis(bromomethyl)cavitand [16], dissolved in 5.0 mL of dimethyl sulfoxide, was added to the reaction mixture drop by drop. The flask was equipped with a reflux condenser and an argon ball, and the reaction mixture was stirred overnight at 60 °C under an argon atmosphere. The next day, the precipitated solution was cooled to room temperature and poured into 100 mL of 4% hydrochloric acid solution. The filtrate was filtered through a glass filter and washed several times with methanol and dried under vacuum at 80 °C. Pale brown powder (462 mg, 93%). Melting point: >300 °C. ^{1}H NMR (500.1 MHz, CDCl$_3$): 1.77 (d, *J* = 7.3 Hz, 12H, C*H$_3$*CH), 4.11 (d, *J* = 7.3 Hz, 4H, inner OC*H$_2$*O), 4.75 (s, 8H, ArC*H$_2$*O), 5.01 (q, *J* = 7.0 Hz, 4H, C*H*CH$_3$), 5.50 (d, *J* = 7.3 Hz, 4H, outer OC*H$_2$*O), and 7.10–7.60 (m, 40H, Ar). ^{13}C NMR (125.1 MHz, CDCl$_3$): 16.1 (*C*H$_3$CH), 31.1 (CH$_3$*C*H), 63.6 (Ar*C*H$_2$O), 99.7 (O*C*H$_2$O), 117.0, 120.4, 122.4, 122.6, 126.8, 127.9, 128.7, 129.5, 131.3, 133.0, 138.8, 153.8, and 156.2.

3. Results and Discussion

A schematic representation of the experimental procedure is shown in Figure 2 showing how the deposition was carried out on the platinum electrode. The solvents methyl isobutyl ketone and mesityl oxide had interesting effects on the electropolymerization reactions; thus, in the first part of our study, the electropolymerization reactions of the three phenylphenol isomers were explored by taking ten subsequent cyclic voltammograms between 0 and 2.5 V with a 0.1 V/s scan rate. In phenylphenols, the neighboring aromatic groups displayed electronic interactions due to the conjugation of the highly delocalized electronic system, which also affected their electrochemical polymerization reactions. When they were investigated, themselves, the differences between isomers could be estimated and a few signs regarding the polymer structures could mostly be found to be related to porosity. A light brown deposit was formed in both solvents from each of the isomers, but the layers deposited from mesityl oxide were thicker. They could easily be removed mechanically from the platinum surface, indicating weak adhesion. The CVs in methyl isobutyl ketone demonstrated deactivation of the platinum electrode in the case of the three phenylphenol isomers (Figure 3). These findings are in accordance with our earlier investigations when phenol was the substrate [14]. This process was very strong (especially remarkable) in the case of 3-phenylphenol. During the entire electropolymerization process, no tendency towards a decrease in the anodic peak currents of the monomers was observed. This was due to the swelling of the organic deposits in methyl isobutyl ketone. However, phenylphenols are bulky substrates due to the phenyl substituents, leading to more open structures of polymers, which is why swelling of their polymers was more pronounced, especially in ketone solvents.
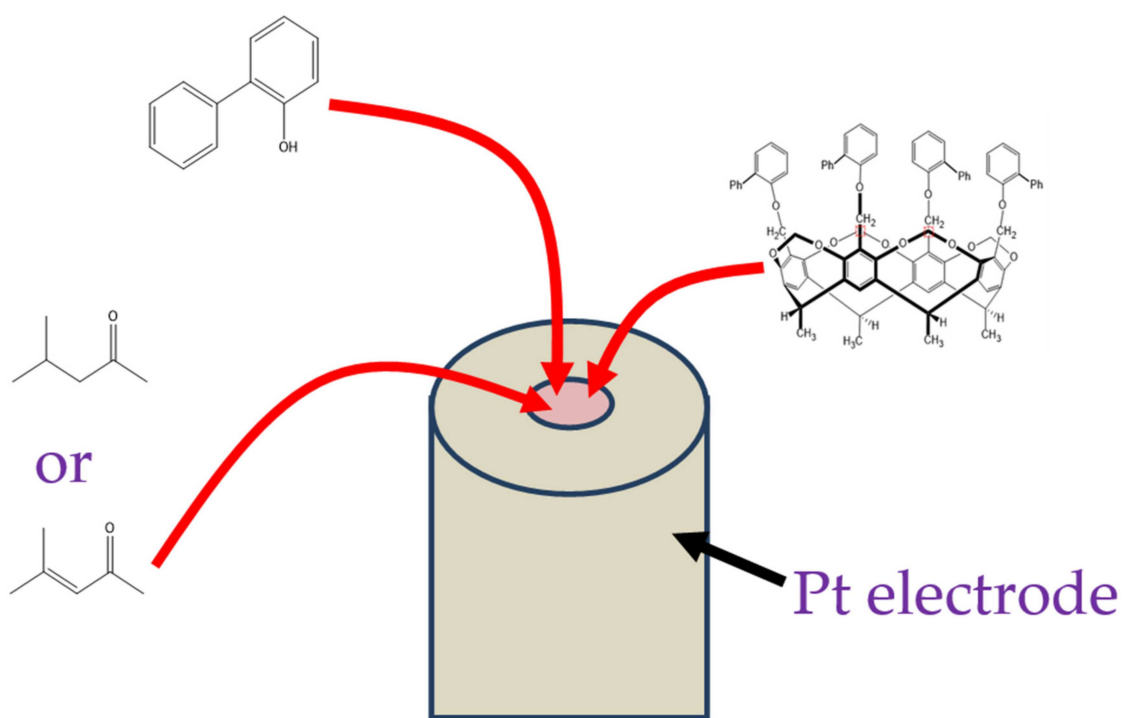
Figure 2. Schematic of the experimental design for the electropolymerization reactions of 2-phenylphenol.
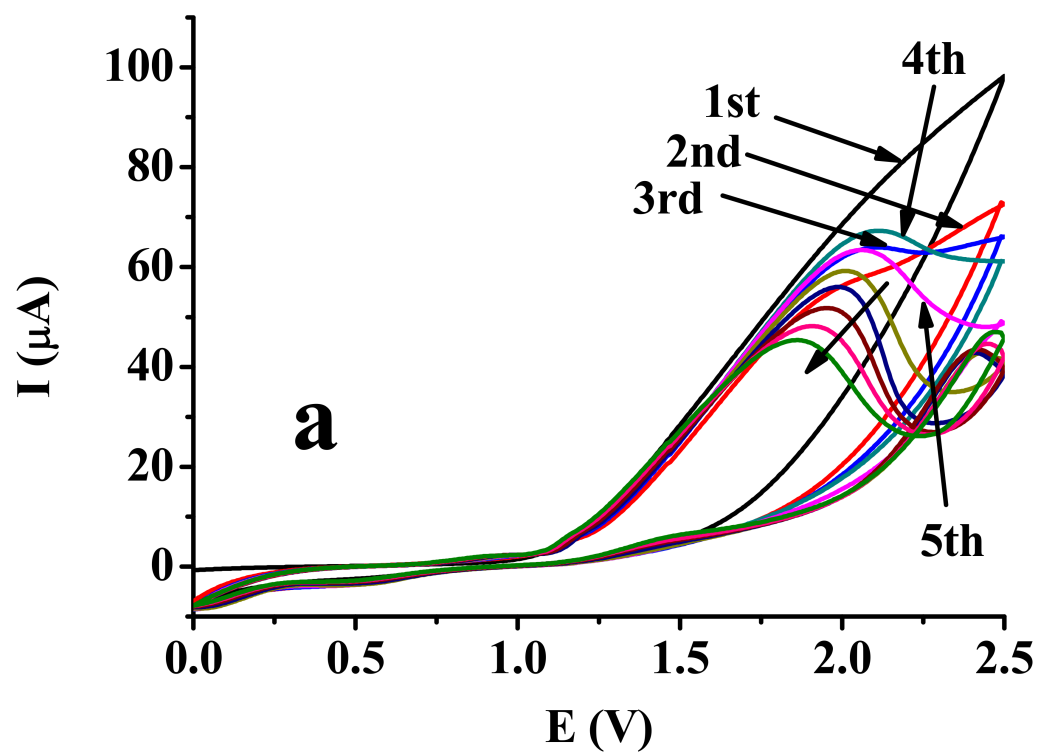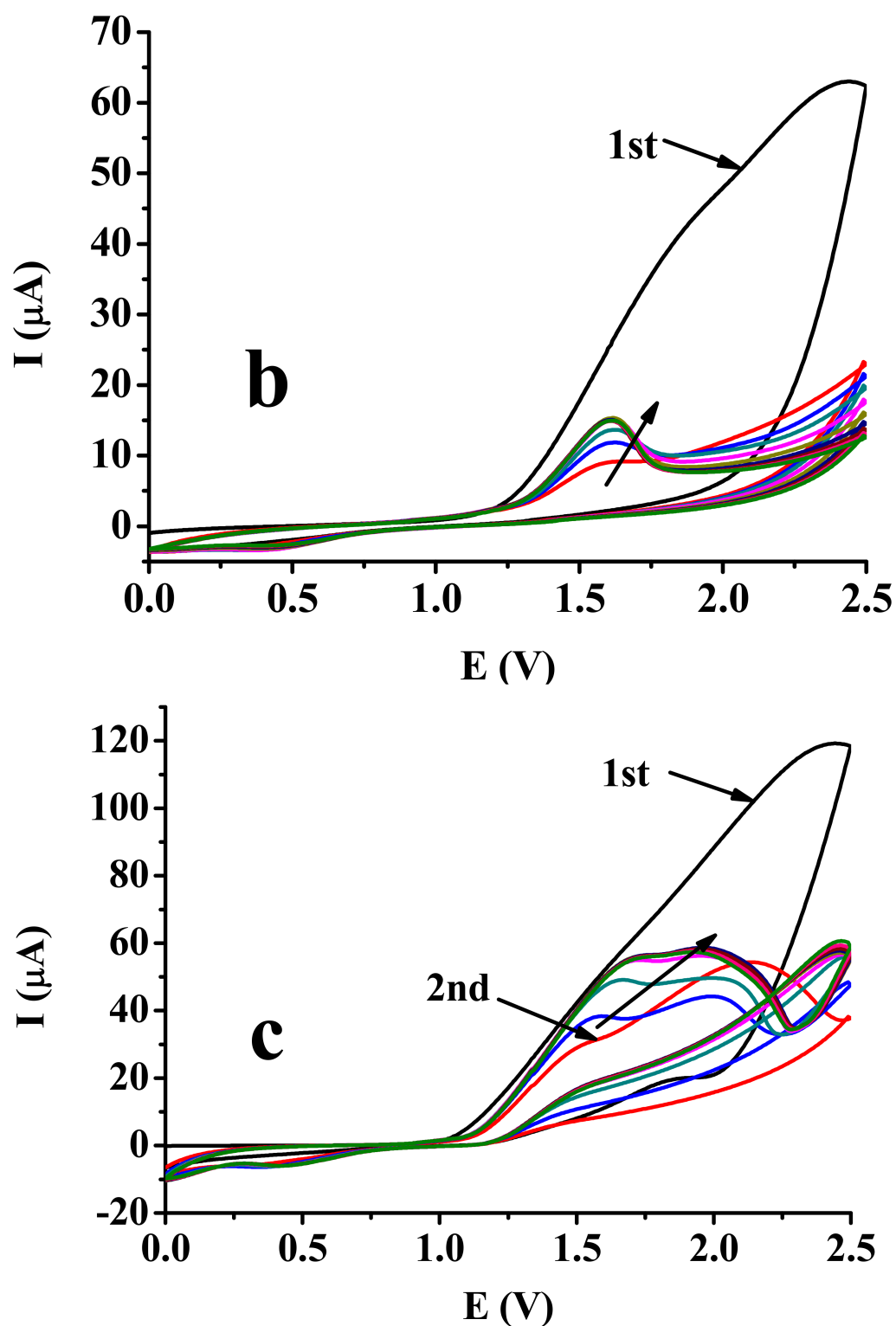

Figure 3. *Cont.*

Figure 3. The ten consecutive cyclic voltammograms of 2-phenylphenol (**a**); 3-phenylphenol (**b**); 4-phenylphenol (**c**) in methyl isobutyl ketone (c = 50 mM, supporting electrolyte = 70 mM TBAP, and v = 0.1 V/s).

The differences resulting from methyl isobutyl ketone were also observed for the phenylphenol isomers in mesityl oxide in the electrochemical polymerization process (Figure 4). This solvent had remarkable features compared to the other commonly used nonaqueous solvents, as could be observed. As expected, in the case of 2-phenylphenol and 3-phenylphenol, the drops in the current after the first cycle were not very high, except

for 4-phenylphenol. For the latter substrate, a significant swelling was observed in the structure of the polymer, as radicals predominantly joined through the para position of the phenyl substituent. This resulted in the formation of fibrous polymers that could easily attach through weak interactions with neighboring aromatic segments based on π−π interactions. The structure became obviously more open with the insertion of solvent molecules into the polymer chains.
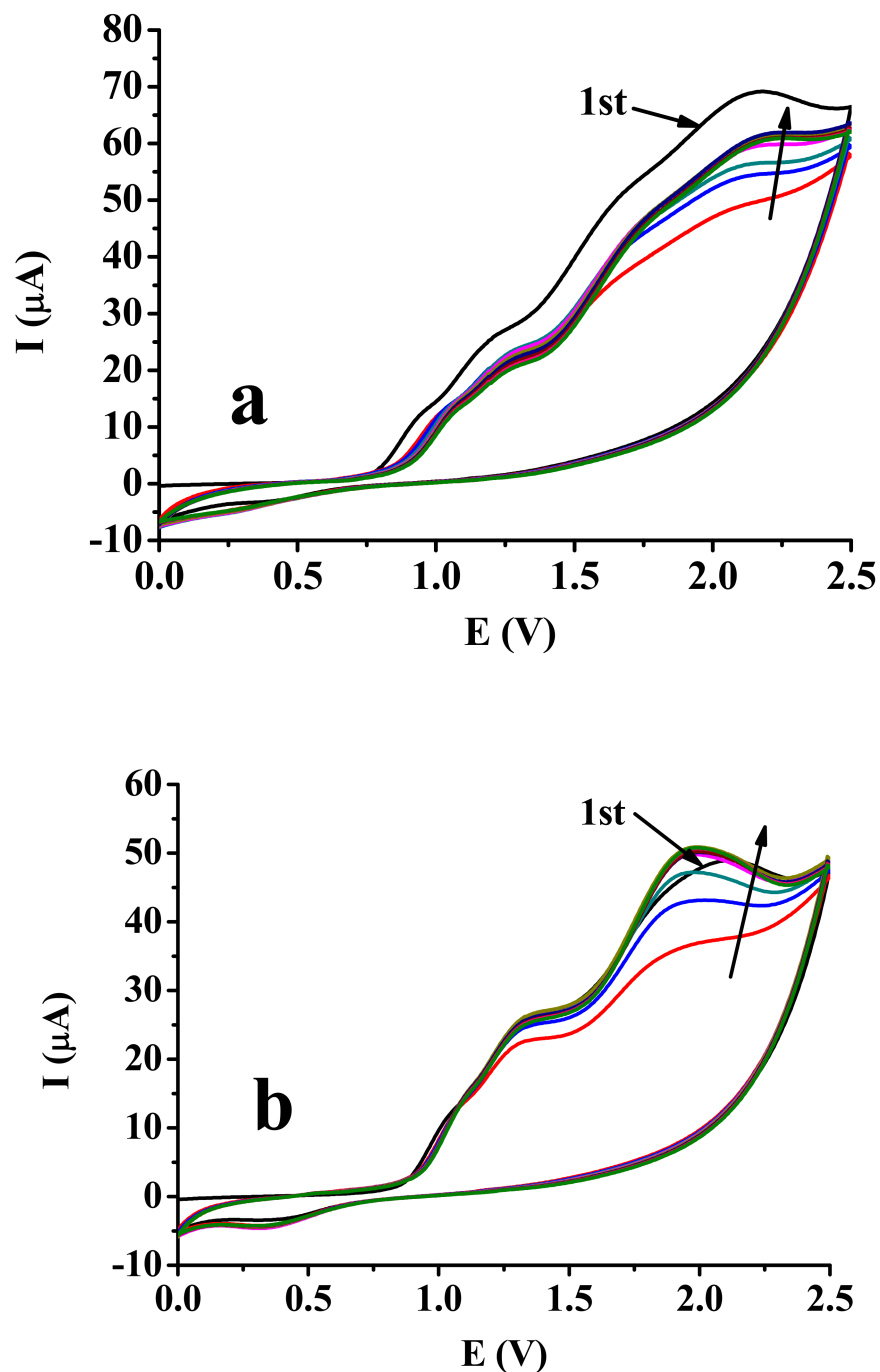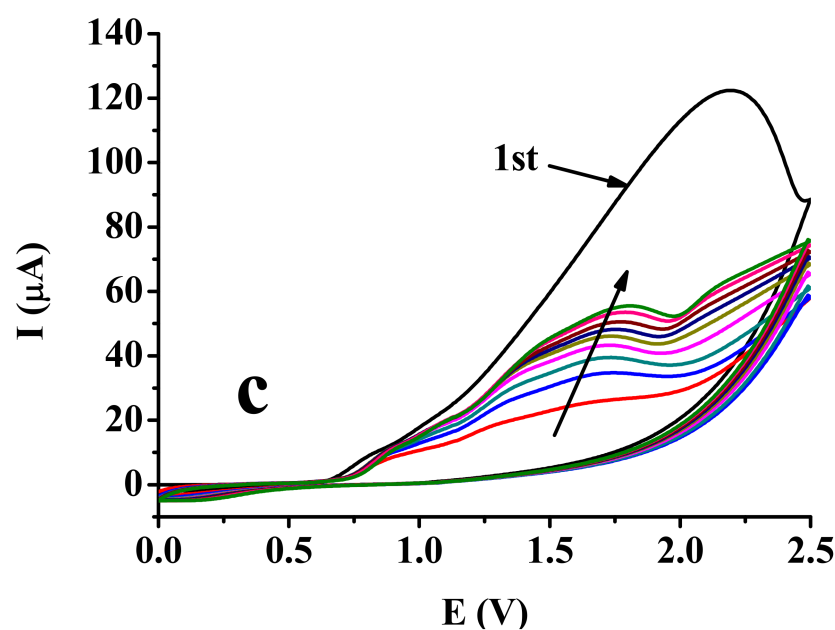

Figure 4. *Cont.*

Figure 4. The ten consecutive cyclic voltammograms of 2-phenylphenol (**a**); 3-phenylphenol (**b**); 4-phenylphenol (**c**) in mesityl oxide (*c* = 50 mM, supporting electrolyte = 70 mM TBAP, and *v* = 0.1 V/s).

3.1. Electrochemical Polymerizations in the Presence of the Cavitand (**1**)

Although many works can be found that report on the reversible redox behavior of many cavitands bearing functional groups that make them capable of fast electron transfer, some investigations focused on the electrochemistry of cavitands susceptible to electropolymerization. A derivative containing phenol moieties in its cavity exhibited electrode fouling during anodic oxidation [17] and calix[4]arenequinones [18]. Cavitands bearing functional groups with pyrrole moieties provide the possibility for their homopolymerization through their pyrrole moieties [19,20]. In this work, a cavitand was selected that had biphenyl groups at the upper rim attached through an ether bond to the ring skeleton. These aryl ether parts make the molecule electrochemically active through formation of a radical, being then capable of involvement in copolymer synthesis through anodic oxidation. This procedure is different from the simple covering of gold surfaces with cavitands, which is also a promising modifying method [21,22].

The cavitand chosen can be oxidized on its biphenyl groups due to the fact of its phenylether moiety, which was verified in an indifferent nonaqueous solvent, acetonitrile. It did not show any deactivation, indicating that the biphenyl groups could attach through oxidative dimerization, and the products diverged from the electrode's surface. The electropolymerization studies were repeated in the presence of the cavitand (**1**) with the phenylphenol isomers in either methyl isobutyl ketone or mesityl oxide, and the concentration of the substrates was 20 mM, respectively. The resultant voltammograms are displayed in Figure 5, and they clearly show that there was a remarkable difference between the two solvents. In methyl isobutyl ketone, the curves were almost reproducible, with a small decline in the current indicating that the involvement of cavitand molecules in the deposit had a modifying effect on the polymer's structure. This way, the elevated diffusion of electroactive species could be observed. Surprisingly, in mesityl oxide, the anodic peak currents in the subsequent scans increased gradually to a saturation value. Similar behavior was previously observed for phenylether compounds in mesityl oxide [15], but the current enhancement here was more obvious. The presence of cavitand contributed to the development of a more open structure. The formation of the copolymerization product can be rationalized as depicted in Scheme 1. As can be seen, the oxidized biphenyl moieties of the cavitand attached to the growing polymer chain of the poly(phenylphenols). Some of the biphenyl groups or all four of them can be involved in the polymerization process.
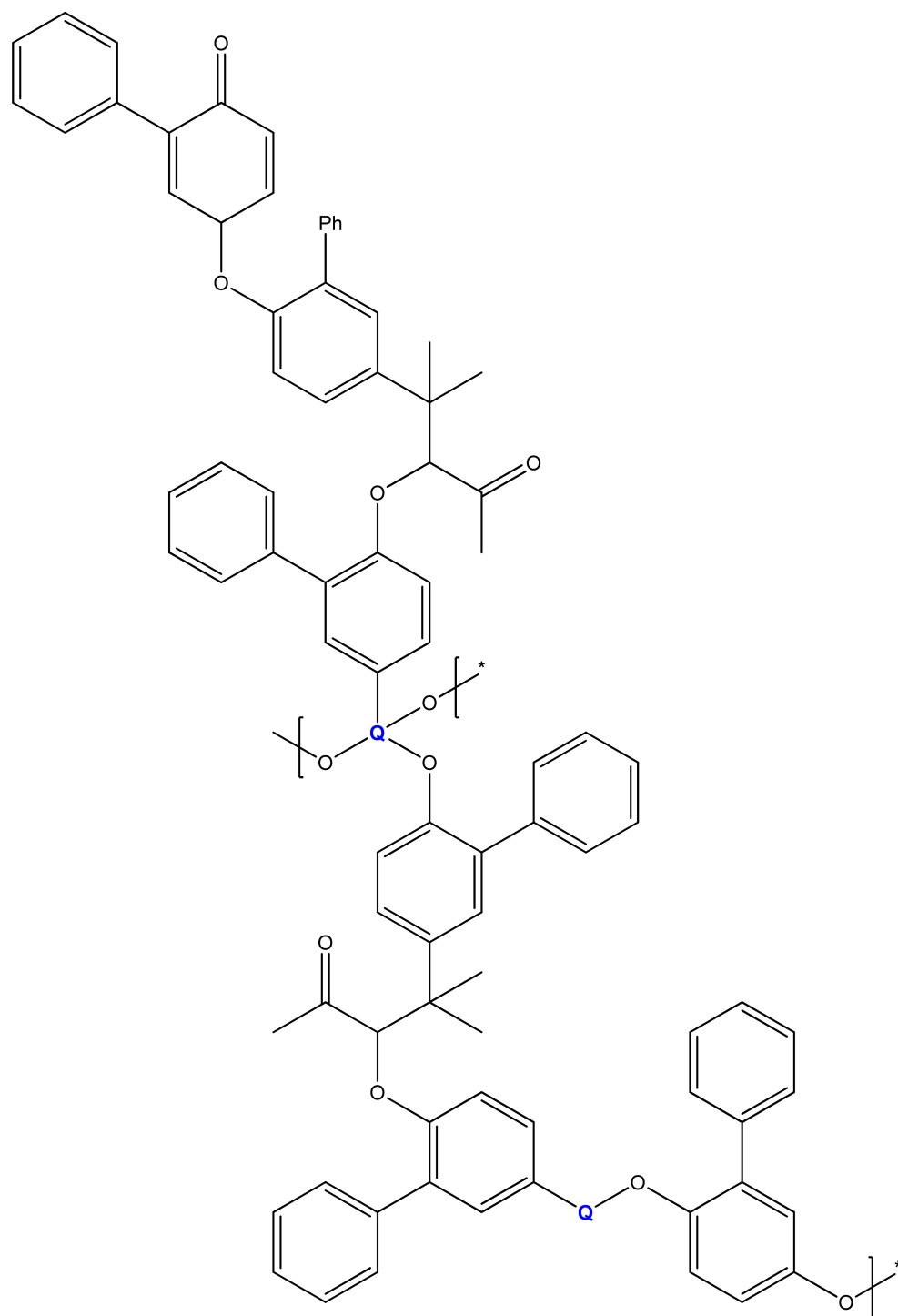
Scheme 1. Schematic representation of the coelectropolymerization reaction of 2-phenylphenol with cavitand (**1**) in mesityl oxide (Q: cavitand (1), Ph: phenyl group).
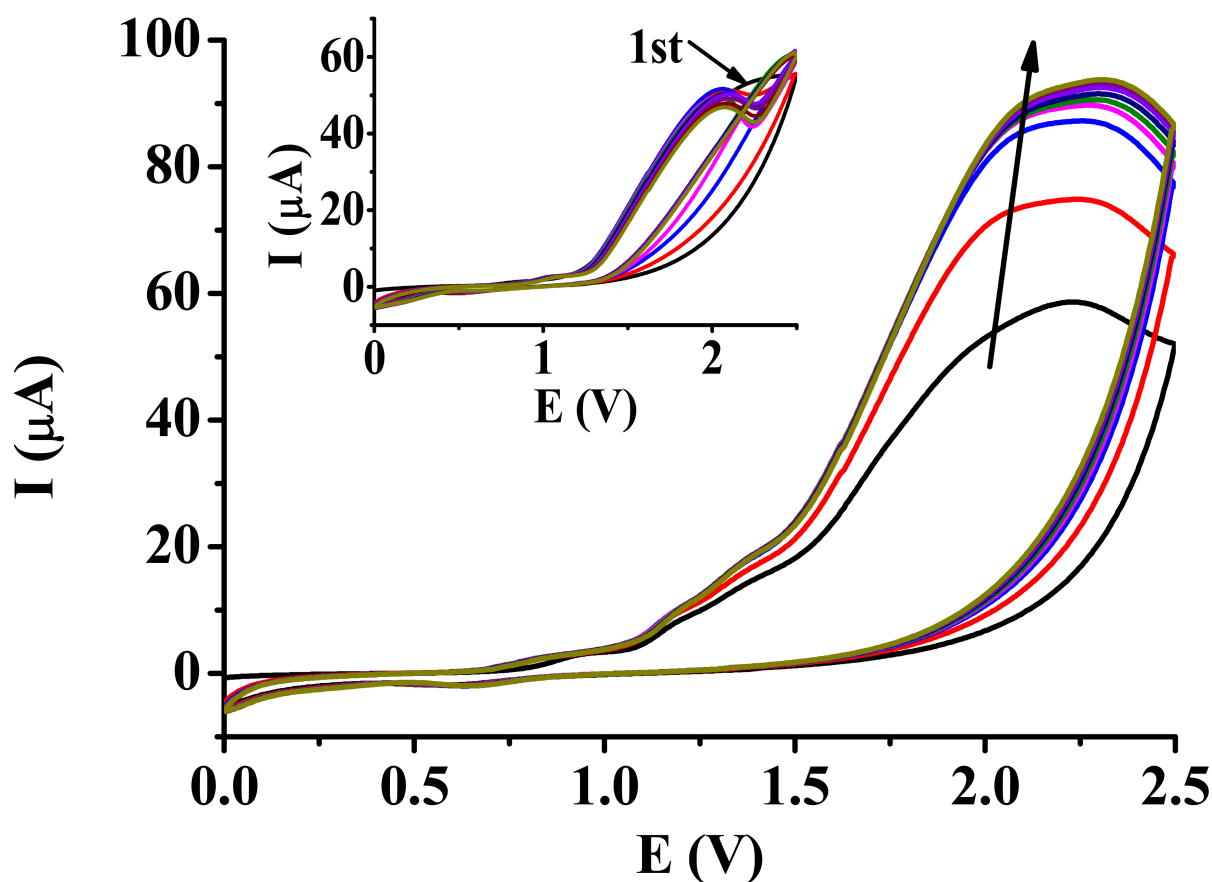
Figure 5. Repetitive cyclic voltammetric curves recorded in a solution prepared with mesityl oxide containing 20 mM 2-phenylphenol and 20 mM cavitand (**1**) (supporting electrolyte = 50 mM TBAP and v = 0.1 V/s; inset graph: the same as with methyl isobutyl ketone).

The micrographs of the deposit of 2-phenylphenol from MIBK and MO reveal some interesting characteristics, which are displayed in Figure 6. They are also proof demonstrating that thick and coherent films build up in substrate concentrations of approximately 50 mM or higher. Brown deposits could not be seen at 20 mM concentrations by the naked eye. Stackings of electrosynthesized polymers were observed in each case, but there were remarkable differences between the two solvents. Many small spherical-shaped particles formed in methyl isobutyl ketone, but they decreased in number when electrodeposition was carried out in the presence of cavitand (**1**). This is also a sign that the cavitand modifies the electrochemical polymerization of phenylphenols. These small particles could not be seen when the electropolymerization was carried out in MO and the materials were concentrated mainly in higher building blocks.

Figure 6. *Cont.*
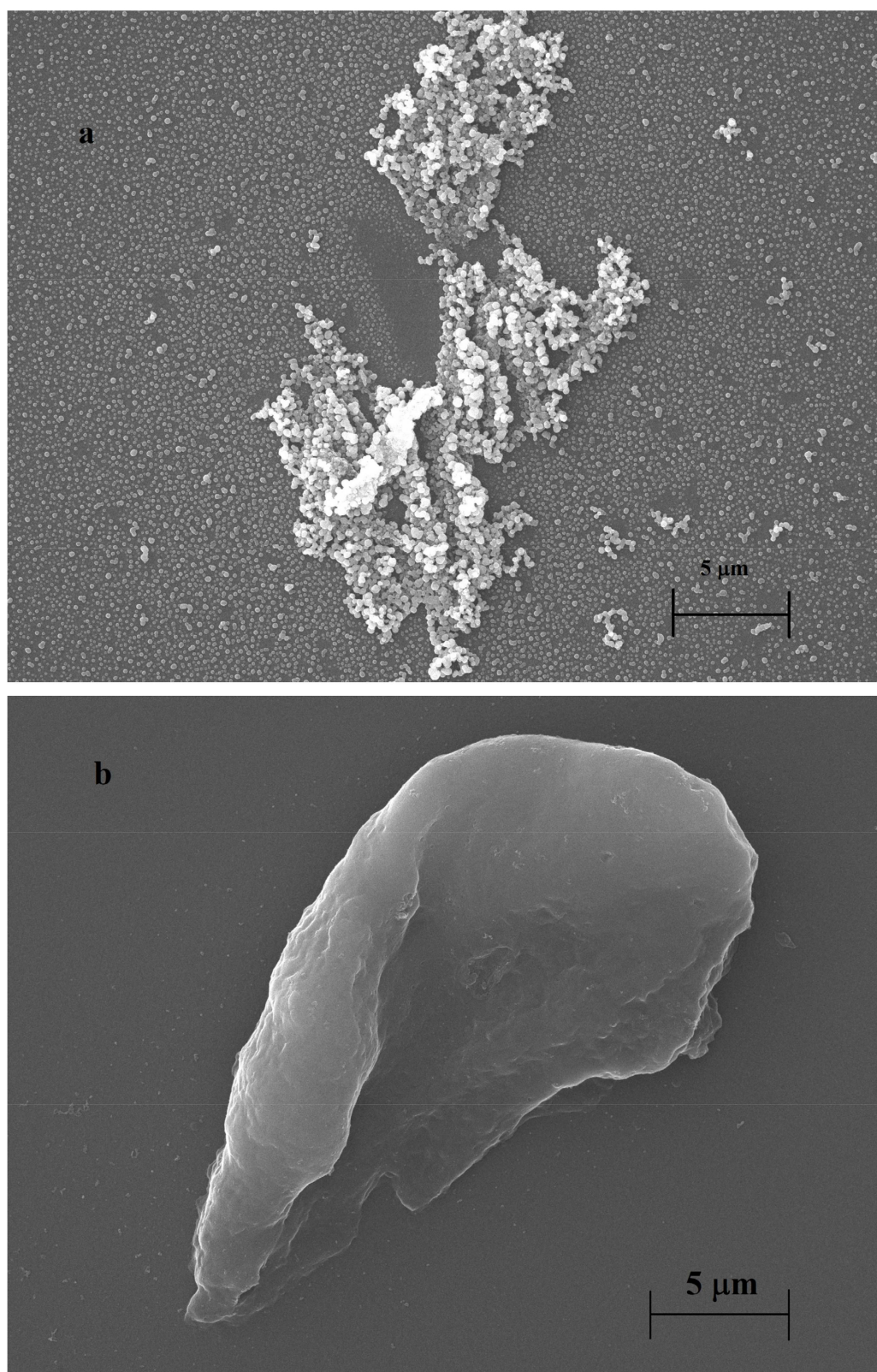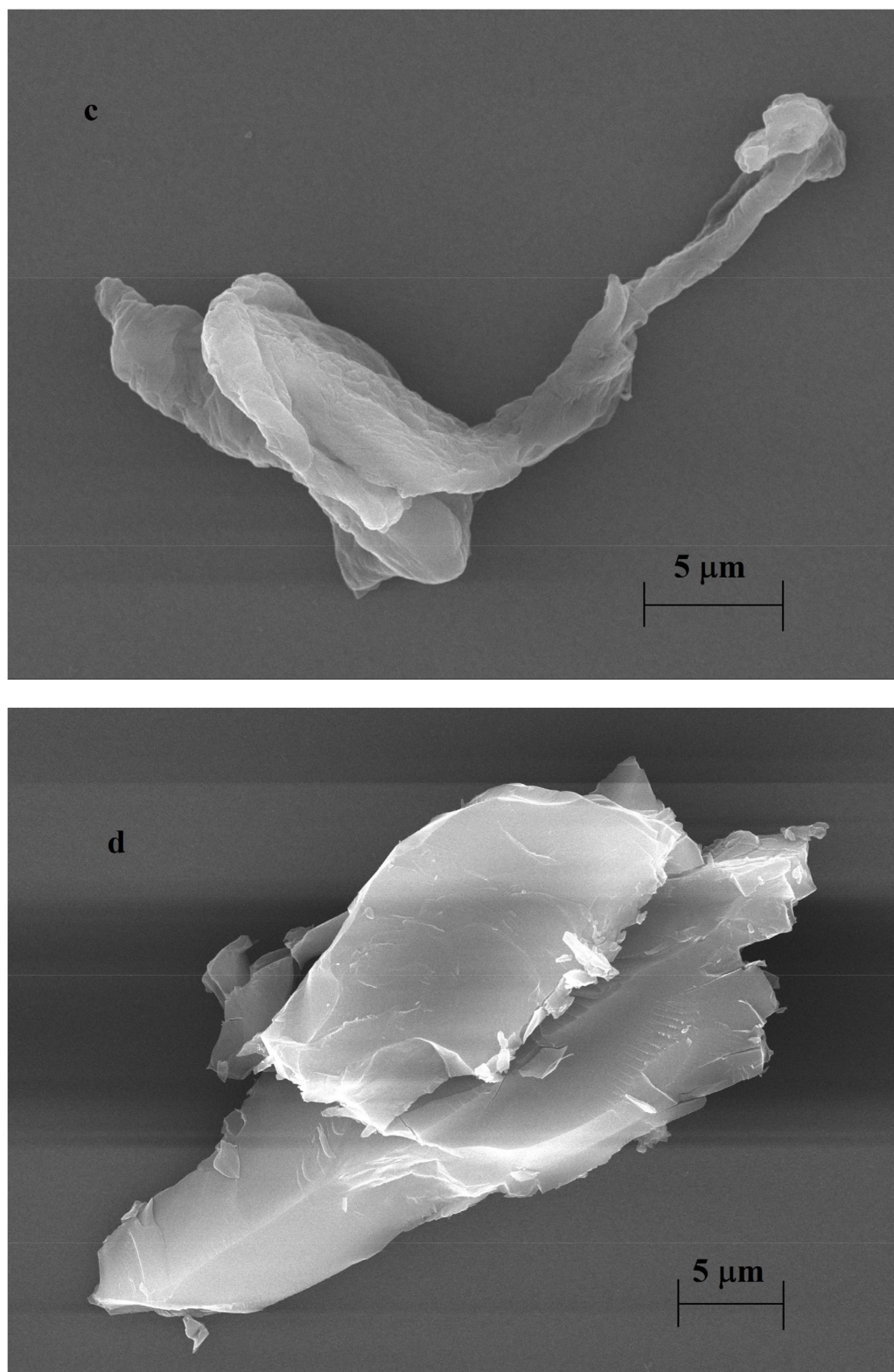
Figure 6. SEM micrographs of deposits of poly(2-phenylphenol) from MIBK (**a**); copolymer of 2-phenylphenol with cavitand (**1**) from MIBK (**b**); poly(2-phenylphenol) from MO (**c**); copolymer of 2-phenylphenol and cavitand (**1**) (**d**) (concentration of the substrates = 20 mM, electrode = ITO-coated glass slide, and acceleration voltage = 30 kV).

3.2. Analytical Performance of the Prepared Films as a Modifying Layer

Many modifying layers can improve the applicability of electrodes in the analysis of selected compounds; therefore, the different deposits were compared in the analysis of 4-chlorophenol and 4-methoxyphenol. Earlier, we found that the oxidation potential of these phenols differed remarkably [23]; thus, they could be detected selectively in their coexistence. As 4-methoxyphenol also has a weak susceptibility to fouling in aqueous environments at concentrations that are not too high, its voltammograms were used for displaying the curves so that the layers could be characterized. However, it is important to mention that 4-chlorophenol also exhibited reproducible voltammograms in nonaqueous solvents up to certain mmol/L concentrations; thus, the effects of the conditions on its analytical signal in such environments will be elevated as well. The results with a modifying layer prepared from 2-phenylphenol and with copolymerization from 2-phenylphenol and cavitand (**1**) in mesityl oxide is displayed (Figure 7).

The voltammetric curves of 4-methoxyphenol taken in an aqueous solution show that with the modified electrodes no anodic peak appeared, and they had a similar shape as was recorded in the background solution (Figure 7a). This suggests that the modifying layers had high hydrophobicity, indicating also that their presence on the platinum was highly disadvantageous. Furthermore, the results indicate that a thin organic layer was present on the surface of the platinum electrode. Contrarily, in the acetonitrile solutions, peaks appeared with the modified electrodes at approximately also the same potential as with the bare electrode (Figure 7b). Moreover, the peak currents were higher for all of the modified electrodes. Comparing the microscopic results with the voltammetric ones, the substrates accumulated on the stackings, causing an increase in the peak currents, attributable partly to cavitand (**1**). The organic layer of 2-phenylphenol, itself, contributed to the increased analytical signal.
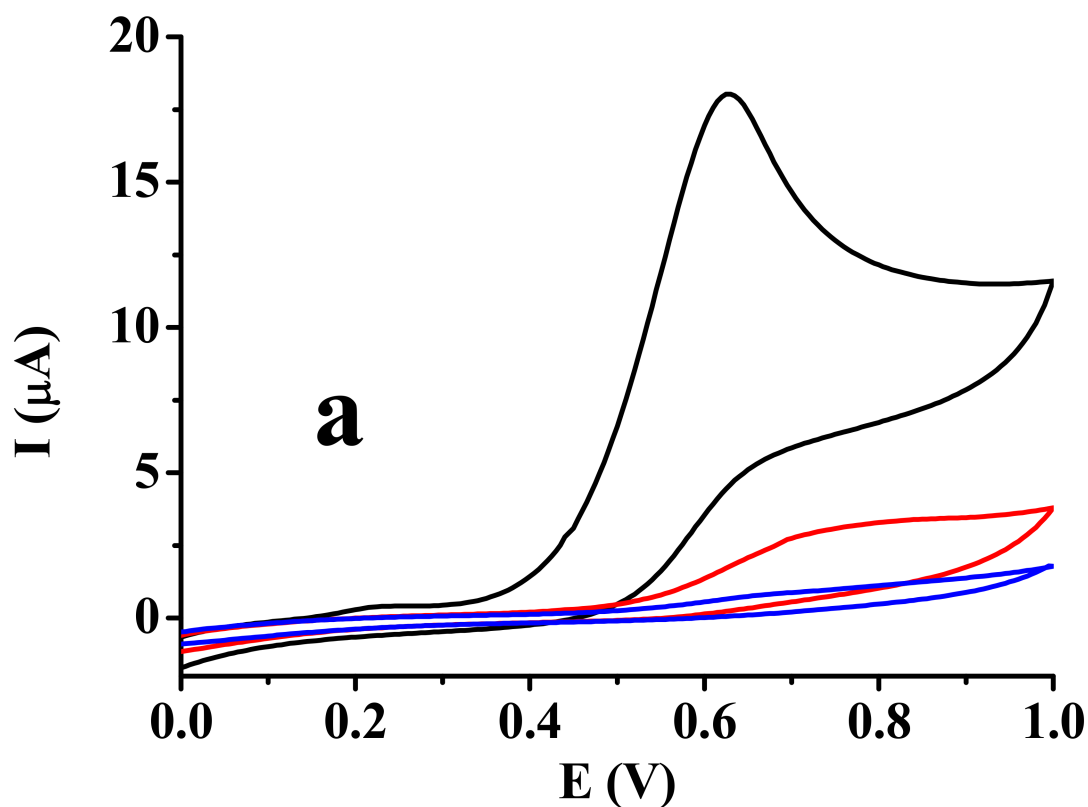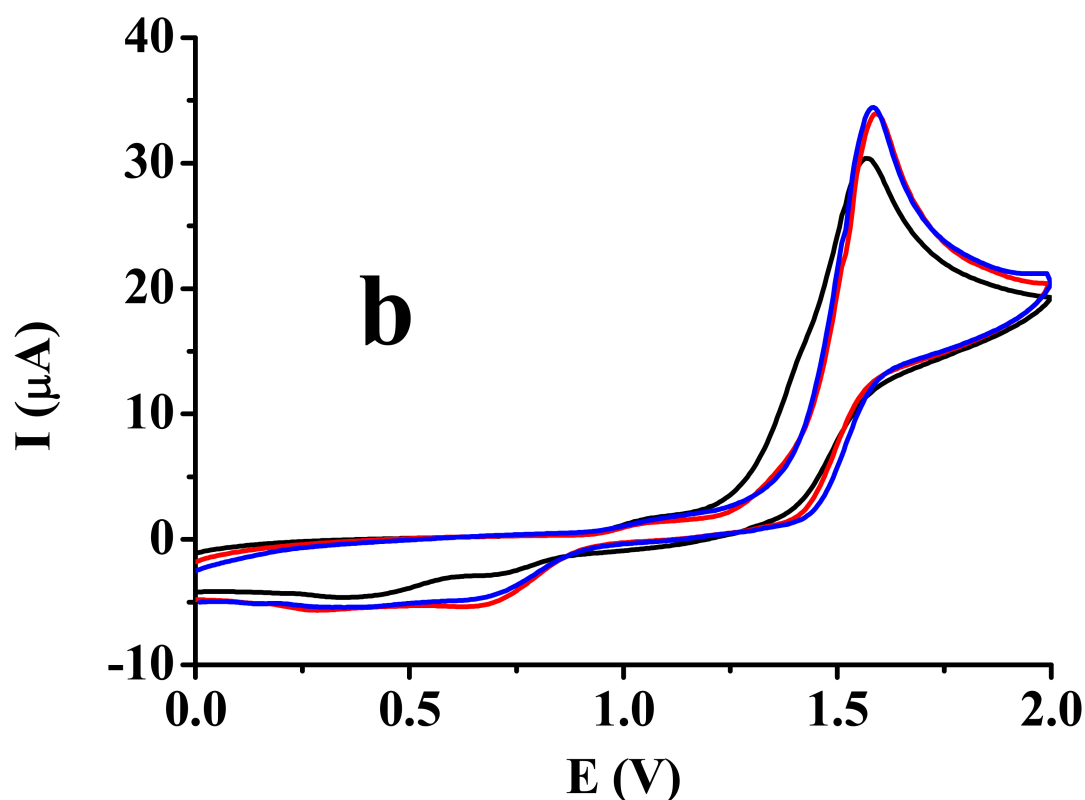

Figure 7. *Cont.*

Figure 7. Cyclic voltammograms of 5 mM 4-methoxyphenol in the aqueous phase (**a**) (supporting electrolyte = 0.1 M at pH = 7 in phosphate buffer) and in acetonitrile (**b**) (supporting electrolyte = 20 mM TBAP) (v = 0.1 V/s; black curve = bare electrode; red curve = electrode modified with poly(2-phenylphenol); blue curve = electrode modified with poly(2-phenylphenol) copolymer with the cavitand (**1**)).

By comparing the modifying layers, it is remarkable that there was only a subtle difference between the polymer prepared electrochemically from 2-phenylphenol and the polymer codeposited from 2-phenylphenol and cavitand (**1**). As 2-phenylphenol is able to bind to other molecules through π–π interactions and, therefore, the resulting polymer with electrooxidation also has aromatic moieties, both of them accommodated readily in the cavity of the cavitand. The latter will be engaged in the prepared layer. As a matter of fact, a segment of the polyphenol oligomer will occupy the inside cavity of the macromolecule. The polymer structure of 2-phenylphenol enables surrounding by multiple aromatic molecules through aromatic segments responsible for signal enhancement.

The above experiments were repeated with the other phenylphenol isomers in mesityl oxide and methyl isobutyl ketone as well. The corresponding data were collected for the two analytes (i.e., 4-methoxyphenol and 4-chlorophenol) in Table 1.

Table 1. Recoveries in % of 4-methoxyphenol and 4-chlorophenol with the electrodeposited films.

Modifying Layer	4-Methoxyphenol	4-Chlorophenol
poly(2-phenylphenol) MIBK	92.55	83.44
poly(2-phenylphenol) MIBK + CAV (**1**)	98.54	91.21
poly(2-phenylphenol) MO	111.52	100.63
poly(2-phenylphenol) MO + CAV (**1**)	113.37	104.45
poly(3-phenylphenol) MIBK	92.68	86.77
poly(3-phenylphenol) MIBK + CAV (**1**)	92.57	79.24
poly(3-phenylphenol) MO	103.84	99.28
poly(3-phenylphenol) MO + CAV (**1**)	104.57	100.49
poly(4-phenylphenol) MIBK	94.53	87.01
poly(4-phenylphenol) MIBK + CAV (**1**)	90.29	91.66
poly(4-phenylphenol) MO	105.88	100.67
poly(4-phenylphenol) MO + CAV (**1**)	106.03	100.28

The recovery data show a pronounced difference between the two solvents, as in each case, the layer deposited from methyl isobutyl ketone exhibited a predominant role in hindering the diffusion influencing the magnitude of the analytical signal of the selected phenols. On the contrary, all layers exhibited some accumulation of analytes prepared in mesityl oxide. In the case of polymers prepared in methyl isobutyl ketone, the tortuosity effect predominately contributed to the decline in the current signals, but, of course, analyte molecules can accumulate also at these deposits; however, their majority is far from the electrode.

As differential pulse voltammetry provides the possibility for the sensitive determination of compounds, calibration was carried out for the selected phenols (Figure 8). This technique uses potential pulses superposed on the potential scanning, extracting the Faradaic current and minimizing the effect of the condenser current. The latter is due to the continuously changing potential. After optimization of the parameters, the curves were recorded in acetonitrile solutions between 0 and 2 V, where the concentrations ranged from 0 to 500 μM. Under the same conditions, as mentioned earlier, the modifying layer was prepared with ten successive scans with cyclic voltammetry. Before any analytical procedure, additional differential pulse voltammetric measurements had to be carried out with the freshly prepared layer, as the currents closer to 2 V dropped significantly in the first measurements. When the curves did not display a decreasing tendency, the modified electrode was capable for quantification experiments. The curve of 4-methoxyphenol showed a linear dependence in the peak currents over the entire concentration range but only from approximately 100 μM in the case of 4-chlorophenol. The $3\sigma/S$ criterion can be used for 4-methoxyphenol due to the linear dependence; therefore, a 9.28 μM detection limit could be established for it (S: slope of the calibration curve; σ; scattering of the background signal). On the contrary, the detection limit for 4-chlorophenol could be determined graphically as the crossing point of the straight line of the best fit of the linear stage and horizontal line at $c = 0$ μM. With this method, a detection limit of 50.8 μM was obtained. The reason for this high value was partly due to the high background currents measured at close to 2 V. Lower adsorption capabilities of the layer towards this phenol derivative are shown in Table 1.
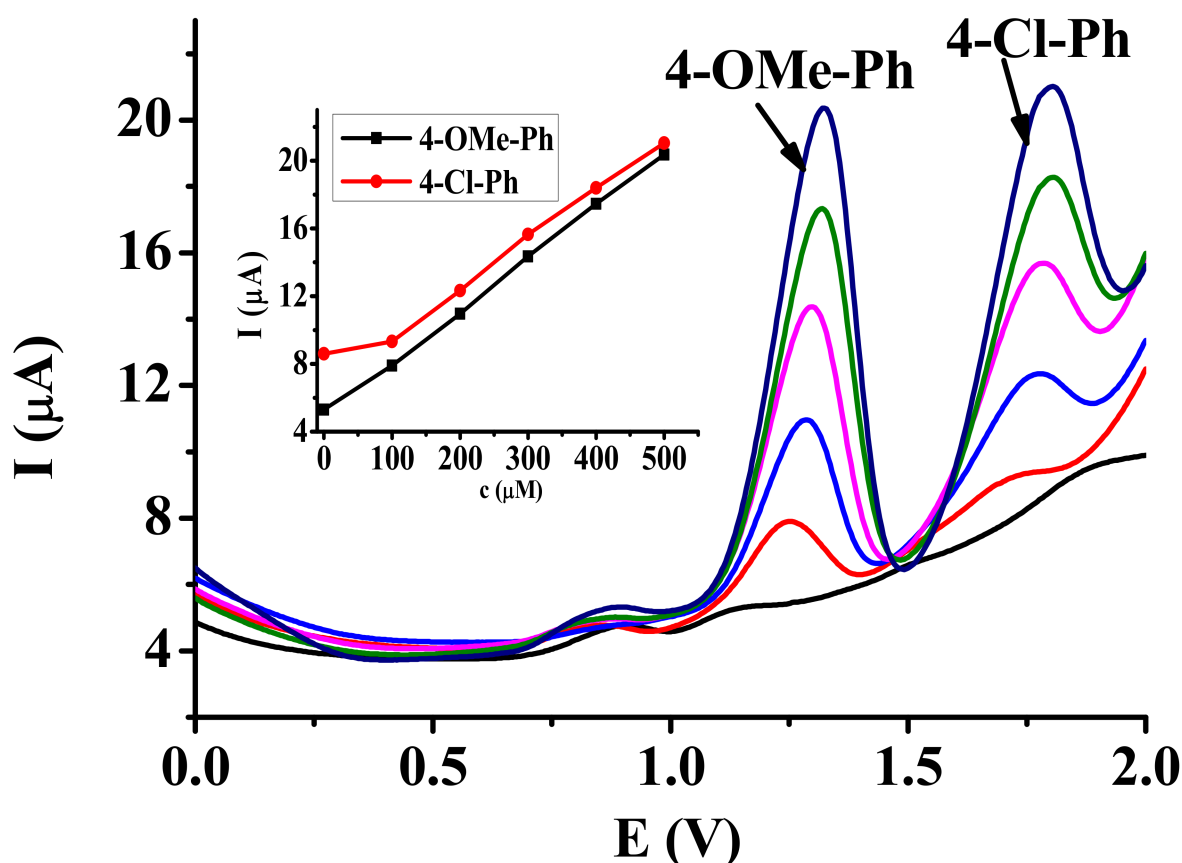
Figure 8. Differential pulse voltammograms of 4-methoxyphenol (4-OMe-Ph) and 4-chlorophenol (4-Cl-Ph) with a modifying layer as the copolymer of 2-phenylphenol and cavitand (**1**) (E_{step} = 0.04 V, E_{pulse} = 0.25 V, t_{pulse} = 5 ms, and v = 0.04 V/s; inset graph = calibration curves).

4. Conclusions

The obtained results showed that electrochemical copolymerization of a cavitand with other monomers enhances the stronger binding of smaller molecules to the modifying layer. The involvement of a cavitand in a polymer film, therefore, contributes to the enhancement of the analytical signals. On the other hand, the discussed polymer layers are useful only in organic solvents; therefore, one of our future plans is to determine more hydrophilic layers with favorable porosity. These findings provide additional proof of the usefulness of mesityl oxide as a solvent in electrodeposition.

Data Availability Statement: The data presented in this study are available on request from the corresponding author.

Conflicts of Interest: The authors declare no conflict of interest.

References

1. Baranowska, I.; Bijak, K. Voltammetric determination of disinfectants at multiwalled carbon nanotube modified glassy carbon electrode. *J. Anal. Chem.* **2013**, *68*, 891–895. [CrossRef]
2. Karimi-Maleh, H.; Fakude, C.T.; Mabuba, N.; Peleyeju, G.M. The determination of 2-phenylphenol in the presence of 4-chlorophenol using nano-Fe$_2$O$_3$/ionic liquid paste electrode as an electrochemical sensor. *J. Colloid Interf. Sci.* **2019**, *554*, 603–610. [CrossRef] [PubMed]
3. Li, H.; Li, J.; Meng, D.; Peng, J.; Qiao, Q.; Yang, Z.; Xu, Q.; Hu, X. Sodium dodecyl sulfate sensitized electrochemical method for subnanomole level determination of ortho-phenylphenol at a novel disposable electrode. *Sci. China Chem.* **2011**, *54*, 1116–1122. [CrossRef]
4. Jeong, H.; Choi, E.; Kang, S.; Nam, K.; Jeon, S. Electrochemistry of a urea-functionalized calix[4]diquinone sulfate-anion selective receptor. *J. Electroanal. Chem.* **2000**, *485*, 154–160. [CrossRef]
5. Guo, D.; Wang, K.; Liu, Y. Selective binding behaviours of *p*-sulfonatocalixarenes in aqueous solution. *J. Incl. Phenom. Macrocycl. Chem.* **2008**, *62*, 1–21. [CrossRef]
6. Li, Y.; Csók, Z.; Szuroczki, P.; Kollár, L.; Kiss, L.; Kunsági-Máté, S. Fluorescence quenching studies on the interaction of a novel deepened cavitand towards some transition metal ions. *Anal. Chim. Acta* **2013**, *799*, 51–56. [CrossRef]
7. Wang, F.; Chi, C.; Yu, B.; Ye, B. Simultaneous voltammetric determination of dopamine and uric acid based on Langmuir-Blodgett film of calixarene modified glassy carbon electrode. *Sensor Actuat. B Chem.* **2015**, *221*, 1586–1593. [CrossRef]
8. Maity, D.; Chakraborty, A.; Gunupuru, R.; Paul, P. Calix[4]arene based molecular sensors with pyrene as fluoregenic unit: Effect of solvent in ion selectivity and colorimetric determination of fluoride. *Inorg. Chim. Acta* **2011**, *372*, 126–135. [CrossRef]
9. Wang, F.; Wu, Y.; Lu, K.; Ye, B. A simple but highly sensitive and selective calixarene-based voltammetric sensor for serotonin. *Electrochim. Acta* **2013**, *87*, 756–762. [CrossRef]
10. Pailleret, A.; Arrigan, D.W. Electrochemical oxidation of a tetraester calix[4]arene. *Electrochem. Commun.* **2001**, *3*, 24–27. [CrossRef]
11. Skinner, A.V.; Han, S.; Balasubramanian, R. Rapid selective colorimetric sensing of polyphosphates by ionic calixarene cavitand interdigitated gold nanoparticles. *Sensor Actuat. B Chem.* **2017**, *247*, 706–712. [CrossRef]
12. Vaze, V.D.; Srivastava, A.K. Electrochemical behaviour of folic acid at calixarene based chemically modified electrodes and its determination by adsorptive stripping voltammetry. *Electrochim. Acta* **2007**, *53*, 1713–1721. [CrossRef]
13. Liska, A.; Rosenkranz, M.; Klíma, J.; Dunsch, L.; Lhoták, P.; Ludvík, J. Formation and proof of stable bi-, tri- and tetraradical polyanions during the electrochemical reduction of *cone*-polynitrocalix[4]arenes. An ESR-UV-vis spectroelectrochemical study. *Electrochim. Acta* **2014**, *140*, 572–578. [CrossRef]
14. Kiss, L.; Kovács, F.; Li, H.; Kiss, A.; Kunsági-Máté, S. Electrochemical polymerization of phenol on platinum and glassy carbon electrodes in mesityl oxide. *Chem. Phys. Lett.* **2020**, *754*, 137642. [CrossRef]
15. Kiss, L.; Kovács, F.; Kunsági-Máté, S. Investigation of anodic behaviour of phenylethers in non-aqueous solvents on platinum and glassy carbon electrodes. *J. Iran. Chem. Soc.* **2021**, *18*, 1677–1687. [CrossRef]
16. Preisz, Z.; Nagymihály, Z.; Kollár, L.; Kálai, T.; Kunsági-Máté, S. Weak Interactions of the Isomers of Phototrexate and Two Cavitand Derivatives. *Int. J. Mol. Sci.* **2021**, *22*, 10764. [CrossRef]
17. Pailleret, A.; Herzog, G.; Arrigan, D.W. Electrochemical activity of phenolic calixarenes. *Electrochem. Commun.* **2003**, *5*, 68–72. [CrossRef]
18. Meddeb-Limem, S.; Besbes-Hentati, S.; Said, H.; Bouvet, M. From the electrochemical generation of calix[4]arenedihydroquinone to the electrodeposition of calix[4]arenediquinone-calix[4]arenedihydroquinone assembly. *Electrochim. Acta* **2011**, *58*, 372–382. [CrossRef]
19. Buffenoir, A.; Bidan, G.; Chalumeau, L.; Soury-Lavergne, I. Immobilisation at an electrode surface of calix[4]arenes bearing electropolymerisable pyrrole moieties at the upper rim. *J. Electroanal. Chem.* **1998**, *451*, 261–266. [CrossRef]
20. Chen, Z.; Gale, P.A.; Beer, P.D. Synthesis and electropolymerization of calix[4]arenes containing *N*-substituted pyrrole moieties. *J. Electroanal. Chem.* **1995**, *393*, 113–117. [CrossRef]
21. Collyer, S.D.; Davis, F.; Lucke, A.; Stirling CJ, M.; Higson SP, J. The electrochemistry of the ferri/ferrocyanide couple at a calix[4]resorcinarenetetrathiol-modified gold electrode as a study of novel electrode modifying coatings for use within electro-analytical sensors. *J. Electroanal. Chem.* **2003**, *549*, 119–127. [CrossRef]
22. Pan, G.; Wan, L.; Zheng, Q.; Bai, C.; Itaya, K. Self-organized arrays of calix[4]arene and calix[4]arene diquinone disulphide on Au(111). *Chem. Phys. Lett.* **2002**, *359*, 83–88. [CrossRef]
23. Kiss, L.; Kunsági-Máté, S. Effect of anodic pretreatment on the performance of glassy carbon electrode in acetonitrile and electrooxidation of para-substituted phenols in acetonitrile on platinum and glassy carbon electrode. *Period. Polytech. Chem.* **2021**, *65*, 133–138. [CrossRef]

Article

Weak Interactions of the Isomers of Phototrexate and Two Cavitand Derivatives

Zsolt Preisz [1,2], Zoltán Nagymihály [3,4], László Kollár [3,4], Tamás Kálai [1,3] and Sándor Kunsági-Máté [1,3,*]

[1] Faculty of Pharmacy, Institute of Organic and Medicinal Chemistry, University of Pécs, Szigeti 12, 7624 Pécs, Hungary; preisz.zsolt@pte.hu (Z.P.); tamas.kalai@aok.pte.hu (T.K.)
[2] Department of Physical Chemistry and Materials Science, Faculty of Sciences, University of Pécs, Ifjúság 6, 7624 Pécs, Hungary
[3] János Szentágothai Research Center, University of Pécs, Ifjúság 20, 7624 Pécs, Hungary; nmzoltan@gamma.ttk.pte.hu (Z.N.); kollar@gamma.ttk.pte.hu (L.K.)
[4] Department of Inorganic Chemistry, Faculty of Sciences, University of Pécs, Ifjúság 6, 7624 Pécs, Hungary
[*] Correspondence: sandor.kunsagi-mate@aok.pte.hu

Abstract: The interactions of two conformers of newly synthesized photoswitchable azobenzene analogue of methotrexate, called Phototrexate, with two cavitand derivatives, have been investigated in dimethyl sulfoxide medium. Photoluminescence methods have been applied to determine the complex stabilities and the related enthalpy and entropy changes associated to the complex formation around room temperature. Results show opposite temperature dependence of complex stabilities. The structure of the upper rims of the host molecules and the reordered solvent structure were identified as the background of the opposite tendencies of temperature dependence at molecular level. These results can support the therapeutic application of the photoswitchable phototrexate, because the formation of inclusion complexes is a promising method to regulate the pharmacokinetics of drug molecules.

1. Introduction

Cancer is among the leading causes of death worldwide. Before the 1940s, only surgical therapy existed to treat cancer. It was demonstrated for the first time in 1942 that chemotherapy can induce tumor regression [1]. In the late 1940s, it was found that antimetabolites that inhibit the function of folate-requiring enzymes can induce remission in children with acute lymphoblastic leukaemia. These antimetabolites are the inhibitors of the enzyme dihydrofolate reductase (DHFR) and cause decreasing thymidylate synthesis which ultimately inhibits DNA synthesis [1].

Methotrexate (4-amino-10-methylfolic acid, MTX, Figure 1) is the most important antimetabolite chemotherapeutic agent, it is primarily used in acute lymphoblastic leukaemia, in certain lymphomas, osteosarcoma and choriocarcinoma [1]. In the 1980s, it was discovered that, at low doses, MTX has "steroid-like" anti-inflammatory and immunosuppressant effects and, in 1985, it was clinically demonstrated to be a potent and effective treatment in psoriatic arthritis and rheumatoid arthritis, so, nowadays, it is a first line drug for these autoimmune diseases [2].

However, MTX and other chemotherapeutic agents can cause several adverse effects, because they affect every fast dividing cell of the body. Some toxicities are unrelated to folate antagonism and cannot be prevented by folate supplementation. These include nodulosis, hepatic fibrosis, pulmonary fibrosis, lethargy, fatigue, and renal insufficiency [3]. Association has been found between MTX use and increased risk for melanoma, lung cancer and non-Hodgkin lymphoma [4].

Alternative strategies to overcome low therapeutic indices, nonspecific targeting, and the off target toxicity of chemotherapeutics have emerged over the last years [5,6]. One

interesting and recent research field is photopharmacology. The principle of photopharmacology is the introduction of a photoswitchable unit into the molecular structure of a bioactive compound itself [7]. One major advantage of photopharmacological agents is that their activation is reversible, which may lead to a significant reduction in adverse drug reactions [8]. In general, this strategy uses molecules that can be efficiently excited to the more active form and spontaneously reisomerize to the less active isomer. The biological functions of photopharmacological molecules can be controlled with synthetic photoswitches. Photoswitches are chromophores that can be reversibly isomerized when exposed to light. Azobenzene is the most widely used photoswitch in biological applications because of the ease of synthesis and functionalization, fast photoisomerization, and low rate of photobleaching [9,10].
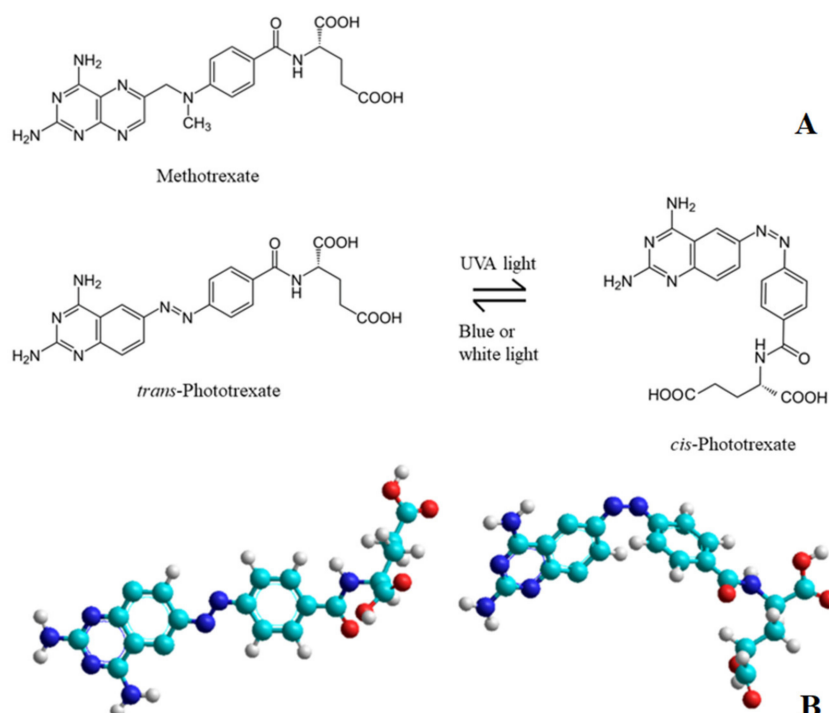
Figure 1. (**A**) Chemical structures of Methotrexate (MTX), *trans*-Phototrexate (*trans*-PHX) and *cis*-Phototrexate (*cis*-PHX) and the reversible isomerization of PHX [11]. (**B**) The 3D structure of the two isomers of the PHX: *trans*-PHX (**left**) and *cis*-PHX (**right**).

Phototrexate (PHX, Figure 1) is a photoswitchable azobenzene analogue of MTX that has been synthesized and described by Matera et al. [11] and by Mashita et al. [12]. PHX contains a diazene stereogenic unit and its pharmacological activity is higher in its *cis* state than in the thermodynamically more stable *trans* state. It can be effectively isomerized from *trans* to *cis* with UVA light and isomerized back from *cis* to *trans* with blue or white light (Figure 1). This transition is reversible and can be repeated several times. The antineoplastic effect (and, also, the adverse effects caused by the cytotoxic activity) appears only in light exposed regions and decreases in dark regions [11]. Target tissues might be those that can be exposed to UV illumination, primarily the skin, the digestive, respiratory and reproductive tracts.

Calixarenes are cyclic oligomer molecules that consist of phenolic units that are condensated in the presence of an aldehyde and linked to each other, typically through a methylene bridge, in an acidic environment [13,14]. They are widely used as host molecules in supramolecular chemistry, separation science and catalysis. They also have pharmaceutical applications as host molecules [14]. Substituents appended to the phenolic rings (upper or lower rim) can greatly influence the physical and chemical properties of

these molecules, but numerous derivatives have been synthesized that have functional groups on the periphery of the molecule, too [15]. Promising results have been described in the literature about calixarenes that have heterocyclic substituents on the periphery, they can be used as selective extractants for amino acids [16], chiral recognition agents [17] or chelators that trap metals [18]. Calix[4]arene-based P-ligands were used in rhodium-catalyzed hydroformylation [19]. Inserting additional methylene bridges between the phenolic oxygen atoms on adjacent aromatic rings, the structure is called a cavitand.

No study has been found in the literature that describes the host–guest complex formation or any weak molecular interaction of PHX, so cavitand–PHX interactions are an entirely unrevealed research field. Therefore, in this work, the thermodynamic parameters of the interaction of PHX with tetrakis(androst-4-en-3-one-17α-ethinyl)-cavitand (TAC) and tetrakis(3,5-dicarboxylatophenoxy)-cavitand (TDC) (Figure 2) were studied. TAC was synthesized as previously described [20]. The synthesis of TDC is based on the Williamson-type ether synthesis, reacting tetrabromo-cavitand [21,22] with dimethyl 5-hydroxyisophthalate, followed by the hydrolysis of the ester functionalities. Fluorimetric measurements were applied to determine the thermodynamic parameters of the PHX–cavitand complex formation reaction.
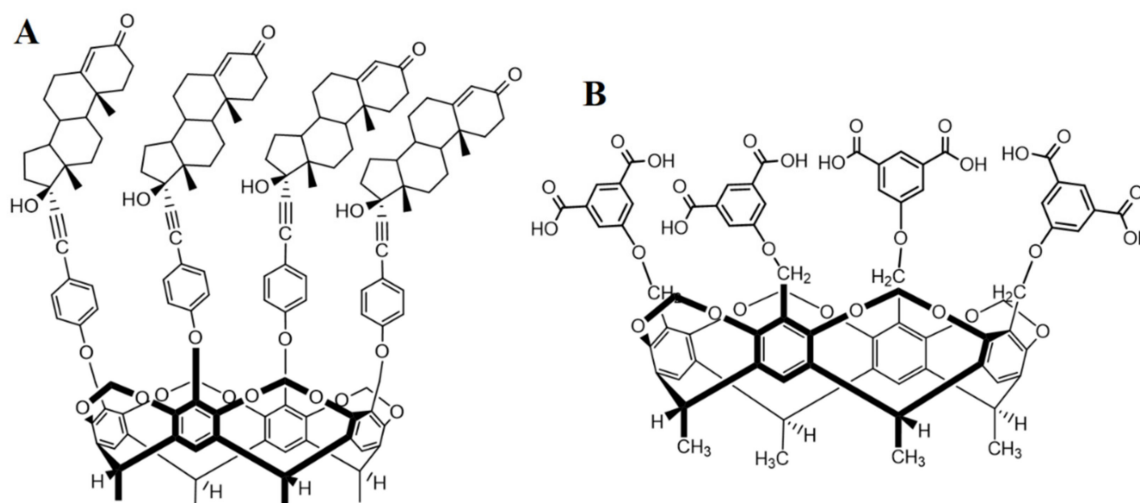
Figure 2. Chemical structures of the macrocyclic host molecules TAC (**A**) and TDC (**B**) (8-H, 9-H and 13-H of the steroidal skeleton are omitted for clarity).

2. Results

2.1. Determination of the Association Constants

To investigate the interaction of *cis*-PHX with the cavitand derivatives (TAC and TDC), the complete isomerization of the thermodynamically more stable *trans*-PHX has to be reached. To this purpose, UV light exposure (λ = 366 nm) was used, as in our previous work [23].

The absorption spectra of the isomers of PHX and the cavitand derivatives were registered (Figure 3). The absorption maxima of *cis*- and *trans*-PHX were at around 370 nm, while TDC and TAC showed significantly lower absorption values at this wavelength. Accordingly, applying a 366 nm excitation wavelength, the emission spectra of PHX were recorded.
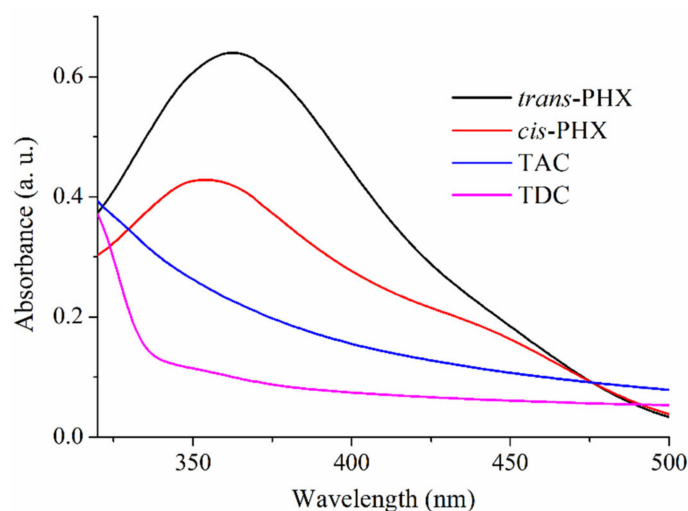
Figure 3. Absorption spectra of *trans*-PHX, *cis*-PHX, TAC and TDC at 50 μM concentration.

The fluorescence spectra of *cis*- and *trans*-PHX show increased emission upon increased concentration of TAC or TDC (Figure 4). The changes induced in the spectra of PHX suggest interactions between the investigated molecules. Samples with different concentrations of the cavitand derivates (0–450 μM) and with constant concentration of *trans*- and *cis*-PHX (50 μM) were prepared and measured using a 366 nm excitation wavelength at 293 K, 298 K, 303 K and 308 K temperatures.
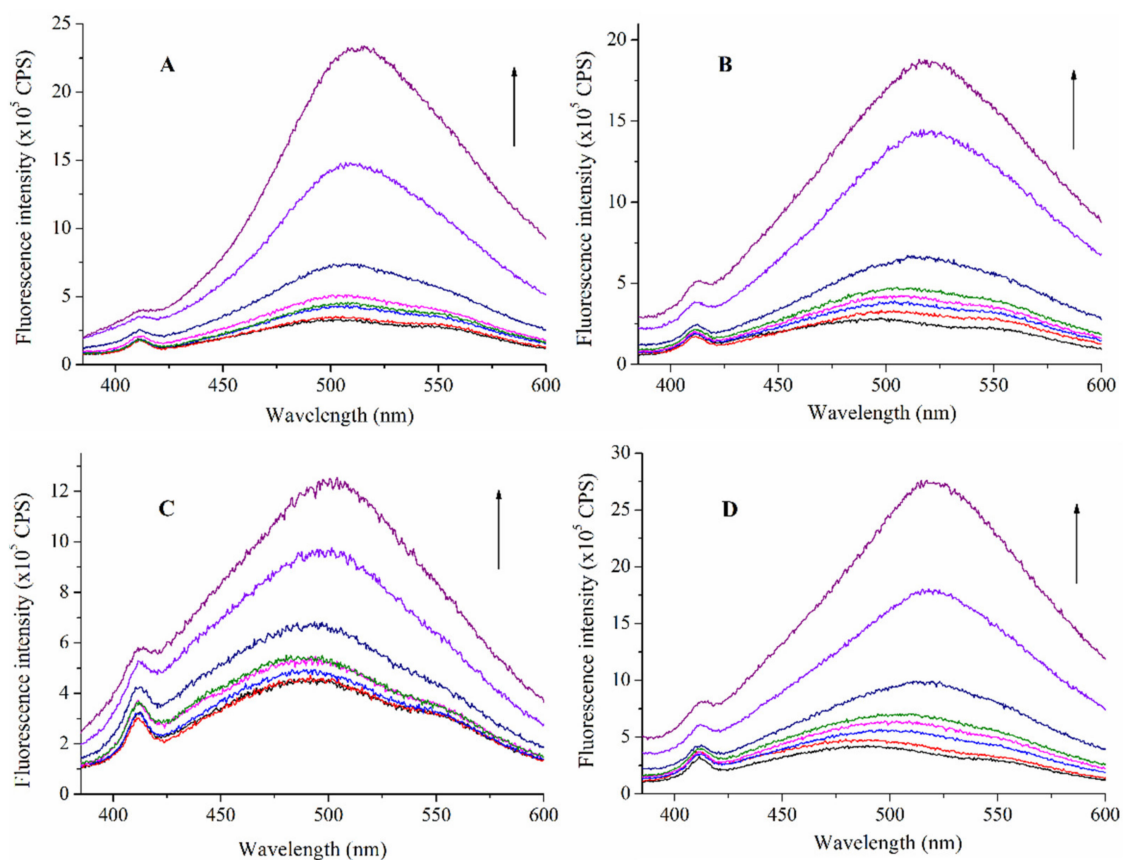
Figure 4. Fluorescence emission spectra of *trans*-PHX (**A,B**) and *cis*-PHX (**C,D**) (50 μM) in the absence and presence of TAC (**A,C**) and TDC (**B,D**) (0–450 μM) (λ_{exc} = 366 nm). The figure depicts the measurements that were carried out at 293 K. Arrows indicate increasing cavitand concentrations. Colors only support the clarity.

The stability constants of the *trans*-PHX-TAC, *trans*-PHX-TDC, *cis*-PHX-TAC and *cis*-PHX-TDC have been determined using the Benesi–Hildebrand method. To determine the thermodynamic parameters, the stability constants have been calculated at temperatures 293 K, 298 K, 303 K and 308 K. In all cases, the intensity values obtained at 490 nm have been used to evaluate the data. Table 1 summarizes the results. The determined stability constants were then used to calculate the thermodynamic parameters (ΔH, ΔS, and ΔG) of the interactions (Table 2).

Table 1. Stability constants of the investigated interactions determined at different temperatures.

Temperature (K)	log K			
	trans-PHX-TAC	*trans*-PHX-TDC	*cis*-PHX-TAC	*cis*-PHX-TDC
293	3.55 ± 0.19	3.05 ± 0.15	2.07 ± 0.17	3.08 ± 0.25
298	3.62 ± 0.21	2.95 ± 0.19	2.40 ± 0.21	3.03 ± 0.21
303	3.89 ± 0.18	2.88 ± 0.17	2.78 ± 0.22	2.90 ± 0.22
308	4.01 ± 0.20	2.73 ± 0.16	3.01 ± 0.20	2.88 ± 0.18

Table 2. Thermodynamic parameters of the complex formation between the cavitands and the isomers of PHX. ΔG values have been determined for 298 K.

	ΔH (kJ·mol^{-1})	ΔS (J·K^{-1}·mol^{-1})	ΔG (kJ·mol^{-1})
trans-PHX-TAC	57.30 ± 2.84	262.97 ± 11.36	-21.10 ± 4.03
trans-PHX-TDC	-35.97 ± 3.69	-64.10 ± 10.43	-16.85 ± 3.21
cis-PHX-TAC	109.65 ± 6.93	414.12 ± 17.51	-13.83 ± 3.35
cis-PHX-TDC	-24.88 ± 3.20	-25.94 ± 4.72	-17.15 ± 3.62

The Van 't Hoff plots of the investigated interactions have been created by plotting the logarithms of the stability constants against the reciprocal temperatures (Figure 5). It can be observed that the thermodynamic parameters of the complex formation of the two cavitand derivates differ significantly.
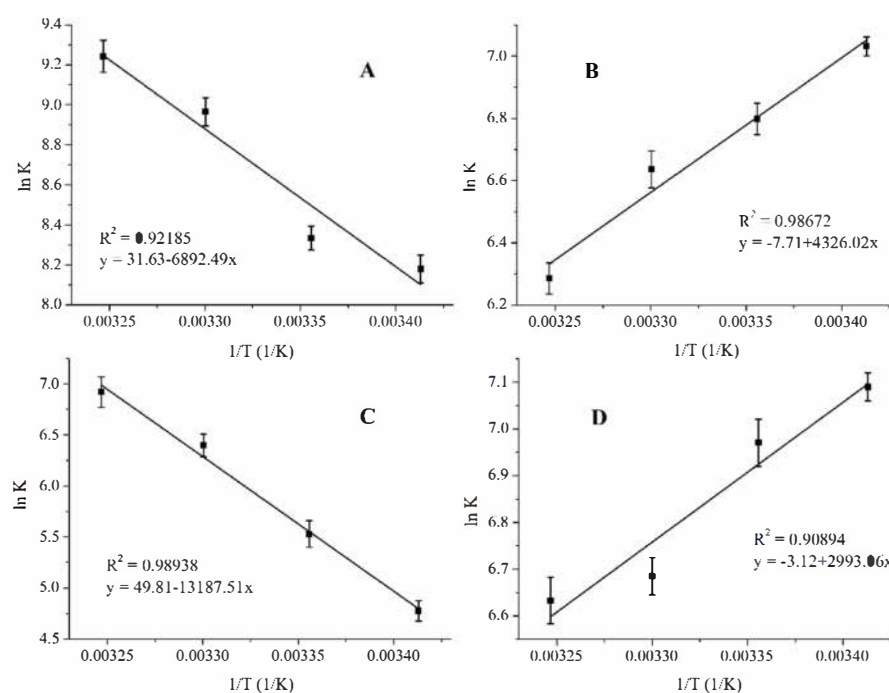
Figure 5. Van 't Hoff plots of the complex formation of *trans*-PHX and TAC (**A**), *trans*-PHX and TDC (**B**), *cis*-PHX and TAC (**C**) and *cis*-PHX and TDC (**D**).

These results imply different complex formation mechanisms for the different cavitand derivates (TAC and TDC). In the presence of TAC, entropy gain is associated with enthalpy gain, while in the samples containing TDC, entropy loss is associated with enthalpy loss.

2.2. Modelling Studies

The calculations, performed to determine the thermodynamic parameters associated with the complex formation of PHX with TAC and TDC molecules, used the explicit solvent model, therefore, motions of solvent molecules were also considered. Table 3 summarizes these results and Figure 6 represents the conformations of the most stable complexes. The agreement of the calculated thermodynamic values and the results of the experiments support the appropriateness of the applied model. Considering the conformations and the accurately determined translation–rotation–vibration terms of the entropy, the translational entropy of the solvent molecules is found to be up to 85 percent responsible for the total entropy gain during formation of PHX–TAC complexes. The contribution of the translational entropy remains high in the case of the formation of PHX-TDC complexes; the decreased vibrational entropy of the dicarboxylatophenoxy moieties reduces the entropy gain.

Table 3. Thermodynamic parameters of the complex formation between the cavitands and the isomers of PHX determined at AM1 level applying the TIP3P solvation model. ΔG values have been calculated for 298 K.

	ΔH (kJ·mol^{-1})	ΔS (J·K^{-1}·mol^{-1})	ΔG (kJ·mol^{-1})
trans-PHX-TAC	42.13	210.99	−20.89
trans-PHX-TDC	−33.63	−58.13	−16.29
cis-PHX-TAC	101.11	392.09	−15.79
cis-PHX-TDC	−23.54	−22.93	−16.70

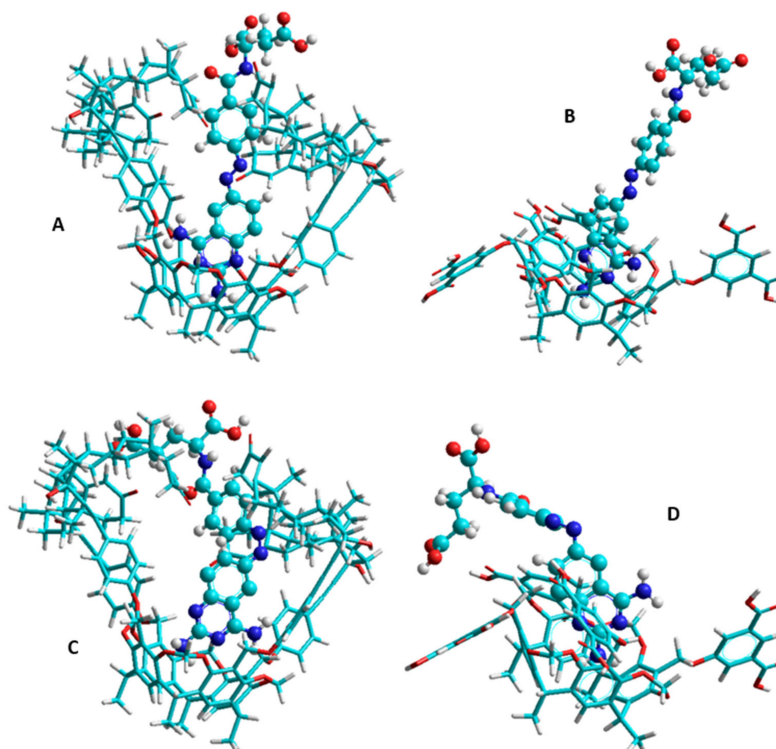**Figure 6.** The 3D structures of the complexes of *trans*-PHX with TAC (**A**), *trans*-PHX with TDC (**B**), *cis*-PHX with TAC (**C**) and *cis*-PHX with TDC (**D**) calculated at AM1 level using the TIP3P solvation model. Solvent molecules are omitted due to the clarity.

3. Discussion

The thermodynamics of the interaction of TAC and TDC molecules with the two isomers of PHX confirm the formation of stable host–guest complexes within the temperature range between 293 K and 308 K in a dimethyl sulfoxide medium. However, the enthalpy and entropy changes associated with the molecular interaction of PHX with TAC and TDC suggest entirely different mechanisms at molecular level. Modelling studies draw attention to the importance of the reorganization and destruction of the solvation shell upon the molecular association, and of the structural properties of the host molecules as well. Accordingly, both the TAC and TDC molecules possess two rims, which are potentially able to bind to the guest molecules: the core skeleton of the cavitands can include guests of an appropriate size, and the functionalized upper rims can also be bound to the guests. In the case of TAC, the large androst-4-en-3-one-17α-ethinyl functions block the entrance of the cavitand cavity prior the interaction with the PHX. This property causes the energy cost of the opening procedure during the interaction, and it results in the positive enthalpy change. As a parallel effect, the removal of the solvent molecules from the solvation shell of the steroidal moieties also costs energy, thereby further increasing the enthalpy change, while the increased freedom of the guest molecules after the leaving of the solvation shell causes the large entropy gain and results in the positive entropy changes of the association process. Modelling studies highlight that about 85 percent of the entropy gain originated from the increased translational freedom of the solvent molecules. This property is more pronounced in the case of *cis*-PHX–TAC complexes. The positive enthalpy and entropy changes, finally, support the formation of stable PHX–TAC complexes, but, considering that the temperature dependence is determined by the enthalpy changes, the stability of the complexes with TAC host increases at higher temperature. In contrast, the interactions of the *cis*- and *trans*-PHX with the TDC molecules are associated with negative enthalpy and entropy changes. This is probably due to the smaller reorganization energies of the 1,3-dicarboxylato-5-phenoxy moieties located at the upper rim of the TDC molecule and also due to the fact that the destruction of the smaller sized solvation shell of the 1,3-dicarboxylato-5-phenoxy arms result less free dimethyl sulfoxide molecules upon the interaction with the PHX guests. It is to be mentioned here, that in this case the increased translational entropy of the solvent molecules cannot overcompensate the reduced entropy of the aforementioned dicarboxylatophenoxy moieties, which is originated from the reduced vibrational freedom of these arms upon complex formation.

Considering the two significantly different complex formation procedures, we can conclude that the opposite temperature dependence of the complex stabilities associated to the formation of PHX-TAC and PHX-TDC complexes is originated from the different functional groups located at the upper rim of the host molecules. Furthermore, the fact that the increased freedom of the solvent molecules can be determinant in the association process is also because dimethylsulfoxide, as a nonprotic solvent, does not form clusters after leaving the solvation shell. Therefore, there is no such process that could decrease the entropy gain.

4. Materials and Methods

4.1. Synthesis of Tetrakis(3,5-dicarboxylatophenoxy)-cavitand (TDC, **3**)

Dimethyl 5-hydroxyisophthalate (2.10 g, 10 mmol) and K_2CO_3 (2.07 g, 15 mmol) were dissolved in 50 mL of DMSO in a 100 mL round bottom flask under argon. The mixture was equipped with a magnetic stirrer and stirred for one hour at room temperature. Subsequently, Tetrabromocavitand **1** [22,23] (964.3 mg, 1.0 mmol) was added to the reaction mixture, the flask was stirred at 80 °C for 18 h under argon atmosphere. The mixture was cooled to room temperature and poured into 250 mL of 2% hydrochloric acid. The precipitate was filtered through a glass filter and washed with ice cold water and small portion of n-hexane, and dried under vacuum at 80 °C. Yield: 1.28 g/84%. The resulting product (Cavitand **2**) was immediately transferred into the following ester hydrolysis (Figure 7.).
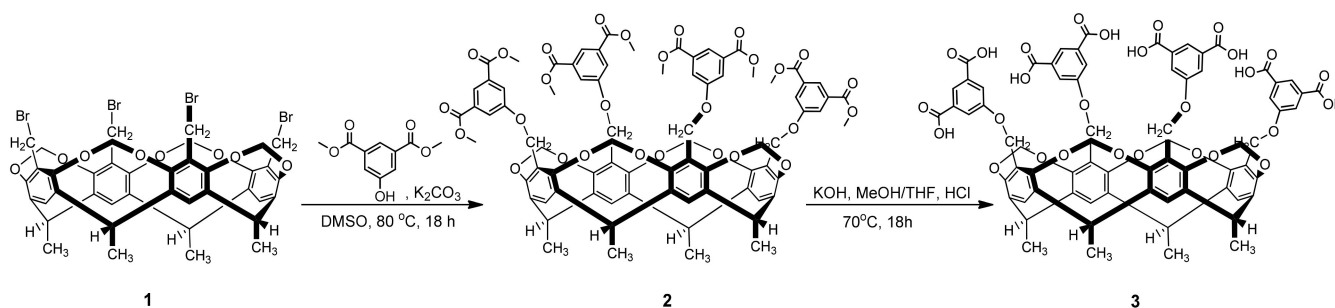
Figure 7. Schematic synthesis of TDC (**3**).

Cavitand **2** (764.8 mg, 0.5 mmol) was dissolved in 20 mL of THF in a 100 mL round bottom flask, then 3 mL of Claisen's alkali (prepared by dissolving 350 g of KOH in 250 cm³ of water, cooling and diluting to 1 L with MeOH) was added to the reaction mixture. The reaction mixture was refluxed at 70 °C for 18 h. The mixture was cooled to room temperature and the solution was acidified with 2 M hydrochloric acid. The precipitate was filtered through a glass filter and washed with ice cold water and small portion of n-hexane, and dried under vacuum at 80 °C. White powder (623.6 mg, 88%) was obtained (TDC, **3**). Melting point: >260 °C, δH (500.1 MHz, DMSO-d6): 1.89 (d, *J* = 7.4 Hz, 12H, C*H*₃CH), 4.48 (d, *J* = 7.6 Hz, 4H, inner OC*H*₂O), 4.85–4.94 (m, 12H, ArC*H*₂O overlapping signals with CH₃C*H*), 5.92 (d, *J* = 7.6 Hz, 4H, outer OC*H*₂O), 7.03 (t, *J* = 7.5 Hz, 4H, Ar-*H*), 7.28 (dd, *J* = 7.6 Hz, 1.4 Hz, 4H, Ar-*H*), 7.49 (t, *J* = 7.5 Hz, 4H, Ar-*H*), 7.59 (dd, *J* = 7.6 Hz, 1.4 Hz, 4H, Ar-*H*), 7.89 (s, 4H, Ar-*H*), 10.62 (brs, 4H, COO*H*), 12.51 (brs, 4H, COO*H*), δC (125.1 MHz, DMSO-d6): 16.4, 30.6, 61.4, 100.0, 119.8, 122.7, 123.0, 125.4, 133.1, 139.6, 153.7, 159.1, 167.3.

4.2. Synthesis of PHX

Trans-Phototrexate (*trans*-PHX) was synthesized in our institute. During the synthesis, we followed the procedure of Matera et al. [11], as shown in Figure 8. Briefly, **4** quinazoline-2,4,6-triamine was conjugated to **5** (S)-diethyl 2-(4-nitrosobenzamido)-pentanedioate to offer compound **6**. The latter was hydrolysed in mixture of sodium hydroxide and ethanol to yield PHX.
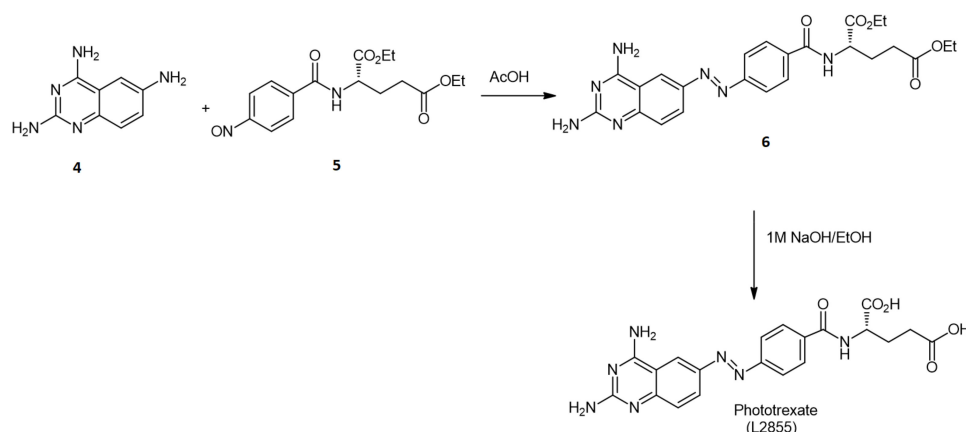
Figure 8. Schematic synthesis of PHX.

After chromatographic purification, the physicochemical data of PHX was in agreement with that of earlier published data. HRMS (ESI): m/z [M+H]⁺ calculated for $C_{30}H_{30}N_7O_5^+$: 438.1520; found: 438.1520 (Figure 9).
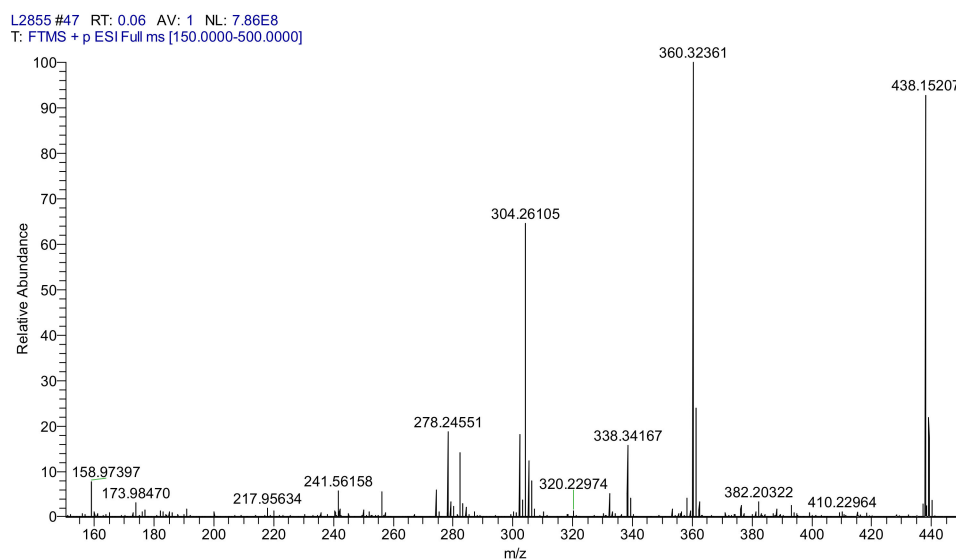
Figure 9. HRMS spectrum of PHX.

4.3. Other Chemicals and Instruments

The applied solvent was dimethyl sulfoxide (DMSO) purchased from Merck (Darmstadt, Germany).

Fluorimetric measurements were performed with a Fluorolog τ3 spectrofluorometer (Jobin-Yvon/SPEX, Longjumeau, France). Fluorescence spectra were recorded using 366 nm excitation wavelength. The emission values obtained at 490 nm were used for data evaluation. For data collection, photon counting method with 0.1 s integration time was used and 2 nm bandwidths set and quartz cuvettes with 1.0 cm thickness were applied.

The temperature dependence of binding constants was measured to determine the thermodynamic parameters associated to the binding of *trans*-PHX and *cis*-PHX to the cavitand derivatives (TAC and TDC). Accordingly, samples with different concentrations of the cavitand derivates (0–450 μM), and with constant concentration of *trans*- and *cis*-PHX (50 μM), were prepared and measured using 366 nm excitation wavelength at 293 K, 298 K, 303 K and 308 K temperatures.

The thermodynamically stable but pharmacologically inactive *trans*-PHX was isomerized with the application of UV-light (λ = 366 nm) provided by a Fluotest lamp (Original Hanau, Hanau, Germany). To ensure the complete isomerization, UV-vis spectra were recorded by a Specord Plus 210 spectrophotometer (Analytik Jena, Jena, Germany).

4.4. Data Evaluation

Stability constants (*K*, dm^3/mol) of PHX–cavitand complexes were calculated either using the Benesi–Hildebrand equation, assuming 1:1 complex stoichiometry:

$$\frac{I_0}{I - I_0} = \frac{1}{A} + \frac{1}{A \cdot K \cdot [C]} \tag{1}$$

where I_0 and I are the fluorescence emission intensities of PHX in the absence and in the presence of the host, respectively; [*C*] is the molar concentration of the host molecule while *A* is a constant.

To determine the thermodynamic parameters, temperature dependence of the complex stabilities was examined, then the thermodynamic parameters were calculated using the Van 't Hoff equation:

$$\ln K = -\frac{\Delta G}{R \cdot T} + \frac{\Delta S}{R} \tag{2}$$

where the ΔH and ΔS stand for the enthalpy and entropy changes of the complex formation, respectively, while ΔG is the Gibbs free energy change. *R* is the gas constant, while *T* is the temperature in Kelvin.

4.5. Modelling

Thermodynamic parameters of the Phototrexate–cavitand complexes were determined as follows. The enthalpy change was considered as the energy change calculated by subtracting the total energies of the reactants from the total energies of the products. Similarly, the entropy changes were calculated by subtracting the entropy terms of the reactants from the entropy terms of the products. Calculation of the entropy term was implemented in the HyperChem code as follows: after calculating the vibrational frequencies using the harmonic approximation, the entropy was then determined by the following equation:

$$S_{vib} = R \sum_i \left\{ \frac{h\nu_i/kT}{e^{(h\nu_i/kT)} - 1} - \ln\left[1 - e^{(-h\nu_i/kT)}\right] \right\} \tag{3}$$

Here, ν_i is the frequency of vibration and *T* is the temperature.

The molecular environment was considered by the TIP3P method while the simulation box randomly filled by the dimethyl sulfoxide molecules. The total energies of the species interacted have been calculated at semi-empirical AM1 level using HyperChem 8 code.

5. Conclusions

In this study, the complex formation thermodynamics of *trans*-PHX and *cis*-PHX was investigated with the host molecules TAC and TDC, both of which are cavitand derivatives. The applied methods were fluorescence spectroscopy and 3D modelling. Opposite temperature dependence of the stability of PHX-TAC and PHX-TDC complexes was found. These results imply different complex formation mechanisms.

The host–guest complex formation of PHX was described for the first time. PHX is a promising new molecule whose cytotoxic effect can be regulated with light. Complex formation can be another method that could make the physiological effect of this molecule more adjustable.

References

1. Chabner, B.A.; Roberts, T.G. Chemotherapy and the war on cancer. *Nat. Rev. Cancer* **2005**, *5*, 65–72. [CrossRef] [PubMed]
2. Shams, S.; Martinez, J.M.; Dawson, J.R.D.; Flores, J.; Gabriel, M.; Garcia, G.; Guevara, A.; Murray, K.; Pacifici, N.; Vargas, M.V.; et al. The Therapeutic Landscape of Rheumatoid Arthritis: Current Stateand Future Directions. *Front. Pharmacol.* **2021**, *12*, 1233. [CrossRef] [PubMed]
3. Tian, H.; Cronstein, B.N. Understanding the mechanisms of action of methotrexate. *Bull. NYU Hosp. Jt. Dis.* **2007**, *65*, 168–173. Available online: http://metoject.ru/wp-content/uploads/files/public_en/34.pdf (accessed on 3 October 2021). [PubMed]
4. Solomon, D.H.; Kremer, J.M.; Fisher, M.; Curtis, J.R.; Furer, V.; Harrold, L.R.; Hochberg, M.C.; Reed, G.; Tsao, P.; Greenberg, J.D. Comparative cancer risk associated with methotrexate, other non-biologic and biologic disease-modifying anti-rheumatic drugs. *Semin. Arthritis Rheu.* **2014**, *43*, 489–497. [CrossRef] [PubMed]
5. Senapati, S.; Mahanta, A.K.; Kumar, S.; Maiti, P. Controlled drug delivery vehicles for cancer treatment and their performance. *Signal Transduct. Target. Ther.* **2018**, *3*, 7. [CrossRef]
6. Baudino, T.A. Targeted Cancer Therapy: The Next Generation of Cancer Treatment. *Curr. Drug Discov. Technol.* **2015**, *12*, 3–20. [CrossRef]
7. Broichhagen, J.; Frank, J.A.; Trauner, D. A Roadmap to Success in Photopharmacology. *Acc. Chem. Res.* **2015**, *48*, 1947–1960. [CrossRef]
8. Reessing, F.; Szymanski, W. Beyond Photodynamic Therapy: Light-Activated Cancer Chemotherapy. *Curr. Med. Chem.* **2017**, *24*, 4905–4950. [CrossRef] [PubMed]
9. Szymanski, W.; Beierle, J.M.; Kistemaker, H.A.; Velema, W.A.; Feringa, B.L. Reversible photocontrol of biological systems by the incorporation of molecular photoswitches. *Chem. Rev.* **2013**, *113*, 6114–6178. [CrossRef]
10. Banghart, M.R.; Mourot, A.; Fortin, D.L.; Yao, J.Z.; Kramer, R.H.; Trauner, D. Photochromic blockers of voltage-gated potassium channels. *Angew. Chem. Int. Ed.* **2009**, *48*, 9097–9101. [CrossRef]
11. Matera, C.; Gomila, A.M.J.; Camarero, N.; Libergoli, M.; Soler, C.; Gorostiza, P. Photoswitchable Antimetabolite for Targeted Photoactivated Chemotherapy. *J. Am. Chem. Soc.* **2018**, *140*, 15764–15773. [CrossRef] [PubMed]
12. Mashita, T.; Kowada, T.; Takahashi, H.; Matsui, T.; Mizukami, S. Light-wavelength based Quantitative Control of Dihydrofolate Reductase Activity Using Photochromic Isostere of Inhibitor. *ChemBioChem* **2019**, *20*, 1382–1386. [CrossRef] [PubMed]
13. Fahmy, S.A.; Brüßler, J.; Alawak, M.; El-Sayed, M.M.H.; Bakowsky, U.; Shoeib, T. Chemotherapy Based on Supramolecular Chemistry: A Promising Strategy in Cancer Therapy. *Pharmaceutics* **2019**, *11*, 292. [CrossRef] [PubMed]
14. Hoskins, C.; Curtis, A.D.M. Simple Calix[n]arenes and Calix[4]resorcinarenes as Drug Solubilizing Agents. *J. Nanomed. Res.* **2015**, *2*, 00028. [CrossRef]
15. Neda, I.; Vollbrecht, A.; Grunenberg, J.; Schmutzler, R. Functionalization of the Periphery of Calix[4]resorcinarenes with P(III)-containing Substituents via Hydroxy-, Trimethylsiloxy- and Ethoxy-Tethered Trimethylsiloxy Intermediates. *Heteroat. Chem.* **1998**, *9*, 553–558. [CrossRef]
16. Franz, M.H.; Iorga, M.; Maftei, C.V.; Maftei, E.; Neda, I. Studies on the constituents of Helleborus purpurascens: Use of derivatives from calix[6]arene, homooxa-calix[3]arene and homoazacalix[3]arene as extractant agents for amino acids from the aqueous extract. *Amino Acids* **2020**, *52*, 55–72. [CrossRef]
17. Maftei, V.; Fodor, E.; Jones, P.G.; Franz, M.H.; Davidescu, C.M.; Neda, I. Asymmetric Calixarene Derivatives as Potential Hosts in Chiral Recognition Processes. *Pure Appl. Chem.* **2015**, *87*, 415–439. [CrossRef]
18. Dieleman, B.; Matt, D.; Neda, I.; Schmutzler, R.; Harriman, A.; Yaftian, R. Hexahomotrioxacalix[3]arene: A scaffold for a C3-symmetric phosphine ligand that traps a hydro-rhodium fragment inside a molecular funnel. *Chem. Commun.* **1999**, 1911–1912. [CrossRef]
19. Kunze, C.; Selent, D.; Neda, I.; Schmuzler, R.; Spannenberg, A.; Börner, A. Synthesis of New Calix[4]arene-Based Phosphorus Ligands and Their Application in the Rh(I) Catalyzed Hydroformylation of 1-Octene. *Heteroat. Chem.* **2001**, *12*, 577–585. [CrossRef]
20. Preisz, Z.; Nagymihály, Z.; Lemli, B.; Kollár, L.; Kunsági-Máté, S. Weak interaction of the antimetabolite drug methotrexate with a cavitand derivative. *Int. J. Mol. Sci.* **2020**, *21*, 4345. [CrossRef]
21. Csók, Z.; Kégl, T.; Párkányi, L.; Varga, Á.; Kunsági-Máté, S.; Kollár, L. Facile, high yielding synthesis of deepened cavitands: A synthetic and theoretical study. *Supramol. Chem.* **2011**, *23*, 710–719. [CrossRef]
22. Sorrell, T.N.; Pigge, F.C. A convenient synthesis of functionalized cavitands via free-radical bromination. *J. Org. Chem.* **1993**, *58*, 784–785. [CrossRef]
23. Preisz, Z.; Hartvig, N.; Bognár, B.; Kálai, T.; Kunsági-Máté, S. Comparative EPR Study on the Scavenging Effect of Methotrexate with the Isomers of Its Photoswitchable Derivative. *Pharmaceuticals* **2021**, *14*, 665. [CrossRef] [PubMed]

Article

Comparative EPR Study on the Scavenging Effect of Methotrexate with the Isomers of Its Photoswitchable Derivative

Zsolt Preisz [1,2], Nóra Hartvig [3], Balázs Bognár [1] , Tamás Kálai [1,3] and Sándor Kunsági-Máté [1,2,3,*]

[1] Institute of Organic and Medicinal Chemistry, Faculty of Pharmacy, University of Pécs, Szigeti 12, H-7624 Pécs, Hungary; preisz.zsolt@pte.hu (Z.P.); balazs.bognar@aok.pte.hu (B.B.); tamas.kalai@aok.pte.hu (T.K.)

[2] Department of General and Physical Chemistry, Faculty of Sciences, University of Pécs, Ifjúság 6, H-7624 Pécs, Hungary

[3] János Szentágothai Research Center, University of Pécs, Ifjúság 20, H-7624 Pécs, Hungary; nora.hartvig@gmail.com

* Correspondence: sandor.kunsagi-mate@aok.pte.hu

Abstract: The scavenging effect of the antimetabolite dihydrofolate reductase inhibitor methotrexate (MTX) and the isomers of its photoswitchable derivate, *cis*- and *trans*-phototrexate (PHX), have been compared by ESR spectroscopy, with the application of a cyclic hydroxylamine spin probe. The results showed the most pronounced scavenging effect in the presence of *trans*-phototrexate (*trans*-PHX). At a low concentration (100 µM) *cis*-PHX also showed a greater scavenging effect than the parent molecule MTX. Direct antioxidant properties of the investigated molecules were measured by ABTS scavenging assay, which showed no significant difference between *trans*-PHX and *cis*-PHX, but both of the isomers of PHX showed a higher antioxidant capacity than MTX. These findings imply that *trans*-PHX may have more pronounced anti-inflammatory and tissue-protective effects than MTX, despite the lack of its cytotoxic, antineoplastic effect.

Keywords: methotrexate; phototrexate; photopharmacology; photoswitchable; electron paramagnetic resonance (EPR); scavenger

1. Introduction

Chemotherapy (the use of cytotoxic agents) is one of the main methods that are applied in cancer treatment, together with radiation therapy, hormone therapy, and surgery. However, the efficacy of chemotherapy is often limited because of the low therapeutic indices and poor adverse effect profiles of these agents [1]. The lack of disease-specific targeting stands in the background of this phenomenon. The most common adverse effects of chemotherapeutic agents are cardiomyopathy, hepatic fibrosis, pulmonary fibrosis, renal insufficiency, nodulosis, lethargy, and fatigue [2,3].

Methotrexate (4-amino-10-methylfolic acid, MTX, Figure 1) is an antimetabolite dihydrofolate reductase (DHFR) inhibitor. It is a widely used chemotherapeutic agent in autoimmune diseases such as rheumatoid arthritis (RA), psoriasis, and some sorts of leukaemia [4]. The anti-inflammatory effect of MTX is well-known, but its mechanisms of action are not well understood, several molecular phenomena are described in the literature that can play a role in the development of this effect (inhibition of purine and DNA synthesis, reduction of antigen-dependent T-cell proliferation, promotion of adenosine release, suppression of transmethylation reaction) [2,4,5].

However, MTX has a poor drug safety profile caused by the ubiquity of DHFR [6]. Its most common adverse effects are ulcerative stomatitis, leukopenia, nausea, abdominal distress, malaise, undue fatigue, chills and fever, dizziness, and decreased resistance to infection [7]. Several attempts were made to reduce the side effects of MTX, and some of

them have proven to be effective, for example, the concurrent use of leucovorin (folinic acid). This adjuvant does not interfere with the efficacy of methotrexate in a clinically significant manner, but significantly reduces the common side effects of low-dose MTX therapy [8].
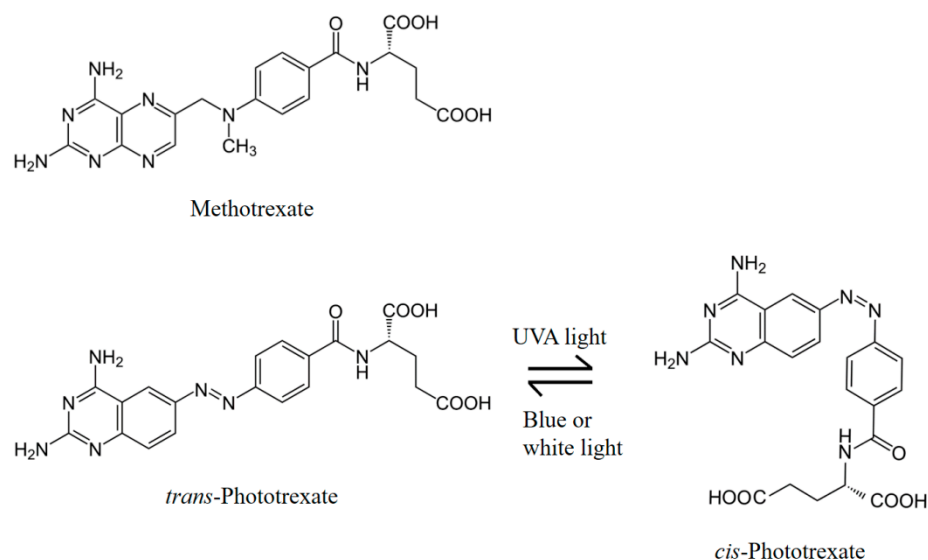
Figure 1. Chemical structures of methotrexate (MTX), *trans*-phototrexate (*trans*-PHX), *cis*-phototrexate (*cis*-PHX), and the reversible isomerization of PHX [6].

To activate the drugs exclusively at their target place of action is a promising approach to improve cancer therapies, and synthetical photoswitches can be suitable tools to achieve this. Photoswitches are chromophores that can be reversibly isomerized when exposed to light. The field that attempts to control biological activity with these molecules is called photopharmacology [9]. Azobenzene is the most widely used photoswitch in biological applications because of the ease of synthesis and functionalization, fast photo-isomerization, and the low rate of photo-bleaching [10,11].

PHX is a photoswitchable azobenzene analogue of MTX that has been synthesized and described by C. Matera et al. [6] and by Mashita et al. [12]. PHX contains a diazene stereogenic unit and its pharmacological activity is higher in its *cis* state than in the more thermodynamically stable *trans* state. It can be effectively isomerized from *trans* to *cis* with UVA light (375 nm) and back-isomerized from *cis* to *trans* with blue (460 nm) or white light (Figure 1). This transition is reversible and can be repeated several times. The antineoplastic effect (and also the adverse effects caused by the cytotoxic activity) appears only in light-exposed regions and decreases in dark regions. Target tissues that can be exposed to UV-illumination are primarily the skin, the digestive, respiratory, and reproductive tracts.

Clinically, MTX reduces the risk of cardiovascular events caused by cardiovascular disease (CVD) which is also recognized as a chronic inflammatory condition [13–15]. Modified lipoproteins are assumed to play an important role in the development and progression of CVD. These modified lipoproteins increase oxidative stress and lipid peroxidation, which lead to the increase of reactive oxygen species (ROS) and malondialdehyde–acetaldehyde (MAA) production. The elevated levels of these reactive products have been detected in RA and also in CVD cases [16,17]. It has been described that MTX inhibits malondialdehyde–acetaldehyde–protein adduct formation and scavenges superoxide radicals [18], but these features have never been investigated in the case of *trans*- or *cis*-PHX yet.

EPR spectroscopy has long been a method of choice for the detection of paramagnetic species, such as free radicals or transition metal ions in vitro. EPR spectroscopy in association with molecular probes has been successfully applied to the evaluation of the

redox status of tumors or in rodent models of diverse pathological conditions, such as hypertension, stroke, epilepsy, and sepsis [19]. In this study, 1-hydroxy-2,2,6,6-tetramethyl-piperidin-4-ol (*N*-hydroxy-TEMPOL), a cyclic hydroxylamine, was used as a spin probe for EPR measurements. Cyclic aminoxyl radicals with tetraalkyl substituents flanking the N–O$^\bullet$ functionality are most often used as probes for the redox status in vivo [20]. Hydroxylamines (in contrast with spin traps) do not have the ability to bind (trap) free radicals. They can undergo oxidation to stable nitroxides, and the nitroxide accumulation can be followed by EPR. Hydroxylamines rapidly react with oxygen-centered free radicals, including superoxide, peroxyl radicals, or peroxynitrite [21]. These stable hydroxylamines can also participate in redox reactions with biological compounds or enzymes and thus report on the redox status of the cell by shuttling between the three forms shown in Figure 2a. Figure 2b summarizes the possible redox process associated with the interaction of the superoxide radical with the MTX and PHX molecules.
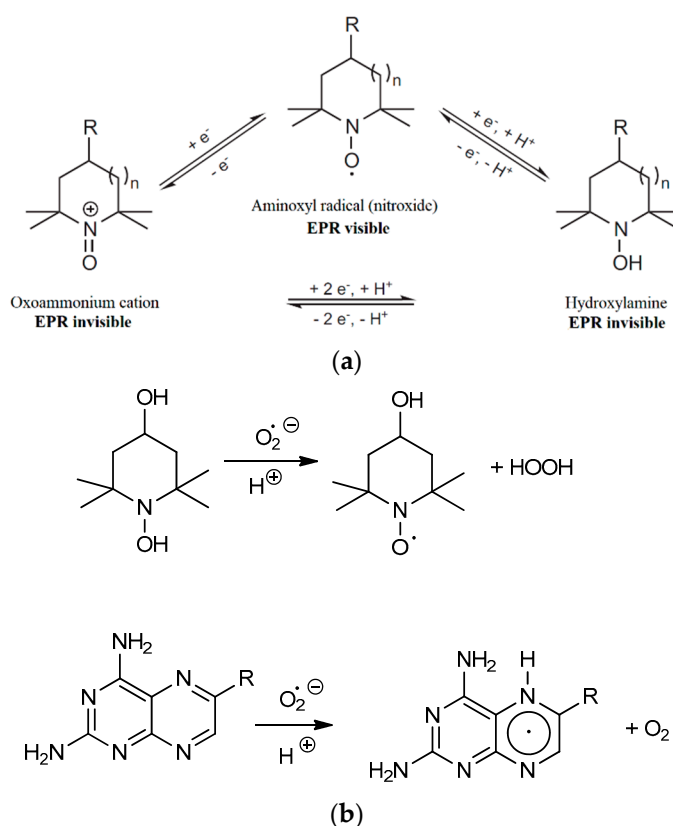
Figure 2. (**a**) (top) Redox species associated with cyclic hydroxylamine spin probe molecules (n = 0 or 1, pyrrolidine or piperidine) [20]. (**b**) (bottom) Proposed redox processes associated with the quenching of superoxide radical by oxidation of hydroxylamine and the reduction of the 1,4-diazine unit of MTX.

By adopting the method established well by Zimmerman et al. [18] we intended to compare the superoxide scavenging activity of methotrexate and *cis*- and *trans*-phototrexate by means of 1-hydroxy-2,2,6,6-tetramethyl-piperidin-4-ol (*N*-hydroxy-TEMPOL), as a $O_2^{\cdot-}$ radical scavenger. The direct antioxidant properties of MTX, *trans*-PHX, and *cis*-PHX, were also investigated by ABTS scavenging assay. PHX is a relatively new molecule, which has already attracted attention [3], but its antioxidant activity has not been investigated before.

2. Results

2.1. Absorbance Spectra of Trans-PHX before and after EPR Measurements

To make sure that *trans*-PHX does not suffer isomerization or other molecular modification as a result of EPR measurements, UV-vis spectra were recorded before and after the EPR measurement (Figure 3). EPR measurements are taken in 30 min. There is no significant difference between the two spectra, so it was found that the 9.1 GHz microwave irradiation of EPR does not cause any change in the *trans*-PHX molecule. The applied concentration of *trans*-PHX was 50 µM.
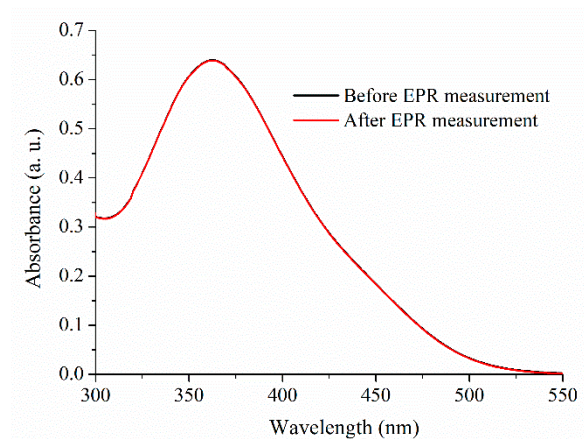
Figure 3. UV-vis absorption spectra of *trans*-PHX samples before and after EPR measurement.

2.2. Isomerization of Trans-PHX

To investigate the direct antioxidant properties of *cis*-PHX, the complete isomerization of the thermodinamically stable trans-PHX has to be reached. To this purpose UV-light exposure was used (λ = 366 nm). To examine the time dependence of the photoisomerization, a sample containing 50 µM of trans-PHX was exposed to UV-light and the process was followed by spectrophotometrical measurements (Figure 4). According to these measurements, the complete isomerization of PHX (from *trans* to *cis*) was reached after approximately 15 min of UV-light exposure.
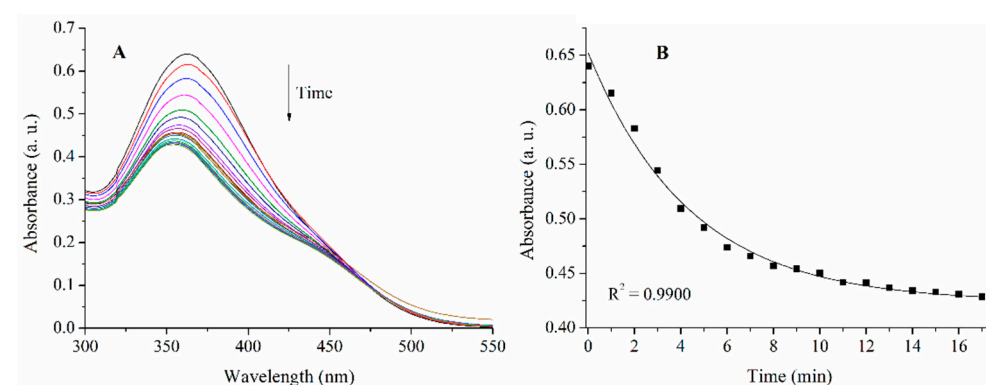
Figure 4. UV-vis spectra of a 50 µM solution of *trans*-PHX exposed to 366 nm light (**A**) and the intensity of the peak at 360 nm plotted against time (**B**). The first spectrum was recorded before the beginning of the UV-light exposure, then measurements were taken every minute.

2.3. Results of EPR Measurements

To determine the direct antioxidant properties of MTX, *trans*-PHX, and *cis*-PHX, EPR spectra of samples containing 0 µM, 100 µM, 500 µM, 2 mM, 5 mM MTX and 0 µM, 100 µM, 500 µM and 2 mM *trans*-PHX, and *cis*-PHX were recorded (Figure 5). The average amplitudes of the EPR-peaks were investigated in all cases.
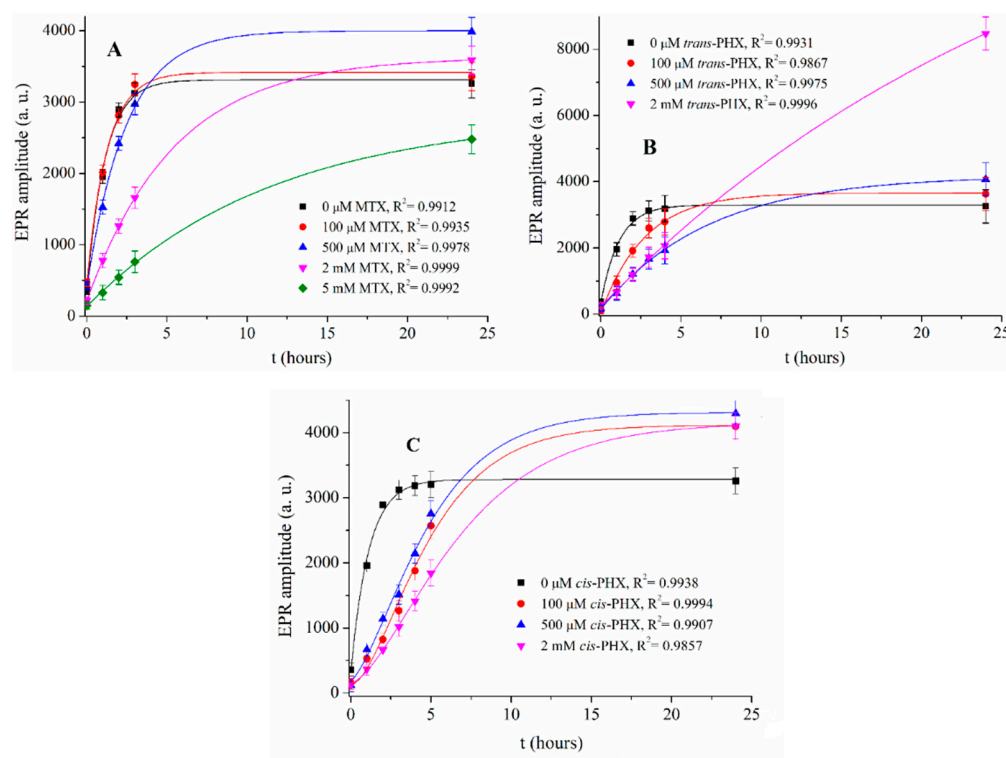
Figure 5. The amplitudes of EPR signals of samples containing 0–5 mM MTX (**A**), 0–2 mM *trans*-PHX (**B**) and, 0–2 mM *cis*-PHX (**C**) plotted against time.

The rate of the production of reactive oxygen species (ROS) has the ability to be very informative, due to the fact that when this rate reaches the saturation level of the biological scavenger systems (e.g., superoxide dismutase, catalase, glutathione peroxidase), the cells will be exposed to oxidative stress. The difference between the maxima of curves is less significant. The reason for the high amplitude values of the sample containing 2 mM *trans*-PHX is not clear yet. The rate of ROS production has not been applied yet for describing the scavenging effect of MTX and PHX. It is observable that the rate of ROS production decreases with the increasing concentrations of MTX and *trans*-PHX, but this effect is more pronounced in the presence of *trans*-PHX. It is important to note that this decrease is not the result of XO inhibition [18]. Based on the curves in Figure 2, the ln k kinetic parameters of all of the samples were determined (Table 1). It was found that *trans*-PHX slows down the ROS production to a greater extent than MTX at all of the investigated concentration levels. This inhibition effect is also more pronounced in the presence of *cis*-PHX when compared to MTX at 100 μM concentration, but at higher concentrations, MTX had a greater effect than *cis*-PHX. This effect is higher in the presence of *trans*-PHX than in *cis*-PHX. We note that the ln k values that were calculated to determine the effect of *cis*-PHX may not be entirely accurate. This is for the reason that the sigmoidal shape of the related curves may reflect for example, the presence of autocatalytic steps. Since the absorption spectra recorded before and after the measurements do not reflect any changes in the *cis*-PHX conformation, further investigations are required to clarify the complex reaction mechanism.

The significance of the scavenging effect of MTX, *cis*-PHX, and *trans*-PHX, has been investigated by performing two-way ANOVA statistics implemented in the OriginLab 8.1 software (OriginLab Corporation, Northampton, MA, USA). The population means related to the concentration of the antimetabolite drugs or their categories (MTX, *cis*-PHX, or *trans*-PHX) were found to be significantly different at the significance level of 0.05 ($p = 2.59 \times 10^{-8}$ and $p = 1.710 \times 10^{-5}$ for concentration and drug categories, respectively).

Table 1. The calculated ln k values of the samples investigated.

| Concentration (μM) | MTX | *trans*-PHX | *cis*-PHX |
	ln k	ln k	ln k
0	-8.70 ± 0.16	-8.69 ± 0.18	-8.68 ± 0.15
100	-8.79 ± 0.23	-9.56 ± 0.15	-9.16 ± 0.25
500	-9.46 ± 0.21	-10.46 ± 0.28	-9.19 ± 0.26
2000	-10.25 ± 0.25	-11.96 ± 0.23	-9.51 ± 0.29
5000	-11.01 ± 0.20	-	-

Control samples that only contained TEMP solution and HX/XO solution were measured as well, to demonstrate that the spin probe (TEMP) alone does not generate any significant EPR signal, but it is needed to indicate the presence of ROS (Figure 6).
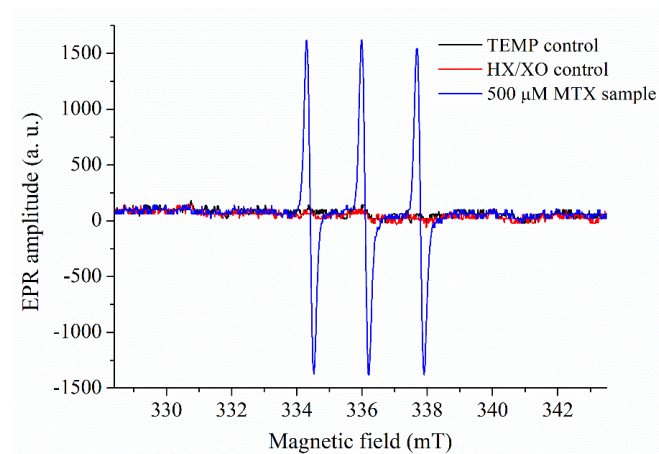
Figure 6. EPR spectra of the controls compared to the sample containing 500 μM MTX. All spectra were recorded 3 h after sample preparation.

2.4. Results of ABTS Scavenging Assay

The Trolox equivalent antioxidant capacities (TEAC) of MTX, *trans*-PHX, and *cis*-PHX, were determined using ABTS (2,2′-azinobis[3-ethylbenzothiazoline-6-sulfonic acid]) assay, which monitors electron and proton donor activity [22]. The method is based on the green-colored ABTS$^{\bullet+}$ radical, which is detected at 734 nm. Results are depicted in Figure 7.
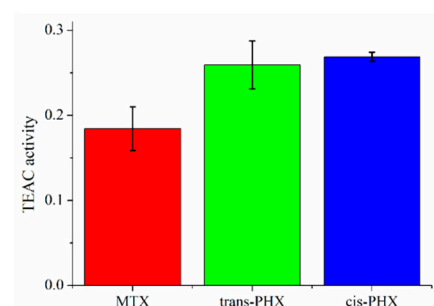
Figure 7. Trolox equivalent antioxidant capacity (TEAC) of methotrexate (MTX), *trans*-phototrexate (*trans*-PHX), and *cis*-phototrexate (*cis*-PHX) measured by ABTS radical scavenging assay. Data represent the mean $\pm$ SD ($n = 3$).

There was no significant difference between the TEAC values of *trans*-PHX and *cis*-PHX, but both of the isomers of PHX showed a higher antioxidant capacity than MTX.

3. Discussion

The role of antirheumatic drugs in cardiovascular disease prevention has been an intensively researched field in the last decade [23–25]. Colchicine is the first anti-inflammatory molecule to have been shown in a randomized, double-blind trial to be effective in the secondary prevention of myocardial infarction [26].

Compared with the general population, patients with rheumatoid arthritis (RA) have an increased risk of cardiovascular disease (CVD) or events (CVE) [27] and reduced survival [28]. In patients with RA, treatment with tumor necrosis factor (TNF) inhibitors or MTX was associated with a 30% and 28% reduction in the risk of CVEs, respectively [29]. The ability to scavenge $O_2^{\cdot -}$ appears to be a mechanism by which MTX inhibits the formation of malondialdehyde–acetaldehyde (MAA) adducts. The inhibition of MAA adduct formation and scavenging of free radicals may reduce the inflammation associated with CVD and RA, thereby reducing tissue damage [18].

Phototrexate is a relatively new molecule, therefore very few publications can be found in the literature about it. It has been synthesized and characterized by Matera et al. and its antifolate and antiproliferative properties have been demonstrated by in vitro and in vivo assays [6]. PHX has been derived by azologization and bioisosteric substitutions of MTX. PHX is a photoswitchable molecule, it can be switched on by UV light exposure and switched off by blue or white light or by thermal relaxation in the dark. Its *cis* isomer's effect is very similar to the effect of MTX, while it is almost inert as an antifolate in its *trans* configuration [6].

In this study, the ROS-scavenging effect of *trans*-PHX, *cis*-PHX, and MTX, was investigated and compared to each other by an EPR spectroscopy method [18]. EPR spectra of *cis*- and *trans*-PHX were recorded and the direct antioxidant properties of these molecules were described for the first time. Kinetic parameters (rate k) were determined and it was found that *trans*-PHX has a more pronounced scavenging effect than MTX and *cis*-PHX. This effect is found to be greater in the presence of *cis*-PHX compared to MTX at lower concentrations. The results of MTX are in line with the study published by Zimmermann et al. [18].

ABTS scavenging assay measurements were also carried out to investigate the antioxidant properties (TEAC values) of MTX and the isomers of PHX. These experiments showed no significant difference between the scavenging effect of *trans*-PHX and that of the *cis*-PHX, but these experiments confirm that both of the isomers of PHX showed a higher antioxidant capacity than MTX.

The reason for the slightly different results of the applied methods is likely due to the methodological difference between these methods. The EPR spectroscopy method is applicable to examine the superoxide radical scavenging activity of the investigated molecules, while by the ABTS scavenging assay the $ABTS^{\bullet +}$ radical scavenging activity was measured.

Despite the slight differences between the two experiments applied here, it can be assumed that *trans*-PHX may have more pronounced anti-inflammatory and tissue-protective effects than MTX. This finding is very interesting because *trans*-PHX lacks the cytotoxic and antineoplastic effects of MTX and *cis*-PHX [6]. Further investigations are required to clarify the mechanism of action of *trans*-PHX and thereby the exact molecular background of this effect.

4. Materials and Methods

Methotrexate (MTX), 1-hydroxy-2,2,6,6-tetramethyl-piperidin-4-ol (*N*-hydroxy-TEMPOL), xanthine oxidase (XO, from bovine milk), and hypoxanthine (HX) were obtained from Sigma-Aldrich (St. Louis, MO, USA). *Trans*-phototrexate (*trans*-PHX) was synthesized in our institute according to the scheme published recently [6].

The applied solvent was a Krebs-HEPES EPR buffer consisting of: NaCl (99 mM), KCl (4.69 mM), $CaCl_2$ (2.5 mM), $MgSO_4$ (1.2 mM), $NaHCO_3$ (25 mM), KH_2PO_4 (1.03 mM), D-glucose (5.6 mM), HEPES (20 mM), diethyl dithio carbamic diethylammonium salt (DETC,

5 µM), and deferoxamine (25 µM) [30]. The buffer was adjusted to pH 7.4 with HCl. All of the compounds were purchased from Sigma-Aldrich.

A MiniScope MS 200 (Magnettech GmbH, Berlin, Germany) spectroscope was utilized to detect the produced free radicals and to examine the scavenging ability of MTX. The amplitude of the EPR signal is proportional to the number of unpaired electrons present in the sample, facilitating the quantification of free radicals [31]. The amplitudes were determined using the MiniScopeCtrl software.

The following EPR spectrometer settings were applied for all experiments: B0-field: 335.9723 mT, range: 15.0727 mT, sweep time: 30.0 s, modulation: 0.200 mT, and microwave attenuation: 10.0 dB. TEMP was utilized as an EPR spin probe. All measurements were carried out at room temperature (298 K).

To determine if MTX, *trans*-PHX, or *cis*-PHX directly scavenges free radicals, hypoxanthine (HX) and xanthine oxydase (XO) were used (the HX/XO system produces free radicals, primarily $O_2^{\cdot-}$). 1 mL samples were prepared with 100 µM TEMP, 20 µM HX, 10 mU/mL XO and 0–5 mM MTX or 0–2 mM PHX in 1 mL of EPR buffer. 50 µL of the sample was then loaded into a glass capillary tube and inserted into the capillary holder of the EPR spectrometer. Control samples with TEMP solution alone and with HX/XO solution alone were measured as well.

The thermodynamically stable but pharmacologically inactive *trans*-PHX was isomerized with the application of UV-light (λ = 366 nm) provided by a Fluotest lamp (Original Hanau, Hanau, Germany). To ensure the complete isomerization, UV-vis spectra were recorded by a Specord Plus 210 spectrophotometer (Analytik Jena, Jena, Germany). For data collection, the photon counting method with 0.1 s integration time was used and 2 nm bandwidths set and quartz cuvettes with 1.0 cm thickness were applied. The EPR spectra were registered every hour for all of the samples. This measurement lasts 5 min. When *cis*-PHX was measured, the samples were continuously exposed to UV-light (λ = 366 nm) to prevent the isomerization.

ABTS scavenging assays were carried out with the application of a Specord 40 spectrophotometer (Analytik Jena, Jena, Germany). 2,2′-azinobis(3-ethylbenzothiazoline-6-sulfonic acid (ABTS) was solved in phosphate-buffered saline (PBS) that was composed of NaCl (137 mM/L), KCl (2.7 mM/L), NaH_2PO_4 (8 mM/L), and K_2HPO_4 (1.5 mM/L). The concentration of ABTS was 7 mM. ABTS radical cation ($ABTS^{\bullet+}$) was produced by reacting ABTS stock solution with potassium persulfate at a final concentration of 2.45 mM and allowing the mixture to stand in the dark at room temperature for 16 h before use. For the study of compounds, the $ABTS^{\bullet+}$ solution was diluted with PBS to an absorbance of 0.70 ($\pm$0.02) at 734 nm and equilibrated at 37 °C. Stock solutions of MTX, *trans*-PHX, *cis*-PHX, and Trolox (a water-soluble derivative of vitamin E with antioxidant properties) in PBS were added to the diluted $ABTS^{\bullet+}$ solution, in final concentrations of 12.5, 10, 7.5, and 2.5 µM. After this step, the mixtures were incubated for 6 min at 37 °C before measuring their absorbance at 734 nm. All measurements were carried out three times. The percentage inhibition of absorbance at 734 nm is calculated with the usual formula:

$$(A_0 - A_{antioxidant})/A_0 = \text{inhibition (\%)} \tag{1}$$

where A_0 is the absorbance of the diluted $ABTS^{\bullet+}$ solution. The concentration–response curves of the investigated molecules were compared with the curve of Trolox.

5. Conclusions

Using cyclic hydroxylamine spin probe the superoxide scavenging effect of the antimetabolite dihydrofolate reductase inhibitor methotrexate (MTX) and the isomers of its photoswitchable derivate, cis- and trans-phototrexate (PHX), have been compared by ESR spectroscopy. The trans-phototrexate (trans-PHX) showed the most pronounced scavenging effect, while at a low concentration (100 µM) cis-PHX also showed a greater scavenging effect than the parent molecule MTX. Trolox equivalent antioxidant capacity

(TEAC) values of these molecules have been determined by ABTS scavenging assay. There was no significant difference between the TEAC values of trans-PHX and cis-PHX, but both of the isomers of PHX showed a higher antioxidant capacity than MTX. These findings imply that trans-PHX may have more pronounced anti-inflammatory and tissue-protective effects than MTX, despite the lack of its cytotoxic, antineoplastic effect.

References

1. Senapati, S.; Mahanta, A.K.; Kumar, S.; Maiti, P. Controlled drug delivery vehicles for cancer treatment and their performance. *Signal Transduct. Target. Ther.* **2018**, *3*, 7. [CrossRef]
2. Tian, H.; Cronstein, B.N. Understanding the mechanisms of action of methotrexate. *Bull. BYU Hosp. Jt. Dis.* **2007**, *65*, 168–173.
3. Mulatihan, D.; Guo, T.; Zhao, Y. Azobenzene Photoswitch for Isomerization-Dependent Cancer Therapy via Azo-Combretastatin A4 and Phototrexate. *Photochem. Photobiol.* **2020**, *96*, 1163–1168. [CrossRef] [PubMed]
4. Chane, E.S.L.; Cronstein, B.N. Molecularaction of methotrexate in inflammatory diseases. *Arthritis Res. Ther.* **2002**, *4*, 266–273. [CrossRef] [PubMed]
5. Cutolo, M.; Sulli, A.; Pizzorni, C.; Seriolo, B. Anti-inflammatory mechanisms of methotrexate in rheumatoid arthritis. *Ann. Rheum. Dis.* **2001**, *60*, 729–735. [CrossRef] [PubMed]
6. Matera, C.; Gomila, A.M.J.; Camarero, N.; Libergoli, M.; Soler, C.; Gorostiza, P. Photoswitchable Antimetabolite for Targeted Photoactivated Chemotherapy. *J. Am. Chem. Soc.* **2018**, *140*, 15764–15773. [CrossRef]
7. Castillo, V.S.; Moyano, L.A. *Methotrexate: Pharmacology, Clinical Uses and Adverse Effects*; Nova Science Publishers: Hauppauge, NY, USA, 2012; ISBN 9781621005964.
8. Shiroky, J.B.; Neville, C.; Esdaile, J.M.; Choquette, D.; Zummer, M.; Hazeltine, M.; Bykerk, V.; Kanji, M.; St-Pierre, A.; Robidoux, L.; et al. Low-dose methotrexate with leucovorin (folinic acid) in the management of rheumatoid arthritis. *Arthritis Rheum.* **1993**, *36*, 795–803. [CrossRef] [PubMed]
9. Broichhagen, J.; Frank, J.A.; Trauner, D. A Roadmap to Success in Photopharmacology. *Acc. Chem. Res.* **2015**, *48*, 1947–1960. [CrossRef]
10. Szymanski, W.; Beierle, J.M.; Kistemaker, H.A.; Velema, W.A.; Feringa, B.L. Reversible photocontrol of biological systems by the incorporation of molecular photoswitches. *Chem. Rev.* **2013**, *113*, 6114–6178. [CrossRef]
11. Banghart, M.R.; Mourot, A.; Fortin, D.L.; Yao, J.Z.; Kramer, R.H.; Trauner, D. Photochromic blockers of voltage-gated potassium channels. *Angew. Chem. Int. Ed.* **2009**, *48*, 9097–10001. [CrossRef]
12. Mashita, T.; Kowada, T.; Takahashi, H.; Matsui, T.; Mizukami, S. Light-wavelength based Quantitative Control of Dihydrofolate Reductase Activity Using Photochromic Isostere of Inhibitor. *ChemBioChem* **2019**, *20*, 1382–1386. [CrossRef] [PubMed]
13. Micha, R.; Imamura, F.; von Ballmoos, M.W.; Solomon, D.H.; Hernán, M.A.; Ridker, P.M.; Mozaffarian, D. Systematic review and meta-analysis of methotrexate use and risk of cardiovascular disease. *Am. J. Cardiol.* **2011**, *108*, 1362–1370. [CrossRef] [PubMed]
14. Libby, P.; Ridker, M.; Hansson, G.K. Inflammation in atherosclerosis: From pathophysiology to practice. *J. Am. Coll. Cardiol.* **2009**, *54*, 2129–2138. [CrossRef] [PubMed]
15. Ross, R. The pathogenesis of atherosclerosis: A perspective for the 1990s. *Nature* **1993**, *362*, 801–809. [CrossRef] [PubMed]
16. Andreson, D.R.; Duryee, M.J.; Shurmur, S.W.; Um, J.Y.; Bussey, W.D.; Hunter, C.D.; Garvin, R.P.; Sayles, H.R.; Mikuls, T.R.; Klassen, L.W.; et al. Unique antibody responses to malondialdehyde-acetaldehyde (MAA)-protein adducts predict coronary artery disease. *PLoS ONE* **2014**, *9*, e107440. [CrossRef]
17. Heinecke, J.W. Oxidants and antioxidants in the pathogenesis of atherosclerosis: Implications for the oxidized low density lipoprotein hypothesis. *Atherosclerosis* **1998**, *141*, 1–15. [CrossRef]

18. Zimmerman, M.C.; Clemens, D.L.; Duryee, M.J.; Sarmiento, C.; Chiou, A.; Hunter, C.D.; Tian, J.; Klassen, L.W.; O'Dell, J.R.; Thiele, G.M.; et al. Direct antioxidant properties of methotrexate: Inhibition of malondialdehyde-acetaldehyde-protein adduct formation and superoxide scavenging. *Redox Biol.* **2017**, *13*, 588–593. [CrossRef]

19. Babić, N.; Peyrot, F. Molecular Probes for Evaluation of Oxidative Stress by In Vivo EPR Spectroscopy and Imaging: State-of-the-Art and Limitations. *Magnetochemistry* **2019**, *5*, 13. [CrossRef]

20. Bačić, G.; Pavićević, A.; Peyrot, F. In vivo evaluation of different alterations of redox status by studying pharmacokinetics of nitroxides using magnetic resonance techniques. *Redox Biol.* **2016**, *8*, 226–242. [CrossRef]

21. Dikalov, S.I.; Polienko, Y.F.; Kirilyuk, I. Electron Paramagnetic Resonance Measurements of Reactive Oxygen Species by Cyclic Hydroxylamine Spin Probes. *Antioxid. Redox Signal.* **2018**, *28*. [CrossRef]

22. Pérez-Jiménez, J.; Saura-Calixto, F. Anti-oxidant capacity of dietary polyphenols determined by ABTS assay: A kinetic expression of the results. *Int. J. Food Sci. Technol.* **2006**, *43*, 185–191. [CrossRef]

23. Bartoloni, E.; Alunno, A.; Valentini, V.; Luccioli, F.; Valentini, E.; La Paglia, G.M.; Leone, M.C.; Cafaro, G.; Marcucci, E.; Gerli, R. Targeting Inflammation to Prevent Cardiovascular Disease in Chronic Rheumatic Diseases: Myth or Reality? *Front. Cardiovasc. Med.* **2018**, *5*, 177. [CrossRef] [PubMed]

24. Thanigaimani, S.; Phie, J.; Krishna, S.M.; Moxon, J.; Golledge, J. Effect of disease modifying anti-rheumatic drugs on major cardiovascular events: A meta-analysis of randomized controlled trials. *Sci. Rep.* **2021**, *11*, 6627. [CrossRef] [PubMed]

25. Lems, W.; Boers, M.; van Vollenhoven, R.F.; Nurmohamed, M. Antirheumatic drugs for cardiovascular disease prevention: The case for colchicine. *RMD Open* **2021**, *7*, e001560. [CrossRef] [PubMed]

26. Tardif, J.; Kouz, S.; Waters, D.D.; Bertrand, O.F.; Diaz, R.; Maggioni, A.P.; Pinto, F.J.; Ibrahim, R.; Gamra, H.; Kiwan, G.S.; et al. Efficacy and Safety of Low-Dose Colchicine after Myocardial Infarction. *N. Engl. J. Med.* **2019**, *381*, 2497–2505. [CrossRef]

27. Avina-Zubieta, J.A.; Thomas, J.; Sadatsafavi, M.; Lehman, A.J.; Lacaille, D. Risk of incident cardiovascular events in patients with rheumatoid arthritis: A meta-analysis of observational studies. *Ann. Rheum. Dis.* **2012**, *71*, 1524–1529. [CrossRef]

28. Solomon, D.H.; Karlson, E.W.; Rimm, E.B.; Cannuscio, C.C.; Mandl, L.A.; Manson, J.E.; Stampfer, M.J.; Curhan, G.C. Cardiovascular Morbidity and Mortality in Women Diagnosed With Rheumatoid Arthritis. *Circulation* **2003**, *107*, 1303–1307. [CrossRef]

29. Roubille, C.; Richer, V.; Starnino, T.; McCourt, C.; McFarlane, A.; Fleming, P.; Siu, S.; Kraft, J.; Lynde, C.; Pope, J.; et al. The effects of tumour necrosis factor inhibitors, methotrexate, non-steroidal anti-inflammatory drugs and corticosteroids on cardiovascular events in rheumatoid arthritis, psoriasis and psoriatic arthritis: A systematic review and meta-analysis. *Ann. Rheum. Dis.* **2015**, *74*, 480–489. [CrossRef]

30. Rosenbaugh, E.G.; Roat, J.W.; Gao, L.; Yang, R.-F.; Manickam, D.S.; Yin, J.-X.; Schultz, H.D.; Bronich, T.K.; Batrakova, E.V.; Kabanov, A.V.; et al. The attenuation of central angiotensin II-dependent pressor response and intra-neuronal signaling by intracarotid injection of nanoformulated copper/zinc superoxide dismutase. *Biomaterials* **2010**, *31*, 5218–5226. [CrossRef] [PubMed]

31. Dikalov, S.; Griendling, K.K.; Harrison, D.G. Measurement of Reactive Oxygen Species in Cardiovascular Studies. *Hypertension* **2007**, *49*, 717–727. [CrossRef] [PubMed]

Article

Weak Interaction of the Antimetabolite Drug Methotrexate with a Cavitand Derivative

Zsolt Preisz [1,2], Zoltán Nagymihály [3,4], Beáta Lemli [1,4], László Kollár [3,4] and Sándor Kunsági-Máté [1,2,4,*]

[1] Institute of Organic and Medicinal Chemistry, Medical School, University of Pécs, Szigeti 12, H-7624 Pécs, Hungary; preisz.zsolt@pte.hu (Z.P.); beata.lemli@aok.pte.hu (B.L.)

[2] Department of General and Physical Chemistry, Faculty of Sciences, University of Pécs, Ifjúság 6, H 7624 Pécs, Hungary

[3] Department of Inorganic Chemistry, Faculty of Sciences, University of Pécs, Ifjúság 6, H 7624 Pécs, Hungary; nmzoltan@gamma.ttk.pte.hu (Z.N.); kollar@gamma.ttk.pte.hu (L.K.)

[4] János Szentágothai Research Center, University of Pécs, Ifjúság 20, H-7624 Pécs, Hungary

[*] Correspondence: sandor.kunsagi-mate@aok.pte.hu; Tel.: +36-72-503600 (ext. 35449)

check for
updates

Abstract: Formation of inclusion complexes involving a cavitand derivative (as host) and an antimetabolite drug, methotrexate (as guest) was investigated by photoluminescence measurements in dimethyl sulfoxide solvent. Molecular modeling performed in gas phase reflects that, due to the structural reasons, the cavitand can include the methotrexate in two forms: either by its opened structure with free androsta-4-en-3-one-17α-ethinyl arms or by the closed form when all the androsta-4-en-3-one-17α-ethinyl arms play role in the complex formation. Experiments reflect enthalpy driven complex formation in higher temperature range while at lower temperature the complexes are stabilized by the entropy gain.

Keywords: methotrexate; antirheumatic; cavitand; inclusion complex; thermodynamics; fluorescence

1. Introduction

Methotrexate (4-{*N*-[(2,4-diaminopteridin-6-yl) methyl]-*N*-methylamino} benzoyl)-L-glutamic acid, MTX, Figure 1) is an antimetabolite drug. It is widely used as a chemotherapeutic agent in rheumatoid arthritis (RA), psoriasis and some sorts of leukemia. MTX is a relatively well-known molecule and is a first-line antirheumatic medication because of its efficacy and safety [1]. It decreases the concentration of tetrahydrofolate (THF) in the cells by the inhibition of dihydrofolate reductase (DHFR) enzyme, therefore it reduces the purine nucleotide and DNA synthesis [2]. Other mechanisms of action were also mentioned in the literature, including reduction of antigen-dependent T-cell proliferation, promotion of adenosine release and suppression of transmethylation reaction [3,4].

Calixarenes are cyclic oligomers that consist of phenolic units that are condensated in the presence of an aldehyde and linked to each other, typically through a methylene bridge, in an acidic environment [5,6]. They are widely used in supramolecular chemistry, separation science and catalysis. They also have pharmaceutical applications as host molecules [6]. Substituents appended to the phenolic rings (upper or lower rim) can greatly influence the physical and chemical properties of these molecules, but numerous derivatives have been synthesized that have functional groups on the periphery of the molecule, too [7]. Promising results have been described in the literature about calixarenes that have heterocyclic substituents on the periphery, they can be used as selective extractants for amino acids [8], chiral recognition agents [9] or chelators that trap metals [10]. Calix[4] arene-based P-ligands were used in rhodium-catalyzed hydroformylation [11].
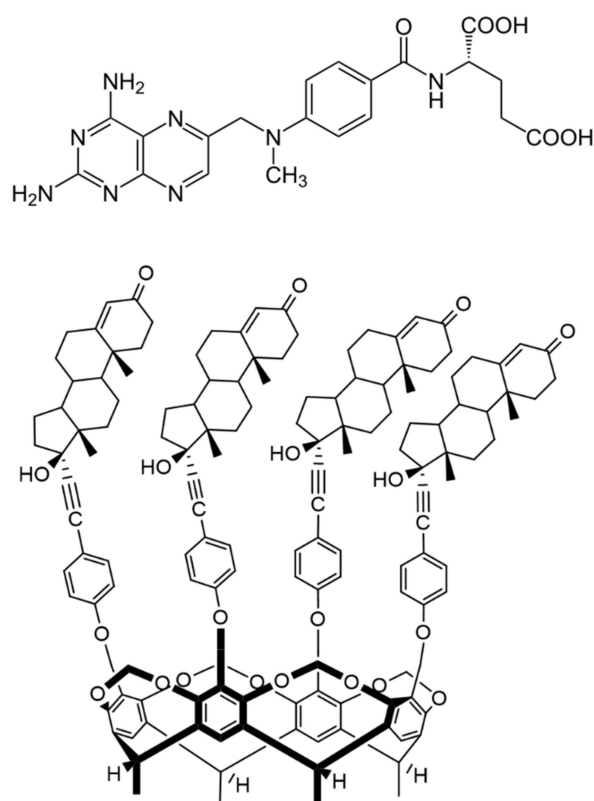
Figure 1. Chemical structure of antirheumatic and antitumor drug methotrexate (MTX, top) and the macrocyclic host molecule tetrakis(androst-4-en-3-one-17α-ethinyl)-cavitand (TAC, bottom) (8β-H, 9α-H and 13α-H are omitted for clarity).

Inserting additional methylene bridges between the phenolic oxygen atoms on adjacent aromatic rings, the structure is called a cavitand.

There is a wide range of literature available on the interactions between MTX and some macrocyclic compounds, e.g., cyclodextrins [12–14] and cucurbiturils [15], but just a limited number of researches were reported about the calixarene derivatives [16]. Moreover, no publication was found to describe the interaction of MTX with cavitands, despite that calixarenes and cavitands have some advantages compared with other host molecules, because they possess an aromatic cavity, which can embed MTX due to the π–π and CH–π interactions both inside and outside the cavity [16].

The MTX-cavitand interaction found to be an entirely unrevealed research field. Therefore, in this work the thermodynamic parameters of the interaction of MTX with tetrakis(androst-4-en-3-one-17-α-ethinyl)-cavitand (TAC) (Figure 1) were studied. This is a calix[4] resorcinarene derivative cavitand, in which ethisterone moieties are appended to the aromatic rings. Fluorimetric measurements were applied to determine the thermodynamic parameters of the MTX-cavitand complex formation reaction.

2. Results

2.1. Spectroscopic Determination of the Association Constants

Absorption spectra of MTX and TAC (Figure 2A) show absorption maximum of MTX at 390 nm, while no considerable emission of TAC can be obtained at this wavelength. Accordingly, applying 390 nm excitation wavelength, emission spectra of MTX were recorded. Fluorescence spectra of MTX show increased emission upon increased concentration of TAC (Figure 3.). The enhancement of the PL signal can be described by two processes: (i) the guest MTX molecules loose the solvation shell

reducing the quenching the PL signal induced by the solvent molecules, or, ii) the flexible MTX skeleton stabilized further by the TAC hosts and the reduced movements also support increasing the PL signal. Therefore, the changes induced in the spectra of MTX reflect interaction between the two molecules.
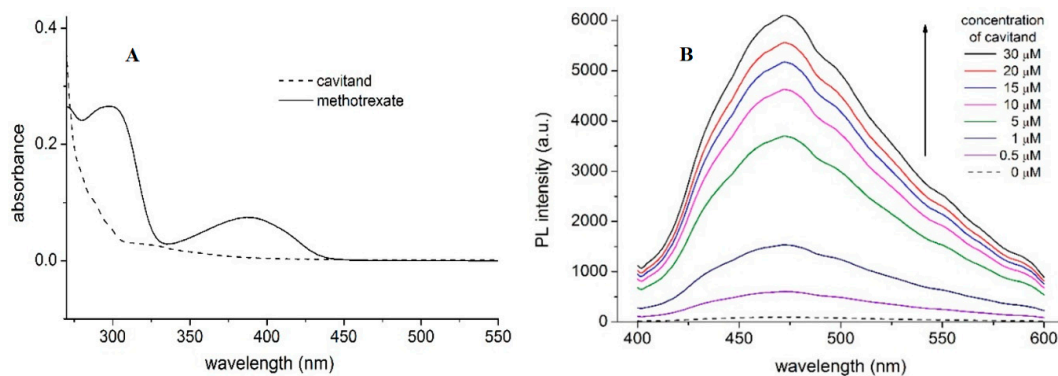
Figure 2. Absorption spectra of MTX (10 µM) and TAC (10 µM) (**A**) and fluorescence emission spectra of MTX (10 µM) in the absence and presence of TAC (0–30 µM) at 393.15 K (**B**) PL and a.u. reflect photoluminescence and arbitrary units, respectively.
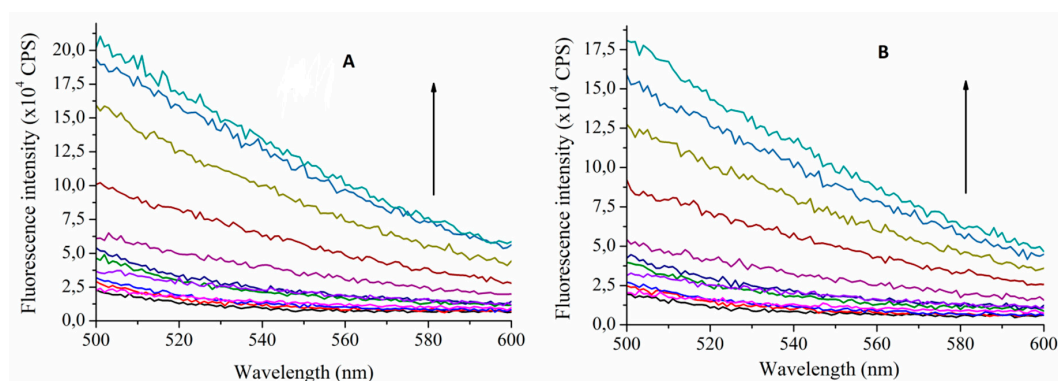
Figure 3. Fluorescence emission spectra of MTX (10 µM) in the absence and presence of TAC (0–80 µM) at 393.15 K (**A**) and at 313.15 K (**B**) ($\lambda_{excitation}$ = 390 nm). Arrows indicate increasing TAC concentrations (CPS reflects counts per s, colors only support the clarity).

The stability constants of this interaction can be calculated using the Benesi–Hildebrand method. To determine the thermodynamic parameters, the stability constants were calculated at temperatures 293.15 K, 296.48 K, 299.82 K, 303.15 K, 306.48 K, 309.82 K and 313.15 K. Considering that the DMSO solvent shows considerable Raman peaks overlapping the emission of MTX, two methods were applied to confirm the complex stabilities: either the HyperQuad code was applied using 10 selected wavelengths around the emission maxima (470–480 nm, see Figure 2.) or applying the Benesi–Hildebrand method, the right leg of the emission spectra is used, where the Raman scattering is negligible. In this case intensities obtained at 540 nm emission wavelength were applied to evaluate the data. Table 1 summarizes these results. These stability constants were then used to calculate the thermodynamic parameters of the interaction (Table 2).

2.2. Formation Thermodynamics

Two different temperature regions can be observed on the van 't Hoff plot (the logarithms of the stability constants were plotted against the reciprocal temperatures, Figure 4) of the interaction where the thermodynamic parameters of the complex formation differ significantly.

Table 1. Stability constants determined at different temperatures

Temperature (K)	log K (BH)	log K (HyperQuad)
293.15	4.16	4.13
296.48	4.20	4.18
299.82	4.22	4.20
303.15	4.19	4.20
306.48	3.75	3.72
309.82	3.64	3.61
313.15	2.94	2.92

BH reflects the Benesi-Hildebrand method.

Table 2. Thermodynamic parameters of the complex formation between TAC and MTX

	Experiments			Modeling	
Temperature (K)	ΔH (kJ mol^{-1})	ΔS (J K^{-1} mol^{-1})	Structure (see Figure 5)	ΔH (kJ mol^{-1})	ΔS (J K^{-1} mol^1)
293.15–299.82	15.79 ± 0.7	133.56 ± 6	closed	8.43	126.11
303.15–313.15	−210.66 ± 1.7	−614.57 ± 12	opened	−154.42	−214.67

ΔH and ΔS are the enthalpy change and entropy change, respectively.
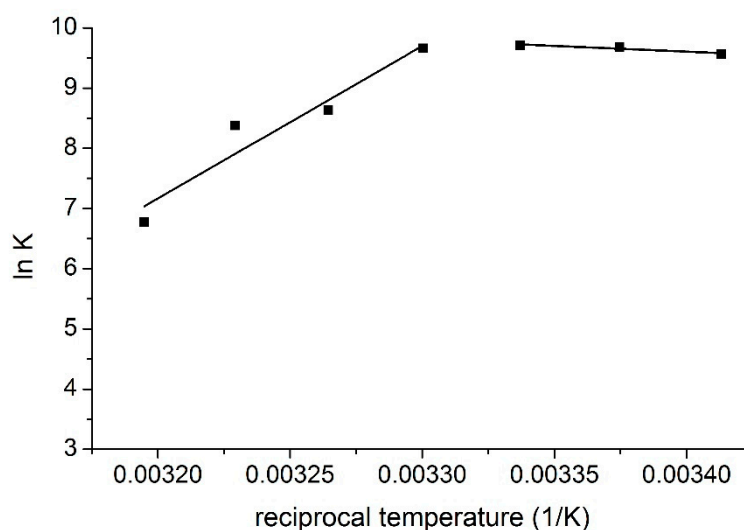
Figure 4. van 't Hoff plot of the complex formation of MTX and TAC.

These results imply different complex formation mechanisms in the different temperature regions. At lower temperatures, entropy gain is associated with enthalpy gain, but at higher temperatures, entropy loss is associated with enthalpy loss. Based on these observations, it is suggested that in the lower temperature region MTX interacts with the ethisterone moieties of TAC, i.e., with the chiral inlet of the host molecule. In this way, the entropy gain is caused by the removal of solvent molecules, but this process costs energy, this is the reason of the moderated positive enthalpy change. However, in the higher temperature region MTX interacts with the rigid inner cavity of TAC, i.e., with the lower lying aromatic 'basket', which causes entropy loss associated with the decreased freedom of the cavitand skeleton during complex formation. The negative enthalpy change reflects attractive interactions between the MTX molecules and the ethisterone arms of the cavitand.

2.3. Modeling Studies

The total energies of the species interacted were calculated first at semi-empirical AM1 level using Hyper Chem 8 code. The host cavitand molecule shows two stable conformers according to the orientation of the large ethisterone moieties on the upper rim (see Figure 5): the opened structure associated with more flexible skeleton compared to the closed structure where the ethisterone moieties possess reduced freedom due to the steric hindering of their motion. The differences between the calculated total Gibbs free energies of the parent 'opened' or 'closed' molecules in gas phase (partition of solvent motions is excluded) was found to be 21.7 kJ/mole at 298.16 K, which property support presence of the opened structure exclusively at around room temperature.
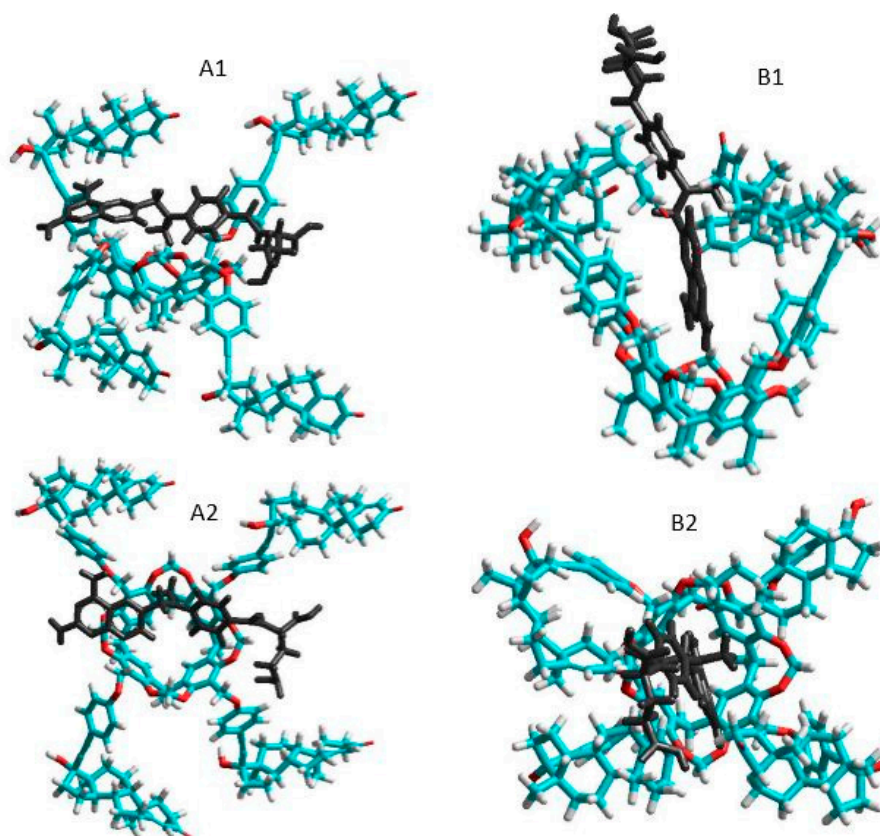
Figure 5. Side and top views of the equilibrium conformations of methotrexate–cavitand complexes associated with the opened (**A1** and **A2**) and closed (**B1** and **B2**) conformations of the cavitand (blue, red, white and black colors mean carbon, oxygen, hydrogen atoms and MTX molecule, respectively).

The thermodynamic parameters associated with the complex formation of the TAC with MTX were then calculated as described in the Materials and methods section. Results show positive enthalpy and entropy change during formation of the closed form complexes, while both the enthalpy and entropy term is negative when the complex show opened structure. Possible reason for these results is that the freedom of the flexible opened cavitand decreased considerably when the closed form complexes are stabilized. In contrast, the entropy gain can be obtained when the flexibility of the cavitand skeleton remains unchanged during formation of the opened complex structure. The good agreement between the experimental results derived in solution phase and that of the theoretical value calculated in gas phase reflects moderated entropy gain associated with the increased freedom of solvent molecules after leaving the solvation shell of the methotrexate guest.

3. Materials and Methods

3.1. Chemicals

Methotrexate (MTX) was obtained from Sigma-Aldrich. Tetrakis (androst-4-en-3-one-17α-ethinyl)-cavitand (TAC) was synthesized in our institute according to a published method [17]. The applied solvent was dimethyl sulfoxide (DMSO) purchased from Merck (Darmstadt, Germany).

Fluorimetric measurements were performed with a Fluorolog τ3 spectrofluorometer (Jobin-Yvon/SPEX, Longjumeau, France). Fluorescence spectra were recorded using 390 nm excitation wavelength. The emission values obtained at 540 nm were used for data evaluation. For data collection, photon counting method with 0.1 s integration time was used. Excitation and emission bandwidths were set to 2 nm. To avoid the inner filter effect, a 2 mm thickness of the fluorescent probes with right-angle detection was applied.

Considering the photosensitive character of MTX, the experimental setup was checked to confirm whether the measurement itself induces photodegradation of the MTX. To do that, the MTX samples were illuminated for 2 h using 390 nm light (the excitation wavelength). No considerable spectral changes were obtained which confirm stability of the MTX for the limited time of the measurements [18].

To determine the thermodynamic parameters associated with the complexation reaction of MTX and TAC, samples with constant concentration of MTX (10 µM) and with different concentrations of TAC (0–80 µM) were prepared in DMSO and measured immediately using 390 nm excitation wavelength at temperatures 293.0 K, 296.3 K, 299.7 K, 303.0 K, 306.3 K, 309.7 K and 313.0 K.

3.2. Data Evaluation

Stability constants (K, dm^3/mol) of MTX-TAC complexes were calculated either using the Benesi-Hildebrand equation, assuming 1:1 complex stoichiometry:

$$\frac{I_0}{I - I_0} = \frac{1}{A} + \frac{1}{A * K * [C]} \ln K \tag{1}$$

where I_0 and I are the fluorescence emission intensities of MTX in the absence and in the presence of the host, respectively; $[C]$ is the molar concentration of the host molecule while A is a constant.

Furthermore, association constants of the complex formation were also calculated by nonlinear fitting, based on the fluorescence emission data obtained, employing the HyperQuad2006 program package [19].

To determine the thermodynamic parameters, temperature dependence of the complex stabilities was examined, then the thermodynamic parameters were calculated using the van 't Hoff equation:

$$\ln K = -\frac{\Delta G}{RT} = \frac{\Delta H}{RT} + \frac{\Delta S}{R} \tag{2}$$

where the ΔH and ΔS stand for the enthalpy and entropy changes of the complex formation, respectively, while ΔG is the Gibbs free energy change. R is the gas constant, while T is the temperature in Kelvin.

3.3. Modeling Studies

Thermodynamic parameters of the MTX-TAC complexes were determined as follows. The enthalpy change was considered as the energy change calculated by subtracting the total energies of the reactants from the total energies of the products. Similarly, the entropy changes were calculated by subtracting the entropy terms of the reactants from the entropy terms of the products. Calculation of the entropy term

is implemented in the HyperChem code [20] as follows: after calculating the vibrational frequencies using the harmonic approximation, the entropy was then determined by the following equation:

$$S_{vib} = R \sum_i \left\{ \frac{h\frac{\nu_i}{kT}}{e^{(h\frac{\nu_i}{kT})} - 1} - \ln[1 - e^{(-h\frac{\nu_i}{kT})}] \right\} \tag{3}$$

where the ν_i is the frequency of vibration and T is the temperature.

The total energies of the species interacted were calculated at semi-empirical AM1 level using HyperChem 8 code.

4. Conclusions

Photoluminescence and molecular modeling studies of inclusion complexes formed by the antimetabolite drug, methotrexate and by the macrocyclic host molecule tetrakis(androst-4-en-3-one-17α-ethinyl)-cavitand highlight two temperature regions where the complexes possess different conformations: opened structure of the host cavitand with free androst-4-en-3-one-17α-ethinyl arms forms enthalpy stabilized structure while the stability of complexes formed by the closed form cavitand is stabilized by the entropy gain. This information can be applicable to design sensitive and selective molecular sensors for methotrexate drug.

Conflicts of Interest: The authors declare no conflicts of interest.

References

1. Friedman, B.; Cronstein, B. Methotrexate mechanism in treatment of rheumatoid arthritis. *Jt. Bone Spine* **2019**, *86*, 301–307. [CrossRef]
2. Tian, H.; Cronstein, B.N. Understanding the mechanisms of action of methotrexate. *Bull. NYU Hosp. Jt. Dis.* **2007**, *65*, 168–173. Available online: http://hjdbulletin.org/files/archive/pdfs/532.pdf (accessed on 18 June 2020).
3. Chane, E.S.L.; Cronstein, B.N. Molecular action of methotrexate in inflammatory diseases. *Arthritis Res.* **2002**, *4*, 266–273. [CrossRef]
4. Cutolo, M.; Sulli, A.; Pizzorni, C.; Seriolo, B. Anti-inflammatory mechanisms of methotrexate in rheumatoid arthritis. *Ann. Rheum. Dis.* **2001**, *60*, 729–735. [CrossRef]
5. Fahmy, S.A.; Brüßler, J.; Alawak, M.; El-Sayed, M.M.H.; Bakowsky, U.; Shoeib, T. Chemotherapy Based on Supramolecular Chemistry: A Promising Strategy in Cancer Therapy. *Pharmaceutics* **2019**, *11*, 292. [CrossRef] [PubMed]
6. Hoskins, C.; Curtis, A.D.M. Simple Calix[n]arenes and Calix[4]resorcinarenes as Drug Solubilizing Agents. *J. Nanomed. Res.* **2015**, *2*, 00028. [CrossRef]
7. Neda, I.; Vollbrecht, A.; Grunenberg, J.; Schmutzler, R. Functionalization of the Periphery of Calix[4]resorcinarenes with P(III)-containing Substituents via Hydroxy-, Trimethylsiloxy- and Ethoxy-Tethered Trimethylsiloxy Intermediates. *Heteroatom Chem.* **1998**, *9*, 553–558. [CrossRef]
8. Franz, M.H.; Iorga, M.; Maftei, C.V.; Maftei, E.; Neda, I. Studies on the constituents of Helleborus purpurascens: Use of derivatives from calix[6]arene, homooxa-calix[3]arene and homoazacalix[3]arene as extractant agents for amino acids from the aqueous extract. *Amino Acids* **2020**, *52*, 55–72. [CrossRef] [PubMed]
9. Maftei, V.; Fodor, E.; Jones, P.G.; Franz, M.H.; Davidescu, C.M.; Neda, I. Asymmetric Calixarene Derivatives as Potential Hosts in Chiral Recognition Processes. *Pure Appl. Chem.* **2015**, *87*, 415–439. [CrossRef]
10. Dieleman, B.; Matt, D.; Neda, I.; Schmutzler, R.; Harriman, A.; Yaftian, R. Hexahomotrioxacalix[3]arene: A scaffold for a C_3-symmetric phosphine ligand that traps a hydro-rhodium fragment inside a molecular funnel. *Chem. Commun.* **1999**, 1911–1912. [CrossRef]

11. Kunze, C.; Selent, D.; Neda, I.; Schmuzler, R.; Spannenberg, A.; Börner, A. Synthesis of New Calix[4]arene-Based Phosphorus Ligands and Their Application in the Rh(I) Catalyzed Hydroformylation of 1-Octene. *Heteroatom Chem.* **2001**, *12*, 577–585. [CrossRef]

12. Bourkaib, N.; Zhou, J.; Yao, J.; Fang, Z.; Mezghrani, O. Combination of β-cyclodextrin inclusion complex and self-microemulsifying drug delivery system for photostability and enhanced oral bioavailability of methotrexate: Novel technique. *Drug Dev. Ind. Pharm* **2013**, *39*, 918–927. [CrossRef] [PubMed]

13. Pattarino, F.; Giovannelli, L.; Giovenzana, G.B.; Rinaldi, M.; Trotta, M. Inclusion of methotrexate in alkyl-cyclodextrins: Effects of host substitutents on the stability of complexes. *J. Drug Del. Sci. Tech.* **2005**, *15*, 465–468. [CrossRef]

14. Aykaç, A.; Martos-Maldonado, M.C.; Casas-Solvas, J.M.; García-Fuentes, L.; Vargas-Berenguel, A. Binding ability properties of β-cyclodextrin dimers linked through their secondary faces towards cancer chemotherapeutic agent methotrexate. *J. Drug Del. Sci. Tech.* **2012**, *22*, 270–272. [CrossRef]

15. Chang, Y.-X.; Zhang, X.-M.; Duan, X.-C.; Liu, F.; Du, L.-M. Supramolecular interaction of methotrexate with cucurbit[7]uril and analytical application. *Spectrochim. Acta* **2017**, *183*, 131–137. [CrossRef] [PubMed]

16. Shalaeva, Y.V.; Morozova, J.E.; Syakaev, V.V.; Ermakova, A.M.; Nizameev, I.R.; Kadirov, M.K.; Kazakova, E.K.; Konovalov, A.I. Formation of cooperative amidoaminocalixresorcinarene–methotrexate nanosized aggregates in an aqueous solution and on the surface of gold nanoparticles. *Supramol. Chem.* **2018**, *30*, 901–910. [CrossRef]

17. Nagymihály, Z.; Wölfling, J.; Schneider, G.; Kollár, L. Synthesis of 2-methylresorcinol-based deepened cavitands with chiral inlet bearing steroidal moieties on the upper rim. *ChemistrySelect* **2020**, *5*, 6933–6938. [CrossRef]

18. Pascu, M.L.; Staicu, A.; Voicu, L.; Brezeanu, M.; Carstocea, B.; Pascu, R.; Gazdaru, D. Methotrexate as a Photosensitiser. *Anticancer Res.* **2004**, *24*, 2925–2930. Available online: http://ar.iiarjournals.org/content/24/5A/2925.long (accessed on 18 June 2020).

19. Gans, P.; Sabatini, A.; Vacca, A. Investigation of equilibria in solution. Determination of equilibrium constants with the HYPERQUAD suite of programs. *Talanta* **1996**, *43*, 1739. [CrossRef]

20. HyperChem, Hypercube Inc. 2007. Available online: http://www.hyper.com/ (accessed on 18 June 2020).

Effect of exposure time and pre-heating on the conversion degree of conventional, bulk-fill, fiber reinforced and polyacid-modified resin composites

Edina Lempel[a,*], *Zsuzsanna Őri*[b,c], *József Szalma*[d], *Bálint Viktor Lovász*[a], *Adél Kiss*[a], *Ákos Tóth*[e], *Sándor Kunsági-Máté*[b,c]

[a] *Department of Restorative Dentistry and Periodontology, University of Pécs, Pécs, Hungary*
[b] *Department of General and Physical Chemistry, University of Pécs, 6 Ifjúság Street, Pécs, H-7624, Hungary*
[c] *János Szentágothai Research Center, 20 Ifjúság Street, Pécs, H-7624, Hungary*
[d] *Department of Oral and Maxillofacial Surgery, University of Pécs, Pécs, Hungary*
[e] *Faculty of Sciences, University of Pécs Pécs, Hungary*

ABSTRACT

Objective. To determine the degree of conversion (DC) of different type of resin-based composites (RBC) in eight-millimeter-deep clinically relevant molds, and investigate the influence of exposure time and pre-heating on DC.

Methods. Two-millimeter-thick samples of conventional sculptable [FiltekZ250 (FZ)], flowable [Filtek Ultimate Flow (FUF)] and polyacid-modified [Twinky Star Flow (TS)] RBCs, and four-millimeter-thick samples of flowable bulk-fill [Filtek Bulk Fill Flow (FBF), Surefil SDR (SDR)] and sculptable fibre-reinforced [EverX Posterior (EX)] RBCs were prepared in an eight-millimeter-deep mold. The RBCs temperature was pre-set to 25, 35 and 55 °C. The RBCs were photopolymerized with the recommended and its double exposure time. The DC at the top and bottom was measured with micro-Raman spectroscopy. Data were analyzed with ANOVA and Scheffe post-hoc test ($p < 0.05$).

Results. The differences in DC% between the top/bottom and the recommended/extended exposure time were significant for the materials, except SDR (64.5/63.0% and 67.4/63.0%). FUF (69.0% and 53.4%) and TS (64.9% and 60.9%) in 2 mm provided higher DC% at the top and bottom with the recommended curing time, compared to the other materials, except SDR. Pre-heating had negative effect on DC at the bottom in flowable RBCs (FUF: 48.9%, FBF: 36.7%, SDR: 43%, TS: 54.7%). Pre-heating to 55 °C significantly increased the DC% in fibre-reinforced RBC (75.0% at the top, 64.7% at the bottom).

Significance. Increased exposure time improves the DC for each material. Among bulk-fills, only SDR performed similarly, compared to the two-millimeter-thick flowable RBCs. Pre-heating of low-viscosity RBCs decreased the DC% at the bottom. Pre-heating of fibre-reinforced RBC to 55 °C increased the DC% at a higher rate than the extended curing time.

© 2018 The Academy of Dental Materials. Published by Elsevier Inc. All rights reserved.

* *Corresponding author at*: Department of Restorative Dentistry and Periodontology, University of Pécs, 5. Dischka Gy Street, Pécs, H-7621 Hungary.
E-mail address: lempel.edina@pte.hu (E. Lempel).

1. Introduction

The marginal seal is an essential factor in the longevity of a dental restoration. Leakage at the deep gingival margin can lead to secondary caries development resulting in the failure of the restoration and compromising the health of the vital pulp tissue [1]. In root canal treated teeth the penetration of microorganisms through the coronal orifice of the root canal may also cause recontamination and subsequent failure of the endodontic treatment [2].

Resin-based composite restorative materials (RBC) are widely used among dentists as the most common restorative material. Evolution in both filler and polymer technology led to a wide selection of materials that provide the adequate characteristics required for each clinical situation [3]. Besides the conventional RBCs, bulk-fill and fiber reinforced RBCs are also available in the market as improved materials. Low and high viscosity bulk filling composites usually have higher translucency, and sometimes a modified initiator system to ensure better curing in depth, as compared to conventional composites. These materials are recommended to use in 4 mm or even 5 mm in thickness without stratification [4], and promise adequate curing depth, physical and mechanical properties. Many bulk-fill composite resins have been investigated regarding different parameters like mechanical features, degree of conversion, polymerization stress or microleakage. On the one hand, such studies have shown that bulk-fill composite resins have similar physical and chemical properties as conventional RBCs [5–8], on the other hand, bulk filling RBCs were found to have lower mechanical properties, higher shrinkage rate and lower degree of conversion in the recommended 4 mm thickness compared to 2 mm of the conventional RBC's [9–11].

Fiber reinforcement of conventional dental composites were also introduced with the aim of enhancing their physical properties [12]. The enhancement was due to the stress transfer from the matrix to the fibers depending on the fibers length and diameter, leading to high resistance to fracture [13,14]. Besides the above mentioned developments, manufacturers are looking for continuous improvements to eliminate disadvantageous properties, like the polymerization shrinkage and the inadequate rate of polymerization. The presence of the aforementioned drawbacks adversely affects the marginal or coronal leakage. To avoid it, flowable RBCs could be used at the gingival margins of a proximal cavity or as a barrier to seal the orifices of the root canals [15]. Flowable RBCs have better adaptation to the cavity walls owing to their high tooth surface wetting ability, ensuring penetration into all irregularities [16].

Pre-heating of RBC can also decrease microleakage. Increasing the polymerization temperature leads to lower viscosity thus increasing the fluidity and improving the adaptation of the RBC material to the cavity [17,18]. Pre-heating in turn results in greater mobility of monomer molecules within the resin matrix, enhances free radical formation, which results in a higher value of the DC and shorten curing time [19,20]. The increased mobility of monomers at elevated temperature can lead to delayed autodeceleration stage of the polymerization reaction thus contribute to increased monomer conversion [21]. In addition, pre-heating signifi-

cantly reduces the generation of shrinkage forces in both high-viscosity bulk-fill and conventional resin composites [22].

Clinical restoring procedures meet complex cavity shapes which could be challenging. Occasionally, cavity preparations that are 7–10 mm deep with a narrow orifice, as well as the angulation of the light curing tip may influence the polymerization rate of RBCs. Incomplete curing can lead to the early degradation, wear of the RBC restoration and also affect the functional durability, eventually leading to failure [23]. Light-curing an RBC is a complex process, as the depth of cure is affected by material composition, layer thickness, irradiance, curing time and variety of other factors [24]. For adequate polymerization the conventional RBC should receive a radiant exposure within the 16–24 J/cm^2 range [25]. This radiant exposure or energy density is calculated by multiplying the irradiance level coming from the light curing unit (LCU) by its duration [25]. Curing time is set depending of the irradiance level of the LCU. The "exposure reciprocity low" proposes reciprocity between the irradiance level and exposure duration to achieve equivalent DC of RBCs. This low has been evaluated in the literature and found not to apply, as it depends on the photoinitiator- and monomer-system of the RBC, the spectral radiant power of the LCU and is even time-dependent [26–28]. Selig et al. showed that an exposure time of only 10 s and above gave a sufficient DC [29], thus increasing the light exposure time results in higher radiant exposure reaching the RBC increment, especially with conservative cavity preparation (small orifice) and increased distance between the LCU tip and the RBC surface [30].

Selecting the proper material from the wide range available in the market is also a hard decision. In deep, occasionally irregular cavities the RBC should be easy to handle – if it is possible without the conventional layering – well adaptable and must be converted at an acceptable degree to provide good sealing and mechanical properties with low solubility. When sealing the orifices in root canal treated teeth, the use of a well distinguished material could be also advisable supposing a possible future re-treatment.

The purpose of this study was to measure the conversion degree with micro-Raman spectroscopy at the top and bottom of the first layer of a conventional sculptable and flowable, two flowable bulk-fill, a fibre-reinforced high-viscosity bulk-fill and a low-viscosity, coloured polyacid-modified RBC applied in a clinically relevant *in vitro* model, where an 8 mm distance from the light guide tip to the bottom side of the cavity was compiled. Further aim was to determine the effect of the recommended and the doubled curing time, as well as the RBC's pre-heating to 35 °C or 55 °C on the polymerization rate of the investigated materials.

2. Materials and methods

2.1. Preparation of the composite resin specimens

During this *in vitro* study six brands of resin composite material – a conventional sculptable microhybrid, a flowable nanofill, two flowable bulk-fill RBC, a fibre-reinforced bulk-fill material and a polyacid-modified RBC – were analyzed.

Table 1 – Materials, manufactures and composition.

Group	Material layer thickness	Code	Manufacturer	Shade	Organic matrix	Filler	Filler loading
Conventional RBC	Filtek Z250 2 mm	FZ	3M ESPE, St. Paul, MN, USA	A2	Bis-GMA, UDMA, Bis-EMA, TEGDMA	0.6 μm zirconia-silica	78 wt%
Conventional flowable RBC	Filtek Ultimate Flow 2 mm	FUF	3M ESPE, St. Paul, MN, USA	A2	BisGMA, TEGDMA, Procrylat resin	Zirconia/silica, ytterbium trifluoride	65 wt%
Bulk-fill RBC	Filtek Bulk Fill 4 mm	FBF	3M ESPE, St. Paul, MN, USA	U	BisGMA, UDMA, BisEMA, Procrylat resin	Zirconia/silica, ytterbium trifluoride	64.5 wt%
	SureFil SDR Flow 4 mm	SDR	Dentsply, Milford, DE, USA	U	Modified UDMA, EBPADMA, TEGDMA	Ba-Al-F-B silicate glass, Sr-Al-F silicate glass	68 wt%
Short glass fiber-reinforced RBC	EverX Posterior 4 mm	EX	GC Europe, Leuven, Belgium	U	BisGMA, TEGDMA, PMMA	Barium glass, short E-glass fibers	74.2 wt%
Polyacid-modified RBC	Twinky Star Flow Blue 2 mm	TS	VOCO GMBH, Cuxhaven, Germany	Blue	BisGMA, TEGDMA, UDMA, carboxylic acid modified methacrylate	Ba-Al-F-B silicate glass, silicon dioxide, glimmer	65 wt%

Abbreviation: RBC: resin-based composite; U: universal; UDMA: urethane dimethacrylate; EBPADMA: ethoxylated Bisphenol A dimethacrylate; TEGDMA: triethylene glycol dimethacrylate; BisEMA: Bisphenol A polyethylene glycol diether dimethacrylate; BisGMA: Bisphenol A diglycidil ether dimethacrylate; PMMA: polymethyl methacrylate.

The brand, the chemical composition and the manufacturer are presented in Table 1. According to the sample preparation and polymerization method, four experimental groups of specimens were divided. In each group, from each material, 5 specimens were prepared. Table 2 shows the experimental groups according to the method of polymerization and the abbreviations of the investigated materials.

Cylindrical Teflon molds with 5 mm internal diameter and 8 mm in height (representing a pulp chamber or deep proximal cavity) were constructed from two parts stacked on top of one another, according to the recommended thickness of the investigated materials. The schematic figure of sample preparation is presented in Fig. 1. For conventional sculptable and flowable RBCs and for the polyacid-modified resin composite the mold was built up from a 2 and a 6 mm high parts. For the bulk-fill RBCs the mold was constructed from two 4 mm high parts. Specimen preparation was performed inside a temperature-controlled chamber set at 25 °C. Materials with recommended 2 mm layer thickness were condensed or filled with a canula into the 2 mm high mold part, which was positioned on a glass slide. Thereafter, the uncured RBC was covered with a polyester (Mylar) strip in order to avoid contact with oxygen, which is an inhibitor of the polymerization. Immediately after that the 6 mm mold was positioned on top of the 2 mm mold filled with the investigated material providing the distance between the light curing guide and the material. The specimen was irradiated with a Light Emitting Diode (LED) curing unit (λ = 420–480 nm; LED.D, Woodpecker, Guilin, China) in standard mode, at an average tip irradiance of 1450 mW/cm^2 with an 8 mm diameter fiberglass light guide. The irradiance of the LED source was monitored before and after curing with a radiometer (Cure Rite, Dentsply, Milford, DE, USA). The curing light guide was centrally positioned directly on the mold entrance and the tip

of the light guide was ensured to be parallel to the sample. Recommended curing time was applied for Group 1 (control), whereas double exposure time for group 4 (Table 2). For the bulk-fill RBCs the 4 mm high mold was positioned on the glass slide and was filled with the material in the recommended 4 mm thickness. The top of the sample was covered with a Mylar strip and the second 4 mm high mold was positioned on top of the first one, then the specimen was irradiated as mentioned above. In case of pre-heated groups, the RBC pre-heating was performed using a resin composite heating device (Ena Heat, Micerium, Avegno, Italy) preset to 35 °C (Group 2) and 55 °C (Group 3). The attained RBC's temperature was measured with a thermocouple probe (Type K thermocouple device; Ø = 0.5 mm; Cu/CuNi; TC Direct, Budapest, Hungary) which was coupled to a digital thermometer (EL-EnviroPad-TC, Lascar Electronics Ltd., Salisbury, UK), with a resolution of 0.1 per 1 °C and a data sampling frequency of 1 measurement per second. The preparation for the pre-heated specimens followed the above described protocol and was photoactivated with the recommended irradiation time for each material, respectively.

Additionally, the irradiance which reached the top of the 2 mm conventional and the 4 mm bulk-fill RBC, was measured with the radiometer. The 6 mm high mold part with 5 mm internal diameter was positioned at the center of the radiometer sensor and the incident irradiance was recorded, representing the radiant power which reaches the top of the conventional sculptable and flowable, or polyacid-modified RBC sample, filled into the 2 mm high mold. Then the procedure was repeated with the 4 mm high mold to indicate the irradiance, that reached the top of the bulk-fill RBC, filled into the 4 mm high mold part. According to this information the radiant exposure (J/cm^2) could be calculated with the product of the irradiance (mW/cm^2) and the exposure time (s).

Table 2 – Methods of polymerization and abbreviations of the investigated materials.							
Methods of polymerization	Material temperature	Materials, exposure time, abbreviations, calculated radiant exposure					
		Filtek Z250	Filtek Ultimate Flow	Filtek Bulk Fill Flow	Surefil SDR	EverX Posterior	Twinky Star Blue
Group1	Exposure time recommended by the manufacturer	25 °C	20 s FZ_20 9 J/cm^2	20 s FUF_20 9 J/cm^2	10 s FBF_10 5.1 J/cm^2	20 s SDR_20 10.2 J/cm^2	10 s EX_10 5.1 J/cm^2	40 s TS_40 18 J/cm^2
Group2	Pre-heating to 35 °C and recommended exposure time	35 °C	20 s FZ_35_20 9 J/cm^2	20 s FUF_35_20 9 J/cm^2	10 s FBF_35_10 5.1 J/cm^2	20 s SDR_35_20 10.2 J/cm^2	10 s EX_35_10 5.1 J/cm^2	40 s TS_35_40 18 J/cm^2
Group3	Pre-heating to 55 °C and recommended exposure time	55 °C	20 s FZ_55_20 9 J/cm^2	20 s FUF_55_20 9 J/cm^2	10 s FBF_55_10 5.1 J/cm^2	20 s SDR_55_20 10.2 J/cm^2	10 s EX_55_10 5.1 J/cm^2	40 s TS_55_40 18 J/cm^2
Group4	Double exposure time	25 °C	40 s FZ_40 18 J/cm^2	40 s FUF_40 18 J/cm^2	20 s FBF_20 10.2 J/cm^2	40 s SDR_40 20.4 J/cm^2	20 s EX_20 10.2 J/cm^2	80 s TS_80 36 J/cm^2

Methods of polymerization	Material temperature	Filtek Z250	Filtek Ultimate Flow	Filtek Bulk Fill Flow	Surefil SDR	EverX Posterior	Twinky Star Blue
Group1: Exposure time recommended by the manufacturer	25 °C	20 s FZ_20 9 J/cm^2	20 s FUF_20 9 J/cm^2	10 s FBF_10 5.1 J/cm^2	20 s SDR_20 10.2 J/cm^2	10 s EX_10 5.1 J/cm^2	40 s TS_40 18 J/cm^2
Group2: Pre-heating to 35 °C and recommended exposure time	35 °C	20 s FZ_35_20 9 J/cm^2	20 s FUF_35_20 9 J/cm^2	10 s FBF_35_10 5.1 J/cm^2	20 s SDR_35_20 10.2 J/cm^2	10 s EX_35_10 5.1 J/cm^2	40 s TS_35_40 18 J/cm^2
Group3: Pre-heating to 55 °C and recommended exposure time	55 °C	20 s FZ_55_20 9 J/cm^2	20 s FUF_55_20 9 J/cm^2	10 s FBF_55_10 5.1 J/cm^2	20 s SDR_55_20 10.2 J/cm^2	10 s EX_55_10 5.1 J/cm^2	40 s TS_55_40 18 J/cm^2
Group4: Double exposure time	25 °C	40 s FZ_40 18 J/cm^2	40 s FUF_40 18 J/cm^2	20 s FBF_20 10.2 J/cm^2	40 s SDR_40 20.4 J/cm^2	20 s EX_20 10.2 J/cm^2	80 s TS_80 36 J/cm^2

A. Sample preparation in 2 mm layer thickness

B. Sample preparation in 4 mm layer thickness

Fig. 1 – Schematic figure of the 2 mm thick (A) and the 4 mm thick (B) sample preparation.

2.2. Micro-Raman spectroscopy measurement

The 24 h post-cure DC values of the polymerized composite resin samples were examined using Labram HR 800 Confocal Raman spectrometer (HORIBA Jobin Yvon S.A.S., Longjumeau Cedex, France). The following sets of parameters were applied during the micro-Raman measurements: 20 mW He–Ne laser with 632.817 nm wavelength, spatial resolution ∼1.5 μm, spectral resolution ∼2.5 cm⁻¹, magnification x 100 (Olympus UK Ltd., London, UK). The spectra were taken on the top surface of the composite specimens at three random locations with 10 s integration time and ten acquisitions were averaged for each geometrical point. Spectra of uncured composite were taken as reference. Post-processing of spectra was performed using the dedicated software LabSpec 5.0 (HORIBA Jobin Yvon S.A.S., Longjumeau Cedex, France). The ratio of double-bond content of monomer to polymer in the composite resin was calculated according to the following equation:

$$DC\% = (1 - (R_{cured}/R_{uncured})) \times 100$$

where R is the ratio of peak intensities at 1639 cm⁻¹ and 1609 cm⁻¹ associated to the aliphatic and aromatic (unconjugated and conjugated) C–C stretching in cured and uncured composite resins, respectively.

2.3. Statistical analysis

The statistical analysis was performed using the SPSS (Statistical Package for Social Science, SPSS Inc., Chicago, USA) software for Windows. The values for degree of conversion between the studied test groups and between each material were compared by one-way analysis of variance (ANOVA) test. For multiple comparisons the significance between the groups, materials and between the top and bottom surfaces was determined by Scheffe's post-hoc test at $\alpha = 0.05$ level.

3. Results

Fig. 2 shows the degree of conversion at the top of the investigated materials according to the method of polymerization.
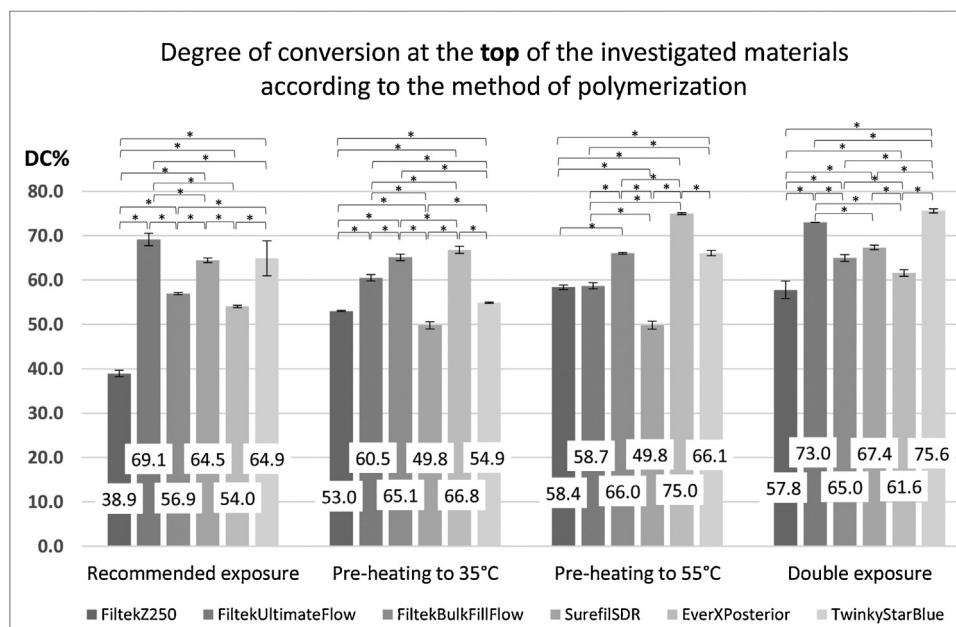
Fig. 2 – Degree of conversion at the top of the investigated materials according to the method of polymerization. The * mark indicates statistically significant difference between the investigated materials.
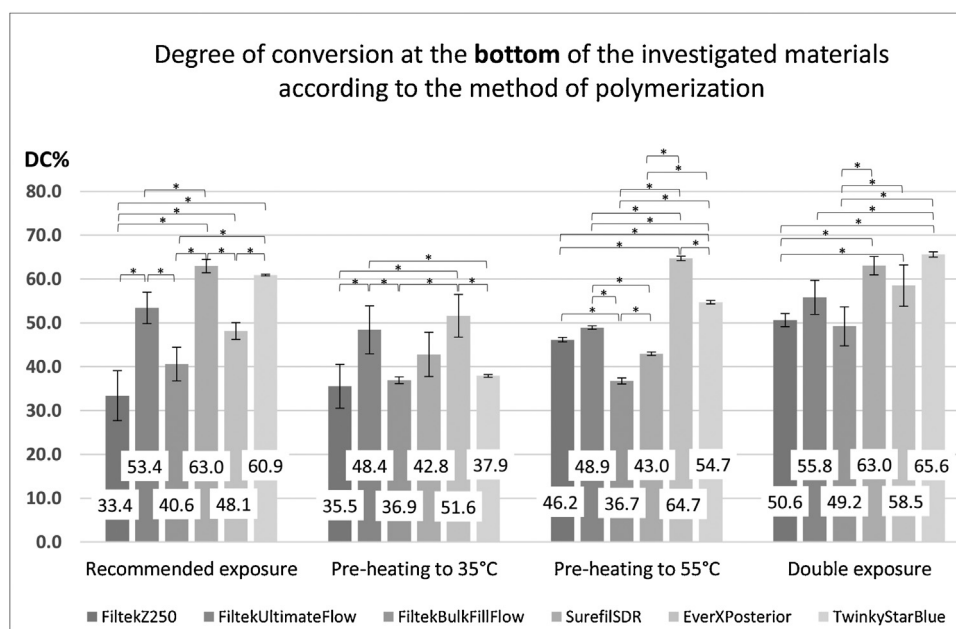
Fig. 3 – Degree of conversion at the bottom of the investigated materials according to the method of polymerization. The * mark indicates statistically significant difference between the investigated materials.

Regarding the top of the samples, conversion degree of the different materials ranged between 38.9% and 75.6%. The lowest value was measured in case of conventional sculptable micro-hybrid RBC (FZ_20) irradiated with the recommended exposure time at room temperature, meanwhile the highest DC% was detected in the case of the polyacid-modified resin composite (TS_80) with double exposure time at room temperature. In Group 1 the highest DC was measured in case of conventional flowable RBC (FUF_20) in 2 mm layer thickness. Similar values were detected on SDR_20 in 4 mm layer thickness and on TS_40 in 2 mm layer thickness. In Group 2 the effect of pre-heating to 35 °C was divisive. For FZ_35_20, FBF_35_10 and EX_35_10 there was a statistically significant increase in DC% on the top surface compared to the FZ_20, FBF_10 and EX_10 belong to Group 1. On the other hand, in most of the low viscosity materials (FUF_35_20, SDR_35_20 and TS_35_40) a statistically significant decrease was detected. In group 3. similar distribution in DC% was observed. In group 4. significantly higher DC
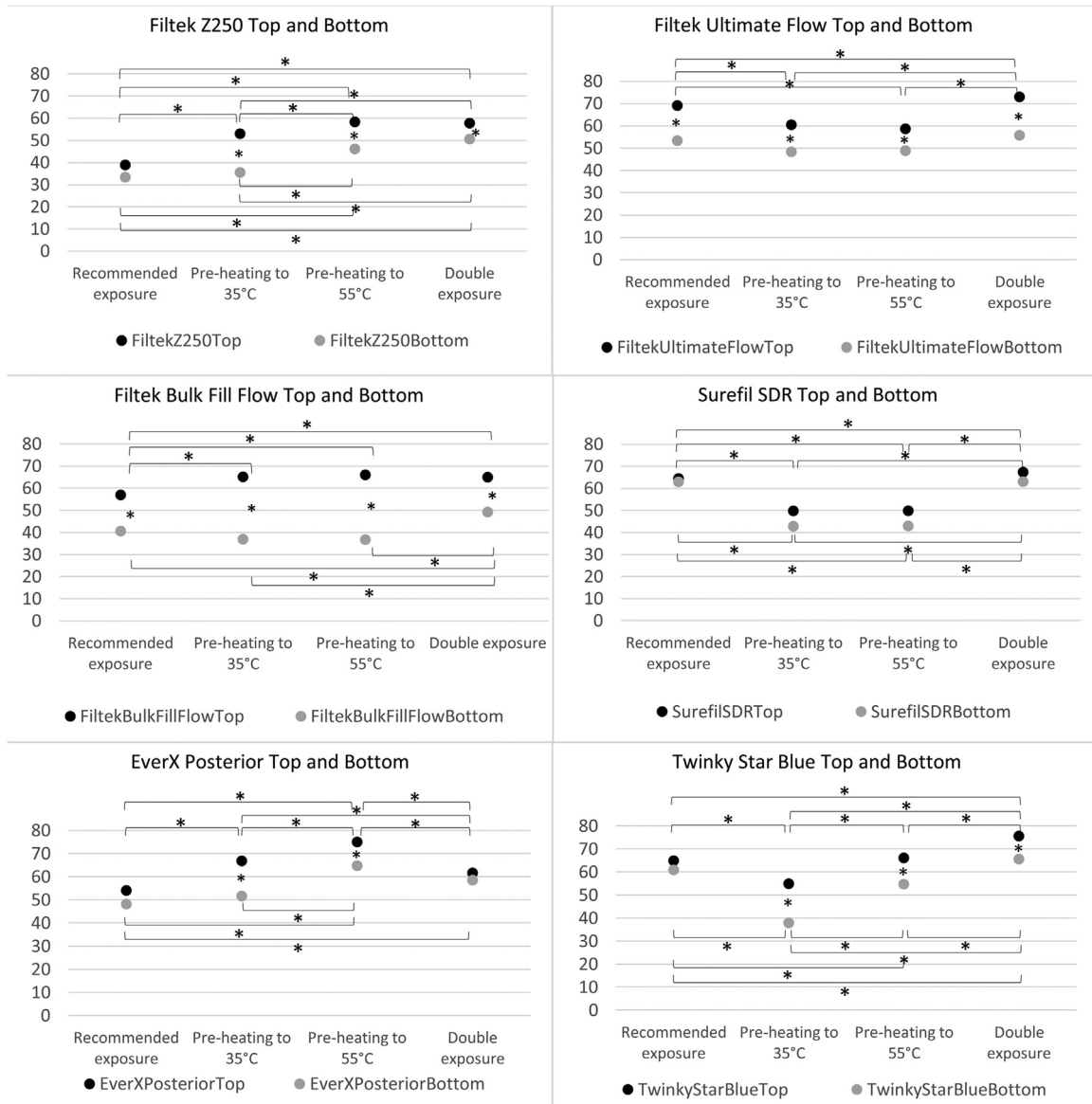
Fig. 4 – Degree of conversion at the top and the bottom of the investigated materials according to the polymerization methods. The * mark indicates a statistically significant difference between the investigated groups and as well as between top and bottom surfaces.

values (˜5–15% more) were measured compared to the single exposure at room temperature, except for SDR, which showed similar DC values both in Group 1 and 4. Double exposure time provided significantly higher DC for each material compared to the pre heated groups, except for EX, on which the effect of pre-heating to 55 °C dramatically improved the rate of polymerization. Fig. 3 demonstrates the degree of conversion at the bottom of the investigated materials according to the method of polymerization. Focusing on the bottom of the samples, the conversion degree of the different materials ranged between 33.4 and 65.6%. Similarly to the results of the top DC%, the lowest value was measured in case of FZ_20 and the highest was detected on TS_80. In general, at the bottom of the samples, in all cases, a lower value (˜5–15% less) could be measured than at the top. However, the decrease in DC was not

statistically significant in any of the materials. Fig. 4 shows the degree of conversion and the statistical significance at the top and the bottom of the investigated RBCs according to the polymerization methods. In the case of FZ_20, EX_10, TS_40 (Group 1) and in EX_20 (Group 4) the difference was not statistically significant between the top and bottom DCs. In the case of SDR the DC of the top and bottom surfaces was similar in all groups. In the low viscosity materials pre-heating to 35 °C inhibited the DC level at the bottom to reach the DC values of Group 1(FUF_35_20, FBF_35_10, SDR_35_20, TS_35_40) and had no statistically significant effect on the high viscosity materials (FZ_35_20, EX_35_10). In Group 3, the same result was observed in almost all low viscosity materials and a significant increase was detected in the high viscosity RBCs (FZ_55_20, EX_55_10). Double exposure unequivocally increased the DC values at the

bottom of the samples compared to Group 1, 2 and 3, except EX_20, where the highest DC was observed in Group 3, when the material was pre-heated to 55 °C.

The irradiance decreased from 1450 mW/cm^2 to 510 mW/cm^2 in the 4 mm deep mold, while in the case of the 6 mm deep mold with 5 mm internal diameter, it decreased to 450 mW/cm^2. The calculated radiant energy delivered to the samples is presented in Table 2.

4.   Discussion

In this study a clinically relevant 8 mm deep, 5 mm wide mold was filled with six different RBCs in the recommended layer thicknesses, irradiated with the recommended and its doubled exposure time as well as pre-heated to 35 and 55 °C. The degree of conversion at the top and bottom surfaces was assessed using micro-Raman spectroscopy. Different type of RBC materials were included in this investigation: a commercial sculptable microhybrid RBC (FZ), a conventional flowable nanofill RBC (FUF), a nanofill flowable bulk-fill RBC (FBF), another flowable bulk-fill RBC (SDR), a short glass-fiber reinforced bulk-fill RBC (EX) and a colored polyacid- modified RBC (TS).

The polymerization process has a major influence on the mechanical and biological properties of light cured RBCs [3]. Resin composite polymerization depends on the chemical structure of the monomer, filler particle characteristics, the photoinitiator concentration and the polymerization conditions, such as the spectral irradiance, exposure duration, distance between the curing guide and the material, layer thickness, just to mention a few of them [31,32]. An increment thickness of 2 mm is the gold standard for composite resin placement and curing [23]. It is technique sensitive and time consuming in cases of deeper posterior restorations or during coronal sealing of an endodontically treated tooth. To address these problems, various manufactures have recently introduced the newest type of resins, so called bulk-fill materials which claim to cure at a maximum increment thickness of 4 mm.

According to our results, with the recommended exposure time (Group 1) the commercial sculptable RBC in 2 mm layer thickness with 20 s irradiation showed the lowest DC% at the top and bottom surface of the samples. This RBC has the highest amount of filler content (78 wt%) among the investigated materials, which exhibited the highest light distribution. Halvorson et al. demonstrated, that increasing the filler-matrix ratio progressively decreases conversion, because an increased amount of filler particles is an obstacle for polymeric chain propagation [33]. To provide acceptable depth of cure in 4 mm or more layer thickness, the manufacturers of bulk-fill RBCs were able to improve polymerization depth by the use of potent photoinitiator systems along with an increased translucency [34]. However, with the recommended exposure time, bulk-fill RBCs (except SDR) did not reach the DC level of the 2 mm thick commercial as well as the polyacid-modified flowable RBC's DC value at the top of the samples in our investigation. Each RBC product revealed an inverse correlation between DC and depth. The monomer to polymer conversions showed 5–15% lower values at the bottom, except

for SDR, where the DC % reached the value measured at the top. It also exceeded the polymerization rate of the materials used in 2 mm layer thickness. The unique combination of glass filler loading with SDR resin provides high depth of cure in the recommended 4 mm thickness [35]. Besides the filler-matrix ratio, the DC is affected by the viscosity and reactivity of the monomers, as well [36,37]. In our study, only the SDR monomer system does not contain BisGMA, which is considered the most viscous, thus the less mobile monomer. SDR is a UDMA/EBPADMA-based bulk-fill flowable composite with additional TEGDMA, which has a synergistic effect on the rate of polymerization. Thus, the DC value of this monomer is significantly higher than that of the other investigated bulk-fill materials [38]. In addition, a photo-active modulator – embedded in the polymerizable resin backbone of the SDR resin monomer – may cooperate with camphorquinone (CQ), thereby facilitating polymerization.

In Group 4 with double exposure, the materials showed almost the same order, but with a 5–15% higher DC level on the top of the samples. It has been concluded by Zorzin et al., that extended curing time (30 s) had a positive effect on polymerization properties, so enhanced light curing of bulk-fills in deep cavities is recommended [39]. It is well-documented that radiant exposure (irradiance x exposure duration) of the light cure influences the DC and DOC of RBCs, thus a given radiant exposure can be delivered with different combinations of irradiance and exposure duration [25–27,40] Daugherty et al. concluded that the polymerization kinetics have been found to be highly complex, and a simple reciprocal relationship between radiant exposure and exposure time does not exist since irradiance and exposure can independently affect DC and DOC [41]. Increased depth of the cavity implies a radiant exposure reduction, whereas the irradiance of the light exponentially decreases with distance. Rueggeberg et al. and Emami and Söderholm concluded, that in order for a 2 mm thick conventional RBC increment to have adequate polymerization, it should receive a radiant exposure within the 16–24 J/cm^2 range [25,26]. In our study, an 8 mm deep cavity was simulated, where the distance between the light curing tip and the material top surface is increased, thus a decreased irradiance could initiate the polymerization. At 2 mm layer thickness (FZ, FUF, TS) the photons travel through 6 mm to reach the material's surface. This distance decreased the 1450 mW/cm^2 irradiance provided by the LED curing unit to ~740 mW/cm^2, however the small – 5 mm in diameter – orifice of the cavity further decreased the irradiance to 450 mW/cm^2. At 4 mm layer thickness (FBF, SDR, EX) in the 8 mm deep simulated cavity the photons travel through 4 mm distance, which decreases their radiant power to 930 mW/cm^2, and the shuttering effect of the narrow orifice resulted in 510 mW/cm^2 irradiance. The beneficial effect of the longer exposure duration is evident in group 4 in these conditions, however the DC of the different materials was not in correlation with the radiant exposure. The exception was TS, where the doubled exposure time increased the radiant exposure to 36 J/cm^2, resulted in 75.6% DC at the top surface and 65.6% at the bottom of the sample, which was the highest rate of polymerization among the investigated materials. The conventional flowable RBC (FUF) in also 2 mm layer thickness received 18 J/cm^2 radiant exposure and performed well with its 73% DC level at the top surface. The

bulk-fill materials failed to reach the DC value of the 2 mm thick flowable RBC's, but exceeded the polymerization rate of the sculptable FZ. At the bottom of the specimens, however, the bulk-fill RBCs performed better than the conventional RBCs used in 2 mm thickness, except FBF. The composition and initiator system of SDR and EX provided a convincing DC% through its 4 mm layer thickness without significant difference between the top and the bottom surfaces, cured in an 8 mm deep simulated cavity. Although, the highest DC was provided by TS (received 36 J/cm^2), there was no significant difference found between TS and SDR (received 20.4 J/cm^2), or TS and EX (received 10.2 J/cm^2) at the bottom surface in Group 4. According to our results, SDR was unique among the investigated materials with its 63% degree of conversion at the bottom of the samples, both in Group 1 and 4. It means, the rate of polymerization was the same (63%) with the recommended (20 s) and its double (40 s) exposure time in an 8 mm deep simulated cavity with 4 mm layer thickness.

Considering EX, in spite of the fact, that the 4 mm thick EX sample received less energy density (10.2 J/cm^2) compared to the 2 mm thick conventional one (18 J/cm^2), provided higher DC% at the bottom of the 4 mm thick sample. In fact, did not differ significantly from the highest values of TS and SDR, which received greater radiant exposure, 36 J/cm^2 and 20.4 J/cm^2, respectively. Certainly the short glass fibers have great significance in providing high depth of cure with the extended curing time (20 s) at the bottom of the samples. Similarity between the fiber/matrix refractive indices may allow light penetration into the deeper parts of the material. Goracci et al. concluded in their experiment, that EX exhibited DOC over 4 mm, the maximum thickness recommended for bulk placement [42]. From the available bulk-fill RBCs, besides SDR and EX, FBF was also investigated in this study. A universal shade was selected for all three brands. The absence or low amount of pigments in universal shaded, more translucent composite resin materials also have a beneficial effect on DC or depth of cure because pigments are opaque particles that will limit light penetration and reduce the degree of polymerization at greater depths [43] Although, Ilie found no correlation among DC and light transmittance. It was concluded, that light transmission changes during polymerization do not alter polymerization kinetics in modern bulk-fill RBCs [44]. Among bulk-fill materials in the present study, FBF has the lowest filler loading and the highest translucency parameter [45]. Despite of these advantageous parameters, FBF failed to reach the DC of the other investigated materials, especially at the bottom of the 8 mm deep simulated cavity in Group 1 and 4, except for FZ. In accordance with previous studies, the DC values for FBF were lower compared to the conventional flowable RBCs or to the other investigated bulk-fill materials [6,44]. Considering the chemical composition of FBF, it has the same filler content than the conventional flowable RBC (FUF) from the same manufacturer, however the matrix composition is different. FUF contains highly viscous BisGMA, low molecular weight, highly mobile and reactive TEGDMA as a diluting monomer and a Procrylate monomer. In case of FBF, besides Procrylate resin, BisGMA was combined with UDMA and BisEMA, instead of TEGDMA. Although the viscosity of UDMA is much lower than that of BisGMA, when it is mixed with the high molecular weight BisEMA, it can significantly restrict the mobility

of UDMA monomers and decrease their reactivity and conversion value [6,46]. The other influencing factor of DC is the radiant exposure delivered to the material. With the recommended 10 s curing time and 1450 mW/cm^2 irradiance, the delivered energy density was only 5.1 J/cm^2, which increased to 10.2 J/cm^2 with the extended irradiation time.

In Group 2 and 3 the effect of pre-heating on degree of conversion was investigated. Increasing the temperature of the RBC before application, decreases their viscosity, therefore enhances the marginal adaptation, reduces microleakage [17], and significantly reduces shrinkage force formation [22], while maintaining or increasing the degree of conversion and crosslinking by enhancing free radical and monomer mobility and increasing collisions among molecules [20,21]. The restoration of deep cavities with a narrow orifice – i.e. pulp chamber – could be difficult, considering the decreased irradiance of the curing light, that can reach the surface of the first RBC layer. Based on these considerations, the aim of increasing the temperature of the investigated materials was to determine the influence on degree of conversion in 8 mm deep – clinically relevant – simulated cavities. Two temperature values were used, 35 °C and 55 °C. As Fig. 3 shows, both in Group 2 and 3 two main effect was detected. In case of sculptable conventional RBC (FZ) and sculptable glass-fibre reinforced bulk-fill RBC (EX) a significant increase in DC% was found as a positive influence of pre-heating. In Group 2, the increase was remarkable at the top and less, but significant, at the bottom of the samples. In Group 3 the pre-heating to 55 °C increased the DC level by 20% at the top and around 15% at the bottom. This increase at the top of FZ and EX exceeded the DC values found in group 4, however, the DC% was higher at the bottom only for EX, compared to the double exposure. On the other hand, in case of the flowable RBCs, a negative effect on DC% was detected both in Group 2 and 3, especially at the bottom of the samples, compared to Group 1. Interestingly, there was not significant difference in DC values of flowable RBCs at the bottom between Group 2 and 3. At the top, the results were not as homogenous than at the bottom: in case of FUF, SDR and TS_35_40 a significant decrease was detected, meanwhile FBF showed a significant increase. The unexpected decrease of DC level of pre-heated (both 35 °C and 55 °C) flowable RBCs from the top to the bottom may be caused by the rapid cooling process of materials with lower filler content [47]. In our study the material was placed in an 8 mm deep mold under a non-isothermal condition, where the composite temperature reached after pre-heating is not stabilized, in order to simulate a clinically realistic scenario. Plasmans et al. reported an intraoral temperature of 25.1 °C around the treatment area after rubber dam isolation [48]. Studies, that have shown improvement in monomer conversion upon pre-heating generally maintained the resin composite temperature constant during the experimentation [20,21]. Once RBC temperature is elevated, there is a time delay between removing it from the heating device, dispensing it from a canula or syringe, placing it into an occasionally deep cavity, contouring it, and subsequently light-curing it. Our preliminary investigations revealed that during the 40 s manipulation time interval between RBC removal from the heater and start of photoactivation with 20 s, the temperature of the 55 °C pre-heated flowable test materials decreased to 26.2 °C. Results

provided by Lohbauer et al. also confirm that RBC's temperature rapidly drops to the physiological level upon removal from the pre-heating device [18]. Polymerization is an exothermic process and the heat liberated tends to accelerate the curing reaction. Generated heat increases the system temperature leading to decrease of viscosity and improves molecular mobility, increasing collision frequency of reactive radicals and postponing diffusion-controlled propagation, also known as autodeceleration, thus increasing final conversion [21]. However, during cooling the polymer formation has an excess heat loss. It deprives energy from the system, which is necessary for polymer chain propagation. The gel-phase interval may be decreased, autodeceleration takes place and leads to early vitrification, decreasing the degree of conversion. The polymerization as an exothermic process is influenced by the environmental temperature, curing time, monomer and filler content and nature of the filler surface [49]. Our results show different effect of pre-heating thermal changes on RBCs, probably depending on their filler content. On highly filled RBCs (FZ, EX) the pre-heating had a positive effect, it could increase significantly the DC% at the top and bottom, however on RBCs with lower filler content, the pre-heating even resulted in a negative effect on the bottom of the samples. These results are contradictious to most of the previous experiments [20,21], however Tauböck et al. reported similar, non-isothermal, real scenario pre-heating experiments and among the five investigated materials, only one showed significant DC% increase resulted from the pre-heating and in case of three materials, a non-significant DC% decrease was presented [22]. The observed DC% values and changes reflect overall result of the temperature dependent complex processes. It is speculated, that, on one hand, the higher volume content of inorganic fillers kept more energy and allowed for a delayed autodeceleration. According to another aspect, Plueddemann stated, that organofunctional silane coupling agents are hybrid organic-inorganic compounds which act as an interface between inorganic filler and organic polymer matrix and can help overcome the obstacle resulting from the mismatch of thermal coefficient [50]. In sculptable RBCs the filler content, thus the filler/matrix interface is higher. The dynamic equilibrium created at the silane interface between the filler and the polymer may provide higher exotherm reaction and dense bond formation at the deeper regions as well. This effect is stronger when the temperature increased to a higher level. On the other hand, in case of the less-filled RBCs, the highest DC% values were resulted on room temperature and most of them showed a negative effect of the pre-heating, indicating that, some part of the exothermic polymerization reaction is shifted towards the reactants, or the chain propagation is inhibited. Itś worth to mention here also, that in most cases of polymerization the entropy change associated with the building of one new segment into the chain continuously decreases since the rotational freedom of the chain decreases with an increasing length of the chain. The large negative entropy change inhibits the spontaneous growth of the chain due to the very small or positive free enthalpy (Gibbs free energy). Due to its complexity, further investigations are necessary to clarify this phenomenon. Preliminary testing of FZ and FUF in 8 mm deep cavity at isothermic (55 °C) condition resulted in 65 DC% and 63 DC% at the top

and 59 DC% and 60.5 DC% at the bottom, respectively. These are higher DC values, compared to the results observed in this present study under clinically relevant conditions, therefore supporting the results that were concluded in previous experiments [20,21]. However, the above mentioned measurements are under work, supplemented with continuous testing of thermal changes during the restorative procedures. In some cases of flowable RBCs (FUF and TS_55_40) the pre-heating provided enough energy to reach higher DC level at the top, however the sudden drop of temperature decreased the diffusion-controlled propagation towards the bottom of the samples leading to lower DC, compared to the control group (Group 1).

The minimum DC% for clinically acceptable restoration has not yet been exactly recognized [51]. Soares et al. reported that, for occlusal restorative layers, DC values should be at least 55% [52]. In our investigation the samples represented the first layer of light-cured RBC, which are covered with more subsequent layers in clinical situation. However, the adequate degree of monomer conversion is also essential at the bottom of the cavity close to the pulp space or at the proximal gingival margin. According to our results in Group 1 only SDR and TS, only EX in Group 3 and FUF, SDR, EX and TS in group 4 provided this DC level at the bottom of the samples in an 8 mm deep and 5 mm wide simulated cavity.

Present study, however, has some limitations. Firstly, this is an *in vitro* study and the specimens were prepared in a teflon mold and irradiated from an "occlusal" direction. In case of *in vivo* circumstances there is a possibility to irradiate the composite resin specimen from a buccal or lingual aspect as well, to improve the DC. Although, indirect polymerization of the RBCs through a substance significantly reduces the radiant exposure delivered to the material, since the tooth absorbs the energy originated from the photocuring device [53]. Secondly, the DC measurements do not yield information about the mechanical properties or the development of contraction stress in the investigated materials in response to recommended or doubled duration exposures and pre-heating. Although, direct correlation existed between hardness and DC, further mechanical testing, like three-point bending is planned to get more information about the relation of DC and mechanical characteristics. Thirdly, a commercial handheld dental radiometer was used in this survey to measure the radiant exitance from the curing unit and to calculate the radiant exposure received by the RBC through the mold with 4 and 6 mm depth and 5 mm internal orifice diameter. Price et al. discourages the use of irradiance values derived from a dental radiometer to describe the real spectral radiant power from an LCU [32]. However, in our study only one type of LCU was used and all the specimens were prepared in molds with the same dimension in diameter and with standardized LCU tip positioning to the mold's orifice, thus the spectral radiant power was similar for all the investigated materials and the received energy density was influenced only by the distance between the light curing tip and the material. Although, the values of the calculated radiant exposure are not accurate due to the usage of a radiometer, it is presumed, that the comparison of resulted DC data for the investigated materials is relevant. Finally, further investigations are necessary to

clarify the negative effect of pre-heating on the DC of flowable RBCs.

5. Conclusion

Within the limitations of this *in vitro* study – simulating an eight mm deep clinically relevant simulated cavity – the following conclusions can be stated:

1) Significantly higher DC levels were measured at the top of the samples compared to the bottom in each investigated material, in each experimental group, except SDR in Group 1 and 4.
2) Doubling the exposure time had a significant effect on DC% except for SDR. It provided the highest DC% at the bottom of the samples in Group 1 and 4, regardless the exposure time, thus the radiant exposure.
3) Radiant exposure had no direct correlation with DC especially in bulk-fill RBCs.
4) Pre-heating had a positive effect on the DC% of the high-viscosity RBCs (especially 55 °C on the DC% of EX) and had negative effect on DC% of the low-viscosity RBCs at the bottom of the samples.

Acknowledgments

REFERENCES

[1] Demarco FF, Correa MB, Cenci MS, Moraes RR, Opdam NJM. Longevity of posterior composite restorations: not only a matter of materials. Dent Mater 2012;28:87–101.

[2] Mandke L. Importance of coronal seal: preventing coronal leakage in endodontics. J Res Dent 2016;4:71–5.

[3] Cramer NB, Stansbury JW, Bowman CN. Recent advances and developments in composite dental restorative materials. J Dent Res 2011;90:402–16.

[4] Ilie N, Stark K. Curing behavior of high-viscosity bulk-fill composites. J Dent 2014;42:977–85.

[5] Alshali RZ, Salim NA, Satterthwaite JD, Silikas N. Long-term sorption and solubility of bulk-fill and conventional resin-composites in water and artificial saliva. J Dent 2015;43:1511–8.

[6] Alshali RZ, Silikas N, Satterthwaite JD. Degree of conversion of bulk-fill compared to conventional resin-composites at two time intervals. Dent Mater 2013;29:e213–7.

[7] Van Ende A, De Munck J, Van Landuyt KL, Poitevin A, Peumans M, Van Meerbeek B. Bulk-filling of high C-factor posterior cavities: effect on adhesion to cavity-bottom dentin. Dent Mater 2013;29:269–77.

[8] Roggendorf MJ, Krämer N, Appelt A, Naumann M, Frankenberger R. Marginal quality of flowable 4-mm base vs. conventionally layered resin composite. J Dent 2011;39:643–7.

[9] Ilie N, Bucuta S, Draenert M. Bulk-fill resin-based composites: an in vitro assessment of their mechanical performance. Oper Dent 2013;38:618–25.

[10] Jang JH, Park SH, Hwang IN. Polymerization shrinkage and depth of cure of bulk-fill resin composites and highly filled flowable resin. Oper Dent 2015;40:172–80.

[11] Lempel E, Czibulya Z, Kovács B, Szalma J, Tóth Á, Kunsági-Máté S, et al. Degree of conversion and BisGMA, TEGDMA, UDMA elution from flowable bulk fill composites. Int J Mol Sci 2016;17:e732.

[12] Vallittu PK. An overview of development and status of fiber-reinforced composites as dental and medical biomaterials. Acta Biomater Odontol Scand 2018;4:44–55.

[13] Garoushi S, Säilynoja E, Vallittu PK, Lassila L. Physical properties and depth of cure of a new short fiber reinforced composite. Dent Mater 2013;29:835–41.

[14] Fráter M, Forster A, Keresztúri M, Braunitzer G, Nagy K. In vitro fracture resistance of molar teeth restored with a short fibre-reinforced composite material. J Dent 2014;42:1143–50.

[15] Majety KK, Pujar M. In vitro evaluation of microleakage of class II packable composite resin restorations using flowable composite and resin modified glass ionomers as intermediate layers. J Conserv Dent 2011;14:414–7.

[16] Baroudi K, Rodrigues JC. Flowable resin composites: a systematic review and clinical considerations. J Clin Diagn Res 2015;9:e18–24.

[17] Fróes-Salgado NR, Silva LM, Kawano Y, Francci C, Reis A, Loguercio AD. Composite pre-heating: effects on marginal adaptation, degree of conversion and mechanical properties. Dent Mater 2010;26:908–14.

[18] Lohbauer U, Zinelis S, Rahiotis C, Petschelt A, Eliades G. The effect of resin composite pre-heating on monomer conversion and polymerization shrinkage. Dent Mater 2009;25:514–9.

[19] AlShaafi MM. Effects of different temperatures and storage time on the degree of conversion and microhardness of resin-based composites. J Contemp Dent Pract 2016;17:217–23.

[20] Daronch M, Rueggeberg FA, De Goes MF. Monomer conversion of pre-heated composite. J Dent Res 2005;84:663–7.

[21] Daronch M, Rueggeberg FA, De Goes MF, Giudici R. Polymerization kinetics of pre-heated composite. J Dent Res 2006;85:38–43.

[22] Tauböck TT, Tarle Z, Marovic D, Attin T. Pre-heating of high-viscosity bulk-fill resin composites: effects on shrinkage force and monomer conversion. J Dent 2015;43:1358–64.

[23] Ferracane JL. Resin composite-state of the art. Dent Mater 2011;27:29–38.

[24] AlShaafi MM. Factors affecting polymerization of resin-based composites: a literature review. Saudi Dent J 2017;29:48–58.

[25] Rueggeberg FA, Caughman WF, Curtis Jr JW. Effect of light intensity and exposure duration on cure of resin composite. Oper Dent 1994;19:26–32.

[26] Emami N, Söderholm KJ. How light irradiance and curing time affect monomer conversion in light-cured resin composites. Eur J Oral Sci 2003;111:536–42.

[27] Halvorson RH, Erickson RL, Davidson CL. Energy dependent polymerization of resin-based composite. Dent Mater 2002;18:463–9.

[28] Wydra JW, Cramer NB, Stansbury FW, Bowman CN. The reciprocity low concerning light dose relationships applied to BisGMA/TEGDMA photopolymers: theoretical analysis and experimental characterization. Dent Mater 2014;30:605–12.

[29] Selig D, Haenel T, Hausnerova B, Moeginger B, Labrie D, Sullivan B, et al. Examining exposure reciprocity in a resin based composite using high irradiance levels and real-time

degree of conversion values. Dent Mater 2015;31: 583–93.

[30] Erickson RL, Barkmeier WW. Curing characteristics of a composite. Part 2: the effect of curing configuration on depth and distribution of cure. Dent Mater 2014;30: e134–45.

[31] Leprince JG, Palin WM, Hadis MA, Devaux J, Leloup G. Progress in dimethacrylate-based dental composite technology and curing efficiency. Dent Mater 2013;29:139–56.

[32] Price RB, Ferracane JL, Shortall AC. Light-curing units: a review of what we need to know. J Dent Res 2015;94:1179–86.

[33] Halvorson RH, Erickson RL, Davidson CL. The effect of filler and silane content on conversion of resin-based composite. Dent Mater 2003;19:327–33.

[34] Bucuta S, Ilie N. Light transmittance and micro-mechanical properties of bulk fill vs. conventional resin based composites. Clin Oral Investig 2014;18:1991–2000.

[35] Ilie N, Hickel R. Investigations on a methacrylate-based flowable composite based on the SDR^{TM} technology. Dent Mater 2011;27:348–55.

[36] Baroudi K, Saleh AM, Silikas N, Watts DC. Shrinkage behaviour of flowable resin-composites related to conversion and filler-fraction. J Dent 2007;35:651–5.

[37] Al-Ahdal K, Ilie N, Silikas N, Watts DC. Polymerization kinetics and impact of post polymerization on the degree of conversion of bulk-fill resin-composite at clinically relevant depth. Dent Mater 2015;31:1207–13.

[38] Sideridou ID, Karabela MM. Effect of the amount of 3-methacyloxypropyltrimethoxysilane coupling agent on physical properties of dental resin nanocomposites. Dent Mater 2009;25:1315–24.

[39] Zorzin J, Maier E, Harre S, Fey T, Belli R, Lohbauer U, et al. Bulk-fill resin composites: polymerization properties and extended light curing. Dent Mater 2015;31:293–301.

[40] Peutzfeldt A, Asmussen E. Resin composite properties and energy density of light cure. J Dent Res 2005;84:659–62.

[41] Dougherty MM, Lien W, Mansell MR, Risk DL, Savett DA, Wandewalle KS. Effect of high-intensity curing lights on the polymerization of bulk-fill composites. Dent Mater 2018;34:1531–41.

[42] Goracci C, Cadenaro M, Fontanive L, Giangrosso G, Juloski J, Vichi A, et al. Polymerization efficiency and flexural strength of low-stress restorative composites. Dent Mater 2014;30:688–94.

[43] Garcia D, Yaman P, Dennison J, Neiva G. Polymerization shrinkage and depth of cure of bulk fill flowable composite resins. Oper Dent 2014;39:441–8.

[44] Ilie N. Impact of light transmittance mode on polymerisation kinetics in bulk-fill resin-based composites. J Dent 2017;63:51–9.

[45] Miletic V, Pongprueksa P, De Munck J, Brooks NR, Van Meerbeek B. Curing characteristics of flowable and sculptable bulk-fill composites. Clin Oral Investig 2017;21:1201–12.

[46] Khatri CA, Stansbury JW, Schultheisz CR, Antonucci JM. Synthesis, characterization and evaluation of urethane derivatives of Bis-GMA. Dent Mater 2003;19:584–8.

[47] Daronch M, Rueggeberg FA, Moss L, de Goes MF. Clinically relevant issues related to preheating composites. J Esthet Restor Dent 2006;18:340–50.

[48] Plasmans PJ, Creugers NH, Hermsen RJ, Vrijhoef MM. Intraoral humidity during operative procedures. J Dent 1994;22:89–91.

[49] Mohsen NM, Craig RG, Filisko FE. Effects of curing time and filler concentration on curing and postcuring of urethane dimethacrylate composites: a microcalorimetric study. J Biomed Mater Res 1998;40:224–32.

[50] Plueddemann EP. Silane coupling agents. Plenum; 1982. p. 111.

[51] Galvao MR, Caldas SG, Bagnato VS, Rastelli AN, Andrade MF. Evaluation of degree of conversion and hardness of dental composites photoactivated with different light guide tips. Eur J Dent 2013;7:86–93.

[52] Soares LE, Liporoni PC, Martin AA. The effect of soft-start polymerization by second generation LEDs on the degree of conversion of resin composite. Oper Dent 2007;32: 160–5.

[53] Watts DC, Cash AJ. Analysis of optical transmission by 400-500 nm visible light into aesthetic dental biomaterials. J Dent 1994;2:112–7.

PAPER

Structural properties of methanol–water binary mixtures within the quantum cluster equilibrium model†

G. Matisz,[ab] A.-M. Kelterer,*[c] W. M. F. Fabian[d] and S. Kunsági-Máté[ab]

Density functional theory (B3LYP-D3, M06-2X) has been used to calculate the structures, interaction energies and vibrational frequencies of a set of 93 methanol–water clusters of different type (cubic, ring, spiro, lasso, bicyclic), size and composition. These interaction energies have been used within the framework of the Quantum Cluster Equilibrium Theory (QCE) to calculate cluster populations as well as thermodynamic properties of binary methanol–water mixtures spanning the whole range from pure water to pure methanol. The necessary parameters a_{mf} and b_{xv} of the QCE model were obtained by fitting to experimental isobars of MeOH–H_2O mixtures with different MeOH content. The cubic and spiro motifs dominate the distribution of methanol–water clusters in the mixtures with a maximum of mixed clusters at x(MeOH) = 0.365. Reasonable agreement with experimental data as well as earlier molecular dynamics simulations was found for excess enthalpies H^E, entropies S^E as well as Gibbs free energies of mixing G^E. In contrast, heat capacities C_p and C_p^E showed only poor agreement with experimental data.

Introduction

Preferential or selective solvation[1–4] of a solute in binary solvent mixtures, where the composition of the solvation shell differs from the composition of the bulk solvent phase, can have significant effects on the physicochemical properties of the solution. The observable differences are obviously in connection with the molecular associations present in the binary solvent mixtures. Several studies can be found in the literature addressing the investigation of binary liquids regarding structural aspects. For instance, in a recent study, Wakisaka published a summary of experimental results[5–8] related to the cluster structures possible in binary liquid mixtures of water–MeOH, water–EtOH, water–*n*-PrOH and water–*n*-BuOH using fragmentation of liquid droplets

and mass spectrometric detection of the ionized clusters.[9,10] Solvent relaxation time measurements in mixtures of *n*-BuOH with MeOH, EtOH, and PrOH indicated a substantial change of the solvation shell at a specific molar fraction of *n*-BuOH.[11] Similarly, measurement of the solvent relaxation time by phase fluorimetry of phenols in binary EtOH–water mixtures resulted in a change from mono- to bi-exponential when the EtOH content exceeded a critical value.[12] In view of the importance of such solvent mixtures a detailed understanding of this selective/preferential solvation at an atomic level is essential. Besides experimental investigations quantum chemical calculations also have been used to determine the properties of such clusters formed by different solvent molecules, including *e.g.* methanol–water clusters up to four-membered rings[13] or methanol–benzene clusters.[14] Of particular importance for the present investigation are those dealing with water[15–17] and/or methanol[18–21] clusters addressing mainly the structural properties, binding energies and electronic properties of these clusters. Specifically, rather comprehensive calculations of (MeOH)$_n$ clusters with *n* up to *n* = 15 using a variety of computational procedures have been carried out by Thakkar and coworkers.[21] In addition to methanol clusters those of higher primary alcohols (up to *n*-hexanol) were treated by Golub *et al.*[19]

A powerful tool for the description and theoretical modelling of structure and properties of liquids is the quantum cluster equilibrium (QCE) theory[22] which is based on quantum chemically calculated cluster/molecular properties and the application of statistical thermodynamics. So far this procedure almost

[a] *Department of General and Physical Chemistry, University of Pécs, Ifjúság 6, 7624 Pécs, Hungary*

[b] *János Szentágothai Research Center, Ifjúság 20, 7624 Pécs, Hungary*

[c] *Institute of Physical and Theoretical Chemistry, Graz University of Technology, NAWI Graz, Stremayrgasse 9/I, 8010 Graz, Austria. E-mail: kelterer@tugraz.at*

[d] *Institute of Chemistry, University of Graz, NAWI Graz, Heinrichstr. 28, 8010 Graz, Austria*

† Electronic supplementary information (ESI) available: Fitting parameters a_{mf}, b_{xv} see Tables S1 (with *c8* clusters) and S2 (without *c8* clusters). Table S3 ΔG^{298}/H-bond and populations at different molar fraction. Fig. S1 Number of clusters for specific x(MeOH); Fig. S2 Benchmark of methods against MP2 for ring clusters; M06-2X data are shown in Fig. S3 (E_{int}), S4 (cluster populations), S5 (cluster distributions), S6 (H^E, S^E, G^E), S8 (C_p, C_p^E), and Fig. S7 (C_p^E for B3LYP-D3). Cartesian coordinates of all 93 clusters for B3LYP-D3 and M06-2X method as zip file. See DOI: 10.1039/c4cp05836d

This journal is © the Owner Societies 2015

Phys. Chem. Chem. Phys., 2015, **17**, 8467–8479 | 8467

exclusively has been applied to neat liquids, like water,[23–34] methanol,[28,35–38] ethanol,[28,38–41] propan-1-ol,[38] butan-1-ol,[38] benzyl alcohol,[39] 2,2-dimethyl-3-ethyl-3-pentanol,[39,42] formic acid,[43,44] liquid ammonia,[27,45,46] phosphine,[27] hydrogen sulfide,[27] N-methylacetamide,[47–49] liquid sulfur,[50] and liquid hydrogen-fluoride.[34,51–53] Recently, in addition to the static thermodynamic description by the QCE model, the kinetics of the hydrogen bond formation and proton transfer in water clusters has been studied by Weinhold.[54] To the best of our knowledge, the only binary system for which the QCE model has been applied until now is the water–dimethyl-sulfoxide (DMSO)[55] binary mixture. Evidently the reason is not limited interest in binary (or ternary) systems, but rather arise from technical difficulties for a proper description of such mixtures. These include both the approximations inherent in the QCE model, as well as the more complex structure of liquids consisting of more than one component. While in the binary system treated so far by the QCE model one component acts as a hydrogen bond acceptor (DMSO) and the other (water) as donor, in binary mixtures of alcohols or alcohol–water, as used in our previous experimental investigations,[11,12] both components can act as hydrogen bond acceptors as well as hydrogen bond donors.

As a first step to a detailed understanding of such binary solvent mixtures in this study we want to present a quantum cluster equilibrium study of the MeOH–water system with different composition ranging from pure water to pure MeOH. We have chosen this system not only as it represents the prototype of binary mixture used in our previous investigations but also since several theoretical modeling studies, mainly by molecular dynamics,[56–64] as well as experimental investigations,[65–68] have been published.

Moreover, since apparently the QCE model has for the first time been applied to a binary liquid mixture where both components can act as hydrogen bond acceptors and also as hydrogen bond donors, the MeOH–water system presents an important test case for the quantum cluster equilibrium model of such mixtures.

Computational methods

The methanol–water cluster structures have been optimized using the B3LYP density functional[69–72] augmented with the D3 dispersion correction[73] of Grimme et al. as implemented in the ORCA 2.9.1 program.[74] The TZVP basis set[75] has been used both for the optimizations and for the vibrational analysis. The intracluster interaction energies (E_{int}) were determined using the QZVP basis set[76] according to eqn (1) and are corrected for the basis set superposition error (BSSE)[77]

$$E_{int} = E_{cluster} - \sum E_{monomers} = E_{cluster} - i \cdot E_{MeOH} - j \cdot E_{H_2O} \quad (1)$$

where i, j are the numbers of monomers of methanol and water, respectively, participating in forming the cluster, while E is the electronic energy.

Gibbs free energies of interaction ΔG_{int} were obtained from the BSSE-corrected B3LYP-D3/QZVP interaction energies combined with non-thermal (ZPE) and thermal corrections dG^{corr}

resulting from the TZVP frequency analysis at $T = 298.15$ K and $p = 1$ atm. For the rotational partition function the appropriate symmetry numbers ($\sigma = 2$ for w1, m2w2r, w4r, m4r, m2w6; $\sigma = 3$ for m6r; $\sigma = 4$ for w8c and m4w4c; for all other clusters $\sigma = 1$) were used.

$$\Delta G_{int} = E_{int}(\text{BSSE-QZVP}) + [dG_{cluster}^{corr} - \sum dG_{monomers}^{corr}](\text{TZVP}) \quad (2)$$

All calculations were done with a very tight SCF cutoff and integration grid size of 5, together with tight geometry optimization criteria. In addition to B3LYP-D3 the M06-2X density functional[78–80] as implemented in Gaussian 09 program[81] in combination with the aug-cc-pVTZ basis set[82] was also used. The motivation for choosing these two functional was mainly based on the works of Thakkar[21] and Golub[19] as well as our previous experience.[14]

The QCE calculations have been performed using the developer version of the PEACEMAKER 2.0 program (rev. 572) of the research group of Kirchner.[33] The extension of the program for binary systems is described in detail in ref. 55. Besides the electronic energy, interaction energy, principal moments of inertia and harmonic vibrational frequencies of clusters, to obtain the statistical thermodynamics data via partition functions, two fitting parameters a_{mf} and b_{xv} are used in the QCE theory. The recently developed one-parameter QCE variant so far has only been applied to neat liquids.[34]

Based on the parameter a_{mf}, the interaction energies of each cluster with the surrounding particles/clusters can be defined as an additive term (u_{int}) to the intracluster interaction energies (E_{int}). The parameter b_{xv} gives the correction for the calculation of the excluded volume V_{excl}.

The mean field potential u_{int} in the case of the binary mixture is given by eqn (3), for each cluster individually:

$$u^{int} = -a_{mf}\frac{i+j}{V_m} \quad (3)$$

The excluded volume for the total system is defined as

$$V_{excl} = b_{xv} \cdot V_{vdw} \quad (4)$$

where i, j denote the number of molecules of methanol and water, respectively, which are participating in forming a given cluster, and V_{vdw} denotes total volumes of the clusters. The sum of all cluster volumes V_{vdw} compose 1 mol of monomers.

In the PEACEMAKER program the aforementioned two parameters are sampled with the aims to make agreement between the experimental and the calculated isobars while searching for the phase with the lowest Gibbs energy at the given pressure and temperature. Since only the liquid phase was considered, the mean absolute deviation function was selected in the program for comparison of the calculated and experimental isobars during the sampling process. The experimental isobars were obtained from the Landolt–Börnstein database.[68] Both a_{mf} and b_{xv} were kept constant over the whole temperature range since there is no provision for a temperature dependence of these two parameters in the PEACEMAKER program.

8468 | Phys. Chem. Chem. Phys., 2015, **17**, 8467–8479

This journal is © the Owner Societies 2015

Table 1 The clusters included in the cluster set describing the methanol–water binary liquid mixture[a]

Cluster class	Cluster structure	Number of H-bonds	B3LYP-D3/QZVP			M06-2X/aug-cc-pVTZ		
			E_{int}	ΔG_{int}^{298}	ΔG_{int}^{298}/monomer	E_{int}	ΔG_{int}^{298}	ΔG_{int}^{298}/monomer
mon	m1	0	0.00	0.00	0.00	0.00	0.00	0.00
	w1	0	0.00	0.00	0.00	0.00	0.00	0.00
dim	m2	1	−24.69	16.89	8.44	−24.44	14.98	7.49
	m1w1	1	−21.77	12.06	6.03	−20.90	13.90	6.95
	w1m1	1	−24.39	11.67	5.84	−23.83	12.92	6.46
	w2	1	−21.87	11.06	5.53	−21.31	13.65	6.83
r3	m3r	3	−75.08	19.72	6.57	−72.00	15.42	5.14
	m2w1r	3	−73.16	16.48	5.49	−71.60	17.07	5.69
	m1w2r	3	−71.16	17.29	5.76	−70.96	15.62	5.21
	w3r	3	−69.07	17.96	5.99	−70.39	17.83	5.94
r4	m4r	4	−133.08	17.94	4.48	−121.90	1.25	0.31
	m3w1r	4	−130.20	13.33	3.33	−121.27	6.68	1.67
	m2w2r	4	−127.46	16.78	4.19	−120.71	9.98	2.49
	m1w3r	4	−124.89	11.29	2.82	−119.68	13.07	3.27
	w4r	4	−122.36	14.70	3.68	−118.77	17.15	4.29
r5	m5r	5	−176.80	21.49	4.30	−163.32	14.30	2.86
	m4w1r	5	−173.36	19.23	3.85	−159.68	8.05	1.61
	m3w2r	5	−169.81	21.25	4.25	−157.59	11.13	2.23
	m2w3r	5	−165.96	22.54	4.51	−155.94	18.27	3.65
	m1w4r	5	−163.26	22.90	4.58	−155.59	18.62	3.72
	w5r	5	−160.58	20.76	4.15	−154.13	22.93	4.59
r6	m6r	6	−217.84	35.91	5.98	−200.47	0.60	0.10
	m5w1r	6	−214.21	35.51	5.92	−198.91	6.39	1.07
	m4w2r	6	−210.60	33.30	5.55	−197.35	15.34	2.56
	m3w3r	6	−207.21	30.58	5.10	−195.72	18.73	3.12
	m2w4r	6	−203.84	32.73	5.45	−194.11	24.65	4.11
	m1w5r	6	−200.76	29.77	4.96	−192.28	27.35	4.56
	w6r	6	−197.78	30.39	5.07	−190.47	31.31	5.22
r7	m7r	7	−261.88	42.60	6.09	−242.00	29.90	4.27
	m6w1r	7	−257.54	40.59	5.80	−240.49	34.72	4.96
	m5w2r	7	−253.78	43.01	6.14	−238.75	40.97	5.85
	m4w3r	7	−250.44	40.53	5.79	−237.95	44.14	6.31
	m3w4r	7	−245.83	42.51	6.07	−234.13	48.37	6.91
	m2w5r	7	−239.41	45.81	6.54	−230.56	39.58	5.65
	m1w6r	7	−234.20	37.28	5.33	−226.72	43.78	6.25
	w7r	7	−227.96	49.45	7.06	−220.17	37.24	5.32
bc7(5-4)	m6w1bc	8	−263.59	42.38	6.05	−242.49	34.45	4.92
	m5w2bc	8	−260.87	37.81	5.40	−243.50	36.35	5.19
	m4w3bc	8	−255.85	37.44	5.35	−241.75	41.28	5.90
	m3w4bc	8	−250.83	41.43	5.92	−240.26	37.97	5.42
	m2w5bc	9	−255.42	39.40	5.63	−246.11	31.00	4.43
	m1w6bc	9	−251.33	36.66	5.24	−244.61	36.80	5.26
	w7bc	9	−247.39	34.26	4.89	−241.68	38.40	5.49
s5(3-3)	m4w1s	6	−145.57	52.10	10.42	−140.81	32.08	6.42
	m3w2s	6	−143.10	51.88	10.38	−140.26	34.73	6.95
	m2w3s	6	−140.95	47.91	9.58	−139.93	34.67	6.93
	m1w4s	6	−138.81	42.77	8.55	−139.29	35.73	7.15
	w5s	6	−136.99	42.51	8.50	−138.93	37.01	7.40
s6(3-4)	m5w1s	7	−203.39	48.52	8.09	−190.70	29.28	4.88
	m4w2s	7	−201.22	48.74	8.12	−190.35	32.49	5.41
	m3w3s	7	−198.04	41.48	6.91	−189.37	32.71	5.45
	m2w4s	7	−195.69	41.17	6.86	−188.49	30.42	5.07
	m1w5s	7	−192.80	42.76	7.13	−187.71	33.78	5.63
	w6s	7	−190.27	43.51	7.25	−186.73	38.60	6.43
s9(5-5)	m8w1s	10	−357.17	55.40	6.16	−327.91	46.11	5.12
	m7w2s	10	−352.89	57.28	6.36	−325.19	49.64	5.52
	m6w3s	10	−348.04	59.15	6.57	−328.16	39.34	4.37
	m5w4s	10	−342.96	61.85	6.87	−324.78	42.49	4.72
	m4w5s	10	−339.60	60.48	6.72	−319.22	37.37	4.15

Table 1 (continued)

Cluster class	Cluster structure	Number of H-bonds	B3LYP-D3/QZVP			M06-2X/aug-cc-pVTZ		
			E_{int}	ΔG_{int}^{298}	ΔG_{int}^{298}/monomer	E_{int}	ΔG_{int}^{298}	ΔG_{int}^{298}/monomer
	m3w6s	10	−334.50	60.68	6.74	−316.61	40.36	4.48
	m2w7s	10	−331.41	57.48	6.39	−315.10	43.19	4.80
	m1w8s	10	−328.49	53.80	5.98	−313.82	49.65	5.52
	w9s	10	−325.62	54.85	6.09	−312.61	50.78	5.64
s11(6-6)	m10w1s	12	−445.33	72.99	6.64	−412.86	64.48	5.86
	m9w2s	12	−429.57	90.54	8.23	−406.99	72.29	6.57
	m8w3s	12	−424.96	93.75	8.52	−395.11	52.32	4.76
	m7w4s	12	−421.45	90.79	8.25	−395.51	50.19	4.56
	m6w5s	12	−417.84	87.80	7.98	−393.85	48.42	4.40
	m5w6s	12	−413.08	88.83	8.08	−389.70	46.33	4.21
	m4w7s	12	−409.66	90.71	8.25	−388.05	54.69	4.97
	m3w8s	12	−406.37	86.19	7.84	−386.33	56.45	5.13
	m2w9s	12	−407.83	76.25	6.93	−391.44	57.29	5.21
	m1w10s	12	−404.44	73.24	6.66	−389.72	62.27	5.66
	w11s	12	−401.20	74.77	6.80	−388.26	66.66	6.06
l5(4-1)	m3w1r-m1	5	−160.57	33.92	6.78	−150.76	35.86	7.17
l6(5-1)	m5r-w1	6	−209.40	41.25	6.87	−193.96	33.10	5.52
l6(4-2)	m3w1r-2m1(1,1)	6	−195.04	56.63	9.44	−184.46	50.15	8.36
	m3w1r-2m1(1,3)	6	−189.89	60.69	10.11	−177.78	44.24	7.37
b6(4-4)	m2mwm2	7	−220.47	27.84	4.64	−204.74	21.47	3.58
	mwmwm2	7	−215.86	33.51	5.58	−201.60	18.49	3.08
	mwmwmw	7	−212.42	30.65	5.11	−200.34	22.54	3.76
	w2mwmw	7	−210.13	26.32	4.39	−199.51	23.86	3.98
	mww2mw	7	−208.13	33.47	5.58	−198.48	26.23	4.37
	w2mww2	7	−207.15	27.90	4.65	−198.26	26.78	4.46
	w2w2w2	7	−202.96	31.01	5.17	−196.48	31.91	5.32
	mww2m2	7	−205.30	30.21	5.03	−197.28	28.74	4.79
	m2w2mw	7	−211.51	36.48	6.07	−202.07	27.86	4.64
	m2w2m2	7	−216.05	31.16	5.19	−203.55	25.13	4.19
c8	m5w3c	11	−331.17	24.08	3.01	−307.14	30.56	3.82
	m4w4c	12	−341.18	17.11	2.14	−319.27	21.34	2.67
	m3w5c	12	−337.67	15.94	1.99	−318.44	23.83	2.98
	m2w6c	12	−333.84	20.12	2.51	−317.63	26.52	3.32
	m1w7c	12	−330.03	20.77	2.60	−316.91	28.57	3.57
	w8c	12	−326.18	27.15	3.39	−315.84	30.39	3.80
c8-lasso	m4w4c-m1	13	−369.71	38.44	4.27	−350.33	42.17	4.69

[a] Interaction energies E_{int} and Gibbs free energies of interaction ΔG_{int}^{298} in kJ mol^{-1}. The M06-2X values for the clusters m8w1s, m8w3s, m9w2s, and m10w1s are based on aug-cc-pVDZ geometries, ZPE, and thermal corrections to ΔG_{int}.

In these QCE calculations it is especially important to provide a representative and comprehensive set of cluster motifs as it has been shown earlier.[31] In this study 93 clusters like ring, spiro, book, bicyclic, lasso and cubic structures have been included. The full cluster set (95 including the two monomers) with the naming convention is provided in Table 1 and some representative structures illustrating the notation are presented in Fig. 1. The various structures of the clusters required by the QCE model are denoted as $m_x w_y t$ where m and w indicate the monomers MeOH (m) and water (w); x and y mean the numbers of the corresponding monomers, and t indicates the cluster type i.e. mon: monomer, dim: dimer, r: monocyclic ring, bc: bicyclic ring, s: spiro cluster[31] in which two rings are connected through a common water molecule which establishes four hydrogen-bonds (2 donor and 2 acceptor) towards the two rings; l: lasso, b: book, c: cubic. The ring size

of monocyclic clusters (r-type clusters) equals $x + y$; for spiro cluster besides the total clusters size in parentheses also the numbers of molecules participating in the connected rings are given. For lasso structures in parentheses the numbers of molecules within the ring and of those connected to the ring as well as the points of attachment are given. In the case of seven-membered clusters besides monocyclic rings also bi- and polycyclic structures consisting of a five- and four-membered ring, denoted by bc7(5-4), have been found. Because previously linear chain and lasso structures were found to be less important[35,37,38] in the cases of primary alcohols, especially MeOH, within the QCE model only a few of these type of clusters were included. The reason of their smaller contribution originates from the smaller increase (as absolute value) in the interaction energy with the cluster size compared with cyclic structures where the cooperativity effect[18,83,84] plays a key role.

m5w1r (r6)   m10w1s (s11)

m1w7c (c8)   m2·mw·m2 (b6)
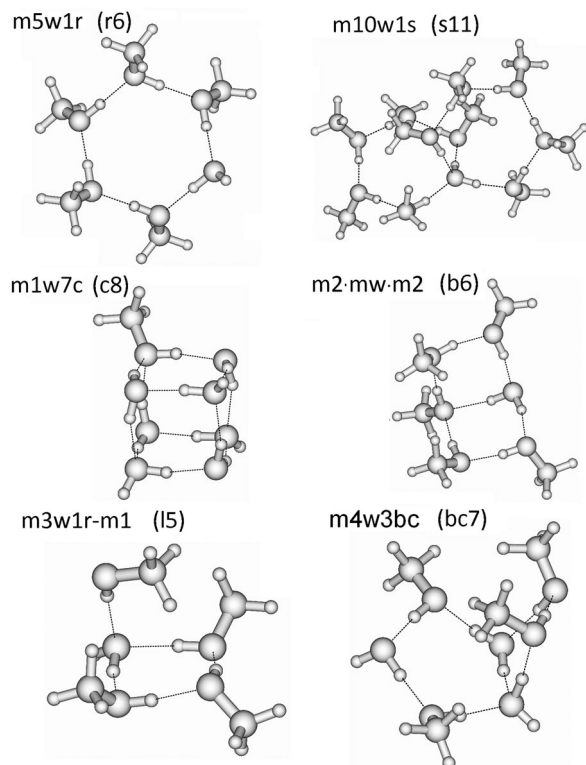
m3w1r-m1 (l5)   m4w3bc (bc7)

Fig. 1   Plot of the main cluster types (ring, spiro, cubic, book, lasso, and bicyclic).

Because not only the temperature but also the composition dependence of the cluster distribution were planned to be studied, the ring, spiro and cubic clusters were created with all the possible compositions. Hence, starting from pure water clusters, water molecules were successively replaced by methanol molecules with the restriction that the cluster motifs remain unchanged. Therefore, in the case of the spiro clusters one water molecule had to be retained; in the case of the cubic $c8$ clusters four water molecules are needed to be kept; in case of the ring type clusters, no such restriction applies. The replacements have been carried out according to the previous findings:[37] in structures with adjacent MeOH molecules the methyl groups were oriented to different directions (*i.e.* up–down, respectively). Furthermore, the replacements have been done more or less randomly within the structures, keeping in mind that the appropriate selection of cluster motifs[31] (*i.e.* inclusion of the cubic, the ring and the spiro cluster classes) is more important than the strict placement of the methyl groups or using strictly the putative global minimum structure of a given cluster type. Cartesian coordinates of all clusters optimized with B3LYP-D3/TZVP and M06-2X/aug-cc-pVTZ methods are available as ESI.†

Results and discussion

Values of a_{mf} and b_{xv} obtained by fitting to experimental isobars for MeOH–water binary mixtures of different composition [molar fraction x(MeOH)] are summarized in ESI,† Table S1. With increasing methanol molar fraction, the a_{mf} value also

increases, from 0.19 up to 0.41 J m^3 mol^{-1}. At the same time, the fitting becomes less accurate as shown by the increase of the mean absolute error (MAE). Importantly, the ratio of a_{mf}/b_{xv} is not constant but shows a parabolic shape. As a consequence, the application of the one-parameter variant of the QCE model to the methanol–water mixture might be problematic.

A similar dependence of the quality of the fitting on the composition has also been found for the DMSO–water binary system.[30] However, while in DMSO–water the deviation increases with increasing water content, in the MeOH–water mixture the quality of the fit becomes less satisfactory with increasing x(MeOH), *i.e.* with decreasing water content. For DMSO–water these deviations had been attributed to the rather small clusters used.[30] In the present case of MeOH–water not only larger clusters but also a more extensive cluster set has been used.

In the case of neat water the cubic $w8c$ cluster has been shown to dominate at low temperatures,[31,32] although neglecting it led to slightly more accurate isobars. To check the importance of this cluster type in binary MeOH–water mixtures, the fitting to experimental isobars has been done with and without these $c8$ clusters. Experimental isobars of neat water, neat MeOH, and of the 30, 60, 80 w% MeOH–water mixtures and those calculated by the QCE model using B3LYP-D3 results are shown in Fig. 2.

Compared with experiment a somewhat too small slope of the isobars – irrespective of the composition – is obtained. As ESI,† Table S2 shows, when cubic $c8$ clusters are excluded, the values of a_{mf} and b_{xv} are only slightly changed. Isobars as well as the values of a_{mf} and b_{xv} obtained from M06-2X calculations differ only marginally from those based on B3LYP-D3 calculations (Tables S1 and S2, ESI†).

The quality of the fit only marginally depends on whether cubic clusters are included in the set or not (Fig. 2). The numbers of clusters corresponding to a specific x(MeOH) is shown in ESI,† Fig. S1. Although the number of clusters vary with x, overall the chosen cluster set should allow for a balanced description of the MeOH–water mixture over the whole range of MeOH content.

Based on these optimal parameters a_{mf} and b_{xv} in the following, first interaction energies and distribution of the individual clusters considered for the MeOH–water binary mixture will be presented. Second, thermodynamic properties (heat capacities C_p, excess enthalpies, entropies, Gibbs free energies, and volumes of mixing, H^E, S^E, G^E, and V^E) derived therefrom will be compared with the corresponding experimental data as well as those obtained from previous calculations (molecular dynamics and Monte Carlo simulations).

Cluster distribution in MeOH–H$_2$O binary mixture

B3LYP-D3 as well as M06-2X interaction energies E_{int} and Gibbs free energies of interaction ΔG_{int}^{298} for the whole cluster set used in the QCE procedure are presented in Table 1.

While interaction energies are strongly negative and approximately correlate with the number of hydrogen bonds, Gibbs free energies of interactions are invariably positive and do not show any correlation with the number of hydrogen bonds.
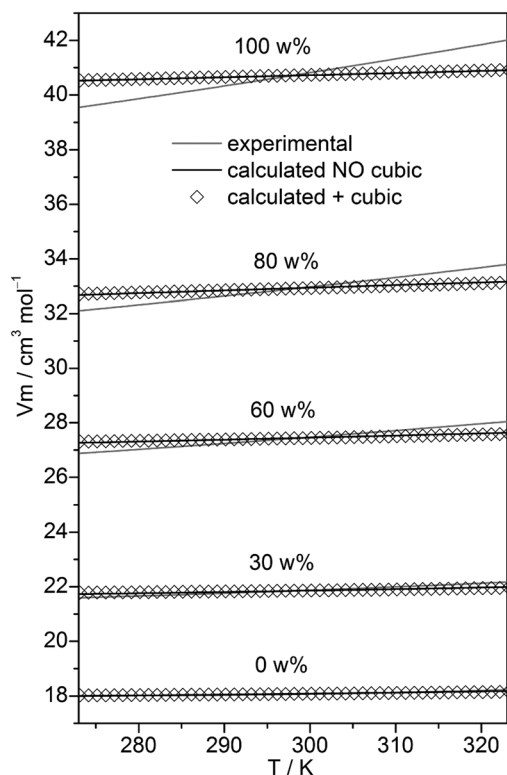
This journal is © the Owner Societies 2015

Phys. Chem. Chem. Phys., 2015, **17**, 8467–8479 | **8471**

Fig. 2 Plot of experimental isobars[68] of neat water, neat MeOH and 10, 30, 60, 80 w% MeOH–water mixtures *versus* those obtained by the QCE model with and without inclusion of the cubic *c8* clusters.

Fig. 3 Population (%) of ■ pure methanol clusters, ● pure water cluster, ▲ mixed MeOH–water clusters at 273 K, 298 K, and 323 K based on the B3LYP-D3 calculations.

According to the study of Thakkar *et al.*[21] dispersion-corrected density functionals work reasonably well for MeOH clusters compared with CCSD(T) results. Furthermore, M06-2X/aug-cc-pVDZ interaction energies per molecule of both linear as well as cyclic MeOH clusters were found to be nearly identical to those obtained by MP2/aug-cc-pVTZ calculations.[19] In contrast, B3LYP without dispersion corrections resulted in larger deviations.[19] Comparison of the present B3LYP-D3/QZVP//TZVP and M06-2X/aug-cc-pVTZ interaction energies with our previous MP2(fc)-CP/6-311++G(d,p) results indicate more negative E_{int} values but nearly identical trends for both density functionals (Fig. S2, ESI†). Moreover, B3LYP-D3 calculated interaction energies for the full cluster set considered in this paper (Table 1) are in close agreement with the corresponding M06-2X/aug-cc-pVTZ values (R^2 = 0.998, Fig. S3, ESI†). Thus, we are confident that the functionals used are appropriate for this study.

The population (based on the B3LYP-D3 calculations) of pure water, pure methanol as well as mixed clusters without further distinction of their composition at three different temperatures (273, 298, and 323 K) is displayed in Fig. 3.

Irrespective of the temperature mixed clusters dominate over a wide range of the composition of the binary MeOH-water system ($\geq$60% in the range x(MeOH) = 0.1 to 0.8). Only a slight decrease of the contribution of mixed clusters with increasing temperature is found (Fig. 3). It is interesting to note that NMR relaxation time measurements of MeOH–water mixtures have indicated that at low temperatures T_k < 245 K
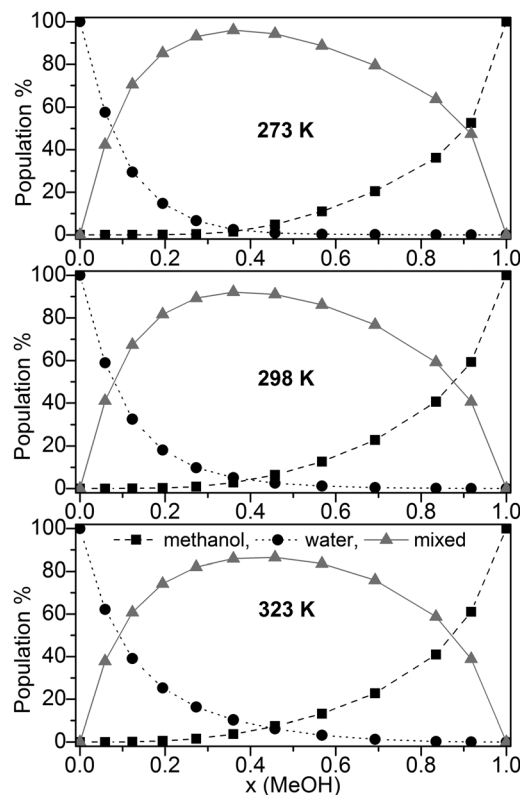
clusters between the same species prevail while above T_k mixed clusters are preferred.[85]

Since the lowest temperature considered here (T = 273 K) is well above T_k the predominance of mixed clusters in the intermediate molar fraction region is in line with these experimental findings. Although we have taken into account only clusters up to 11 molecules, our result obtained for the maximum population of mixed clusters at x = 0.365 (273 K) is in line with the mass spectroscopy experiments of Wakisaka.[5,8] From these experiments it had been concluded that above x(MeOH) = 0.375 the self-association of alcohol clusters becomes more preferred with increasing x(MeOH).[5,8] The gross populations of pure and mixed clusters based on M06-2X/aug-cc-pVTZ calculations are quite similar to those obtained by B3LYP-D3 (Fig. S4, ESI†). The most notable difference concerns mixed clusters which show lower populations over the whole range of x(MeOH) than those based on B3LYP-D3 calculations [<70% (M06-2X) at T = 298 K compared with up to 90% (B3LYP-D3, Fig. 3)]. For DMSO–water binary system a similar distribution of pure water, pure DMSO, and mixed clusters had been found.[30] However, the drop and/or rise of the pure clusters is less steep in DMSO–water than in MeOH–water.

For instance, ~60% pure water clusters at x(DMSO) = 0.2 and ~60% pure DMSO clusters at x(DMSO) = 0.8 had been calculated[30] compared with ~20% pure water clusters at x(MeOH) = 0.2 and ~40% pure MeOH clusters at x(MeOH) = 0.8 (Fig. 3). Consequently, the population of the mixed DMSO–water clusters is

significantly lower ($\leq$60%)[30] than that of mixed MeOH–water clusters.

The population of the various cluster classes irrespective of their composition (based on the B3LYP-D3 calculations) is presented in Fig. 4a (cubic $c8$ clusters included) and Fig. 4b (populations with cubic $c8$ clusters neglected).

The results in Fig. 4a show that only some of the used clusters are important to consider when including cubic clusters. These are the five- and six-membered monocyclic structures with only one ring, the 8-membered cubic clusters and the $s9$ and $s11$ spiro-type clusters. In line with previous findings for neat water[32,33] the population of cubic $c8$ clusters decreases with increasing temperature. Nevertheless, this cluster type by far is dominating up to x(MeOH) = 0.7 (273 K), and x(MeOH) = 0.5 (323 K). Since these clusters contain at least 4 water molecules it is not surprising that at higher MeOH contents their population drops significantly while the populations of monocyclic clusters ($r5$ and especially $r6$) where there is no such restriction with respect to the number of water molecules increase substantially at high x(MeOH). The presence of such cyclic structures in liquids capable of forming hydrogen bonds has been corroborated by experimental studies (soft X-ray emission[86] and X-ray absorption augmented by DFT calculations[87]). Especially at lower temperatures the spiro-type cluster $s11(6\text{-}6)$ is quite important for mixtures with relatively high MeOH content

(maximum of $\sim$25% at x(MeOH) $\sim$ 0.8 and T = 273 K, Fig. 4). The populations of $s9$ spiro type clusters are fairly constant over the whole composition of the MeOH–water mixture at low temperatures; at T = 323 K this cluster type is also populated (10–20%) especially in the water-rich region.

If cubic clusters are neglected in the QCE model (Fig. 4b), the spiro-type clusters $s11(6\text{-}6)$ and especially $s9(5\text{-}5)$ dominate in the water-rich region at lower temperatures (up to x(MeOH) = 0.6 at T = 273 K); with increasing temperature their contribution decreases from $\sim$50% (T = 273 K) to $\sim$35% (T = 323 K) for neat water. Since at least one water molecule is required for the spiro motif, the population steadily decreases with increasing MeOH content. In contrast to spiro clusters, the populations of monocyclic rings ($r5$ and $r6$) steadily increase with x(MeOH). As a consequence, neat MeOH is almost exclusively ($>$90%) composed of five- and six-membered ring clusters. Since cubic clusters require at least four water molecules, this result holds irrespective whether $c8$ clusters are included or not in the cluster set used to describe the MeOH–water system. Interestingly, seven-membered monocyclic rings $r7$ are not negligible at higher temperatures and low MeOH content (Fig. 4b).

Populations of individual clusters, *i.e.* distinguished by composition, are plotted in Fig. 5a (including cubic clusters) and Fig. 5b (neglecting cubic clusters). Dominating clusters are the cubic, spiro ($s9$ and $s11$), and ring-type structures while
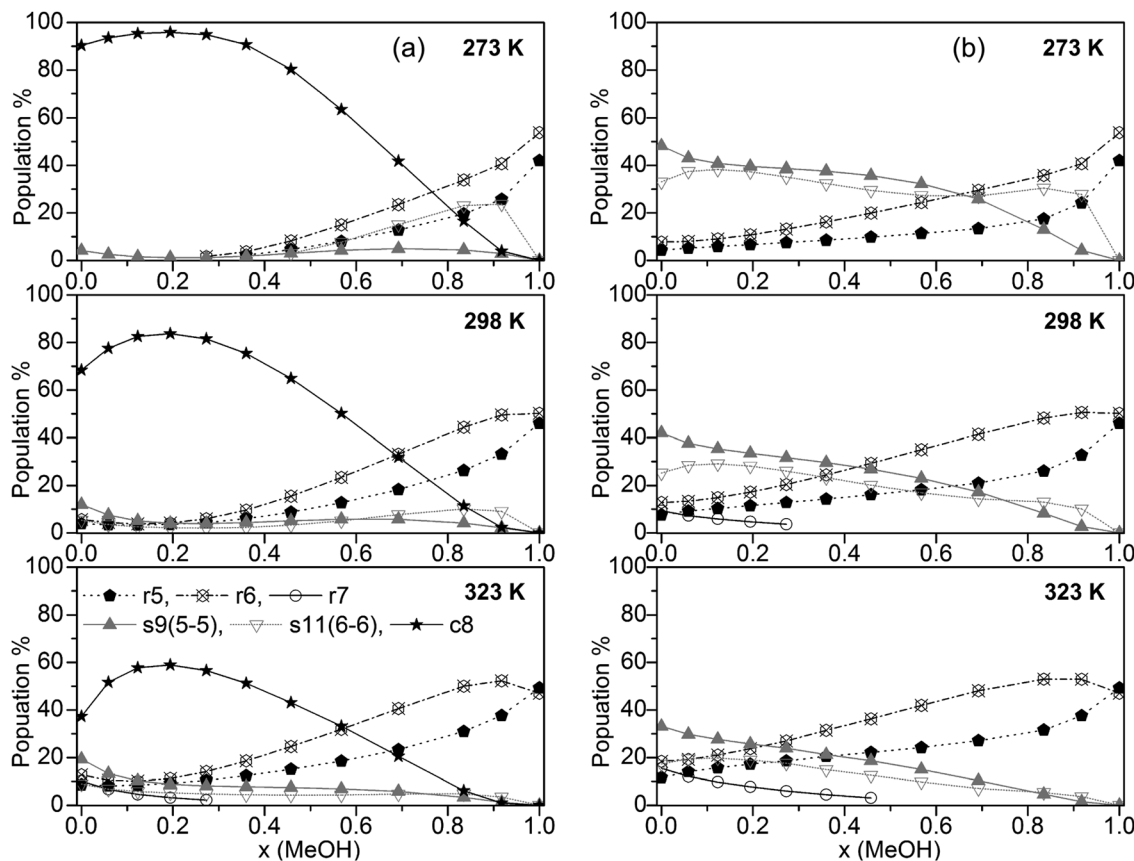

Fig. 4 Plot of the population of the cluster classes (a) including and (b) excluding cubic $c8$ clusters (for clarity, only clusters with populations $>$10% are shown).

This journal is © the Owner Societies 2015

Phys. Chem. Chem. Phys., 2015, **17**, 8467–8479 | 8473

book, lasso and bicyclic clusters are of minor importance. Concerning cubic clusters, for neat water the $w8c$ cluster is by far dominating, $\sim$70% at T = 273 and 298 K, $\sim$40% at T = 323 K. With increasing MeOH content the population of this cluster drops quite quickly ($\sim$10% for x(MeOH) = 0.2). In the water-rich region with x(MeOH) < 0.3 the $m1w7c$ structure becomes the dominating cubic cluster with a relatively sharp maximum at x(MeOH) $\sim$ 0.15. In the intermediate region, x(MeOH) = 0.2 to 0.7 the largest population is obtained for $m3w5c$ and, to a lesser extent, for $m4w4c$. Especially at lower temperatures (T = 273 and 298 K) and low MeOH content (x(MeOH) = 0.1–0.4) the $m2w6c$ cluster is significantly populated. An increase of the temperature results in a decrease of the populations of these cubic clusters. With respect to spiro-type clusters, in neat water and at very low MeOH content ($x \leq 0.15$) only $w9s$ is significantly populated with the population increasing at higher temperatures at the expense of $w8c$. The only other spiro-type cluster is $m10w1s$ at T = 273 K for x(MeOH) > 0.5 (maximum of 20% at x(MeOH) = $\sim$0.9). While monocyclic ring structures consisting solely of water molecules ($w6r$, $w7r$) are of minor importance (<15% at T = 323 K and even less at lower temperatures), the analogous MeOH clusters $m5r$ and $m6r$ become increasingly important with increasing MeOH content. As mentioned above, neat MeOH can almost exclusively be described by these two cluster types. At T = 323 K the dominant

cluster in the region x(MeOH) = 0.6–0.8 is $m5w1r$. The analogous plot obtained with M06-2X for T = 298 K is shown in Fig. S5 (ESI†). Similar to the B3LYP-D3 results, the dominating cluster types at low MeOH content are the cubic clusters $w8c$ and $m1w7c$ and at high MeOH content the $m6r$ ring structure. In the range x(MeOH) = 0.6–0.9 the cyclic cluster $m5w1r$ is already significantly populated (10–20%) at T = 298 K. Interestingly, in contrast to the B3LYP-D3 results, the five-membered cyclic $m5r$ cluster does not show any substantial population at T = 298 K.

Fig. 5b presents cluster populations obtained when cubic clusters are excluded. In the MeOH – rich region (x(MeOH) > 0.8) where cubic clusters are of minor importance, the cluster distribution is quite similar to that obtained with cubic clusters included. The most important contributions are due to the five- and six-membered monocyclic rings $m5r$, $m6r$, and $m5w1r$. Of course, for neat MeOH the population of this latter cluster drops to 0 (Fig. 5b). For neat water and low MeOH content a significant increase of the spiro-type water clusters $w9s$ and $w11s$ can be seen. At higher temperatures the contributions of these clusters decrease in favor of monocyclic rings $w6r$ and $w5r$ (at T = 323 K). This is in agreement with Wakisaka's results,[8] that self-associated clusters are formed predominantly at low molar fraction (water clusters) and high molar fraction ($x \geq 0.375$, methanol clusters).
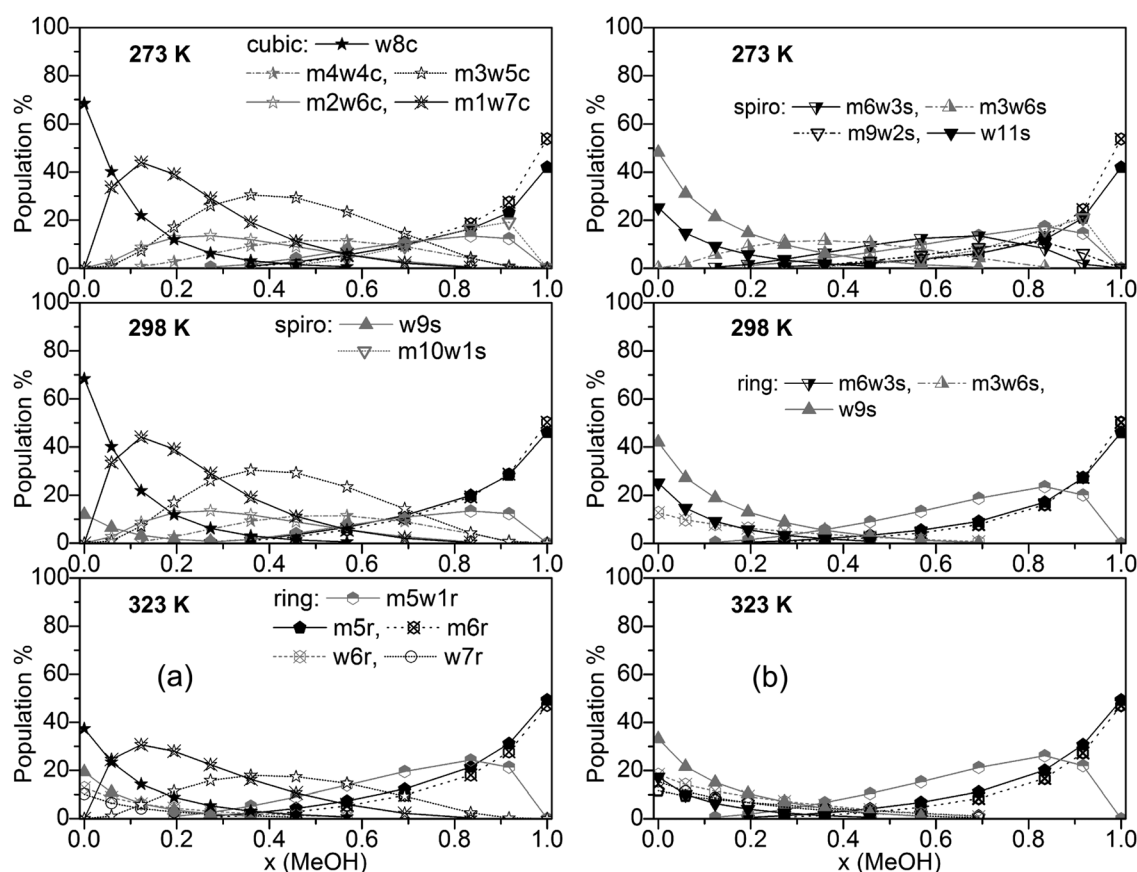

Fig. 5 Plot of individual cluster distributions (a) including and (b) excluding cubic $c8$ clusters (for clarity, only clusters with populations >8% are shown).

8474 | *Phys. Chem. Chem. Phys.*, 2015, **17**, 8467–8479

This journal is © the Owner Societies 2015

Table 2 Comparison of the calculated excess thermodynamic quantities (H^E, S^E, G^E) with data obtained from other experimental and theoretical studies. Units are kJ mol^{-1} and J K^{-1} mol^{-1}

x(MeOH)		Exp.[67,88,91]	MD/2PT[56]	OPLS/TIP4P[64]	QCE B3LYP-D3	QCE M06-2X
0.05	H^E	−0.57	−0.18	−0.25	−0.81	−0.40
	S^E	−2.48	−0.70	−1.01	−2.91	−2.02
	G^E	0.17	0.06	0.05	0.11	0.20
0.27	H^E	−0.88	−0.66	−0.32	−2.18	−0.49
	S^E	−3.93	−3.31	−3.42	−8.44	−4.25
	G^E	0.29	0.37	0.70	0.42	0.78
0.54	H^E	−0.79	−0.82	−0.32	−1.67	−0.17
	S^E	−3.69	−3.93	−3.50	−7.45	−3.84
	G^E	0.31	0.42	0.72	0.63	0.97
0.70	H^E	−0.61	−0.73	−0.22	−1.06	0.16
	S^E	−2.89	−3.39	−2.77	−5.48	−2.99
	G^E	0.25	0.35	0.61	0.61	1.05

Calculated thermodynamic functions for methanol–water binary liquid mixtures

Based on the QCE calculations, the following thermodynamic functions are available from the canonical partition function according to eqn (22)–(29) in ref. 33 for the different temperatures and compositions: internal energy, enthalpy, entropy, Gibbs free energy, Helmholtz free energy as well as second derivatives of the partition function, like constant pressure and constant volume heat capacities.

In Table 2 we compare the experimental excess enthalpies, entropies, and Gibbs free energies of mixing[64,65,67,68,88–91] with those calculated by the QCE model as well as those obtained

from a molecular dynamics simulation/two-phase thermodynamics (MD/2PT)[56] for different compositions of the MeOH–water system.

The excess enthalpies of mixing H^E (eqn (5)) (Fig. 6a) and the excess entropy of mixing S^E (eqn (6)) (Fig. 6b) obtained by the QCE calculations with and without inclusion of cubic clusters are plotted against experimental data.[89,90]

$$H^E(x) = H(x) - [H(H_2O_{liq}) \times (1-x) + H(MeOH_{liq}) \times x] \quad (5)$$

The enthalpy values H are taken from the PEACEMAKER output, where $H(H_2O_{liq})$ and $H(MeOH_{liq})$ are the values for $x = 0.0$ and $x = 100.0$, respectively. Compared with experiment, the values of H^E are too negative but the minima of the curves occur approximately at the same molar fraction ($x \sim 0.36$). In contrast, MD/2PT[56] with the SPC/E model for water (which gave the best results) and even more so OPLS/TIP4P[64] calculations resulted in less negative H^E values than experiment (Table 2). Neglecting cubic clusters leads to considerably less negative excess enthalpies of mixing H^E, i.e. values closer to experiment but with a minimum shifted to much higher MeOH content, x(MeOH) ~ 0.8 (Fig. 6a). The excess entropy of mixing S^E is computed according to eqn (6).

$$S^E(x) = S(x) - [S(H_2O_{liq}) \times (1-x) + S(MeOH_{liq}) \times x] + R[x \ln(x) + (1-x)\ln(1-x)] \quad (6)$$

Similar to the excess enthalpies of mixing too negative values for S^E are obtained when cubic clusters are included. Without cubic clusters nearly perfect agreement with experiment is obtained (Fig. 6b). While OPLS/TIP4P[64] calculations resulted in less negative S^E values than experiment, MD/2PT S^E values
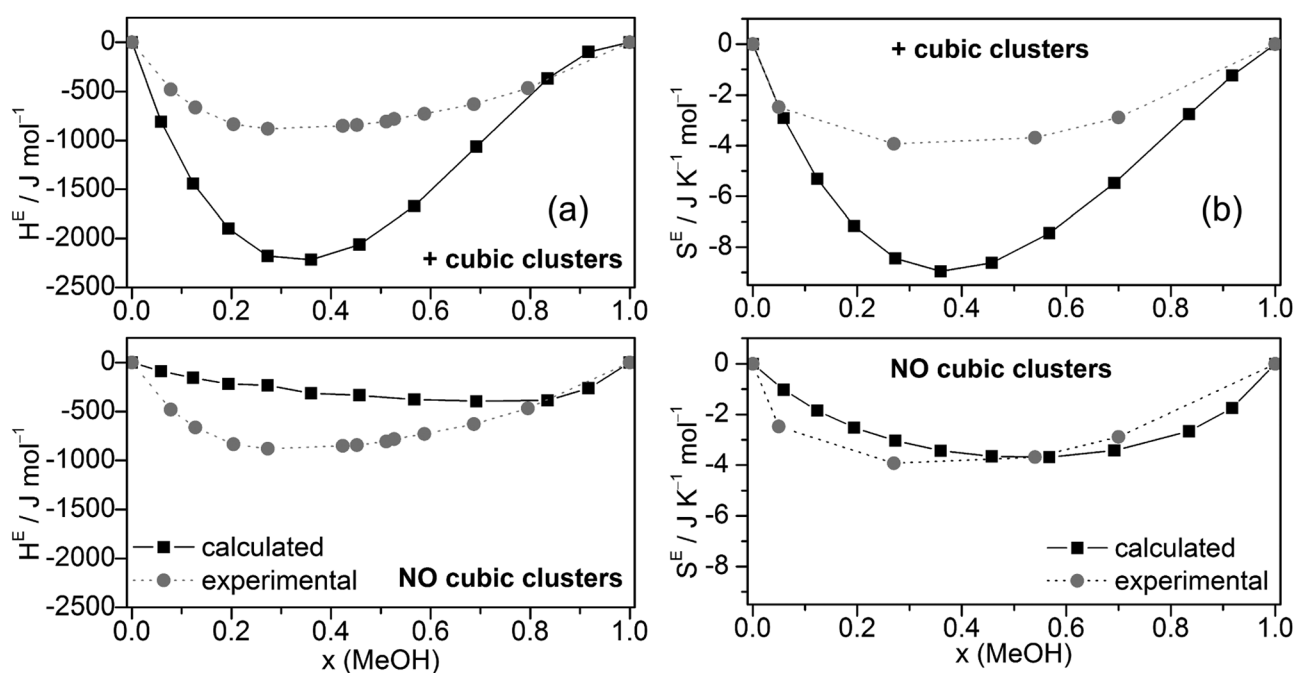

Fig. 6 Comparison of experimental and calculated excess enthalpies of mixing H^E (a),[89,90] excess entropies of mixing S^E (b)[56] for the full cluster set as well as the cluster set without the cubic $c8$ clusters at different molar ratios.

This journal is © the Owner Societies 2015

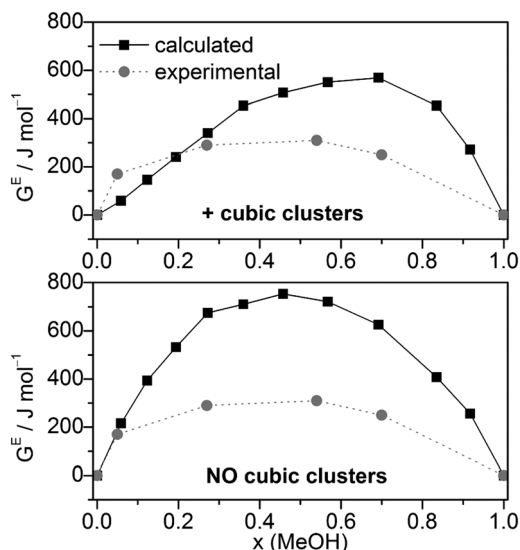Phys. Chem. Chem. Phys., 2015, **17**, 8467–8479 | 8475

Fig. 7 Comparison of experimental[56] and calculated excess Gibbs free energies of mixing G^E for the full cluster set as well as the cluster set without the cubic $c8$ clusters at different molar ratios (T = 298 K).
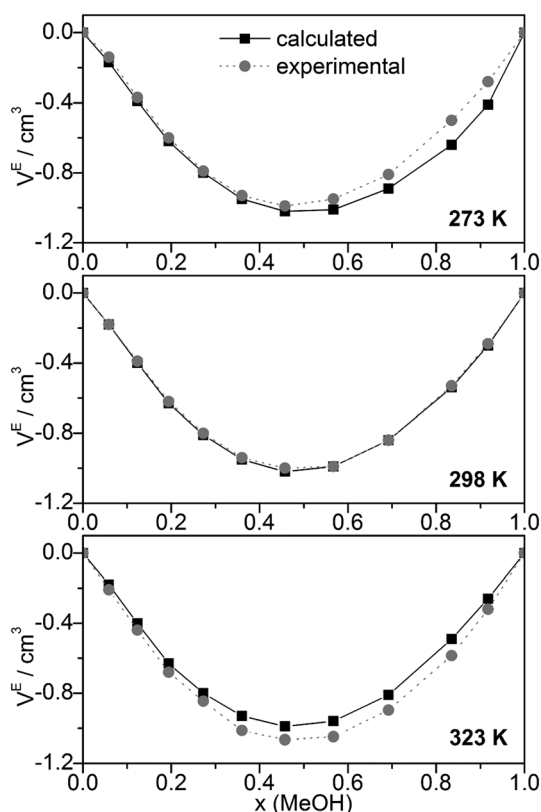

Fig. 8 Comparison of experimental[68] and calculated excess volumes of mixing V^E.

were less negative than experimental data at low and more negative at high x(MeOH), see Table 2.[56]

Combining H^E and S^E results to Gibbs free energies of mixing *via* $G^E = H^E - T \cdot S^E$. G^E values agree relatively well with the experimental data (Fig. 7), although more positive. Compared with the G^E

values obtained by MD/2PT[56] or OPLS/TIP4P[64] the corresponding QCE data are more and less, respectively, positive except at x(MeOH) = 0.05 (Table 2).

Excess thermochemical quantities of mixing obtained by the QCE model using M06-2X interaction energies and vibrational frequencies show the following (Table 2 and Fig. S6, ESI†): the H^E values are less negative than those obtained with B3LYP-D3 or even positive in the methanol rich region ($x > 0.7$); S^E values are in quite good agreement with experimental values especially in the case of the full cluster set. As a consequence, the G^E values are more positive than the experimental ones or those calculated by the B3LYP-D3 functional.

The calculated dependence of the excess Gibbs free energy of mixing for the only other binary solvent system treated so far by the QCE model (DMSO–water) closely matches the experimental curve, especially the minimum at x(DMSO) $\sim$ 0.4. In contrast to MeOH–water, for DMSO–water G^E is negative over the whole range of x(DMSO). However, similar to the MeOH–water results, the QCE model yields for DMSO–water also too positive G^E values compared with experiment.[30]

Other quantities which can be compared with experiment are excess volumes of mixing V^E (Fig. 8), heat capacities C_p (Fig. 9), and excess heat capacities of mixing C_p^E (Fig. S7, ESI†). V^E and C_p^E were calculated in analogy to eqn (5). Since the parameter fits have been carried out to get good agreement between experimental and calculated molar volumes (V_m), the calculated V^E values agree nearly perfectly with the corresponding experimental data[68] as well as those obtained from a Monte Carlo simulation of TIP4P water and OPLS MeOH mixtures.[63]

The heat capacities C_p or the excess heat capacities of mixing C_p^E are the least satisfactorily reproduced quantities by the QCE calculations, irrespective of whether B3LYP-D3 or M06-2X results were used (Fig. 9, Fig. S7 and S8, ESI†). Such discrepancies
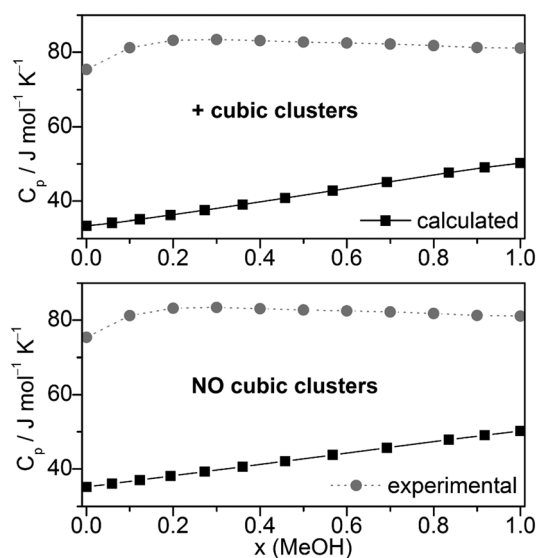

Fig. 9 Comparison of experimental[67,92,93] and calculated heat capacities C_p at T = 298.15 K.

8476 | *Phys. Chem. Chem. Phys.*, 2015, **17**, 8467–8479

This journal is © the Owner Societies 2015

had already been noticed in the original QCE publication.[23] One possible explanation of this deviation is the application of harmonic oscillator approximation even for the low frequency vibrations. In line with this, the vibrational contribution ($C_{p,vib}$) obtained from the vibrational partition function possess the largest amount of contribution to C_p, also in accordance with ref. 33.

Furthermore, it should be considered that the heat capacity is the second derivative of the partition function. Thus it is affected more by the applied approximations in the model than the other first derivative quantities.

Conclusions

The quantum cluster equilibrium model has been applied for the binary mixture of MeOH–water. Structures and interaction energies for a set of 93 clusters of different size, composition as well as class (chain, monocyclic rings, spiro, lasso, bicyclic, cubic) have been calculated by density functional theory (B3LYP-D3/QZVP and M06-2X/aug-cc-pVTZ including counterpoise BSSE corrections). B3LYP-D3 results in somewhat more negative interaction energies but the observed trend closely matches that obtained by M06-2X. The two fitting parameters a_{mf} and b_{xv} used in the QCE model were obtained by fitting to experimental isobars of MeOH–water binary mixtures with varying composition. Isobars based on B3LYP-D3 and M06-2X calculations were quite similar. With increasing MeOH content an increasing deviation between calculated and experimental isobars was found. Cluster distributions calculated by the QCE model using either B3LYP-D3 or M06-2X were quite similar with one notable exception: while the monocyclic ring-type clusters *m5r* and *m6r* both were found quite significant at high MeOH content with B3LYP-D3, only *m6r* showed a substantial population (50–100% in the range $x(MeOH) = 0.7$–1.0) based on M06-2X interaction energies and vibrational frequencies. Cubic *c8* cluster structures like *w8c* or *m1w7c* were found to dominate at low MeOH content whereas monocyclic ring structures, especially *m6r* were the most important clusters for $x(MeOH) > 0.8$. In the intermediate region, $x(MeOH) \sim 0.4$ to 0.7 the cubic cluster *m3w5c* is the dominant species. With increasing temperature the populations of these clusters decrease with a concomitant increase of other cluster populations, *e.g.* the monocyclic ring structure *m5w1r*.

Compared with experiment the calculated (B3LYP-D3) excess enthalpies of mixing H^E of methanol–water are somewhat too negative, those based on M06-2X are less negative and show larger overall deviations from the experimental curve in the methanol rich region. Excess entropies of mixing S^E are also too negative with B3LYP-D3 while those based on M06-2X nearly perfectly match the experimental S^E *vs.* $x(MeOH)$ curve. Calculated excess Gibbs free energies of mixing G^E by either density functional are more positive than experimental values With respect to previous molecular dynamics simulations of the MeOH–water mixtures,[56,64] the QCE model based on B3LYP-D3 calculations consistently results in excess enthalpies H^E and especially entropies S^E of mixing which are more negative. Excess Gibbs free energies of mixing G^E are slightly

more positive than the MD/2PT results of Pascal and Goddard[56] and slightly less positive than or even equal to the MD results of Tanaka and Gubbins.[64] The calculated excess volumes of mixing compare well with experiment. Significant deviations between calculated and experimental heat capacities C_p and excess heat capacity of mixing C_p^E were found.

Acknowledgements

Notes and references

1 R. Mecke and H. Kempter, *Naturwissenschaften*, 1939, **27**, 583.
2 Y. Marcus, *Solvent Mixtures*, Properties and Selective Solvation, CRC Press, 2002.
3 A. Ben-Naim, *J. Phys. Chem. B*, 2007, **111**, 2896.
4 C. Reichardt, *Solvents and Solvent Effects in Organic Chemistry*, Wiley-VCH Verlag, Weinheim, 3rd edn, 2003.
5 A. Wakisaka and T. Iwakami, *J. Mol. Liq.*, 2014, **189**, 44.
6 A. Wakisaka and K. Matsuura, *J. Mol. Liq.*, 2006, **129**, 25.
7 A. Wakisaka, S. Mochizuki and H. Kobara, *J. Solution Chem.*, 2004, **33**, 721.
8 A. Wakisaka, S. Komatsu and Y. Usui, *J. Mol. Liq.*, 2001, **90**, 175.
9 A. Wakisaka and T. Ohki, *Faraday Discuss.*, 2005, **129**, 231.
10 A. Wakisaka and Y. Yamamoto, *J. Chem. Soc., Chem. Commun.*, 1994, 2105.
11 S. Kunsagi-Mate and K. Iwata, *Chem. Phys. Lett.*, 2009, **473**, 284.
12 S. Kunsagi-Mate and K. Iwata, *J. Solution Chem.*, 2013, **42**, 165.
13 A. Mandal, M. Prakash, R. M. Kumar, R. Parthasarathi and V. Subramanian, *J. Phys. Chem. A*, 2010, **114**, 2250.
14 G. Matisz, A.-M. Kelterer, W. M. F. Fabian and S. Kunsagi-Mate, *J. Phys. Chem. A*, 2011, **115**, 10556.
15 V. S. Bryantsev, M. S. Diallo, A. C. T. van Duin and W. A. Goddard, *J. Chem. Theory Comput.*, 2009, **5**, 1016.
16 R. Wieczorek, L. Haskamp and J. J. Dannenberg, *J. Phys. Chem. A*, 2004, **108**, 6713.
17 R. N. Barnett and U. Landman, *J. Phys. Chem. A*, 1997, **101**, 164.
18 S. L. Boyd and R. J. Boyd, *J. Chem. Theory Comput.*, 2007, **3**, 54.
19 P. Golub, I. Doroshenko and V. Pogorelov, *Phys. Lett. A*, 2014, **378**, 1937.

20 F. C. Hagemeister, C. J. Gruenloh and T. S. Zwier, *J. Phys. Chem. A*, 1998, **102**, 82.

21 S. Kazachenko, S. Bulusu and A. J. Thakkar, *J. Chem. Phys.*, 2013, **138**, 224303.

22 F. Weinhold, *J. Chem. Phys.*, 1998, **109**, 367.

23 F. Weinhold, *J. Chem. Phys.*, 1998, **109**, 373.

24 R. Ludwig and F. Weinhold, *J. Chem. Phys.*, 1999, **110**, 508.

25 R. Ludwig and F. Weinhold, *Phys. Chem. Chem. Phys.*, 2000, **2**, 1613.

26 R. Ludwig and F. Weinhold, *Z. Phys. Chem.*, 2002, **216**, 659.

27 R. Ludwig, *Phys. Chem. Chem. Phys.*, 2002, **4**, 5481.

28 P. Borowski, J. Jaroniec, T. Janowski and K. Wolinski, *Mol. Phys.*, 2003, **101**, 1413.

29 R. Ludwig, *ChemPhysChem*, 2007, **8**, 938.

30 A. Lenz and L. Ojamae, *J. Chem. Phys.*, 2009, **131**, 134302.

31 S. B. C. Lehmann, C. Spickermann and B. Kirchner, *J. Chem. Theory Comput.*, 2009, **5**, 1640.

32 S. B. C. Lehmann, C. Spickermann and B. Kirchner, *J. Chem. Theory Comput.*, 2009, **5**, 1650.

33 B. Kirchner, C. Spickermann, S. B. C. Lehmann, E. Perlt, J. Langner, M. von Domaros, P. Reuther, F. Uhlig, M. Kohagen and M. Brüssel, *Comput. Phys. Commun.*, 2011, **182**, 1428.

34 M. Brüssel, E. Perlt, M. von Domaros, M. Brehm and B. Kirchner, *J. Chem. Phys.*, 2012, **137**, 164107.

35 R. Ludwig, *ChemPhysChem*, 2005, **6**, 1369.

36 R. Ludwig, *ChemPhysChem*, 2005, **6**, 1376.

37 G. Matisz, W. M. F. Fabian, A.-M. Kelterer and S. Kunsagi-Mate, *THEOCHEM*, 2010, **956**, 103.

38 G. Matisz, A.-M. Kelterer, W. M. F. Fabian and S. Kunsagi-Mate, *J. Phys. Chem. B*, 2011, **115**, 3936.

39 M. Huelsekopf and R. Ludwig, *J. Mol. Liq.*, 2000, **85**, 105.

40 R. Ludwig, F. Weinhold and T. C. Farrar, *Mol. Phys.*, 1999, **97**, 465.

41 R. Ludwig, F. Weinhold and T. C. Farrar, *Mol. Phys.*, 1999, **97**, 479.

42 M. Huelsekopf and R. Ludwig, *J. Mol. Liq.*, 2002, **98**, 163.

43 M. A. Wendt, F. Weinhold and T. C. Farrar, *J. Chem. Phys.*, 1998, **109**, 5945.

44 M. J. Hansen, M. A. Wendt and F. Weinhold, *Mol. Phys.*, 2003, **101**, 1147.

45 R. Ludwig, F. Weinhold and T. C. Farrar, *Ber. Bunsen-Ges.*, 1998, **102**, 197.

46 R. Ludwig, F. Weinhold and T. C. Farrar, *Ber. Bunsen-Ges.*, 1998, **102**, 205.

47 R. Ludwig, F. Weinhold and T. C. Farrar, *J. Phys. Chem. A*, 1997, **101**, 8861.

48 R. Ludwig, O. Reis, R. Winter, F. Weinhold and T. C. Farrar, *J. Phys. Chem. B*, 1998, **102**, 9312.

49 M. Huelsekopf and R. Ludwig, *Magn. Reson. Chem.*, 2001, **39**, S127.

50 R. Ludwig, J. Behler, B. Klink and F. Weinhold, *Angew. Chem., Int. Ed.*, 2002, **41**, 3199.

51 J. Friedrich, E. Perlt, M. Roatsch, C. Spickermann and B. Kirchner, *J. Chem. Theory Comput.*, 2011, **7**, 843.

52 C. Spickermann, E. Perlt, M. von Domaros, M. Roatsch, J. Friedrich and B. Kirchner, *J. Chem. Theory Comput.*, 2011, **7**, 868.

53 E. Perlt, J. Friedrich, M. von Domaros and B. Kirchner, *ChemPhysChem*, 2011, **12**, 3474.

54 F. Weinhold, *J. Phys. Chem. B*, 2014, **118**, 7792.

55 M. Brüssel, E. Perlt, S. B. C. Lehmann, M. von Domaros and B. Kirchner, *J. Chem. Phys.*, 2011, **135**, 194113.

56 T. A. Pascal and W. A. Goddard, *J. Phys. Chem. B*, 2012, **116**, 13905.

57 L. Vlcek and I. Nezbeda, *J. Mol. Liq.*, 2007, **131**, 158.

58 B. Hribar-Lee and K. A. Dill, *Acta Chim. Slov.*, 2006, **53**, 257.

59 D. P. Geerke and W. F. van Gunsteren, *ChemPhysChem*, 2006, **7**, 671.

60 D. Gonzalez-Salgado and I. Nezbeda, *Fluid Phase Equilib.*, 2006, **240**, 161.

61 K. Liltorp, P. Westh and Y. Koga, *Can. J. Chem.*, 2005, **83**, 420.

62 E. J. W. Wensink, A. C. Hoffmann, P. J. van Maaren and D. van der Spoel, *J. Chem. Phys.*, 2003, **119**, 7308.

63 C. A. Koh, H. Tanaka, J. M. Walsh, K. E. Gubbins and J. A. Zollweg, *Fluid Phase Equilib.*, 1993, **83**, 51.

64 H. Tanaka and K. E. Gubbins, *J. Chem. Phys.*, 1992, **97**, 2626.

65 S. W. Cochran, J. C. Holste, K. N. Marsh, B. E. Gammon and K. R. Hall, *Fluid Phase Equilib.*, 1993, **88**, 171.

66 S. Z. Mikhail and W. R. Kimel, *J. Chem. Eng. Data*, 1961, **6**, 533.

67 J. M. Simonson, D. J. Bradley and R. H. Busey, *J. Chem. Thermodyn.*, 1987, **19**, 479.

68 C. Synowietz, in *1.1 Introduction*, Springer Materials - The Landolt–Börnstein Database, ed. K. Schäfer, http://www.springermaterials.com, DOI: 10.1007/10201852_1.

69 A. D. Becke, *J. Chem. Phys.*, 1993, **98**, 5648.

70 C. T. Lee, W. T. Yang and R. G. Parr, *Phys. Rev. B: Condens. Matter Mater. Phys.*, 1988, **37**, 785.

71 P. J. Stephens, F. J. Devlin, C. F. Chabalowski and M. J. Frisch, *J. Phys. Chem.*, 1994, **98**, 11623.

72 S. H. Vosko, L. Wilk and M. Nusair, *Can. J. Phys.*, 1980, **58**, 1200.

73 S. Grimme, J. Antony, S. Ehrlich and H. Krieg, *J. Chem. Phys.*, 2010, **132**, 154104.

74 F. Neese, The ORCA program system, *WIREs Comput. Mol. Sci.*, 2012, **2**, 73.

75 A. Schäfer, H. Horn and R. Ahlrichs, *J. Chem. Phys.*, 1992, **97**, 2571.

76 F. Weigend and R. Ahlrichs, *Phys. Chem. Chem. Phys.*, 2005, **7**, 3297.

77 S. F. Boys and F. Bernardi, *Mol. Phys.*, 2002, **100**, 65.

78 Y. Zhao and D. G. Truhlar, *J. Chem. Theory Comput.*, 2008, **4**, 1849.

79 Y. Zhao and D. G. Truhlar, *Acc. Chem. Res.*, 2008, **41**, 157.

80 Y. Zhao and D. G. Truhlar, *Theor. Chem. Acc.*, 2008, **120**, 215.

81 M. J. Frisch, G. W. Trucks, H. B. Schlegel, G. E. Scuseria, M. A. Robb, J. R. Cheeseman, G. Scalmani, V. Barone, B. Mennucci, G. A. Petersson, H. Nakatsuji, M. Caricato, X. Li, H. P. Hratchian, A. F. Izmaylov, J. Bloino, G. Zheng,

J. L. Sonnenberg, M. Hada, M. Ehara, K. Toyota, R. Fukuda, J. Hasegawa, M. Ishida, T. Nakajima, Y. Honda, O. Kitao, H. Nakai, T. Vreven, J. A. Montgomery Jr, J. E. Peralta, F. Ogliaro, M. Bearpark, J. J. Heyd, E. Brothers, K. N. Kudin, V. N. Staroverov, R. Kobayashi, J. Normand, K. Raghavachari, A. Rendell, J. C. Burant, S. S. Iyengar, J. Tomasi, M. Cossi, N. Rega, J. M. Millam, M. Klene, J. E. Knox, J. B. Cross, V. Bakken, C. Adamo, J. Jaramillo, R. Gomperts, R. E. Stratmann, O. Yazyev, A. J. Austin, R. Cammi, C. Pomelli, J. W. Ochterski, R. L. Martin, K. Morokuma, V. G. Zakrzewski, G. A. Voth, P. Salvador, J. J. Dannenberg, S. Dapprich, A. D. Daniels, Ö. Farkas, J. B. Foresman, J. V. Ortiz, J. Cioslowski and D. J. Fox, *Gaussian 09, Revision C.01*, Gaussian, Inc., Wallingford, CT, 2010.
82 T. H. Dunning, *J. Chem. Phys.*, 1989, **90**, 1007.
83 R. Ludwig, *Angew. Chem., Int. Ed.*, 2001, **40**, 1808–1827.
84 G. Z. Han, Y. L. Ding, P. Qian, C. Zhang and W. Song, *Int. J. Quantum Chem.*, 2013, **113**, 1511.

85 C. Corsaro, J. Spooren, C. Branca, N. Leone, M. Broccio, C. Kim, S. H. Chen, H. E. Stanley and F. Mallamace, *J. Phys. Chem. B*, 2008, **112**, 10449.
86 S. Kashtanov, A. Augustson, J. E. Rubensson, J. Nordgren, H. Agren, J. H. Guo and Y. Luo, *Phys. Rev. B: Condens. Matter Mater. Phys.*, 2005, **71**, 104205.
87 K. R. Wilson, M. Cavalleri, B. S. Rude, R. D. Schaller, T. Catalano, A. Nilsson, R. J. Saykally and L. G. M. Pettersson, *J. Phys. Chem. B*, 2005, **109**, 10194.
88 R. F. Lama and B. C. Y. Lu, *J. Chem. Eng. Data*, 1965, **10**, 216.
89 L. Abello, *J. Chim. Phys. Phys.-Chim. Biol.*, 1973, **70**, 1355.
90 I. Tomaszkiewicz, S. L. Randzio and P. Gierycz, *Thermochim. Acta*, 1986, **103**, 281.
91 J. A. V. Butler, D. W. Thomson and W. H. Maclennan, *J. Chem. Soc.*, 1933, **136**, 674.
92 M. W. Chase, NIST-JANAF Thermochemical Tables, J. Phys. Chem. Ref. Data, Monograph No. 9, 4th edn, 1998.
93 T. S. Khasanshin, T. B. Zykova and S. P. Bunko, *High Temp.*, 1997, **35**, 149.

This journal is © the Owner Societies 2015

Phys. Chem. Chem. Phys., 2015, **17**, 8467–8479 | 8479

Some Unexpected Behavior of the Adsorption of Alkali Metal Ions onto the Graphene Surface under the Effect of External Electric Field

Beáta Peles-Lemli,[†,‖] Dániel Kánnár,[†] Jia Cai Nie,[‡] Heng Li,[§] and Sándor Kunsági-Máté*[,†,‖]

[†]Department of General and Physical Chemistry, University of Pécs, Ifjúság 6, Pécs, H-7624, Hungary
[‡]Department of Physics, Beijing Normal University, 100875 Beijing, People's Republic of China
[§]Department of Physics, Xiamen University, 361005 Xiamen, People's Republic of China
[‖]János Szentágothai Research Center, Ifjúság 20, Pécs H-7624, Hungary

ABSTRACT: In this work the interaction between alkali metal ions and a graphene surface with the absence and the presence of an external electric field applied perpendicular to the surface was investigated. M05-2X/6-31G(d) DFT calculations were performed to describe the adsorption properties. Results show that the electric field pushes the positively charged ion closer to the graphene, where the charge transfer between the alkali metal cations and the electron rich graphene surface increases. At a species-dependent certain strength of the electric field, the excess electrons cause negative charge on the alkali metal ion. This effect will promote the removal of the ion from the surface.
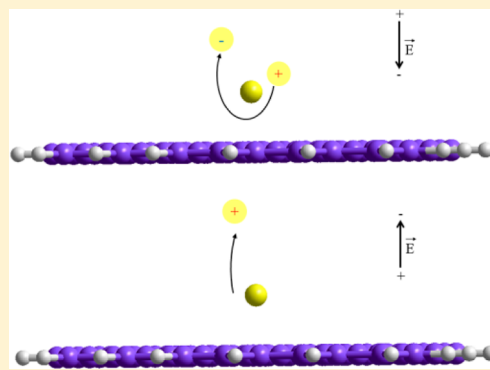
1. INTRODUCTION

Two-dimensional graphene, carbon nanotubes (CNTs), and graphene nanoribbons represent a novel class of low dimensional materials that could serve as building blocks for future carbon-based nanoelectronics. However, there are some wonderful properties of these nanomaterials (e.g., conductivity, flexibility, adsorptive behavior, and ability to form inclusion complexes) that are already known, and with much attention focused on these, the wide application still seems to be a big challenge.

It is well-known that the external electric field can modify the physical properties of carbon nanomaterials like CNTs[1] or graphene.[2] The application of the electric field as a reversible switch makes practical importance not only because of its easily controllable direction and intensity but also because it has the ability to control the surface properties for a short time such as seconds or less. In particular, the perpendicular electric field leads to a polarization of the charge density that could affect the adsorption properties of graphene, the importance of which has been widely recognized. Therefore, nowadays more and more studies investigate the atomic structures and adsorption property dependence of graphene under different strengths of external electric field. In this way, CO adsorption on graphene nanodots,[3] the interaction between O_2 and Au-doped graphene,[4] or the dissociative adsorption of H_2O on graphene[5] have been analyzed by taking the external electric field into account. These studies showed that the applied electric field can enhance or weaken the adsorption of different particles onto the graphene surface as well as provide possible new and/or energetically more favorable reaction pathways which can not be reached otherwise.

In our previous works noncovalent interactions between single-walled CNTs and aromatic "packer" molecules were analyzed with the aim to clarify the related solubilization processes.[6,7] Furthermore, the dispersion of hydroxylated multiwalled CNTs (MWCNTs) was modified in nonprotic acetonitrile solvent using a treatment by ethanol.[8] From this solution phase the MWCNTs were deposited onto the nanostructured CeO_2 films grown on sapphire substrate.[9,10] High resolution images by both transmission and scanning electron microscopy showed that the nanographite fractions existed in the solution and they were also reorganized on the surface. These graphene multilayers could be separated from the remaining MWCNTs by an entropy driven selective adsorption process.[11] On the nanostructured surface with specific morphology, the nanographite fractions are deposited into the valleys between the CeO_2 islands, and therefore a selective pattern of nanographite was formed. Molecular dynamics calculations highlighted that adsorption and reorganization properties of the nanographite layers have considerable dependence on the morphology of CeO_2 nanostructures.[12] Considering that the CeO_2 surface morphology is fully controlled by the experimental setup of growth, properties of the CNT layers are tunable toward the requirements of practical applications.

This generated graphene−CeO₂−sapphire layer with electrochemical modifications could be a potential surface of ion diffusion controlled by an external electric field. In this way, we might be able to get transported ions selectively by changing the applied perpendicular and parallel electric fields. To reach the practical benefits of this method, it is necessary to clarify the diffusion and adsorption mechanism of the ions on graphene layers. Therefore in this work the interaction between alkali ions and the graphene surface with the absence and the presence of external electric field applied perpendicular to the graphene surface was investigated using density functional theory (DFT) methods.

2. THEORETICAL METHODS

First, the model cluster with a molecular formula of $C_{54}H_{18}$ was constructed and fully optimized using the M05-2X hybrid meta-GGA functional[13,14] with the 6-31G(d) basis set. Then the alkali metal cation, namely a lithium, sodium, or potassium ion, was positioned above the surface. Three different orientations of the ion with respect to the graphene surface, namely, top, hollow, and bridge, were considered as starting structures (Figure 1). In the top site geometry the alkali metal ion located
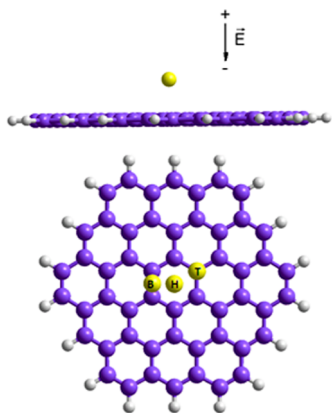

Figure 1. During the calculations the applied electric field was perpendicular to the graphene surface (up). The different orientations of the ion with respect to the graphene surface: (T) top, (H) hollow, and (B) bridge (down).

directly above the C atom, in the hollow site conformation the ion is above the center of a hexagon in the graphene layer and in the bridge site structure the ion is positioned above the center of a C−C bond. During the calculation the rigid model was used: the geometry of the cluster was frozen as it obtained in the first step and the optimized ion position was determined by varying the distance between the ion and the graphene plane until the most stable position is found. The site with the largest adsorption energy was referred to as the most stable one. The adsorption energy was calculated using the eq 1.

$$E_{ads} = E_{ion} + E_{graphene} - E_{ion/graphene} \qquad (1)$$

In good agreement with the previous theoretical works (see, e.g., ref 15), we also found that the alkali metal ions are adsorbed preferably on top of the hollow site. Therefore in this work the hollow site adsorption of the ions in the middle of the $C_{54}H_{18}$ graphene cluster was analyzed in detail. The effect of homogeneous external electric field applied perpendicular to the graphene surface on the ion adsorption was analyzed (Figure 1). For the quantum chemical calculations the Gaussian

09 program package was used.[16] Preparation, manipulation, and visualization of coordinate files were done with HyperChem Professional 7.[17]

3. RESULTS AND DISCUSSION

3.1. Structures and Adsorption Energies under Neutral Field. Quantum chemistry is a fruitful testing technique for molecular-scale analysis; therefore, it is not surprising that a mass of computational or theoretical studies on carbon nanomaterials can be found in the literature. The adsorption of aromatic molecules such as benzene,[18] phenol,[19] dibenzothiophene,[20] cytosine,[21] or aniline[7] on single-walled carbon nanotubes has attracted increased attention in the past few years. Nowadays the synthesis[22] and characterizations[23] of graphene nanoribbons have been brought into focus. Furthermore, because of its practical applications in more efficient Li-ion batteries, the investigations of the interaction between alkali metal atoms and ions such as lithium and the graphitic surface have been also analyzed theoretically by several groups.[15,24−26] In the related theoretical works the first question always is how to describe the graphene and its interaction with different species: to model the surface one can use finite graphene clusters or two-dimensional periodic boundary conditions (PBC) applied on graphene unit cells. Furthermore, to obtain the adsorption energies the rigid model with frozen cluster is similarly popular as the fully relaxed approach. Uthaisar and Barone investigated the adsorption and diffusion properties of the Li atom on graphene and graphene nanoribbons.[27] Their results did not show significant difference between the structures determined by the rigid model or fully relaxed approach. Contrarily, Umadevy and Sastry found[24] that only in the case of small molecules is it possible to neglect the deformation of the graphene cluster. At the same time the metal atoms and ions induce considerable strain in the graphene cluster, although increasing the cluster size decreases the surface deformation. In this present work the cluster calculation combined with the rigid model was chosen to describe the alkali metal cation−graphene interaction under electric field. However, to take into account the possible effect of the cluster deformation, the fully optimized structures of the $Li^+C_{54}H_{18}$, $Na^+C_{54}H_{18}$, and $K^+C_{54}H_{18}$ systems were also determined at the M05-2X/6-31G(d) level of theory. Table 1 summarizes the calculated equilibrium distances (R_e) between the ion and the graphene, the adsorption energies (E_{ads}), and the Mulliken atomic charges (Z_{ion}) of the alkali ions. R_e was defined as the difference in the z coordinates where the graphene surface is located in the xy plane.

Table 1. Optimized Parameters of the Alkali Metal Ions on Graphene[a]

	R_e [Å]	E_{ads} [kJ mol⁻¹]	Z_{ion} [e]
$Li^+C_{54}H_{18}$ (rm)	1.835	220.20 (214.48)	0.548
$Li^+C_{54}H_{18}$ (fr)	1.826	222.14 (216.21)	0.542
$Na^+C_{54}H_{18}$ (rm)	2.289	163.50 (158.02)	0.740
$Na^+C_{54}H_{18}$ (fr)	2.285	164.63 (158.95)	0.737
$K^+C_{54}H_{18}$ (rm)	2.729	125.27 (120.56)	0.910
$K^+C_{54}H_{18}$ (fr)	2.723	126.03 (120.68)	0.909

[a]Adsorption energy (E_{ads}) with the BSSE-corrected value in parentheses, Mulliken atomic charge of the ion (Z_{ion}) and the equilibrium distance between the ion and the graphene (R_e). The use of a rigid model (rm) or fully relaxed (fr) approach are indicated.

The data show that the investigated parameters are slightly depending on the freezing of the graphene cluster. The calculated equilibrium distances between the Li⁺ ion and graphene surface are 1.835 or 1.826 Å using the rigid model or fully relaxed approach, respectively. These distances are in good agreement not only with the calculated data by Umadevy and Sastry using the cluster model with fully relaxed approach at the same level of theory[17] but also with the data determined by Zheng et al. with the combination of the PBC calculation and the rigid model approach at GGA-PAW level.[15] However, the most popular B3LYP method results in a 17% larger adsorption distance[25] indicating that the choice of the DFT method can play an important role in describing the weak or nonbonding interactions.

It is not surprising that the Li⁺ ion with the smallest ionic radius located the closest to the graphene surface and the K⁺ ion the furthest. The adsorption energies indicate chemisorptions as the most pronounced role in the adsorption processes although it is well-known that the cation−π interaction is a noncovalent interaction between an electron rich π-system and a positively charged ion. The strength of this weak interaction can be modulated by the molecular environment, e.g., the used solvent permittivity or by the characterics of the aromatic hydrocarbons determined by the number of the fused aromatic rings and the effect of substituent. Our calculated data are about 1 order magnitude larger than the average physisorption energy. The account for these large adsorption energy values is the size of the graphene cluster because the increasing size of the polycyclic aromatic hydrocarbons results in the increase of the cation−π interaction energy.[24]

As it can be seen in Table 1 there is no significant difference between the data determined by the rigid model or the fully relaxed approach. However in the fully optimized structure the graphene surface slightly bends like a convex lens.

3.2. Electric Field Induced Deformation of the Graphene Cluster.

In this work the homogeneous and directed electric field was generated by the 'Field' keyword of the Gaussian program code. The electric field induced bending of graphene nanoribbons was described by Wang;[28] therefore, first the geometry of the $C_{54}H_{28}$ cluster was analyzed under homogeneous external electric field applied perpendicular to the graphene plane. Our results also show the mechanical sensitivity of the graphene surface to the external electric field; the $C_{54}H_{28}$ cluster bends as if it would fit on the surface of a tube while the C−C distances increase by 0.5%.

However the question is still opened that how the geometry of the graphene will change when it is deposited onto a carrier surface, e.g., onto a nanostructured CeO_2 films grown on a sapphire substrate. Lee and co-workers studied the atomic and electronic structures of single-layer graphene on the Si-terminated surface of SiC.[29] They found that the atomic positions of the graphene layer on the SiC surface are insensitive to the electric field, although the electronic band structures of the layer depend strongly on the direction and strength of the applied electric fields. We can assume that it is not necessary to take into consideration the electric field induced change of the graphene geometry. Therefore to model the graphene layers formed on the CeO_2 surface, the atomic positions of the $C_{54}H_{28}$ cluster were kept frozen as they were obtained under neutral field.

3.3. Li⁺ Ion Adsorption under External Electric Field.

In this work the effect of a homogeneous external electric field on the ion adsorption properties on graphene was modeled.

Because of its electrochemical aspects the electric field ($\overline{E}$) was applied perpendicular to the surface. The electric field is directed from the ion toward the graphene surface (Figure 1). During the calculations the $C_{54}H_{28}$ cluster was kept frozen with the aim to eliminate the electric field induced bend of the graphene plane and the strength of the applied field was changed.

First the changes of the equilibrium distance between the Li⁺ ion and the graphene surface were investigated. At first when increasing the strength of the electric field the distance between the Li⁺ ion and the graphene surface decreases because the positively charged ion moves to the negative direction of the electric field. It can be clearly seen in Figure 2a that the electric
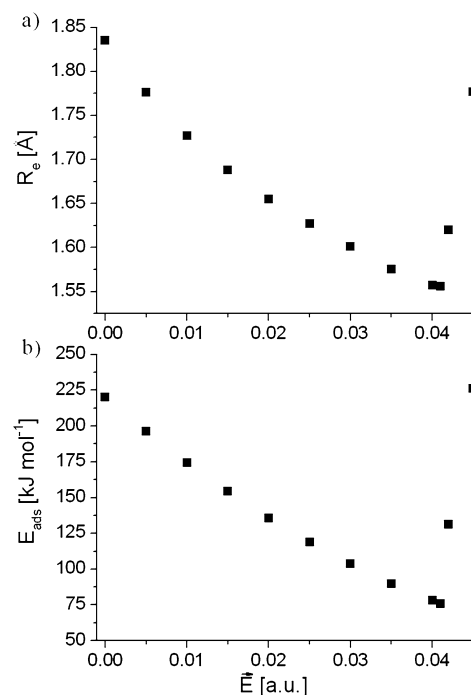

Figure 2. Equilibrium distance (R_e) between the Li⁺ ion and graphene surface (a) and the adsorption energy (E_{ads}) (b) as a function of the applied electric field ($\overline{E}$). 1 au of electric field = 5.14×10^{11} V m⁻¹.

field pushes the Li⁺ ion to the surface, and at a certain strength of the electric field, the system reaches the accessible lowest distance. Even after a little strengthening of the electric field, a large moving of the ion from the surface is induced. The minimum equilibrium distance between the graphene surface and the lithium particle was calculated to be 1.556 Å under the electric field strength of 0.041 au. Furthermore, the change of the adsorption energy as a function of the electric field was analyzed (Figure 2b). One can expect that the decrease of the equilibrium distance between the ion and the cluster results in an increase of the adsorption energy because of the increasing Coulomb attraction between the positively charged Li⁺ ion and the negatively charged C atoms of the graphene located the closest to the alkali metal ion. However Figure 2b shows the opposite trend. The long-range electrostatic attraction is balanced by the repulsive interaction between the atoms and molecules at short distances. The repulsion between oppositely charged molecules is very weak but it increase rapidly at very small intermolecular distances. This phenomenon can explain why the shortest equilibrium distance results in the weakest interaction between the Li particle and the graphene cluster.

The calculated adsorption energy (BSSE corrected data in parentheses) is 75.98 (69.43) kJ mol^{-1}.

The molecule placed in an electric field undergoes deformation while the electric field partially polarizes the molecule, resulting in the separation of its charge. The polarizability is the measure of the change of the molecule to respond to an applied electric field. The polarizability determines the energy of the work done on electrons by the electric field to move along the direction of the field. The mean polarizabilty ($\langle \alpha \rangle$) was calculated

$$\langle \alpha \rangle = (\alpha_{xx} + \alpha_{yy} + \alpha_{zz})/3 \tag{2}$$

where the subscripts indicate the triangular orders. The values are calculated in atomic units (au); 1 au of polarizability = 1.65 × 10^{-41} C^2 m^2 J^{-1}. The polarizability of the C$_{54}$H$_{18}$ cluster is 268.06 au and almost independent of the strength of the applied electric field. Not surprisingly the interaction with the positively charged ion decreases the polarizability of the Li$^+$C$_{54}$H$_{18}$ system compared with the pure cluster containing electron rich aromatic rings. The mean polarizability of Li$^+$C$_{54}$H$_{18}$ monotonously decreases under electric field, and the determined values are 228.52, 226.01, and 213.81 au under the applied electric field strength of 0.000, 0.041, and 0.045 au, respectively. The data show that the change is about 1% until the system reaches the minimum equilibrium distance between the graphene surface and the lithium particle, and after that point the polarizabilty decreases more rapidly.

It is not surprising that the electrostatic repulsion between the nuclei stops the lithium from getting any closer to the graphene surface than the determined minimum equilibrium distance. However, a question arises as to why the lithium particle would remove from the surface after the system reaches the accessible lowest distance. After the system reached the minimum equilibrium distance, the intensive decrease of the polarizability of the Li$^+$C$_{54}$H$_{18}$ system and the movement of the originally positive ion to the positive direction of the electric field indicate the electric field induced change of the electron distribution of the Li$^+$C$_{54}$H$_{18}$ system.

To analyze the charge transfer between the ion and graphene surface the change of charge on the Li particle was analyzed. As it can be seen in Table 1 there is an intensive charge transfer from the graphene surface to the Li$^+$ ion. According to these data the Li$^+$−graphene cluster interaction results in an almost 50% decrease of the positive charge of the Li$^+$ ion under neutral field of which the effect seems to be overestimated. Therefore to describe the charge transfer between the ion and graphene surface, Mulliken charge distribution and also natural bond orbitals (NBO) analysis[30] were performed. In both cases the charge transfer was described as the change of the atomic charge on the lithium particle. In a deeper view, one can see that the atomic charges calculated using NBO by summing the occupancy of the natural atomic orbitals (NPA) are different from Mulliken charges (Figure 3). However the differences in charge distribution barely depend on the methods and the two different analysis show similar trends: as the electric field pushes the positively charged ion closer to the surface the charge transfer from the graphene increases. Once the lithium reaches the shortest equilibrium distance it becomes a negatively charged ion. This effect results in an intensive removing of the lithium from the surface because the negative ion simply moves with the electric field. Furthermore, it is in good agreement with the change of the polarizability of the
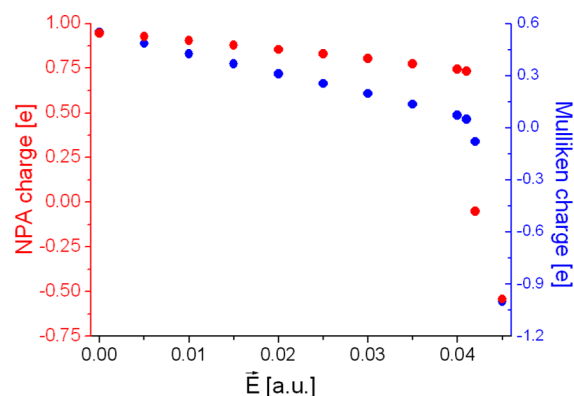

Figure 3. Charge of the lithium particle calculated by Mulliken charge distribution and NBO analysis.

Li$^+$C$_{54}$H$_{18}$ system and explains the intensive decrease of the polarizability while the Li ion is removed from the graphene surface.

The electron configuration of lithium particles in the Li$^+$C$_{54}$H$_{18}$ system is calculated to be 1s^2 2s$^{0.01}$ 2p$^{0.04}$, 1s^2 2s$^{0.05}$ 2p$^{0.20}$ 3s$^{0.01}$ 3p$^{0.01}$, and 1s^2 2s$^{0.77}$ 2p$^{0.75}$ 3p$^{0.02}$ under the applied electric field strengths of 0.000, 0.041, and 0.045 au, respectively. The relatively high adsorption energy (220.20 kJ mol^{-1} under neutral field) shows that the electron donation from the 2p orbitals of the C atoms located in the middle of the cluster first promotes the binding of the Li$^+$ ion to the graphene. The strengthening of the electric field results that the 2sp and 3sp orbitals of the lithium particles occupied by slightly higher electron density.

Umadevy and Sastry found correlation between the strength of the Li$^+$ ion−graphene interaction and the pattern as well as the energy of the highest occupied molecular orbital (HOMO) of the graphene.[24] Tachikawa and co-workers showed that the Li$^+$ ion diffused along the HOMO of the graphene surface.[25] Furthermore, they found that the adsorption of the Li$^+$ ion induced almost no change on the pattern of the lowest unoccupied molecular orbital (LUMO) of the graphene.[31] However our results indicate that the LUMO was also affected by the Li$^+$ ion−graphene interaction. We have calculated the electric field effect on the energies of the HOMO and LUMO of C$_{54}$H$_{18}$ and Li$^+$C$_{54}$H$_{18}$ systems. Our results show (Figure 4) that under electric field both energies of the HOMO and LUMO decrease but at different rates. Hence the HOMO−
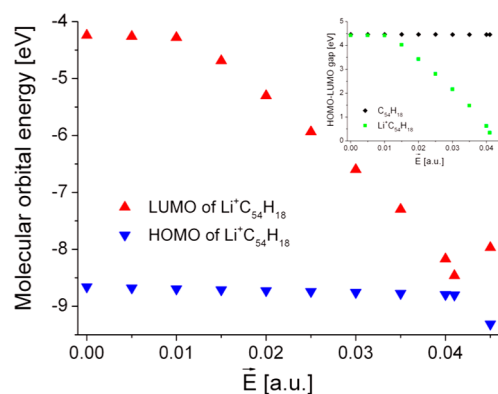

Figure 4. HOMO and LUMO energies of the Li$^+$C$_{54}$H$_{18}$ system and the HOMO−LUMO gap of C$_{54}$H$_{18}$ and Li$^+$C$_{54}$H$_{18}$ (inset) as a function of the electric field strength.

LUMO gap decreases, and it becomes the smallest when the electric filed pushes the closest of the Li^+ ions to the surface. Then the energy of the HOMO and LUMO decreases and increases, respectively. Therefore, it can be concluded that the change of the HOMO−LUMO gap and the energy of the LUMO show similar tendencies as the adsorption energy changes.

3.4. Adsorption and Diffusion of the Alkali Metal Ions.
The energetic and structural properties of the adsorption of sodium and potassium ions on graphene are similar to the properties of the adsorption of lithium ion described above. The minimum equilibrium distances are found to be 2.000 Å ($\bar{E}$ = 0.032 au) and 2.437 Å ($\bar{E}$ = 0.025 au) in the case of Na^+ and K^+ ions, respectively. The calculated minimum equilibrium distances depend on the ionic radius (Figure 5). Therefore
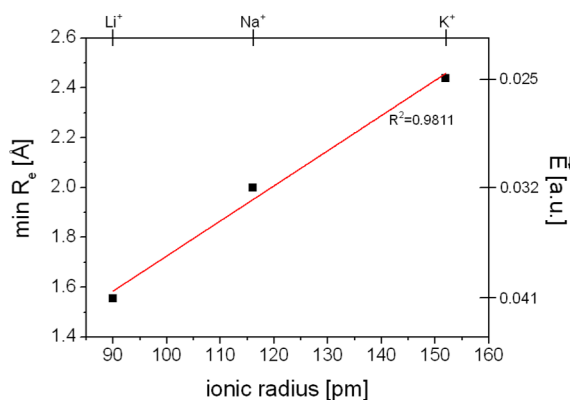

Figure 5. Minimum equilibrium distances between the alkali metal ions and the $C_{54}H_{18}$ graphene cluster.

particles with larger ionic radii reach the closest distance from the surface under weaker electric field, while in the case of smaller ions, it is necessary to apply a stronger field to push the particle as close as possible to the surface.

In order to study the diffusion mechanism of Li^+, Na^+, and K^+ ions on the graphene surface, a larger graphene cluster ($C_{130}H_{28}$) was constructed to eliminate the edge effects. Because of the high symmetry of the cluster, we have studied two different diffusion paths (Figure 6): in both cases the starting position of the ion is the hollow position in the middle of the cluster (H_0) and the ion migrate through the middle of the bond (B) or on the top of the C atom (T), denoted as paths A or B, respectively. To eliminate the electric field induced bending of the graphene plane, the rigid model was used to determine the energies for different adsorption positions. Particle diffusion processes on a lattice can be analyzed as the particle elementary jumps between adsorption sites along the potential energy surface. The activation energies or energy barriers were calculated by the difference between the stable states and saddle points related to the rate of the diffusion. Therefore the relative adsorption energies (ΔE_{ads}) could be calculated with respect to the E_{ads} of starting point in hollow site adsorption (H_0) of the investigated ion.

Figure 6 shows that the determined potential minima and maximum of the $Li^+C_{54}H_{18}$, $Na^+C_{54}H_{18}$ and $K^+C_{54}H_{18}$ systems located in the same sites and the shape of the examined diffusion paths are not depending on the applied electric field. At the same time the heights of the activation barrier are considerably increased under electric field. The bigger energy barriers on the diffusion paths indicate slower diffusion of the investigated particle.
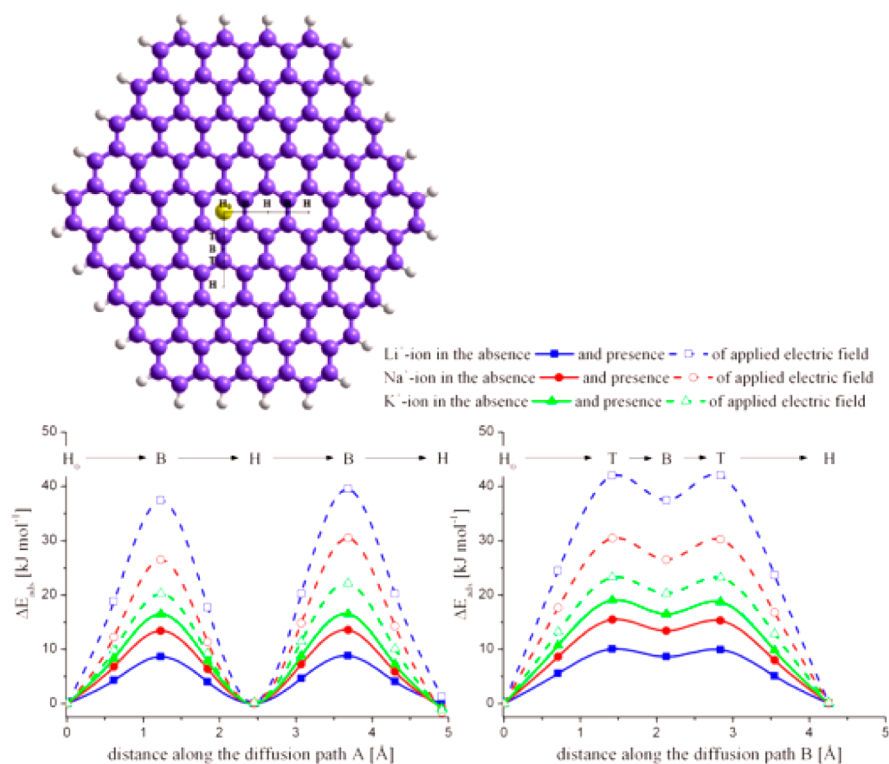

Figure 6. (a) Schematic representation of the $C_{130}H_{28}$ cluster used in the calculation. H, B, and T represent the ion adsorption position on the top of the hexagon, on the middle of the bond, and on the top of a C atom, respectively. (b) Energy barriers of the diffusion of Li^+, Na^+, and K^+ ions on paths A and B in the absence and presence of an applied electric field.

In the graphene cluster of $C_{130}H_{28}$ the two middle rings are equal, therefore the hollow site adsorption of the ions show no differences between these two rings (Figure 6). The diffusion of the ions between these middle rings along path A ($H_0 \rightarrow B \rightarrow H$) is capable to investigate the electric field effect with eliminating other conditions like the edge effect. The calculated energy barriers corresponding to the diffusion of Li, Na, and K ions are 8.65, 13.43, and 16.50 kJ mol^{-1} when the electric field is absent and 37.44, 26.52, and 20.31 kJ mol^{-1} when it is present, respectively. Accordingly, the diffusions of the ions are much slower under electric field than without it. Going along on path A, the next energy barriers related to the $H \rightarrow B \rightarrow H$ diffusion are slightly different from the previous case. The edge effect is hardly noticeable in the absence of an electric field. The difference between the energy barriers are smaller than 0.2 kJ mol^{-1}. At the same time, in the presence of electric field the second energy barriers on path A are at least 2 kJ mol^{-1} higher than the first one. These results indicate the importance of further investigations of the edge effect on the ion diffusion on graphitic surfaces like graphene nanoribbons under external electric field.

Previous studies[15,25] showed that in a neutral field on the graphene surface, the ion diffusion from the middle of the hexagon through the middle of the C−C bond is faster than through the top of the C atom. Therefore it is necessary to investigate how the preferred pathway changes under external electric field. The calculated barrier heights for path B are 10.06, 15.50, and 19.06 kJ mol^{-1} in the absence and 42.00, 30.48, and 23.28 kJ mol^{-1} in the presence of an electric field related to the diffusion of Li, Na, and K ions, respectively. This means that, even though the preferred pathway does not change in the absence or presence of electric field, the electric field induces higher differences between the energy barriers of the investigated two pathways.

The static calculations indicate that the Li$^+$ ion which has the smallest ionic radius diffuses fastest under neutral field. In contrast, the diffusion of the Li$^+$ ion is the slowest in the presence of an external electric field. On the diffusion path above the C−C bond (bridge site), the short-range repulsion between the particles is getting stronger, which causes a higher energy barrier if the particle is closer to the surface even as the Li$^+$ ion.

4. CONCLUSION

In this work the interaction between three kinds of alkali metal ions (namely Li$^+$, Na$^+$, and K$^+$) and the graphene surface in the cases of the absence and presence of the external electric field was investigated. An electric field perpendicular to the surface has been applied which pushes closer the positively charged ion to the graphene surface. Results show the importance of the charge transfer from the graphene surface to the alkali metal ion. At a species-dependent certain strength of the electric field the excess electrons cause negative charge on the alkali metal ion, promoting the shoving off of the ion from the surface. The static calculations indicate that the Li$^+$ ion which has the smallest ionic radius diffuses the fastest or the slowest under neutral or external electric field, respectively.

These findings may promote the more detailed exploration of the ions' adsorption and diffusion mechanism on graphene and graphene-like surfaces and facilitate the design of the experimental investigations and the applications in electrochemical devices and chemical sensors. Moreover, as we showed previously, the energy gap between the HOMO and LUMO orbitals of our systems decreases quite rapidly as the alkali metal ions approach the graphene surface and settle around 0.5−1 eV when the ions reached their lowest equilibrium distances. This low value predicts favorable holdings in photochemical studies at the range of visible light. With this property, the graphene−ion systems may open a new area besides sensor- and electrochemistry and play an important role in future developments of more efficient solar cells.

Although during the calculations the applied electric field strength is unrealistic for a larger device, it is achievable at the atomic level using a field ion microscope or atomic force microscope. Furthermore, the cluster model calculations are approximate, the size of the systems are limited, and in the present case, no surface defects or carrier surface like the nanostructured CeO$_2$ film have been taken into account. Even so we think that the present predictions and determined trends are applicable both in theoretical and experimental studies about how the electric field would affect ion−graphene interactions.

■ AUTHOR INFORMATION

Corresponding Author
*Tel: +36 72 503600. Fax: +36 72 501518. E-mail: kunsagi@gamma.ttk.pte.hu.

Notes
The authors declare no competing financial interest.

■ REFERENCES

(1) Kim, C.; Kim, B.; Lee, S. M.; Jo, C.; Lee, Y. H. Effect of Electric Field on the Electronic Structures of Carbon Nanotubes. *Appl. Phys. Lett.* 2001, 79, 1187−1189.

(2) Guo, Y.; Guo, W.; Chen, C. Tuning Field-induced Energy Gap of Bilayer Graphene via Interlayer Spacing. *Appl. Phys. Lett.* 2008, 92, 243101.

(3) Liu, H.; Lee, J. Y. Electric Field Effects on the Adsorption of CO on a Graphene Nanodot and the Healing Mechanism of a Vacancy in a Graphene Nanodot. *J. Phys. Chem. C* 2012, 116, 3034−3041.

(4) Zhang, T.; Xue, Q.; Shan, M.; Jiao, Z.; Zhou, X.; Ling, C.; Yan, Z. Adsorption and Catalytic Activation of O$_2$ Molecule on the Surface of Au-Doped Graphene under an External Electric Field. *J. Phys. Chem. C* 2012, 116, 19918−19924.

(5) Jiang, Q. G.; Ao, Z. M.; Chu, D. W.; Q. Jiang, Q. Reversible Transition of Graphene from Hydrophobic to Hydrophilic int he Presence of an Electric Field. *J. Phys. Chem. C* 2012, 116, 19321−19326.

(6) Peles-Lemli, B.; Kollár, L.; Kunsági-Máté, S. Thermodynamics of the Solvation of Carbon Nanotubes: Exchange of Aniline to Primary Alcohols on the Surface of Carbon Nanotubes. *Fullerenes, Nanotubes, Carbon Nanostruct.* 2010, 18, 207−215.

(7) Peles-Lemli, B.; Matisz, G.; Kelterer, A. M.; Fabian, W. M. F.; Kunsági-Máté, S. Noncovalent Interaction between Aniline and Carbon Nanotubes: Effect of Nanotube Diameter and the Hydro-

gen-Bonded Solvent Methanol on the Adsorption Energy and the Photophysics. *J. Phys. Chem. C* **2010**, *114*, 5898−5905.

(8) Li, H.; Nie, J. C.; Kunsági-Máté, S. Modified Dispersion of Functionalized Multi-Walled Carbon Nanotubes in Acetonitrile. *Chem. Phys. Lett.* **2010**, *492*, 258−262.

(9) Li, H.; Petz, A.; Yan, H.; Nie, J. C.; Kunsági-Máté, S. Morphology Dependence of Raman Properties of Carbon Nanotube Layers Formed on Nanostructured CeO_2 Films. *J. Phys. Chem. C* **2011**, *115*, 1480−1483.

(10) Li, H.; Nie, J. C.; Kunsági-Máté, S. EtOH Induced Formation of Nanographite Fractions and their Reorganization on Nanostructured CeO_2 Films. *Chem. Phys. Lett.* **2012**, *531*, 183−187.

(11) Li, H.; Nie, J. C.; Li, J. C.; Kunsági-Máté, S. Ethanol Induced Formation of Graphene Fractions Suspended in Acetonitrile. *Carbon* **2013**, *54*, 495−497.

(12) Kunsági-Máté, S.; Nie, J. C. Entropy-driven Adsorption of Carbon Nanotubes on (0 0 1) and (1 1 1) Surfaces of CeO_2 Islands Grown on Sapphire Substrate Surf. *Science* **2010**, *604*, 654−659.

(13) Zhao, Y.; Schultz, Y. E.; Truhlar, D. G. Design of Density Functionals by Combining the Method of Constraint Satisfaction with Parametrization for Thermochemistry, Thermochemical Kinetics, and Noncovalent Interactions. *J. Chem. Theory Comput.* **2006**, *2*, 364−382.

(14) Zhao, Y.; Truhlar, D. G. Density Functionals with Broad Applicability in Chemistry. *Acc. Chem. Res.* **2008**, *41*, 157−167.

(15) Zheng, J.; Ren, Z.; Gou, P.; Fang, L.; Fan, J. Diffusion of Li^+ ion on Graphene: A DFT Study. *Appl. Surf. Sci.* **2011**, *258*, 1651−1655.

(16) Frisch, M. J.; et al. *Gaussian 09*, revision C.01; Gaussian, Inc.: Wallingford, CT, 2009.

(17) *HyperChem Professional 7*; HyperCube: Gainesville, FL, 2002.

(18) Tournus, F.; Charlier, J. - C. Ab Initio Study of Benzene Adsorption on Carbon Nanotubes. *Phys. Rev. B* **2005**, *71*, 165421.

(19) Efremenko, I.; Sheintuch, M. Predicting Solute Adsorption on Activated Carbon: Phenol. *Langmuir* **2006**, *22*, 3614−3621.

(20) Gómez, B.; Martínez-Magadán, J. M. A Theoretical Study of Dibenzothiophene Absorbed on Open-Ended Carbon Nanotubes. *J. Phys. Chem. B* **2005**, *109*, 14868−14875.

(21) Wang, Y.; Bu, Y. Noncovalent Interactions between Cytosine and SWCNT: Curvature Dependence of Complexes via $\pi\cdots\pi$ Stacking and Cooperative $CH\cdots\pi/NH\cdots\pi$. *J. Phys. Chem. B* **2007**, *111*, 6520−6526.

(22) Ma, L.; Wang, J.; Ding, F. Recent Progress and Challenges in Graphene Nanoribbon Synthesis. *Chem. Phys. Chem.* **2013**, *14*, 47−54.

(23) Dai, Q. Q.; Zhu, Y. F.; Jiang, Q. Electronic and Magnetic Engineering in Zigzag Graphene Nanoribbons Having a Topological Line Defect at Different Positions with or without Strain. *J. Phys. Chem. C* **2013**, *117*, 4791−4799.

(24) Umadevi, D.; Sastry, G. N. Molecular and Ionic Interaction with Graphene Nanoflakes: A Computational Investigation of CO_2, H_2O, Li, Mg, Li^+, and Mg^{2+} Interaction with Polycyclic Aromatic Hydrocarbons. *J. Phys. Chem. C* **2011**, *115*, 9656−9667.

(25) Tachikawa, H.; Shimizu, A. Diffusion Dynamics of the Li+ Ion on a Model Surface of Amorphous Carbon: A Direct Molecular Orbital Dynamics Study. *J. Phys. Chem. B* **2005**, *109*, 13255−13262.

(26) Suzuki, T.; Hasegawa, T.; Mukai, S. R.; Tamon, H. A Theoretical Study on Storage States of Li Ions in Carbon Anodes of Li Ion Batteries using Molecular Orbital Calculations. *Carbon* **2003**, *41*, 1933−1939.

(27) Uthaisar, C.; Barone, V. Edge Effects on the Characteristics of Li Diffusion in Graphene. *Nano Lett.* **2010**, *10*, 2838−2842.

(28) Wang, Z. Alignment of Graphene Nanoribbons by an Electric Field. *Carbon* **2009**, *47*, 3050−3053.

(29) Lee, H.; Kim, S.; Ihm, J.; Son, Y. W.; Choi, H. J. Field-induced Recovery of Massless Dirac Fermions in Epitaxial Graphene on SiC. *Carbon* **2011**, *49*, 2300−2305.

(30) Glendening, E. D.; Reed, A. E.; Carpenter, J. E.; Weinhold, F. NBO, version 3.1; Gaussian, Inc.: Wallingford, CT, 2009.

(31) Tachikawa, H.; Shimizu, A. Density functional theory (DFT) study on the effects of Li^+ doping on electronic states of graphene. *J. Power Source* **2010**, *195*, 6148−6152.

21515

dx.doi.org/10.1021/jp403856e | *J. Phys. Chem. C* 2013, 117, 21509−21515

ELSEVIER

Host–guest interaction between water-soluble calix[6]arene hexasulfonate and *p*-nitrophenol

Sándor Kunsági-Máté[a,*], Kornélia Szabó[a], Beáta Lemli[a], István Bitter[b],
Géza Nagy[a,d], László Kollár[c,d]

[a] *Department of General and Physical Chemistry, University of Pécs, Ifjúság 6, H7624 Pécs, Hungary*
[b] *Department of Organic Chemical Technology, Budapest University of Technology and Economics, Budapest, Hungary*
[c] *Department of Inorganic Chemistry, University of Pécs, Pécs, Hungary*
[d] *MTA-PTE Research Group for Chemical Sensors, Pécs, Hungary*

Abstract

The inclusion complexation of calix[6]arene hexasulfonate with *p*-nitrophenol has been studied by photoluminescence (PL), differential scanning calorimetry (DSC) and quantum-chemical methods in aqueous media. The results indicate 1:1 complex stoichiometry. The directly measured molar enthalpy of inclusion shows strong interaction between the host and the guest, however the entropy change of the complex formation is negative and quite high. Therefore, the Gibbs free enthalpy change of the complex formation is small resulting in a relatively low complex stability. This well-known enthalpy–entropy-compensation effect is probably due to the increased freedom of guest molecules relative to the host calixarenes and also due to the increased disorder of solvent molecules after the complex has been dissociated. The good correlation between the van't Hoff enthalpy determined by PL studies and the calorimetric enthalpy reflects the two-state character of complexation. Quantum-chemical investigation suggests π–π interaction between the host and the guest in agreement with earlier results.
© 2004 Elsevier B.V. All rights reserved.

Keywords: Inclusion compound; Host–guest complex; DSC; Enthalpy of inclusion; Calixarenes

1. Introduction

The recognition of neutral organic molecules by synthetic receptors is a topic of current interest in supramolecular- and also in analytical chemistry [1,2]. Calix[*n*]arenes (*n* = 4–6, 8) represent a fascinating class of macrocycles due to the simplicity of their well-defined skeleton, which is associated with versatile recognition properties towards metal or organic ions and neutral molecules [3,4]. Recent reviews summarize their thermodynamic [5] and redox properties [6], applications in analytical and separation science [7], modeling of their molecular dynamics [8–10] and the extent of their metal ion binding character in solution [11,12].

The selectivity of complexation with different species can be modified by changing the cavity size and by the incorporation of functional groups in the lower and/or upper rim of the calixarene molecule. In our recent papers [13–15] the complexation behavior and the factors controlling the thermodynamic and kinetic stability or selectivity of some calixarene derivatives towards neutral π-electron deficient aromatics were reported. In addition, the binding characteristics of water-soluble calixarenes with iron ions [16] and with C_{60} fullerene [17] have also been published.

The interactions of calixarenes with neutral species involve competition between complexation and solvation processes. Non-electrostatic forces arising from the interaction of the electronic systems of neutral hosts and guests are of primary importance. For example, calixarenes and electron-deficient aromatics can form complexes predominantly through π–π type interaction, whilst the inclusion of

* Corresponding author. Tel.: +36 72 503600x4208; fax: +36 72 501518.
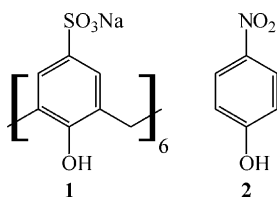 *E-mail address:* kunsagi@ttk.pte.hu (S. Kunsági-Máté).

Fig. 1. Calix[6]arene-hexasulfonate sodium salt **1** as host and *p*-nitrophenol **2** as guest.

aliphatic guests into the hydrophobic cavity can be stabilized by CH–π contacts.

Calix[4]arene tetrasulfonate [18], and the thia-calix[4]arene counterpart [19] have been reported to bind small polar organic molecules (alcohols, carbonyl compounds, nitriles, acid derivatives, etc.) in aqueous solution and the complexation was monitored mostly by ^{1}H NMR spectroscopy. In these cases the importance of charge assistance of the sulfonate groups in apolar binding of the guests was confirmed. Because of the ^{1}HNMR is relatively seldom applied for identification of complexation, it may worth to note that this technique has been successfully used to identify the clathrate formation of 2,2′-bis(9-hydroxy-9-fluorenyl)biphenyl with small solvent molecules (acetone and methanol). This reaction has been also studied by means of simultaneous TG–DSC measurement using isothermal and scanning mode of operation [20].

In this paper, the interaction between calix[6]arene-hexasulfonate sodium salt **1** as a host and *p*-nitrophenol **2** as a guest (Fig. 1) in aqueous media was investigated by photoluminescence (PL), differential scanning calorimetry (DSC) and quantum-chemical methods. The stoichiometry and the van't Hoff enthalpy of the complex formation were determined by spectrofluorometric method. The calorimetric molar enthalpy of the inclusion was determined from the heat flow directly measured by DSC method. The fluorometrically determined van't Hoff enthalpy and the calorimetric enthalpy were compared to examine the two-state behavior of the formation of such a complex. Quantum-chemical investigations were carried out to determine the most stable conformation of the host–guest complex.

2. Experimental

Calix[6]arene-hexasulfonate salt **1** was prepared by the direct sulfonation of the parent calix[6]arene with concentrated sulfuric acid [21]. *p*-Nitrophenol (p.a. grade) was purchased (Merck, Germany) and used without further purification.

Calorimetric measurements were carried out with a highly sensitive nano-II-DSC 6100 (Setaram, France) instrument. The calorimeter is configured with a platinum capillary cell (volume = 0.299 ml). The samples were pressurized to $3 \pm 0.02 \times 10^5$ Pa during all scans. Using oil rotation pump, standard degassing procedure for 15 min at about 15 Pa was applied before loading the samples into the capillary. The heat

flow was scanned between 0 and 50 °C. A typical scanning rate of 0.5 K/min was applied, however it was varied from 0.1 up to 2 K/min for each sample to check the effect of diffusion of particles interacted and that of on the reaction rate of complexation. The experimental deviation of the calorimetric results were estimated to be ± 5 mJ.

To avoid any interaction other than the interaction related to the host – guest complex formation, the DSC curves of solutions of calixarene in buffer (i), calixarene in water (ii) and buffer by oneself (iii) were recorded against water. No significant differences between the curves of summed (ii) with (iii) and (i) were obtained, proving that no considerable interaction between the buffer and the host calixarene exists. Similar result was found for the guest *p*-nitrophenol species.

The PL spectra of the different solutions were investigated by means of Fluorolog τ3 spectrofluorometric system (Jobin-Yvon/SPEX). For data collection a photon counting method with 0.2 s integration time was used. Excitation and emission bandwidths were set to 1 nm. A 1 mm layer thickness of the fluorescent probes with front face detection was used to eliminate the inner filter effect.

The acid–base equilibria in the solutions of calixarene **1** was studied by potentiometry using a combined pH sensitive glass electrode (Triode pH electrode, ORION) and Orion 420 Aplus pH meter. The potentiometric measurements were carried out at 25 ± 0.1 °C. The protonation was studied in aqueous solution of **1** at concentration of 10^{-2} M with ionic strength of 0.1 M tetraethylammonium-perchlorate ([Et$_4$N][ClO$_4$]) background salt. The estimated error of the pH measurements was found to be about 0.02 pH unit. Values of the stepwise protonation constants K_i and the overall protonation constants β_i were computed with the HyperQuad 2000 (Protonic Software) computer program [22–24].

Both calorimetric and fluorometric experiments were carried out at pH 6.9 using phosphate buffer. 0.025 mol/kg disodium hydrogen phosphate (Merck) + 0.025 mol/kg potassium dihydrogen phosphate (Merck); pH 6.961, 6.912, 6.873, 6.843, 6.823, 6.814 at temperatures of 0, 10, 20, 30, 40, 50 °C, respectively.

The equilibrium conformations of calixarene **1** and their complexes with *p*-nitrophenol **2** were studied with semi-empirical AM1 (Austin Model) method, followed by ab initio HF/6-31G* calculations. The Fletcher-Reeves geometry optimization method was used for the investigation of the conformers. The interaction energy of the studied species was described at an ab initio level using HF/6-31G* calculation. TIP3P method [25] with extension to the solvent used [26] was applied for considering the solvent effect. All types of calculations were carried out with the HyperChem Professional 7 program package [27].

3. Results and discussion

Fig. 2 shows the distribution diagram of the differently protonated species of **1** derived from the acid–base titration
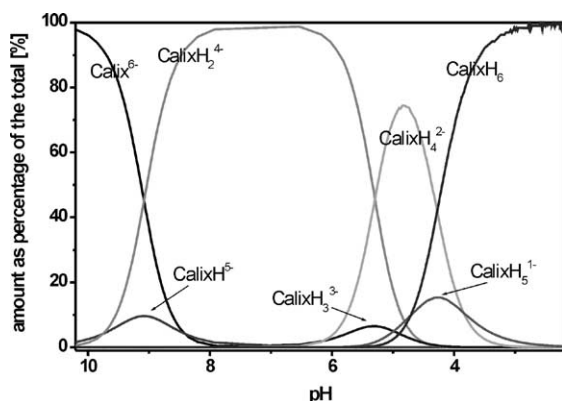
Fig. 2. Distribution diagram of the differently protonated calixarene **1** as a function of pH.

by adjusting ionic strength with 0.1 M tetraethylammonium-perchlorate background salt. Measurements were carried out under purified nitrogen atmosphere. It can be clearly seen that near pH 7, compound **1** exists in double protonated form. It has to be noted, that the distribution curve of $CalixH_2^{4-}$ has a wide maximum between pH 6 and pH 8.5 providing excellent conditions for the investigation of its host properties. Since no considerable abundance of other species has been observed at this pH range, therefore pH 6.9 was chosen for the further examinations. To minimize the effect of the temperature change on pH, phosphate buffer was used which keeps the pH constant at a wide range of temperature (see Section 2).

3.1. Effect of complexation on PL intensity

In order to investigate the interaction of **1** with **2**, 10^{-4} M solutions were prepared in phosphate buffer and the PL spectra were recorded. Their evaluation revealed that the guest molecule induced some changes in the spectra. The PL spectrum of **1** exhibits two peaks at 330 nm and at 495 nm, the intensities of which were decreased in the presence of **2** (Fig. 3). According to our earlier results [13–17] we supposed that the spectral changes were induced by the formation of an inclu-
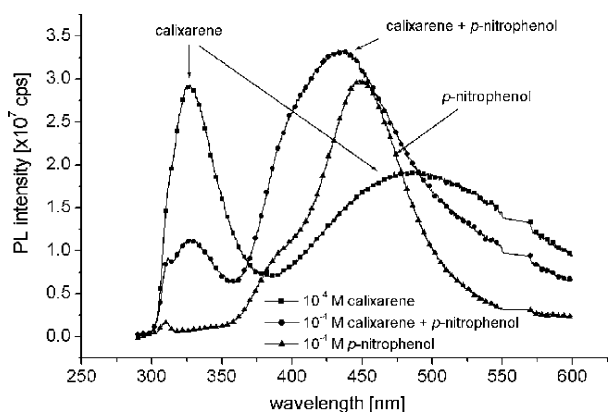

Fig. 3. The change of the PL spectra of calixarene derivative **1** obtained in the absence and in the presence of 10^{-4} M p-nitrophenol.

sion complex. Since p-nitrophenol **2** also shows considerable emission and its emission band overlaps with the 495 nm band of **1**, the 330 nm peak of calixarene was used for the determination of complex stability.

3.2. Determination of the complex stoichiometry and complex stability

Assuming a 1:1 stoichiometry, the complexation reaction can be written as follows ("H" refers to host while "G" means the guest):

$$H + G \overset{K_s}{\rightleftharpoons} HG \tag{1}$$

It is well known that in this particular case the concentration of the complex formed can be expressed as the function of the initial concentrations ($[H]_0$ and $[G]_0$):

$$[HG] = \frac{1}{2} \left\{ \left([H]_0 + [G]_0 + \frac{1}{K_s} \right) \pm \sqrt{ \left([H]_0 + [G]_0 + \frac{1}{K_s} \right)^2 - 4[H]_0[G]_0 } \right\} \tag{2}$$

Assuming that the observed PL signal varies linearly with the concentration of the complex formed, ΔF is described by Eq. (3).

$$\Delta F = f_{HG}[HG] \tag{3}$$

wherein $\Delta F = F - F_0$ is a difference between the PL intensity obtained with the calixarene/p-nitrophenol system and that of the free calixarene with the same concentration. The measure of the PL signals, f_{HG} can be obtained for the individual HG species relative to the PL signal of pure calixarene species at the same concentrations. By definition,

$$f_{HG} = \left. \frac{F([G]) - F([HG])}{F([H])} \right|_{[HG]=[H]} \tag{4}$$

Job's method [28] is widely used for the spectroscopic determination of complex stability constants also in calixarene chemistry [29–33]. The stability constant of the inclusion complex can be determined by the curve fitting of Eq. (3) to the experimental data using the expression of [HG] from Eq. (2).

However, it is known that the equilibrium in similar systems strongly depends on the temperature [e.g. [34]]. The thermodynamic parameters for the individual complexes formed in the calixarene/p-nitrophenol system can be determined from the van't Hoff equation:

$$\ln K = -\frac{\Delta G}{RT} = -\frac{\Delta H}{RT} + \frac{\Delta S}{R} \tag{5}$$

where ΔG is the Gibbs energy change, ΔS the entropy change and ΔH the enthalpy change associated with complex formation.
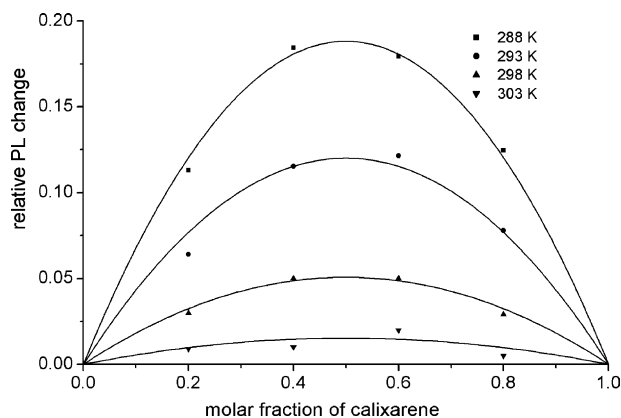
Fig. 4. Job's plot of calixarene **1**–*p*-nitrophenol system at different temperatures.

Inserting Eq. (5) for the formation constants into the Eqs. (2) and (3), the fluorescence change in Eq. (3) can be expressed as a function of the ΔH, ΔS values and the f_{HG} coefficient.

The thermodynamic parameters associated with the K value were determined from the Job's curves by an iterative solution of Eqs. (2) and (3) using the expression of K value from the van't Hoff equation (Eq. (5)).

In order to determine the thermodynamic parameters mentioned above, 10^{-3} M stock solutions of **1** and **2** were mixed in four different [H]/([G] + [H]) ratio by stepwise addition of $n \times 300\,\mu$l host to $(5 - n) \times 300\,\mu$l guest solutions (n = 1–4) keeping 10^{-3} M total concentration ([G] + [H]). The measurements were carried out at four different temperatures and the iterative curve-fitting procedure was done simultaneously for the experimental data (Fig. 4). The plot of ΔF as a function of molar fraction of host gives an excellent fit, verifying the 1:1 complex stoichiometry assumed above. Table 1 summarizes the thermodynamic parameters determined from PL studies.

3.3. DSC measurements on the host–guest system

Fig. 5 shows a typical DSC scan of the mixture of equimolar (10^{-3} M) solutions of **1** and **2** recorded against the phosphate buffer with a scanning rate of 1 K/min. The excess heat capacity was calculated by substraction of the baseline (see later). The broad DSC curve reflects to fast dissociation process compared to the speed of change of concentration. This change is induced by the decreased complex stability at higher temperature, and therefore, its speed is determined by
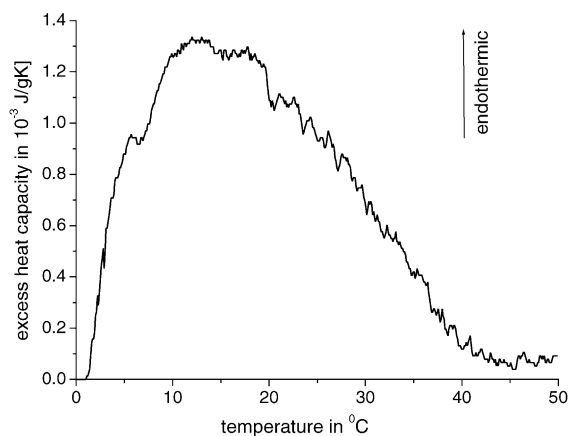

Fig. 5. The excess heat capacity of the equimolar (10^{-3} M) mixture of **1** and **2** recorded against the phosphate buffer. Scanning rate is 1 K/min.

the scanning rate. This shape of the DSC curve is usual in case of weak host–guest complexes [20].

Fig. 6 shows the excess heat capacity of the equimolar mixture of **1** and **2** scanned by the rate of 0.5 K/min. Five different concentrations varying between 1×10^{-3} and 4.1×10^{-4} M were applied, keeping the same host–guest concentration ratio at each individual run. The more diluted solutions show lower excess heat capacities at each temperature. Furthermore, the curves display that the excess heat capacity decreases with increasing the temperature for each solution. This is consistent with the theoretical expectations: the amount of complexes, dissociated during the temperature changes in a temperature unit, decreases by increasing the temperature (see Eqs. (2) and (5)). Accordingly, the measured excess heat capacity decreases with increasing temperature. Overall, this shape of the DSC curves shows that the dissociation process is fast related to the speed of the change of complex concentration, which is induced by the change of temperature at a given scanning rate. Consequently, the system is in quasi-equilibrium state at each temperature. Therefore, the change of the host–guest complex concentration
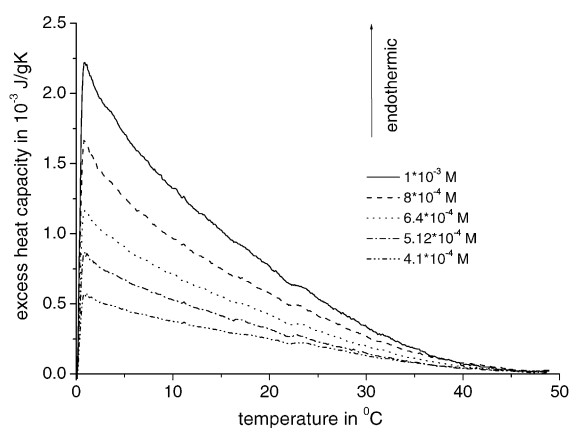
Table 1
Thermodynamic parameters of complexation of **1** with **2**

Method	K_s (25 °C) (dm³/mol)	ΔG (kJ/mol)	ΔH (kJ/mol)	ΔS (J/K mol)
DSC	192.6	−5.3 (5)	−68.2 (3)	−185 (9)
PL	145.4	−4.9 (4)	−66.4 (5)	−181.3 (3)

Fig. 6. Excess heat capacity of the equimolar solutions of **1** and **2** scanned with the rate of 0.5 K/min.
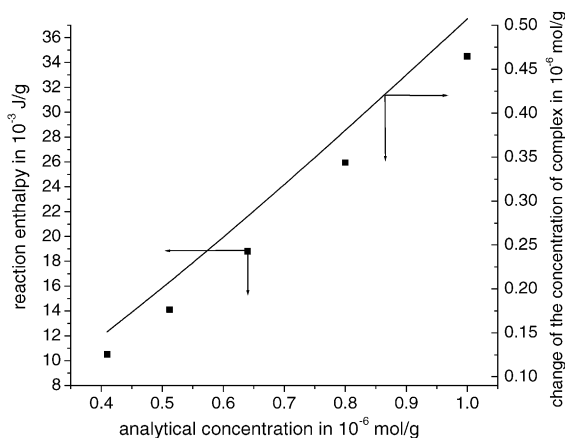
Fig. 7. The enthalpy change (■) of decomposition of the host–guest complexes (left axis) plotted against analytical concentration of equimolar solutions of **1** with **2**. The solid line shows the change of the concentration of the complex (right axis) while the temperature increases from 0 to 50 °C.

driven by the temperature change is reflected in the DSC curve.

The calculation of calorimetric enthalpies is based on the integration of the area under the excess heat capacity curve. The baseline for these calculations was generated using the software of the calorimeter: a polynomial baseline was generated by fitting it to the experimental baseline in the pre- and post-transition regions. Although this approximation of setting the baseline with a polynomial fitting was found to be widely used in such type of experiments, it is not free of an error, which is inversely proportional to the height to width ratio of the calorimetric peak. However, in our case this error was found below 0.5% of the total reaction enthalpy.

Fig. 7 shows the enthalpy changes of the dissociation plotted against the analytical concentration of equimolar solutions of **1** and **2**. The solid line shows the change of the complex concentration while the temperature increases from 0 to 50 °C. As it is well known, the concentration of a host–guest complex varies with the temperature as the complex stability constant is affected by the temperature during a DSC run. Therefore, we are unable to determine the concentration of the analyte and consequently, the thermodynamic parameters from a single DSC run.

However, using the expression of the stability constant K from the van't Hoff equation (Eq. (5)) the concentration of a 1:1 host–guest complex can be described as a function of the molar enthalpy, entropy change and of the temperature. The amount of the complex being dissociated while the temperature increases from 0 to 50 °C ($[HG]_{diss}$) can be expressed as the difference of concentrations of the complex at the two temperatures:

$$[HG]_{diss} = [HG(\Delta H, \Delta S, 0\,°C)] - [HG(\Delta H, \Delta S, 50\,°C)]$$
(6)

The reaction enthalpy measured by DSC is the product of the concentration of the complex dissociated and the molar enthalpy change of the reaction:

$$\begin{aligned}
\Delta_R H &= \Delta H[HG]_{diss} \\
&= \Delta H\{[HG(\Delta H, \Delta S, 0\,°C)] \\
&\quad -[HG(\Delta H, \Delta S, 50\,°C)]\}
\end{aligned}$$
(7)

After the measurements were carried out with five different, however equimolar concentrations of host and guest, iterative curve-fitting procedure by a variation of ΔH and ΔS was done for the experimental data plotted on Fig. 7. Table 1 summarizes the results determined by the procedure described above using the data of the DSC measurements. It has to be noted, that the enthalpy and entropy values in Table 1 are the averaged values over the temperature interval between 0 and 50 °C, where the complexation/decomplexation process is studied.

3.4. The stabilization energy of the inclusion complexes

The binding of *p*-nitrophenol **2** by calixarene **1** detected by PL and DSC studies, was examined by quantum-chemical method, too. The interaction energy between the host and the guest molecules was calculated by the procedure described earlier [15]. All energies were determined in the presence of solvent cage using TIP3P method [25,26], i.e. the solvation enthalpies of the interacting species were considered in this way. Only those conformations with the *p*-nitrophenol molecule located inside the calixarene cavity (i.e. interacts with calixarene from the side of the upper rim) were found
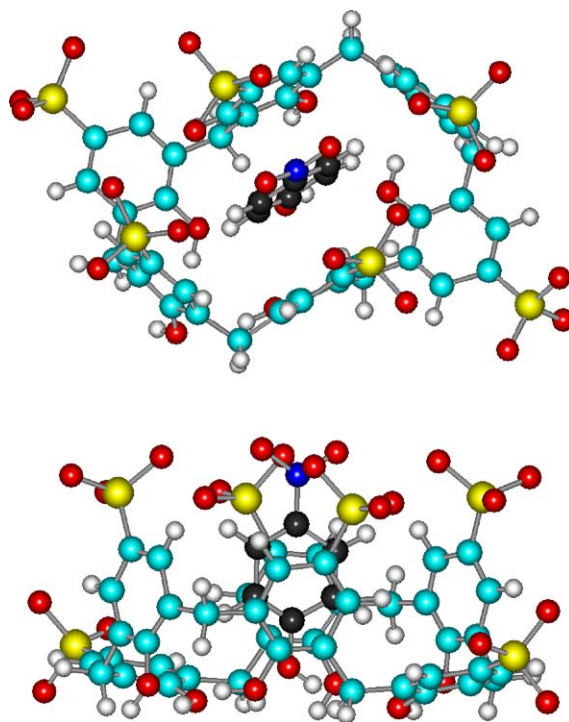

Fig. 8. Two views on the optimized structure of the inclusion complex of **1** with **2**.

stable. The stabilization energy of the complex was evaluated as the absolute value of the interaction energy, i.e. the difference between the total energy of the optimized structure of the complex and that of the separated host plus guest molecules. Fig. 8 shows the top and side view of the optimized structure of the host–guest complex. The stabilization energy was found to be 48.3 kJ/mol. This value can be compared with the enthalpy change of complexation since the entropy effect was not considered in the quantum chemical calculation. The ca. 30% deviation from the experimental value is probably due to the approximation used in the theory and also because this value is derived from the static calculation and relates to the temperature of 0 K.

4. Conclusion and summary

PL and DSC measurements have been successfully applied to study the inclusion complexation of calix[6]arene hexasulfonate with *p*-nitrophenol in aqueous solution. Both the PL and DSC signals indicate a 1:1 complex stoichiometry. The directly measured molar enthalpy of inclusion shows a strong interaction between the host and the guest. However, the entropy change during the complexation is a relatively high negative value, which decreases the Gibbs free enthalpy change of the reaction, thereby the complex stability. The highly exothermic complexation enthalpy parallel with the significant decrease of the entropy during complex formation reflects to the so-called enthalpy–entropy-compensation effect. It is probably due to the increased freedom of guest molecules relative to the host calixarenes and also due to the increased disorder of solvent molecules after the complex has been dissociated. Quantum-chemical investigation suggests that the *p*-nitrophenol guest resides in the calixarene cavity and the complex is stabilized by π–π interaction.

References

[1] T. Kuwabara, H. Nakajima, M. Nanasawa, A. Ueno, A. Anal. Chem. 71 (1999) 2844–2849.
[2] P.D. Beer, P.A. Gale, G.Z. Chen, Coord. Chem. Rev. 186 (1999) 3–36.
[3] C.D. Gutsche, Monographs in Supramolecular Chemistry, vol. 1. Calixarenes, The Royal Society of Chemistry, Cambridge, 1989.
[4] C.D. Gutsche, Monographs in Supramolecular Chemistry, vol. 6. Calixarenes Revisited, The Royal Society of Chemistry, Cambridge, 1998.
[5] A.F. Danil de Namor, R.M. Cleverly, M.L. Zapata-Ormachea, Chem. Rev. 98 (1998) 2495–2525.
[6] P.D. Beer, P.A. Gale, G.Z. Chen, J. Chem. Soc., Dalton Trans. 12 (1999) 1897–1909.
[7] R. Ludwig, Fresenius J. Anal. Chem. 367 (2000) 103–128.
[8] A. Varnek, G. Wipff, J. Comput. Chem. 17 (1996) 1520–1531.
[9] M. Lauterbach, G. Wipff, in: L. Echegoyen, A. Kaifer (Eds.), Physical Supramolecular Chemistry, Kluwer Academic Publishers, Dordrecht, 1999, pp. 65–102.
[10] A. Varnek, G. Wipff, J. Mol. Struct. (THEOCHEM) 363 (1996) 67–85.
[11] A. Ikeda, S. Shinkai, Chem. Rev. 97 (1997) 1713–1734.
[12] A.T. Yordanov, D.M. Roundhill, Coord. Chem. Rev. 170 (1998) 93–124.
[13] S. Kunsági-Máté, G. Nagy, L. Kollár, Sens. Actuators B: Chem. 76 (2001) 545–550.
[14] S. Kunsági-Máté, G. Nagy, P. Jurecka, L. Kollár, Tetrahedron 58 (2002) 5119–5124, and references cited therein.
[15] S. Kunsági-Máté, I. Bitter, A. Grün, G. Nagy, L. Kollár, Anal. Chim. Acta 461 (2002) 273–279.
[16] S. Kunsági-Máté, L. Nagy, G. Nagy, I. Bitter, L. Kollár, J. Phys. Chem. B 107 (2003) 4727–4731, and references cited therein.
[17] S. Kunsági-Máté, K. Szabó, I. Bitter, G. Nagy, L. Kollár, Tetrahedron Lett. 45 (2004) 1387–1390.
[18] G. Arena, A. Contino, F.G. Guliano, A. Magri, D. Sciotto, R. Ungaro, Tetrahedron Lett. 41 (2000) 9327–9330.
[19] N. Iki, T. Suzuki, K. Koyama, C. Kabuto, S. Miyano, Org. Lett. 4 (2002) 509–512.
[20] J. Seidel, G. Wolf, E. Weber, Thermochim. Acta 271 (1996) 141–148.
[21] S. Shinkai, T. Mori, T. Tsubaki, T. Sone, O. Manabe, Tetrahedron Lett. 25 (1984) 5315–5318.
[22] HyperQuad 2000. Ver. 2.1. Protonic Software, 2002.
[23] P. Gans, A. Sabatini, A. Vacca, Talanta 43 (1996) 1739–1753.
[24] L. Alderighi, P. Gans, A. Ienco, D. Peters, A. Sabatini, A. Vacca, Coord. Chem. Rev. 184 (1999) 311–318.
[25] W.L. Jorgensen, J. Chandrasekhas, J.D. Madura, R.W. Impey, M.L. Klein, J. Chem. Phys. 79 (1983) 926–935.
[26] T. Bender, Solvent Cage, Excel Macros to HyperChem, Hypercube, www.hyper.com, 2000.
[27] HyperChem Professional 7, HyperCube, 2002.
[28] F.J.C. Rossotti, H. Rossotti, The determination of stability constants, McGraw-Hill, New York, 1961 (pp. 47–51).
[29] Y. Inoue, K. Yamamoto, T. Wada, S. Everitt, X.-M. Gao, Z.J. Hou, L.H. Tong, S.K. Jiang, H.M. Wu, J. Chem. Soc., Perkin Trans. 2 (1998) 1807.
[30] Y. Liu, L. Jin, S.-X. Sun, Microchem. J. 64 (2000) 59.
[31] Y. Liu, S.-Z. Kang, H.-Y. Zhang, Microchem. J. 70 (2001) 115.
[32] I. Mohammed-Ziegler, M. Kubinyi, A. Grofcsik, A. Grün, I. Bitter, J. Mol. Struct. 480–481 (1999) 289.
[33] Y. Okada, M. Mizutani, F. Ishii, Y. Kasai, J. Nishimura, Tetrahedron 57 (2001) 1219.
[34] T. Wharton, V.U. Kini, R.A. Mortis, L.J. Wilson, Tetrahedron Lett. 42 (2001) 5159–5162.

Host–guest interaction of calixarene molecules with neutral benzotrifluorides
Comparison of luminescence spectral data with results of model calculations relating to complex formation

Sándor Kunsági-Máté [a], Géza Nagy [a,c,*], László Kollár [b,c]

[a] *Department of General and Physical Chemistry, University of Pécs, 7624 Pécs, Ifjúság 6, Hungary*
[b] *Department of Inorganic Chemistry, Faculty of Sciences, University of Pécs, 7624 Pécs, Ifjúság 6, Hungary*
[c] *MTA-PTE Research Group for Chemical Sensors, 7624 Pécs, Ifjúság 6, Hungary*

Abstract

The 'host' properties of calix[4]arene and 4-*tert*-butyl-calix[6]arene molecules under the effect of different neutral pesticide related trifluoromethyl-benzene molecules as 'guests' have been investigated by spectrofluorometric method. Significant dependence of the photoluminescence behaviour of calixarene derivatives on the structure of interactive molecules was detected in chloroform and dimethylformamide solvent. The formation of stable host–guest complexes was checked by quantum-chemical method. The results show that the photoluminescence signal reflects the supramolecular interaction. This makes calixarenes promising candidates as host molecules to be used in chemical sensors measuring neutral organic molecules. © 2001 Elsevier Science B.V. All rights reserved.

Keywords: Calixarenes; Organic guests; Photoluminescence; Chemical sensors

1. Introduction

It is a common sense that the function of a selective chemical sensor is based on two equally important steps, on the selective recognition and on the signal transduction. Supramolecular interactions between host molecules incorporated in a sensor and an analyte acting as guest could be used successfully in sensor research.

Calixarenes because of their well defined frame and chemically stable intermolecular cavity of tunable size and co-ordination selectivity are frequently selected as host molecules in sensor research [1,2] or in separation sciences [3–5].

Calix[4]arene ester was successfully used as active ionophore incorporated in elasticised PVC membrane preparing cesium-selective potentiometric electrodes [6]. Kimura and co-workers prepared sodium selective electrode [7] and ion selective field effect transistors [8] with calix[4]arene ionophore. Calixarene based solid state sodium ion selective electrode was also reported [9]. Calix[4]arene containing PVC membrane showed amine and alkaline ion selectivity [10].

* Corresponding author. Tel.: +36-72-327622 (-4681);
fax: +36-72-327622 (-4680).
E-mail address: g-nagy@ttk.pte.hu (G. Nagy).

The application of calixarenes in electroanalysis was reviewed by O'Connor et al. [11].

For an ionic species measuring chemical sensors — as it can be seen — often potentiometric signal transduction is used. However, considerable interest has been focused to prepare calixarene ionophore based optodes [12–14].

Lynch and co-workers investigated the interactions of calixarene ionophore derivatives with metal ions in solution using fluorescence and absorption spectroscopy [15]. On the other hand, Schierbaum and co-workers studied the interaction of calixarene derivative containing layers with organic molecules using experimental techniques and force field calculations [16].

Since calixarene derivatives can form host–guest type complexes with neutral organic molecules, it is likely that they can be used for selective molecular recognition in chemical sensors measuring neutral species, too. Therefore, it was obvious to investigate the possible signal transduction mechanisms. Since fluorescence generation is a very sensitive signal forming technique, in our laboratories studies have been carried out with different calixarene derivatives and organic guest molecules to collect data about the influence of the supramolecular interaction on the fluorescence signal. It was hoped that comparing the fluorescence spectroscopic data with interaction energy values obtained by model calculation can be used in designing selective host molecules. As model guest molecules different trifluoromethylbenzene derivatives possessing electron-withdrawing groups-EWG-were selected. It could be expected that the electron-deficiency in their aromatic ring might give a chance for the interaction with the relatively electron-rich calixarene aromatic moieties. However, the analysis of these neutral molecules can be of practical importance because of their pesticides relating structure [17]. In this short paper presented here, our preliminary results are summarised.

2. Chemicals, apparatus and methods

Calixarenes (calix[4]arene, MW = 424.8, 99% and 4-tert-butyl-calix[6]arene, MW = 973.39, 99%) were obtained from Aldrich Chemical Co. and were

used as received. Benzotrifluoride derivatives were obtained from Budapest Chemical works Co. Ltd. Dimethylformamide (Reanal, Hungary) and chloroform (Fluka) solvents were distilled freshly before the measurements.

Highly sensitive Fluorolog τ3 spectrofluorometric system was used to investigate the photoluminescence (PL) spectral behaviour of the different solutions prepared. For data collection photon counting method with 0.2 s integration time was used. Excitation and emission bandwidths were set to 2 nm. All measurements were carried out at 20°C.

The equilibrium conformation of calixarenes and benzotrifluoride derivatives and the interaction energy of the studied species were described at *ab initio* level using HyperChem Professional 5.1 program package.

n=1   calix[4]arene
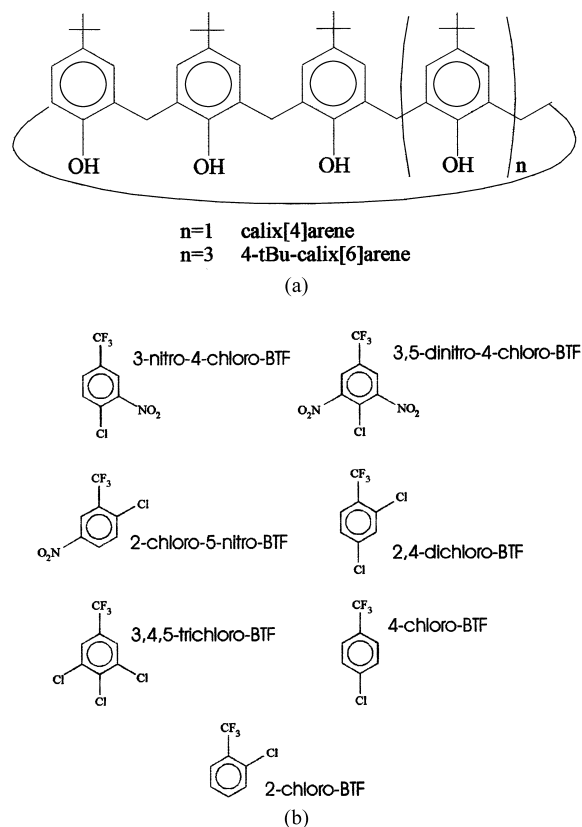n=3   4-tBu-calix[6]arene

(a)

(b)

Fig. 1. Calixarenes (a) as host and benzotrifluoride derivatives (b) as guests were chosen for this model studies (BTF stands for benzotrifluoride).

For the calculations 6–31 G Gaussian-type basis set with Fletcher–Reeves geometry optimisation method were used. The solvent effect of chloroform and DMF was described by TIP3P method (HyperChem package) and by Onsager method (Gaussian 94 package), respectively.

3. Results and discussion

Since the aromatic ring of calixarenes can be considered electron rich due to the slightly positive inductive effects of *tert*-butyl and methylene groups, electron deficient neutral aromatics as guest
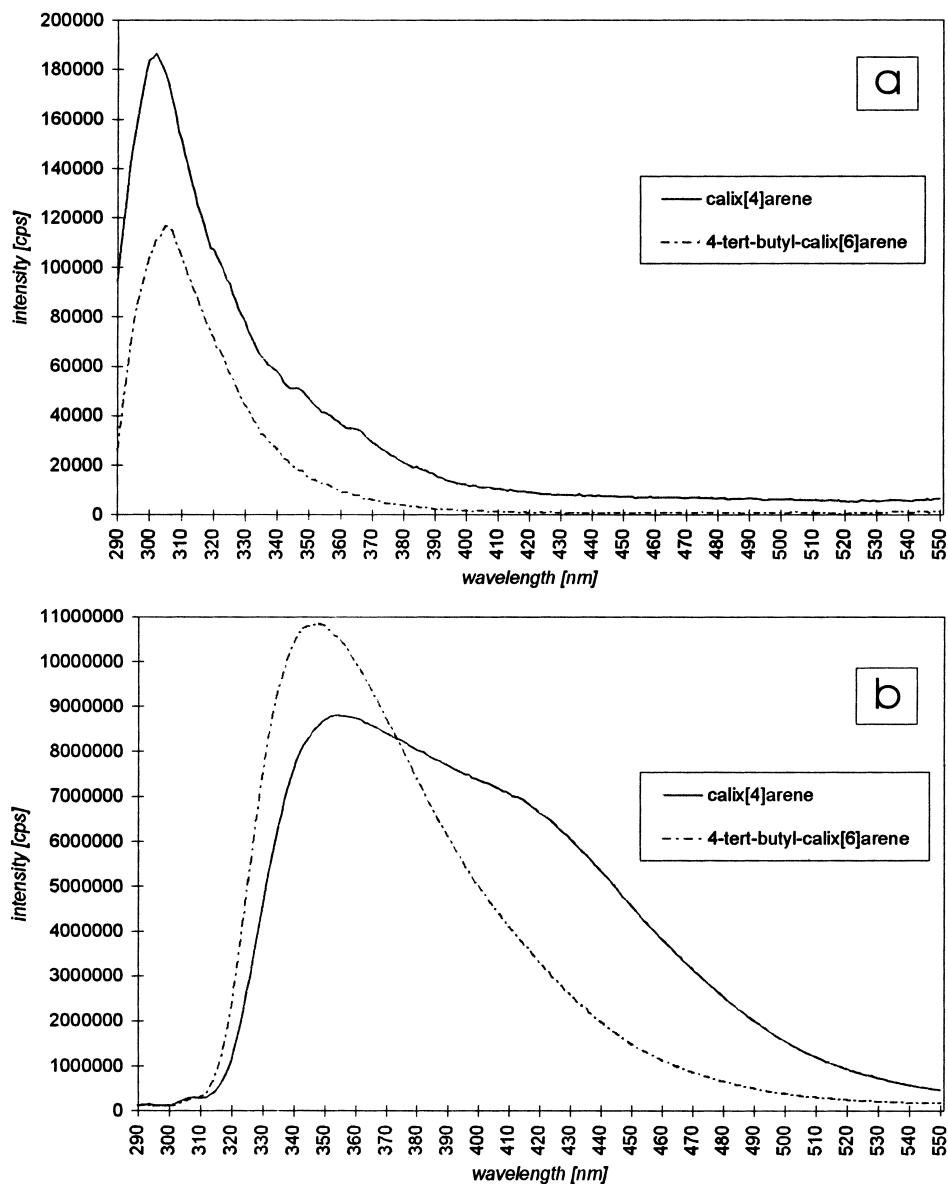

Fig. 2. PL spectra of calix[4]arene and 4-*tert*-butyl-calix[6]arene dissolved in chloroform (a) and dimethylformamide (b) solvents using 280 nm for excitation.
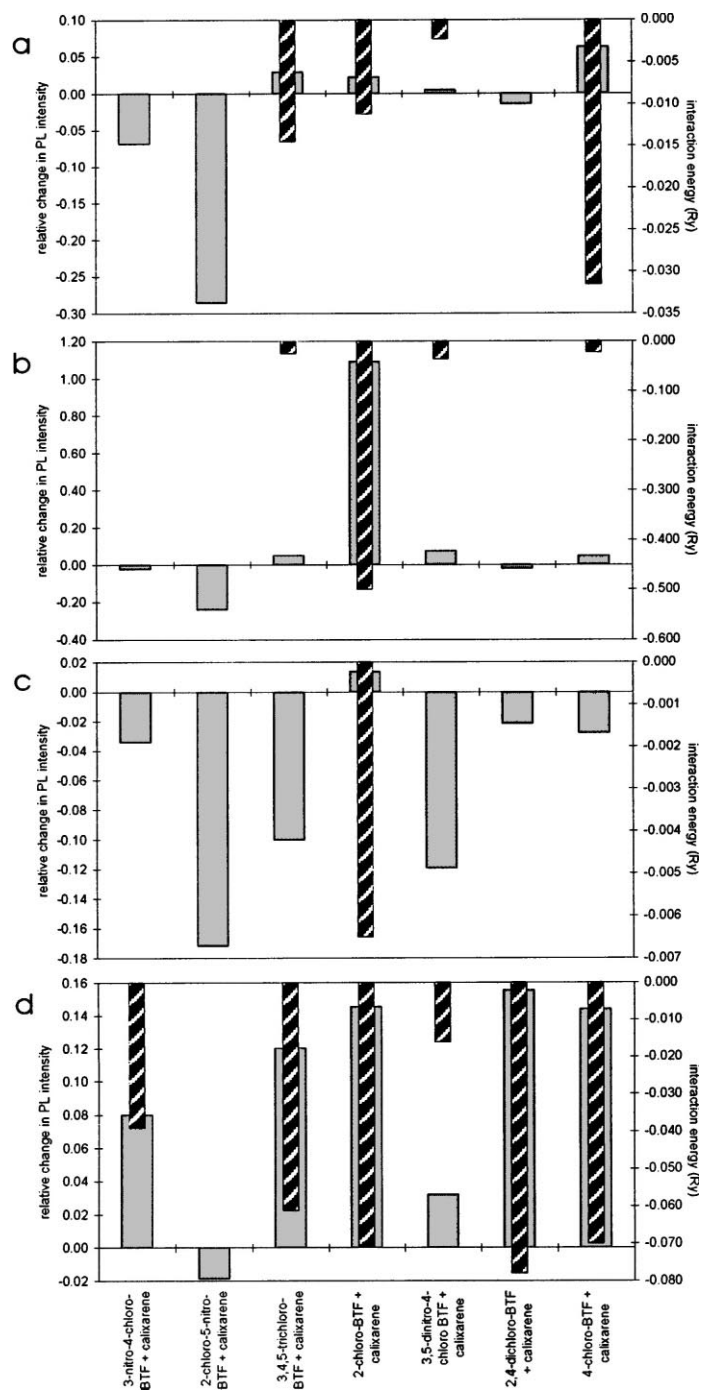
Fig. 3. Relative changes in PL intensity of the 1:1 calixarene:benzotrifluoride mixtures and the interaction energy of the corresponding stable complexes. (a) Calix[4]arene + BTF in chloroform; (b) 4-*tert*-butyl-calix[6]arene + BTF in chloroform; (c) calix[4]arene + BTF in dimethylformamide; (d) 4-*tert*-butyl-calix[6]arene + BTF in dimethylformamide.

molecules were chosen for model studies. The structures of molecules investigated are shown in Fig. 1. Preliminary experiments indicated that nitro- and chloro-substitued benzotrifluorides (3-nitro-4-chloro-benzotrifluoride (**1**), 2-chloro-5-nitro-benzotrifluoride (**2**), 3,4,5-trichloro-benzotrifluoride (**3**), 2-chloro-benzotrifluoride (**4**), 3,5-dinitro-4-chloro-benzotrifluoride (**5**), 2,4-dichloro-benzotrifluoride (**6**), 4-chloro-benzotrifluoride (**7**)) interact with calix[4]arene and 4-*tert*-butyl-calix[6]arene according to photoluminescence spectra.

Fig. 2 shows the PL spectra of calix[4]arene and 4-*tert*-butyl-calix[6]arene dissolved in chloroform (a) and dimethylformamide (b) solvents using 280 nm for excitation. In the case of dimethylformamide solvent, the peaks of spectra are shifted to the longer wavelength by about 40 nm. The calix[4]arene shows the higher light emission in chloroform and 4-*tert*-butyl-calix[6]arene shows the higher emission in DMF. On the other hand, the intensity of the emitted light is higher in case at both molecules in DMF. Most likely the difference between the permittivities of the two solvents is responsible for the changes of the band shape of the spectra.

In order to investigate the effect of interaction of the different benzotrifluoride derivatives 1:1 calix-arene:benzotrifluoride solution of 10^{-4} M of the different species was prepared with the two different solvents and the PL spectra were recorded. Evaluating them it could be seen that the presence of the different benzotrifluorides induced some changes in the spectra. The shapes of the PL spectra of the mixtures were very similar to those of the PL spectra of the pure corresponding calixarene solution, however, significant changes of the intensities appeared in each cases. For certain benzotrifluorides, the intensity increased while in other cases it decreased. Since no light emission could be observed from 10^{-4} M solutions of the benzotrifluoride molecules using the same condition, it could be expected that the obtained spectral changes were induced by the changes of the optical properties of the calixarene species.

Fig. 3 shows the relative changes found in the PL intensity of calixarenes included by the effect of the different benzotrifluoride molecules studied. The relative change of PL intensity (ΔI_{rel}) shown in the bar graph were calculated by the following form:

$$\Delta I_{rel} = \frac{I_{mix} - I_{pure}}{I_{pure}}$$

where I_{mix} is the intensity maximum of the PL spectra of calixarene–benzotrifluoride mixture and I_{pure} is the intensity maximum of the spectra of pure calixarene solutions. The ΔI_{rel} values clearly indicate that the PL signal of the studied calixarenes is influenced by the molecular structures of benzotrifluoride derivatives being present. It also can be seen that the effect of uncharged benzotrifluoride molecules on the PL behaviour of calixarenes depends on the properties of the solvent.

The interaction between the calixarene and benzotrifluoride molecules proposed by PL studies, was examined by quantum-chemical method using the
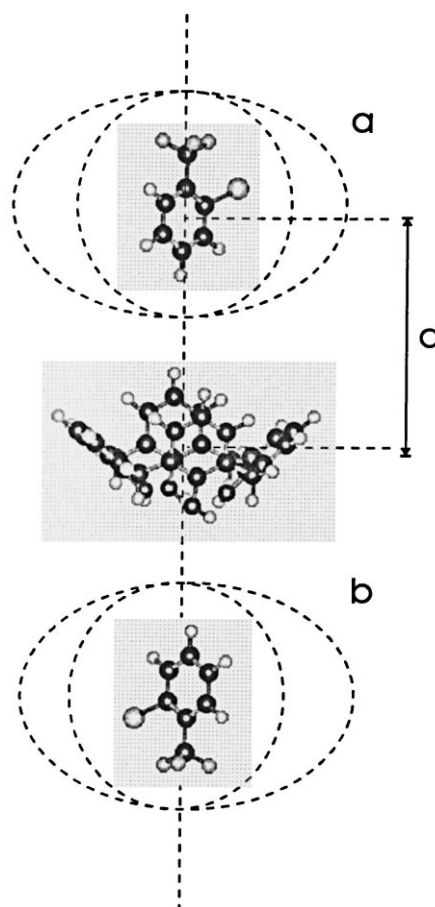

Fig. 4. The model for the calculation of interaction energy. *d* is the distance between the centres of gravity of the molecules.

HyperChem and Gaussian 94 packages. Doing so the interaction energy between the host calixarene and the guest benzotrifluoride molecules were calculated using the following procedure (for illustration see Fig. 4). The benzotrifluoride molecule was fixed with its centre of gravity on the symmetry axis C above (a) or below (b) of calixarene molecule, Fig. 4. Beginning from these initial conditions, the free rotation of benzotrifluoride molecules around its centre of gravity was allowed. In this model, the reaction path is given by the minimal total energy positions of the calixarene–benzotrifluoride system and it can be described by the distance between the centres of gravity of the two molecules. The total energies of the system are determined by *ab initio* calculations as mentioned above. When the stable conformation of calixarene–benzotrifluoride system found, full geometry optimisation were done for the complex and the total energy of the unforced state was used to determine the interaction energy E_{inter} using the following equation:

$$E_{inter} = E_{syst} - E_{tot,calix} - E_{tot,BTF}$$

where E_{syst} is the total energy of the calixarene–benzotrifluoride system, $E_{tot,\ calix}$ and $E_{tot,\ BTF}$ is the total energy of the separated calixarene and benzotrifluoride molecules, respectively.

Fig. 3 and Table 1 summarize the PL and quantum-chemical results. It can be seen clearly that the interaction energy (E_{inter}) shows negative values (indicating stable conformations) only in those cases when the relative change (ΔI_{rel}) in PL intensity are positive ($I_{mix} > I_{pure}$). The change in the PL intensity corresponds to the absolute value of the interaction energy. Model calculations did not find stable calixarene–benzotrifluoride complex for $I_{mix} > I_{pure}$ cases.

It turned out that calix[4]arene forms stable complexes with higher number of the BTF molecules studied in chloroform (**3**, **4**, **5** and **7**) than in dimethylformamide (**4**). It has been found also previously [18] that the solvent polarity has a great influence on the rate of conformational inversion and therefore on the predominating conformer under given conditions. In less polar solvents such as $CHCl_3$ the interconversion of the cone conformer was found very slow at low temperature. The hole of the cone conformer of calix[4]arene seems to be appropriate for the inclusion of benzotrifluorides of smaller sizes (**3**, **4**, **5**) with the exeption of **7**. We can postulate that in dimethylformamide the disruption of 'circular hydrogen bonding' takes place. This intramolecular hydrogen bonding at the 'low rim' is a contributing force in maintaining the calixarene in cone conformation. In the lack of the hydrogen bonding the aromatic rings become nearly

Table 1
The relative change (I_{rel}) in PL intensity of calixarene molecules in presence of benzotrifluoride derivatives and the interaction energy (E_{inter}) of calixarene–benzotrifluoride complexes

Calixarene	Benzotrifluoride	Chloroform solvent			Dimethylformamide solvent		
		Complex	ΔI_{rel}	E_{inter} (Ry)	Complex	ΔI_{rel}	E_{inter} (Ry)
Calix[4]rene	3-Nitro-4-chloro-BTF	No	−0.068390	>0	No	−0.034230	>0
	2-Chloro-5-nitro-BTF	No	−0.285670	>0	No	−0.171790	>0
	3,4,5-Trichloro-BTF	Yes	0.029294	−0.0145	No	−0.100320	>0
	2-Chloro-BTF	Yes	0.022640	−0.0112	Yes	0.013598	−0.0065
	3,5-Dinitro-4-chloro-BTF	Yes	0.004693	−0.0023	No	−0.119320	>0
	2,4-Dichloro-BTF	No	−0.013970	>0	No	−0.021720	>0
	4-Chloro-BTF	Yes	0.063336	−0.0316	No	−0.027970	>0
4-*Tert*-butyl-calix[6]arene	3-Nitro-4-chloro-BTF	No	−0.024840	>0	Yes	0.079852	−0.0391
	2-Chloro-5-nitro-BTF	No	−0.240240	>0	No	−0.018820	>0
	3,4,5-Trichloro-BTF	Yes	0.049012	−0.0251	Yes	0.120170	−0.0611
	2-Chloro-BTF	Yes	0.073883	−0.0361	Yes	0.145255	−0.0712
	3,5-Dinitro-4-chloro-BTF	No	−0.021500	>0	Yes	0.031662	−0.0161
	2,4-Dichloro-BTF	Yes	0.046391	−0.0231	Yes	0.155336	−0.0782
	4-Chloro-BTF	Yes	0.070868	−0.0352	Yes	0.143638	−0.0711

parallel, i.e. the size of the hole becomes smaller, and also the interconversion barrier decreases. As a consequence of that, the sterically more favoured **4** shows some effects only.

It is well-known from the temperature dependent NMR studies that 4-*tert*-butyl-calix[6]arene is more flexible than the cyclic tetramers even in less polar solvents [18]. Surprisingly, the same benzotrifluoride derivatives show interactions as in case of calix[4]-arene. Even more suprising is the fact, that practically all benzotrifluoride guest molecules seem to form inclusion complex with 4-*tert*-butyl-calix[6]arene in dimethylformamide. It validates that a 'plated loop' conformer must be stabilised by the interaction with the benzotrifluoride. Similarly, the interaction of phenolic OH groups with the solvent and the complexation of benzotrifluorides from the side of the 'upper rim' might result in a calixarene conformer which resembles much more to a basket-like hole than that obtained in $CHCl_3$.

4. Conclusion

The preliminary experimental results clearly indicate that the photoluminescence signal reflects the supramolecular host–guest interaction. It validates that calixarenes can be used as host molecules to gain sensor response detecting neutral substituted aromatics possessing electron-withdrawing groups (EWG). In the present stage, about 25% luminescence intensity change as signal has been observed. The high sensitivity of the luminescence detection can accurately measure relative intensity changes of this size. Further molecular engineering needed to develop practical sensors may result also in improved signal to noise ratio.

Acknowledgements

References

[1] P.L.H.M. Cobben, R.J.M. Egbernik, J.G. Bomer, P. Bergveld, W. Verboom, D.N. Reinhoudt, J. Am. Chem. Soc. 114 (1992) 10573.
[2] D.N. Reinhoudt, Sens. Actuators B 6 (1992) 179.
[3] J.-C. Bunzli, J.A. Harrowfield, in: J. Vicens, V. Bohmer (Eds.), Calixarenes: A Versatile Class of Macrocyclic Compounds, Kluwer, Boston, 1991.
[4] P. Munk, L.J. Feltl, Chromatography A 696 (1) (1995) 101.
[5] D. Shohat, E. Grushka, Anal. Chem. 66 (1994) 747.
[6] A. Cadogan, D. Diamond, M.R. Smyth, G. Svehla, M.A. McKervey, E.M. Seward, S.J. Harris, Analyst 115 (9) (1990) 1207.
[7] K. Kimura, T. Miura, M. Matsuo, T. Shono, Anal. Chem. 62 (14) (1990) 1510.
[8] K. Kimura, T. Matsuba, Y. Tsujimura, M. Yokoyama, Anal. Chem. 64 (1992) 2508.
[9] A. Gao, Z.Q. Cadogan, A. Lewenstam, A. Ivaska, D. Diamond, Anal. Chem. 64 (1992) 2496.
[10] K. Odashima, K. Yagi, K. Tahda, Y. Umezava, Anal. Chem. 65 (1993) 1074.
[11] K.M. O'Connor, D.W.M. Arrigan, G. Svehla, Electroanalysis 7 (1995) 205.
[12] Y. Kawabota, T. Mashiro, Y. Kitazaki, T. Imasaka, Sens. Actuators B B29 (1995) 135.
[13] M. Carrick, S.J. Harris, D. Diamond, Analyst 118 (9) (1993) 1127.
[14] W.H. Chan, A.W. Lee, D.W. Kwong, W.L. Tam, K.M. Wang, Analyst 121 (4) (1996) 531.
[15] B.M. Lynch, M.M. Ryan, B.S. Creaven, G. Barrett, M.A. McKervey, S.J. Harris, Anal. Proc. (London) 30 (1993) 150.
[16] K.D. Schierbaum, A. Gerlach, W. Goepel, W.M. Mueller, F. Voegtle, A. Dominik, H.J. Roth, Fresenius' J. Anal. Chem. 349 (1994) 372.
[17] E. Wegler, Chemie der Pflanzenschutz und Schädlingsbekämpfungsmittel, Band 5, Springer, Berlin, Heidelberg, New York, 1977, Pages 73–80 and 401–407.
[18] C.D. Gutsche, in: J.F. Stoddart (Ed.), Calixarenes: Monographs in Supramolecular Chemistry, Royal Society of Chemistry, Cambridge, 1989, pp. 90–97.

Coordination of Methanol Clusters to Benzene: A Computational Study

Gergely Matisz,[†,‡] Anne-Marie Kelterer,[§] Walter M. F. Fabian,[‡] and Sándor Kunsági-Máté[*,†]

[†]Department of General and Physical Chemistry, University of Pécs, Pécs, H-7624, Hungary

[‡]Institute of Chemistry, Karl-Franzens University Graz, Heinrichstr. 28, Graz, A-8010, Austria

[§]Institute of Physical and Theoretical Chemistry, Graz University of Technology, Stremayrgasse 9/I, A-8010 Graz, Austria

Ⓢ *Supporting Information*

ABSTRACT: Benzene—methanol cluster structures were investigated with theoretical chemistry methods to describe the microsolvation of benzene and the benzene-methanol azeotrope. Benzene—methanol (MeOH) clusters containing up to six methanol molecules have been calculated by ab initio [MP2/6-311++G(d,p)//MP2/6-31+G(d,p) + BSSE correction] method. The BSSE was found quite large with this basis set, hence, different extrapolation schemes in combination with the aug-cc-pVxZ basis sets have been used to estimate the complete basis set limit of the MP2 interaction energy [ΔE(MP2/CBS)]. For smaller clusters, n

$C_6H_6(MeOH)_n$ $C_6H_6 + (MeOH)_n$ 2:3 azeotrope

≤ 3, DFT procedures (DFTB+, MPWB1K, M06-2X) have also been applied. Geometries obtained for these clusters by M06-2X and MP2 calculations are quite similar. Based on the MP2/CBS results, the most stable $C_6H_6(MeOH)_3$ cluster is characterized by a hydrogen bonded MeOH trimer chain interacting with benzene via $\pi\cdots$H—O and O$\cdots$H—C(benzene) hydrogen bonds. Larger benzene—MeOH clusters with $n \geq 4$ consist of cyclic $(MeOH)_n$ subclusters interacting with benzene by dispersive forces, to be denoted by $C_6H_6 + (MeOH)_n$. Interaction energies and cooperativity effects are discussed in comparison with methanol clusters. Besides MP2/CBS calculations, for selected larger clusters the M06-2X/6-311++G(d,p)//M06-2X/6-31+G(d,p) procedure including the BSSE correction was also used. Interaction energies obtained thereby are usually close to the MP2/CBS limit. To model the benzene—MeOH azeotrope, several structures for $(C_6H_6)_2(MeOH)_3$ clusters have been calculated. The most stable structures contain a tilted T-shaped benzene dimer interacting by $\pi\cdots$H—O and O$\cdots$H—C (benzene) hydrogen bonds with a $(MeOH)_3$ chain. A slightly less negative interaction energy results for a parallel displaced benzene sandwich dimer with a $(MeOH)_3$ chain atop of one of the benzene molecules.
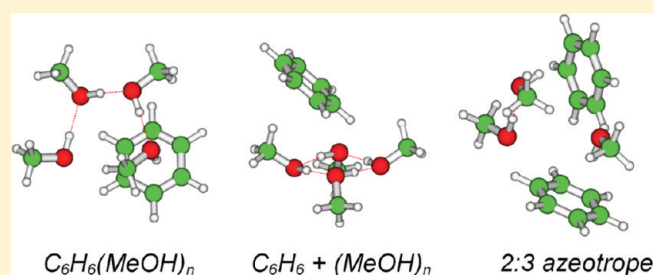
■ INTRODUCTION

The structures and energetics of weakly bound complexes between π-systems and solvents capable of forming hydrogen bonds have attracted much interest.[1-3] Water and alcohols as prototypes for such solvents themselves are known to form clusters of various sizes and structures. For instance, Pauling has proposed that liquid methanol mainly is composed of cyclic hexamers.[4] The very existence of such clusters forms the basis for the description of thermodynamic properties of the liquid phase by the quantum cluster equilibrium model (QCE).[5-12] Even interaction of nonfunctionalized aromatic molecules with alcohols or their clusters can induce significant changes in their hydrogen bond topology.[3] Besides the O—H···O hydrogen bond present in water or alcohol clusters, weak nonconventional O—H···π, C—H···π, and C—H···O hydrogen bonds have been identified as important in molecular recognition, supramolecular chemistry, the 3D-structure of biological macromolecules, and for clusters of aromatic molecules microsolvated by water or alcohols.[13-15] In view of the importance of such weak interactions, a number of experimental and computational studies on clusters between aromatic molecules and water[16-23] or alcohols,

mostly methanol,[24-34] have been published. In addition to clusters of the type Ar(H$_2$O)$_n$ or Ar(MeOH)$_n$, ternary benzene—(H$_2$O)$_n$—(MeOH)$_m$[35,36] and (benzene)$_2$—(MeOH)$_3$ clusters[33] have been investigated. The molecular formula of these latter clusters formally corresponds to the composition of the benzene—methanol azeotrope for which recently a unit structure $[(C_6H_6)_2]_4[(MeOH)_4]_3$ has been proposed.[28] Finally, preferential solvation of anthracene in binary alcoholic solutions has been investigated.[37]

Calculations on benzene — methanol complexes C_6H_6-(MeOH)$_n$, $n \leq 3$, mostly have been done by density functional theory;[25,38] larger systems were treated by Monte Carlo simulations using the OPLS force field [e.g., $C_6H_6(MeOH)_4$][39] or semiempirical (PM3) methods [e.g., $(C_6H_6)_2(MeOH)_3$].[33] Second order Møller—Plesset calculations are available for fluorobenzene—(MeOH)$_n$, $n = 1,2$ and p-difluorobenzene—MeOH.[24] Although strong hydrogen bonds usually are
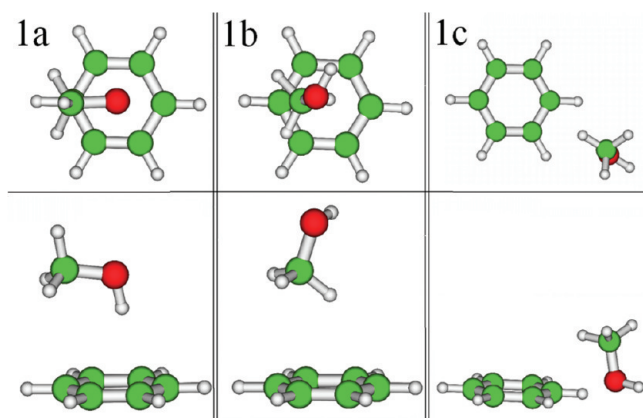
Figure 1. M06-2X/6-31+G(d,p) optimized structures of C_6H_6-$(MeOH)_1$ showing $O-H\cdots\pi$ (**1a**), $C-H\cdots\pi$ (**1b**), and $O\cdots H-C$-(benzene) (**1c**) hydrogen bonds.

reasonably well described by the more popular density functionals,[40] questionable results might be obtained for $C-H\cdots O$ or $C-H\cdots\pi$ interactions.[41−43] In view of the importance of clusters between aromatic molecules and alcohols as models for microsolvation, we found it worthwhile to investigate computationally larger benzene−methanol clusters $C_6H_6(MeOH)_n$ than done previously, up to $n = 6$. Moreover, different theoretical levels, tight-binding DFT and DFT using various functionals as well as ab initio procedures (MP2), have been applied. Finally, complexes of the type $[(C_6H_6)_2(MeOH)_3]$, corresponding to the molar composition of the benzene−methanol azeotrope have been treated. These clusters are described with regard to structure, interaction energy and cooperativity effect in this work.

■ COMPUTATIONAL DETAILS

The initial structures for benzene−methanol complexes $C_6H_6(MeOH)_n$, $n = 1−3$, were generated by packing optimization.[44] In each case, 2000 structures resulted from placing the methanol molecules randomly within a sphere with $r = 10$ Å and one benzene at the center of that sphere. These randomly generated structures were then first optimized by the self-consistent charge tight-binding density functional method[45] with inclusion of dispersion corrections (SCC-DFTB+).[46] Further optimization was done by density functionals developed for the correct description of weak intermolecular interactions (MPWB1K[47] and M06-2X[48,49]) and ab initio methods (MP2[50] in the frozen core approximation) using the 6-31+G(d,p) basis set. Based on the results for these species, larger clusters $C_6H_6(MeOH)_n$, $n = 2−6$, were constructed from $C_6H_6(MeOH)_1$ by successively adding methanol molecules according to the methanol dimer geometry, $r(O\cdots H) = 1.8895$ Å, $\alpha(C-O\cdots H) = 110.3$[51] and subsequent optimization. In these clusters, thereafter denoted by $C_6H_6(MeOH)_n$, interaction between the benzene ring and the methanol molecules occurs via $O-H\cdots\pi$ and (benzene)-$C-H\cdots O$ hydrogen bonding. In other words, cyclic structures comprised of methanol molecules connected by $O-H\cdots O$ hydrogen bonds and the aromatic ring, that is, rings consisting of $\pi(\text{benzene})\cdots H-O\cdots(H-O)_{n-1}\cdots H-C$ (benzene) hydrogen bonds, are formed. A second type of structures, thereafter denoted by $C_6H_6 + (MeOH)_n$ consists of a benzene molecule placed above cyclic $(MeOH)_n$ subclusters obtained previously by MP2/6-31+G(d,p) optimizations.[51] BSSE-corrected[52] interaction

energies for these clusters were obtained by MP2/6-311++ G(d,p)//MP2/6-31+G(d,p) calculations. The complete basis set (CBS) limit has been evaluated using Martin's extrapolation scheme,[53] originally proposed for CCSD(T) energies, combined with the aug-cc-pVxZ ($x = 2−4$) basis sets,[54] eq 1 (N corresponds to x in the aug-cc-pVxZ basis sets).

$$E_{corr}(N) = A + B/(N + 1/2)^4$$
$$+ C/(N + 1/2)^6 \qquad (1)$$

The term for $N = 5$ has been reported to be rather small,[53,54b] hence, we have restricted the calculations to $N \leq 4$. For a number of weakly interacting systems, including the benzene dimer and the hydrogen bonded benzene−water cluster, it has been shown that an analogous CBS extrapolation scheme can also be used for the MP2 procedure.[55] These authors also proposed a modified formulation of the CBS limit for small basis sets ($N = 2, 3$), eq 2

$$E_{CBS,N} = [E_N(N + 1/2)^3 - E_{N-1}(N - 1/2)^3]/$$
$$[(N + 1/2)^3 - (N - 1/2)^3] \qquad (2)$$

Alternatively, eq 3, where x is the largest angular momentum of the given basis set, has been proposed[56] to estimate the MP2 CBS limit.

$$E(MP2, CBS) = E(MP2, x) + \text{constant} \times x^{-3} \qquad (3)$$

Here we used each one of these schemes.

Programs used were Packmol,[57] DFTB+,[58] GAMESS-US 2009 R3,[59] Gaussian 09,[60] NWChem 6.0,[61] Hyperchem 7.0,[62] and MOLDEN[63] for visualization.

■ RESULTS AND DISCUSSION

First we will describe structural features obtained by various computational procedures (tight-binding DFT, DFT, and MP2) for $C_6H_6(MeOH)_n$, $n = 1−3$, clusters. The corresponding interaction energies (DFTB+, MPWB1K, M06-2X, and MP2) are given in Table S1. In the second section, the energetics obtained by MP2 calculations for benzene−methanol clusters up to six methanol molecules will be discussed. In section three, results for $[(C_6H_6)_2(MeOH)_3]$ clusters will be presented.

Structural Features. For the first member of this series, $C_6H_6(MeOH)_1$, in principle, three types of noncovalent interaction, namely, $O-H\cdots\pi$ (**1a**), $C-H\cdots\pi$ (**1b**), and (benzene)$C-H\cdots O$ (**1c**) hydrogen bonding, Figure 1, are possible. Pribble et al.[38] have performed B3LYP/6-31+G(d) calculations on $C_6H_6(MeOH)_1$ showing the $O-H\cdots\pi$ type of interaction. In their calculated structure, the methanol molecule was pulled off the 6-fold axis of benzene. Our DFTB+ calculations result in a similar structure for **1a** with $O-H$ binding to a carbon atom rather than to the center of the aromatic ring. No complex of type **1b**, that is, $C-H\cdots\pi$ interaction was found by MP2 optimizations; instead, this structure collapsed to **1a**. In the case of (benzene)$C-H\cdots O$ hydrogen bonding, both DFTB+ and MPWB1K calculations resulted in structures with one such interaction; in contrast, M06-2X and MP2 yielded a largely symmetric structure **1c** with two (benzene)$C-H\cdots O$ hydrogen bonds with $r(H\cdots O) = 2.51$ Å (M06-2X) and $r(H\cdots O) = 2.67$ Å (MP2). The oxygen atom of the methanol molecules lies approximately in the plane of the benzene ring (Figure 1c). In larger clusters, $n = 2$ and 3, slight deviations from
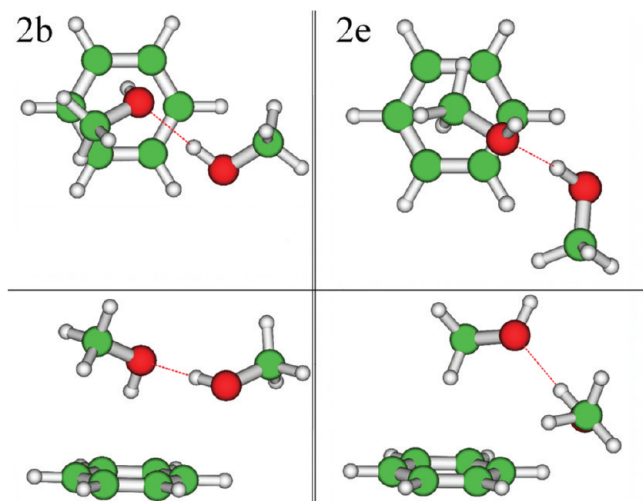
10557

dx.doi.org/10.1021/jp206248w |*J. Phys. Chem. A* 2011, 115, 10556−10564

Figure 2. MP2/6-31+G(d,p) optimized structures of $C_6H_6(MeOH)_2$.

Figure 3. MP2/6-31+G(d,p) optimized structures of $C_6H_6(MeOH)_3$.

this symmetric C—H···O hydrogen bonding occurred. Moreover, the methanol involved in this type of hydrogen bond is pulled off the benzene plane (see Figure 2 for $n = 2$ and Figure 3 for $n = 3$).

Irrespective of the computational procedure used, structure **1a**, characterized by a O—H···π hydrogen bond, is the most stable cluster. Experimentally, formation of such a $C_6H_6(MeOH)_1$ involving interaction between the OH group of methanol and the π-system of benzene had been inferred from the observed red shift of the OH stretching vibration of $\Delta\nu = -43$ cm^{-1} compared with free methanol,[38] much smaller than that resulting from O—H···O hydrogen bonds ($\Delta\nu = -107$ cm^{-1} in the gas phase methanol dimer[64]) but still significant. Calculated shifts are close to this experimental value: $\Delta\nu = -33$ cm^{-1} (B3LYP[38]), -10 cm^{-1} [MP2/6-31+G(d)],[24] and -24 cm^{-1} [MP2/6-31+G(d,p)].

For $C_6H_6(MeOH)_2$ two main types, for example, **2b** and **2e** in Figure 2, can be distinguished at the MP2 level. The first type is characterized by a π···H—O···H—O···H—C(benzene), the second one by a π···H—CO···H—O···H—C(benzene) hydrogen bonding pattern; the notation *type 1* and *type 2* will be used in the following. Common to the lower energy clusters is formation of cyclic structures with participation of the benzene ring. Similar to $C_6H_6(MeOH)_1$ (**1c**), in the $C_6H_6(MeOH)_2$ clusters only one O···H—C(benzene) hydrogen bond is obtained by DFTB+ and MPWB1K. In contrast, nearly symmetric hydrogen bonds between the methanol oxygen and two benzene hydrogens result for **2b** with M06-2X [$r(CH···O) = 2.78$ and 2.84 Å] and MP2 [$r(CH···O) = 2.92$ and 2.95 Å]. Again, a shift of one methanol away from the center of the benzene ring toward a carbon atom in *type 1* complexes is found by DFTB+ calculations. Clusters of the *type 1*, that is, those involving a π···H—O hydrogen bond are more stable than clusters of *type 2*. The observed increased red shift of the OH stretching frequency, $\Delta\nu = -76$ cm^{-1} for π···H—O, and $\Delta\nu = -175$ cm^{-1} for O···H—O hydrogen bonds has been attributed to a cooperative strengthening of both hydrogen bonds.[38] Calculations also reveal this effect, $\Delta\nu = -57$ cm^{-1} (B3LYP[38]) and $\Delta\nu = -72$ cm^{-1} [MP2/6-31+G(d,p)] for π···H—O; $\Delta\nu = -189$ cm^{-1} (B3LYP[38]) and $\Delta\nu = -207$ cm^{-1} [MP2/6-31+G(d,p)] for O···H—O hydrogen bonds.

Similar to $C_6H_6(MeOH)_2$ clusters, two types (*type 1* or *type 2*) of structures containing either a π···H—O···H—O···H—O···H(benzene) or a π···H—C···H—O···H—O···
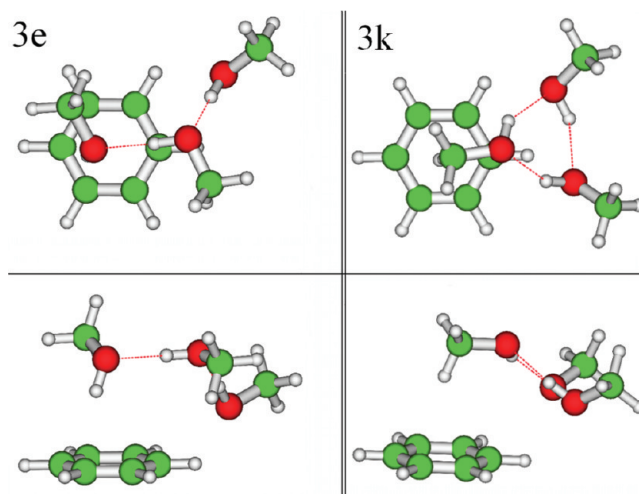
H—C(benzene) hydrogen bonding pattern, were found for $C_6H_6(MeOH)_3$, see **3e** and **3k** in Figure 3. At the MP2 level *type 1* structure **3e** is the most stable one. M06-2X calculations yield *type 2* structure **3c** as the lowest energy cluster. The lowest *type 2* MP2 structure **3k** actually corresponds to a cyclic $(MeOH)_3$ subcluster weakly interacting with benzene, that is, a cluster of the type benzene + $(MeOH)_3$ (see below). In both *type 1* and *type 2* series, two benzene hydrogens form an approximately symmetric hydrogen bond to the oxygen atom of methanol. For instance, in **3e** MP2/6-31+G(d,p) calculations yield $r(CH···O) = 2.64$ and 2.54 Å. The experimental shift, $\Delta\nu = -5$ cm^{-1}, of the benzene C—H stretches observed in C_6H_6-$(MeOH)_3$ has been attributed to the interaction between the terminal methanol of the $(MeOH)_3$ chain with the C—H bonds of benzene.[25] In our calculations, a shift of -9 cm^{-1} has been found for conformer **3e**.

Addition of the third methanol molecule results in an even further strengthening of the π···H—O and the O···H—O hydrogen bonds, as evidenced by the respective experimental (-92, -246, and -292 cm^{-1})[38] and MP2/6-31+G(d,p) calculated frequency shifts, $\Delta\nu = -84$, -277, and -341 cm^{-1} in **3e**.

In the free methanol trimer, a cyclic arrangement of the methanol molecules has been observed experimentally with a single OH stretch band red-shifted by 219 cm^{-1} with respect to the methanol monomer.[64] In contrast, experiments clearly show that the $C_6H_6(MeOH)_3$ cluster contains a linear arrangement of the three methanol molecules;[38] a cyclic structure results only by participation of the benzene ring. Interestingly, larger benzene—methanol clusters, $C_6H_6(MeOH)_n$, $n \geq 4$, apparently consist of the benzene molecule interacting with cyclic methanol subclusters $(MeOH)_n$ because only red shifts of the OH stretch characteristics for strong O—H···O hydrogen bonds could be observed.[38] So far structural features of the $C_6H_6 + (MeOH)_n$ clusters with $n \geq 4$ have only be described on the basis of force field calculations.[39] For instance, for $C_6H_6 + (MeOH)_4$ mainly interaction of one methyl group of the cyclic $(MeOH)_4$ subcluster on a single side of benzene had been predicted. Later, alternative structures with benzene interacting edge-on with the $(MeOH)_n$ cavity, were proposed.[38] In the following, both possibilities for benzene—methanol clusters with $n = 3 - 6$, namely, those characterized by π···H—O···[H—O]$_{n-1}$···H—C(benzene) hydrogen bonds ($C_6H_6(MeOH)_n$, **3e** and **4a**—**6a** in Figure 4), as
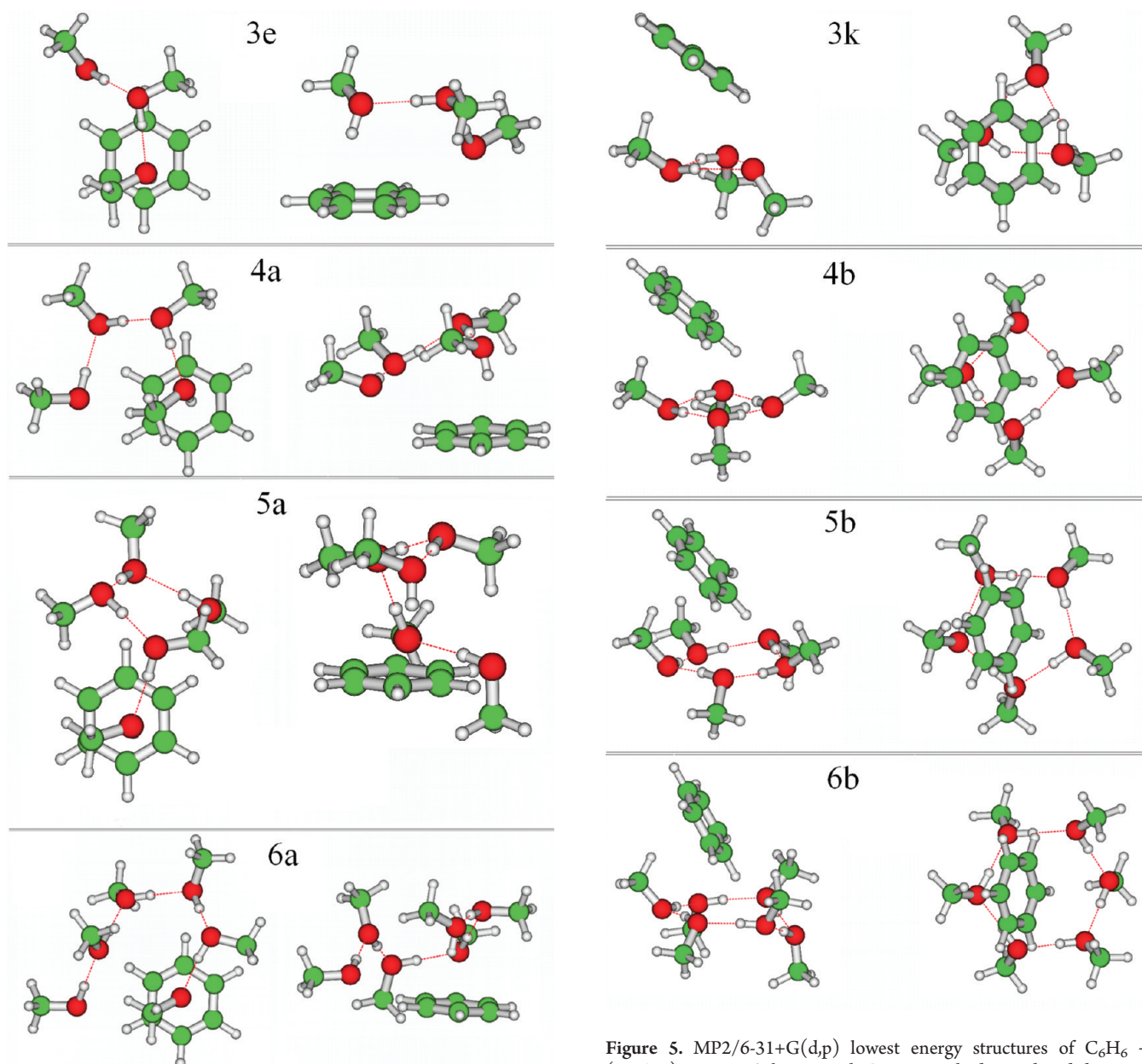
Figure 4. MP2/6-31+G(d,p) lowest energy structures of $C_6H_6(MeOH)_n$, $n = 3-6$ clusters with $O-H\cdots\pi$ hydrogen bonds (**3e**, **4a**–**6a**).

Figure 5. MP2/6-31+G(d,p) lowest energy structures of C_6H_6 + $(MeOH)_n$, $n = 3-6$ clusters with $C-H\cdots\pi$ hydrogen bonds between benzene and $(MeOH)_n$ subclusters (**3k**, **4b**–**6b**).

well as clusters consisting of one benzene molecule interacting with $(MeOH)_n$ subclusters (C_6H_6 + $(MeOH)_n$, **3k** and **4b**–**6b** in Figure 5), will be discussed. In **4a**, the OH group of the first methanol molecule in the $(MeOH)_4$ chain is shifted off the center of the benzene ring toward one carbon atom $[r(C\cdots HO) = 2.44$ Å]; the benzene $C-H$ in *para* position to this carbon atom makes a close contact to the third methanol molecule $[r(C-H\cdots O)] = 2.53$ Å. The distance of the fourth MeOH to the adjacent benzene $C-H$ bond is 2.67 Å. According to the MP2 calculations, in the C_6H_6 + $(MeOH)_n$ species the structure of the cyclic methanol subclusters is largely unchanged compared with the corresponding free $(MeOH)_n$ rings. Interaction with the benzene molecule occurs via a (methanol) $C-H\cdots\pi$ dispersive bond on one side of benzene. The benzene ring is tilted with respect to the normal to the $(MeOH)_n$ plane, pointing

with one single $C-H$ bond toward it, Figure 5. For instance, in **4b**, one of the $C-H$ bonds of the methanol methyl groups is nearly symmetrically placed atop the benzene ring; the distances to the six benzene carbon atoms are in the range 2.83–2.98 Å. The closest benzene $C-H\cdots O$ distance is 2.52 Å.

Energetic Aspects of $C_6H_6(MeOH)_n$ and C_6H_6 + $(MeOH)_n$ Clusters. The following discussion of the energetic aspects of these clusters is largely based on the MP2/6-31+G(d,p) structures of these $C_6H_6(MeOH)_n$, $n = 1-6$, and C_6H_6 + $(MeOH)_n$, $n \geq 3$ clusters. Energies were calculated by M06-2X and MP2 using the 6-311++G(d,p) basis set. In addition, MP2 calculations were also performed with the aug-cc-pVxZ basis set, with $x = 2-4$ for $n \leq 3$ and $2-3$ for $n = 4-6$ and extrapolated to the CBS limit. Unless very large basis sets are used, for example, aug-cc-pV5Z, correcting for basis set superposition error is essential. Hence, this correction has been applied to all the calculated interaction energies. The corresponding BSSE-corrected

Table 1. M06-2X/6-311++G(d,p), and MP2 Calculated Interaction Energies Including BSSE Corrections and Different CBS Extrapolation Schemes

	M06-2X	MP2							
			aug-cc-pVNZ			I^a	II^b		III^c
$E_{WW+BSSE}$	6-311++G(d,p)	6-311++G(d,p)	N = 2	N = 3	N = 4	N = 2−4	N = 3	N = 4	N = 2−4
water−benzene	−16.5	−10.3	−12.7	−14.1	−14.5	−14.7	−14.9	−14.8	−14.7
1a	−19.0	−12.8	−16.7	−18.8	−19.3	−19.6	−19.9	−19.8	−19.6
1c	−12.1	−7.9	−10.0	−10.9	−11.2	−11.4	−11.4	−11.5	−11.3
2b	−53.5	−40.2	−47.6	−51.7	−53.1	−54.0	−54.0	−54.3	−53.7
2e	−39.8	−33.9	−39.3	−42.6	−43.9	−44.7	−44.5	−44.7	−44.3
3e	−97.6	−74.5	−85.7	−92.7	−95.1	−96.7	−96.8	−97.2	−96.2
3k	−99.2	−73.8	−83.8	−90.5	−92.9	−94.7	−94.4	−95.1	−93.9
4a	−137.0	−107.5	−122.8	−132.7			−138.4		
4b	−150.4	−119.5	−134.9	−145.6			−151.8		
5a	−175.1	−138.7	−157.8	−170.5			−177.8		
5b	−195.9	−157.4	−177.4	−191.6			−199.7		
6a	−221.3	−175.7	−197.1	−212.8			−221.8		
6b	−236.0	−192.6	−214.9	−231.7			−241.4		
7a		−92.0	−108.8	−118.0			−123.3		
7d		−89.5	−106.0	−114.7			−119.3		

[a] CBS extrapolation using eq 1. [b] CBS extrapolation using eq 2 with N = 3 and N = 4. [c] CBS extrapolation using eq 3.

interaction energies obtained by M06-2X/6-311++G(d,p), MP2/6-311++G(d,p), as well as MP2/CBS calculations, are given in Table 1. The BSSE corrections to MP2/6-311++G(d,p) results are quite large resulting in a significant reduction of the interaction energies. Previous MP2/6-31+G(d,p) studies[24,65] of benzene containing clusters have indicated an underestimation of interaction energies when BSSE corrections were used. This apparently is also the case when using the 6-311++G(d,p) basis set. Weak O−H···π hydrogen bonding interactions have been thoroughly studied computationally in the benzene−water cluster, including a comparison between MP2 and CCSD(T) BSSE corrections to interaction energies.[55,66−69] These calculations will serve as benchmark for evaluation of the procedures used here (Table 1). Depending on the geometry and extrapolation scheme used MP2/CBS values between −16.3 to −14.5 kJ mol^{-1} have been reported; CCSD(T)/CBS benzene−H$_2$O interaction energies are −14.0[55] and −13.7[70] kJ mol^{-1}. Dispersion corrected DFT (B3LYP-DCP/6-31+G(d,p))[66] and M06-2X calculations[69] yielded −13.4 and −14.2 kJ mol^{-1}, respectively. Compared with these data, our M06-2X and MP2 interaction energies obtained with the 6-311++G(d,p) basis set are slightly over- and underestimated (−16.5 and −10.3 kJ mol^{-1}, Table 1). The MP2/CBS benzene − H$_2$O interaction energies, −14.7 to −14.9 kJ mol^{-1} (Table 1) are in good agreement with those discussed above. Moreover, the different extrapolation schemes, eqs 1−3, yield nearly identical results. Most importantly, MP2/CBS interaction energies obtained by eq 2 with N = 3, that is, the aug-cc-pVDZ and aug-cc-pVTZ basis sets, only marginally differ from those using N = 4, that is, the aug-cc-pVTZ and aug-cc-pVQZ basis sets. Hence, we expect that the MP2/CBS interaction energies for the larger clusters where aug-cc-pVQZ calculations were not feasible, can be estimated with sufficient accuracy by eq 2 with N = 3.

Similar results also hold for the benzene−methanol clusters. Especially, MP2/6-311++G(d,p) calculations significantly underestimate interaction energies. MP2/CBS results are quite insensitive to the extrapolation scheme used. When applying Martin's extrapolation scheme, eq 1, for BSSE-corrected, as well as uncorrected interaction energies the BSSE error in the CBS limit is below 2%; eq 2 with N = 3 results in an error of only ∼5%. Hence, for the following discussion MP2/CBS interaction energies resulting from eq 2 with N = 3 will be used because MP2/aug-cc-pVQZ calculations were not feasible for the larger clusters. Treating electron correlation at a higher level [MP4, CCSD(T) aug-cc-pVDZ basis set] yields interaction energies for **1a** of ΔE_{int} = −15.7 (MP4) and −14.4 [CCSD(T)] kJ mol^{-1}; for **1c** of ΔE_{int} = −14.4 (MP4) and −9.0 [CCSD(T)] kJ mol^{-1}.

M06-2X/6-311++G(d,p) generally yields results closer to the MP2/CBS limit than MP2/6-311++G(d,p) calculations (Table 1). The mean M06-2X BSSE error compared to the uncorrected values is ∼13% and the BSSE-corrected M06-2X results are within 1.5 kJ mol^{-1} of the MP2/CBS limit obtained by eq 2, N = 3. However, as already seen in C$_6$H$_6$(MeOH)$_1$ clusters (cf. **1a** with **1b**), the M06-2X functional apparently overestimates the stability of the C−H···π interaction compared to MP2 (cf. **3e** with **3k**). Hence, for **3k** a larger difference M06-2X versus MP2/CBS of ∼5 kJ mol^{-1} is found (Table 1). Previous extensive calculations on uracil dimers are in line with this finding. Using CCSD(T)/CBS results as reference, the stability of stacked dimers was slightly overestimated compared with hydrogen-bonded structures.[71] For the clusters containing three methanol molecules (n = 3) both C$_6$H$_6$(MeOH)$_3$ and C$_6$H$_6$ + (MeOH)$_3$ have comparable interaction energies with a slight preference for the former structure involving π···H−O and O···H−C-(benzene) hydrogen bonds, ΔE_{int} = −96.8 versus −94.4 kJ mol^{-1}. For larger clusters, n ≥ 4, structures resulting from interaction of benzene with cyclic methanol n-mers (MeOH)$_n$, **4b−6b**, clearly are more stable than their C$_6$H$_6$(MeOH)$_n$ counterparts **4a−6a** (Figure 6).

The magnitude of the O−H stretch frequency shifts have been interpreted in terms of significant cooperative strengthening of
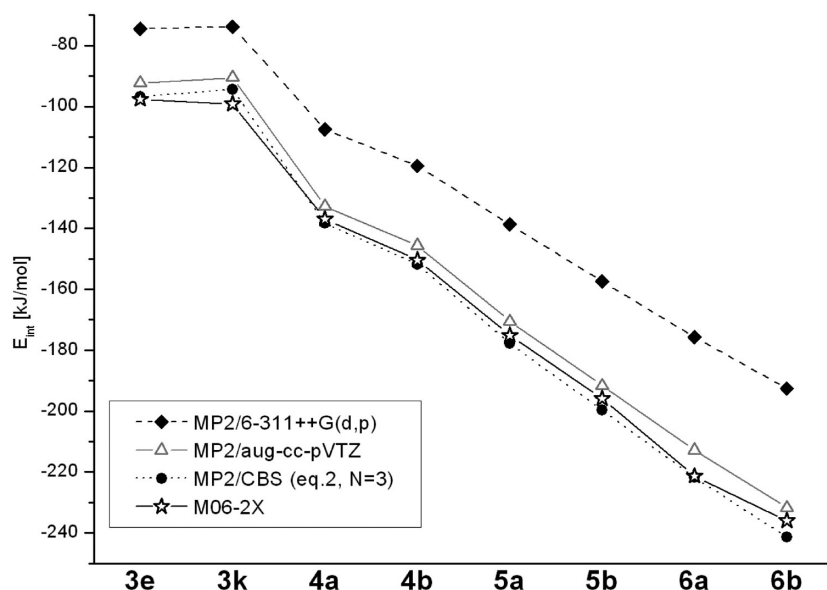
Figure 6. BSSE-corrected interaction energies (MP2/6-311++G(d,p), M06-2X/6-311++G(d,p), MP2/CBS (eq 2, N = 3)) for $C_6H_6(MeOH)_n$, n = 3−6 clusters with O−H···π hydrogen bonds (**3e**, **4a**−**6a**) and C_6H_6 + $(MeOH)_n$, n = 3−6 clusters with C−H···π hydrogen bonds between benzene and $(MeOH)_n$ subclusters (**3k**, **4b**−**6b**).

Table 2. BSSE-Corrected Cooperativity Energy per Hydrogen Bond, ΔE_{coop}/Hydrogen Bond (kJ mol^{-1})

MeOH$_n$	ΔE_{coop}/hydrogen bond			$C_6H_6(MeOH)_n$	ΔE_{coop}/hydrogen bond		
N	I^a	II^b	III^c	n	I^a	II^b	III^c
2	0.0	0.0	0.0	2	0.3	0.4	0.4
3	0.1	−0.1	−0.3	3	−3.3	−4.3	−4.5
4	−6.1	−7.9	−8.1	4	−5.3		−7.1
5	−7.8	−9.9	−9.5	5	−6.2		−8.6
6	−8.9	−11.0	−11.3	6	−7.6		−10.2

^{a} MP2(fc)/6-311++G(d,p). ^{b} MP2/CBS, eq 1. ^{c} MP2/CBS, eq 2, N = 3.

the π···H−O and O···H−O bonds in $C_6H_6(MeOH)_2$ compared with those in $C_6H_6(MeOH)_1$ and $(MeOH)_2$. In the following, the cooperativity on interaction energies of cyclic $(MeOH)_n$ n-mers[51] and $C_6H_6(MeOH)_n$ clusters of the π···H−O···[H−O]$_{n-1}$···H−C(benzene) type, ΔE_{coop}, will be discussed. The BSSE-corrected interaction energy of the methanol dimer is ΔE_{int} = −20.3 [MP2/6-311++G(d,p)][51], −24.2 (MP2/CBS, eq 1), and −23.8 kJ mol^{-1} (MP2/CBS, eq 2, N = 3). Cyclic $(MeOH)_n$ n-mers contain n O−H···O hydrogen bonds, thus, ΔE_{coop} = $\Delta E_{int}[(MeOH)_n]$ − n × $\Delta E_{int}[(MeOH)_2]$. In $C_6H_6(MeOH)_n$ clusters in addition to n − 1 H−O···H hydrogen bonds, one π···H−O and one O···H−C(benzene) interaction occur. Exactly one of these interactions is present in **1a** (π···H−O) and **1c** [O···H−C(benzene)]. Thus, for all presented clusters ΔE_{coop} is given by ΔE_{coop} = $\Delta E_{int}[C_6H_6(MeOH)_n]$ − $(n-1)$ × $\Delta E_{int}[(MeOH)_2]$ − ΔE_{int}(**1a**) − ΔE_{int}(**1c**). The MP2/6-311++G(d,p) BSSE-corrected interaction energies for these two nonconventional hydrogen bonds in $C_6H_6(MeOH)_1$ are −12.8 (**1a**) and −7.9 (**1c**) kJ mol^{-1}; the corresponding MP2/CBS values are −19.6 and −11.4 kJ mol^{-1} (eq 1); and −19.9 and −11.4 kJ mol^{-1} (eq 2, N = 3), Table 1. The cooperativity per hydrogen bond,

ΔE_{coop}/hydrogen bond is larger (more negative) in the C_6H_6-$(MeOH)_3$ cluster than in $(MeOH)_3$, Table 2. In contrast, for $n \geq 4$ the cyclic methanol n-mers have stronger cooperativity, because ΔE_{coop}/H-bond is larger (more negative) than in the $C_6H_6(MeOH)_n$ clusters. Thus, for $n \geq 4$ clusters of the type C_6H_6 + $(MeOH)_n$ will be preferentially formed. Despite the increased red shift of both OH stretching frequencies in C_6H_6-$(MeOH)_2$ (see above), the value of ΔE_{coop}/hydrogen bond does not indicate any cooperativity in forming this structure. Most probably, this discrepancy between conclusions inferred from ΔE_{coop}/hydrogen bond versus $\Delta \nu$ is due to the distortion from the optimal geometry for O···H−C(benzene) hydrogen bonding. Whereas in $C_6H_6(MeOH)_1$ (**1c** in Figure 1) the oxygen atom of the methanol molecule lies in the plane of the benzene ring, the methanol molecule interacting with the benzene C−H bonds in $C_6H_6(MeOH)_2$ is significantly pulled off this plane (**2b** in Figure 2).

[(C$_6$H$_6$)$_2$(MeOH)$_3$] Clusters. By a combination of resonant two-photon ionization, resonant ion-dip infrared and IR-UV hole-burning spectroscopies two structural isomers of [(C$_6$H$_6$)$_2$-(MeOH)$_3$] clusters have been identified[33] and possible structures suggested based on semiempirical (PM3) calculations. In the construction of these models it had been assumed that the T-shaped structure of the benzene dimers[72−74] will be largely retained in these two isomers.[33] In one of these isomers (Isomer B), the top benzene of the tee interacts with the $(MeOH)_3$ chain via a π···H−O hydrogen bond (and possibly also by a O···H−C(benzene) hydrogen bond to the same benzene ring). In the second isomer (Isomer A), a π···H−O to the stem and a O···H−C(benzene) hydrogen bond to the top benzene, respectively, of the benzene dimer was suggested.[33] Besides this T-shaped structure of the benzene dimer, the parallel displaced arrangement of the two benzene molecules is nearly isoenergetic.[75−77] Hence, besides several structures similar to Isomer A, Figure 7a−c, with nearly equal interaction energies also a parallel displaced sandwich dimer of benzene with a $(MeOH)_3$ chain atop one of the benzene rings, Figure 7d, were
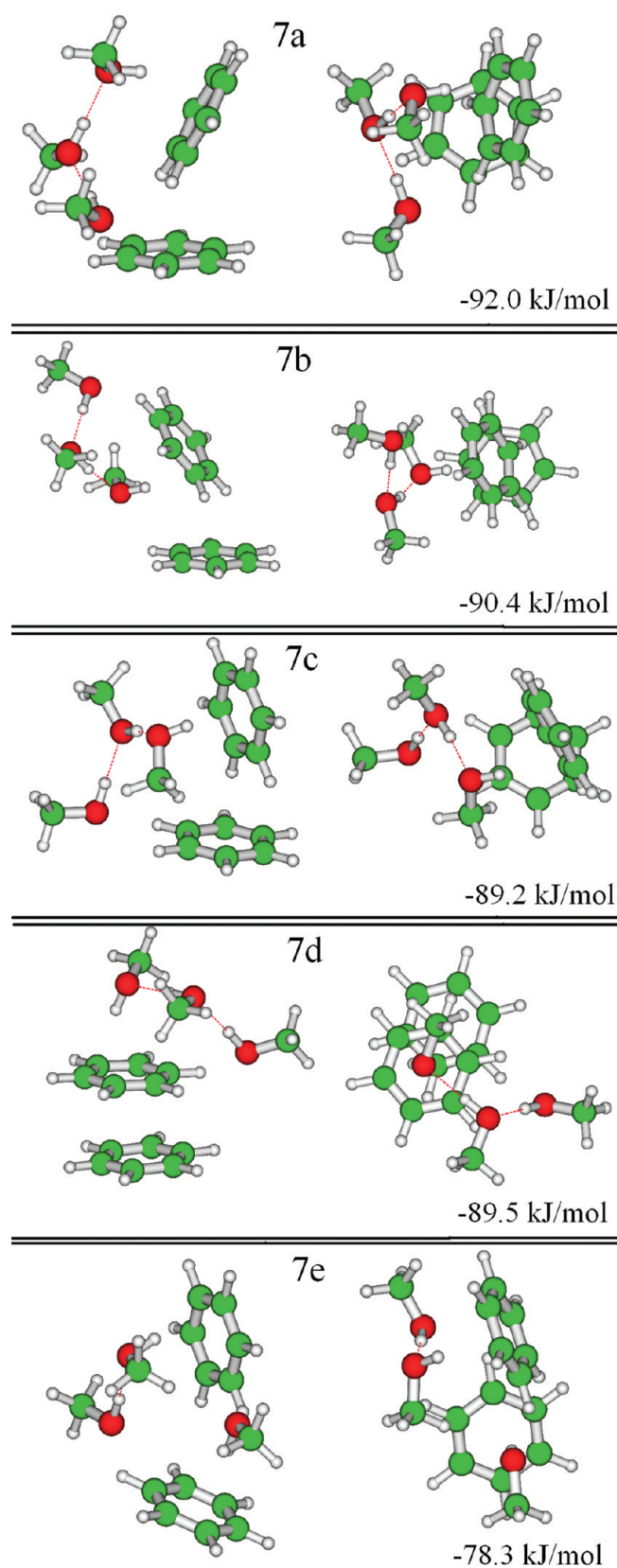
Figure 7. MP2/6-31+G(d,p) lowest energy structures of $(C_6H_6)_2$-$(MeOH)_3$ clusters and BSSE-corrected interaction energies..

found. In contrast, no $[(C_6H_6)_2(MeOH)_3]$ cluster corresponding to Isomer B could be obtained. Benzene and methanol form a

binary azeotrope in the mole ratio 2:3 with a minimum boiling point at 55.76 °C at 678 mm Hg.[28] Recently, a unit-structure for the azeotrope composed of four benzene sandwich dimers and three cyclic methanol tetramers, $[(C_6H_6)_2]_4[(MeOH)_4]_3$, has been proposed.[28] Structure **7d** closely resembles a simplified model for this proposed structure. Besides $\pi\cdots H-O$ and $O\cdots H-O$ hydrogen bonds benzene—benzene $\pi\cdots\pi$ interactions are present in **7d**. This isomer actually can be considered as cluster **3e** with an additional $\pi\cdots\pi$ interaction between two parallel displaced benzene molecules. The MP2 calculated interaction energies for such an arrangement (structure "Daa" in ref [75b]) are -17.2 (aug-cc-pVTZ) and -20.6 kJ mol^{-1} (CBS limit).[75b] The CCSD(T) CBS limit for the DZ-TZ basis set[75b] was given as -9.6 kJ mol^{-1}. Also comparable to the benzene dimer in **7d** is structure "Bz2/D", for which the RI-MP2 and CCSD(T) CBS limits are given as -20.6 and -11.0 kJ mol^{-1}, respectively.[55] Using the MP2/aug-cc-pVTZ BSSE-corrected interaction energy for **7d** and the corresponding data for **3e** and "Daa",[75b] the cooperativity in **7d** can be estimated as -2.3 kJ mol^{-1}.

The relatively compact structure **7e** with the maximum number of $O-H\cdots\pi$ and $C-H\cdots O$ hydrogen bonds and one $O-H\cdots O$ hydrogen bond has a lower interaction energy than all the other $[(C_6H_6)_2(MeOH)_3]$ clusters. The benzene—benzene interaction is broken in **7e** by one methanol shifted between the two tee benzenes and therefore exhibits less dispersion interaction. Furthermore, one $O-H\cdots O$ has also been broken, thus contributing to the lowering of the interaction energy.

■ CONCLUSION

Ab initio (MP2), tight-binding self-consistent charge DFT with dispersion correction (SCC-DFTB+) and DFT methods using various functionals (MPWB1K, M06-2X) were used to investigate benzene—methanol clusters $C_6H_6(MeOH)_n$, $n = 1-6$. Two different types of cluster structures were found. The first type consists of $(MeOH)_n$ chains connected through $\pi\cdots$ $H-O$ and $O\cdots H-C$(benzene) hydrogen bonds to the benzene ring; thus, for $n \geq 2$ a cyclic cluster resulting from participation of the benzene ring, characterized by a $\pi\cdots H-O\cdots[H-O]_{n-1}\cdots H-C$(benzene) hydrogen bond pattern, was formed. The second type consists of cyclic $(MeOH)_n$ subclusters ($n \geq 3$) weakly interacting with the benzene molecule. For $n = 3$, both types have nearly the same interaction energy, with a small preference for the first type containing a $(MeOH)_3$ chain over the second type, benzene + cyclic $(MeOH)_3$ subcluster, ΔE_{int} [BSSE-corrected MP2/CBS// MP2/6-31+G(d,p), eq 2, $N = 3$] $= -96.8$ and -94.4 kJ mol^{-1}, respectively. For $n \geq 4$ there is a clear preference for the second type of clusters, $C_6H_6 + (MeOH)_n$, as found by experiment.[38] BSSE-corrected M06-2X/6-311++G(d,p) interaction energies usually are close to the MP2/CBS values.

In addition to structures of the molecular formula C_6H_6-$(MeOH)_n$, also isomeric (benzene)$_2$—$(MeOH)_3$ clusters, corresponding to the composition of the benzene—methanol azeotrope, were considered. Several structures closely resembling that of Isomer A,[33] containing a $(MeOH)_3$ chain connected by $O-H\cdots\pi$ and $O\cdots H-C$(benzene) interactions to the stem and top benzene molecules, respectively, of a T-shaped benzene dimer, were found. In contrast, optimization of a structure corresponding to Isomer B resulted in a geometry consisting of a parallel displaced benzene sandwich dimer with a $(MeOH)_3$ chain atop one of the benzene molecules. The calculated

interaction energies [BSSE-corrected MP2/6-311++G(d,p)// MP2/6-31+G(d,p)] of these clusters are quite similar, ΔE_{int} = −89.2 to −92.0 kJ mol^{-1}. The BSSE-corrected MP2/CBS interaction energies for clusters **7a** (T-shaped benzene dimer) and **7d** (parallel displaced benzene dimer) are −123.3 and −119.3 kJ mol^{-1}. Cooperativity effects play a key role in the stabilization of the cluster geometries. Finally, it should be pointed out that the BSSE correction is both approximate and absolutely necessary. Only with very large basis sets, for example, aug-cc-pV5Z, this correction goes to zero. The relatively good performance of M06-2X, even with relatively small basis sets, may be attributed to the presence of weakly interacting molecules in the database used for parametrization of this functional. Calculations on the benzene dimer and its solvation are generally accurate to 4 kJ mol^{-1}. Hence, in any present day experiment, for example, in supersonic beams, all structures within this energy range can be expected to be present in the sample under investigation.

■ ASSOCIATED CONTENT

ⓢ Supporting Information. Interaction energies (DFTB +, MPWB1K, M06-2X, MP2/6-31+G(d,p); Table S1); Cartesian coordinates of the optimized cluster geometries (MP2-(fc)/6-31+G(d,p); DFTB+, MPWB1K/6-31+G(d,p), and M06-2X/6-31+G(d,p)) plot of MP2(fc)/6-31+G(d,p) optimized structures for **2a** versus **2b** and **2d** versus **2e** (Figure S1). This material is available free of charge via the Internet at http://pubs.acs.org.

■ AUTHOR INFORMATION

Corresponding Author
*Phone: + 36 72-503-600 (4208). Fax: + 36 72-503-635. E-mail: kunsagi@gamma.ttk.pte.hu.

■ ACKNOWLEDGMENT

■ REFERENCES

(1) Brutschy, B. *Chem. Rev.* **2000**, *100*, 3891–3920.
(2) Kim, K. S.; Tarakeshwar, P.; Lee, J. Y. *Chem. Rev.* **2000**, *100*, 4145–4185.
(3) Suhm, M. A. *Adv. Chem. Phys.* **2009**, *142*, 1–57.
(4) Pauling, L. In *The Nature of the Chemical Bond*; Cornell University Press: Ithaca, NY, 1960.
(5) Weinhold, F. *J. Chem. Phys.* **1998**, *109*, 367–373.
(6) Weinhold, F. *J. Chem. Phys.* **1998**, *109*, 373–384.
(7) Kirchner, B. *Phys. Rep.-Rev. Sec. Phys. Lett.* **2007**, *440*, 1–111.
(8) Ludwig, R.; Weinhold, F.; Farrar, T. C. *Mol. Phys.* **1999**, *97*, 479–486.
(9) Huelsekopf, M.; Ludwig, R. *J. Mol. Liq.* **2000**, *85*, 105–125.
(10) Huelsekopf, M.; Ludwig, R. *J. Mol. Liq.* **2002**, *98−99*, 163–171.
(11) Ludwig, R. *ChemPhysChem* **2005**, *6*, 1369–1375.
(12) Lehmann, S. B. C.; Spickermann, C.; Kirchner, B. *J. Chem. Theory Comput.* **2009**, *5*, 1640–1649.
(13) Desiraju, G. R.; Steiner, T. *The weak hydrogen bond in structural chemistry and biology*; Oxford University Press: Oxford, 1999.
(14) Jeffrey, G. A. *An introduction to hydrogen bonding*; Oxford University Press: Oxford, 1997.
(15) Nishio, M.; Hirota, M.; Umezawa, Y. In *The CH/π interaction: evidence, nature, and consequences*; Wiley-VCH: New York, 1998.
(16) Ahn, D. S.; Park, S. W.; Lee, S.; Kim, B. *J. Phys. Chem. A* **2003**, *107*, 131–139.
(17) Barth, H. D.; Buchhold, K.; Djafari, S.; Reimann, B.; Lommatzsch, U.; Brutschy, B. *Chem. Phys.* **1998**, *239*, 49–64.
(18) Gruenloh, C. J.; Carney, J. R.; Hagemeister, F. C.; Zwier, T. S.; Wood, J. T.; Jordan, K. D. *J. Chem. Phys.* **2000**, *113*, 2290–2303.
(19) Reimann, B.; Buchhold, K.; Barth, H. D.; Brutschy, B.; Tarakeshwar, P.; Kim, K. S. *J. Chem. Phys.* **2002**, *117*, 8805–8822.
(20) Sakai, M.; Daigoku, K.; Ishiuchi, S.; Saeki, M.; Hashimoto, K.; Fujii, M. *J. Phys. Chem. A* **2001**, *105*, 8651–8657.
(21) Tarakeshwar, P.; Choi, H. S.; Lee, S. J.; Lee, J. Y.; Kim, K. S.; Ha, T.-K.; Jang, J. H.; Lee, J. G.; Lee, H. *J. Chem. Phys.* **1999**, *111*, 5838–5850.
(22) Tarakeshwar, P.; Kim, K. S.; Djafari, S.; Buchhold, K.; Reimann, B.; Barth, H. D.; Brutschy, B. *J. Chem. Phys.* **2001**, *114*, 4016–4024.
(23) Prakash, M.; Samy, K. G.; Subramanian, V. *J. Phys. Chem. A* **2009**, *113*, 13845–13852.
(24) Buchhold, K.; Reimann, B.; Djafari, S.; Barth, H. D.; Brutschy, B.; Tarakeshwar, P.; Kim, K. S. *J. Chem. Phys.* **2000**, *112*, 1844–1858.
(25) Gruenloh, C. J.; Florio, G. M.; Carney, J. R.; Hagemeister, F. C.; Zwier, T. S. *J. Phys. Chem. A* **1999**, *103*, 496–502.
(26) Hagemeister, F. C.; Gruenloh, C. J.; Zwier, T. S. *J. Phys. Chem. A* **1998**, *102*, 82–94.
(27) Hu, Y.; Bernstein, E. R. *J. Phys. Chem. A* **2009**, *113*, 639–643.
(28) Jalilian, M. R.; Tayyari, S. F. *Spectrochim. Acta A* **2009**, *73A*, 828–832.
(29) Larsen, G.; Ismail, Z. K.; Herreros, B.; Parra, R. D. *J. Phys. Chem. A* **1998**, *102*, 4734–4741.
(30) Palmer, P. M.; Chen., Y.; Topp, M. R. *Chem. Phys. Lett.* **2000**, *321*, 62–70.
(31) Palmer, P. M.; Topp, M. R. *Chem. Phys. Lett.* **1998**, *292*, 307–316.
(32) Palmer, P. M.; Topp, M. R. *Chem. Phys. Lett.* **1998**, *286*, 113–120.
(33) Pribble, R. N.; Gruenloh, C.; Zwier, T. S. *Chem. Phys. Lett.* **1996**, *262*, 627–632.
(34) Saeki, M.; Ishiuchi, S.; Sakai, M.; Fujii, M. *J. Phys. Chem. A* **2001**, *105*, 10045–10053.
(35) Gruenloh, C. J.; Hagemeister, F. C.; Carney, J. R.; Zwier, T. S. *J. Phys. Chem. A* **1999**, *103*, 503–513.
(36) Hagemeister, F. C.; Gruenloh, C. J.; Zwier, T. S. *Chem. Phys.* **1998**, *239*, 83–96.
(37) Kunsági-Máté, S.; Iwata, K. *Chem. Phys. Lett.* **2009**, *473*, 284–287.
(38) Pribble, R. N.; Hagemeister, F. C.; Zwier, T. S. *J. Phys. Chem.* **1997**, *106*, 2145–2157.
(39) Garrett, A. W.; Severance, D. L.; Zwier, T. S. *J. Chem. Phys.* **1992**, *96*, 7245–7258.
(40) Rankin, K. N.; Boyd, R. J. *J. Comput. Chem.* **2001**, *22*, 1590–1597.
(41) Dkhissi, A.; Blossey, R. *Chem. Phys. Lett.* **2007**, *439*, 35–39.
(42) Murdachaew, G.; Mundy, C. J.; Schenter, G. K. *J. Chem. Phys.* **2010**, *132*, 164102.
(43) Ireta, J.; Neugebauer, J.; Scheffler, M. *J. Phys. Chem. A* **2004**, *108*, 5692–5698.
(44) Martínez, J. M.; Martínez, L. *J. Comput. Chem.* **2003**, *24*, 819–825.
(45) Elstner, M.; Porezag, D.; Jungnickel, G.; Elsner, J.; Haugk, M.; Frauenheim, T.; Suhai, S.; Seifert, G. *Phys. Rev. B* **1998**, *58*, 7260–7268.
(46) Elstner, M.; Hobza, P.; Frauenheim, T.; Suhai, S.; Kaxiras, E. *J. Chem. Phys.* **2001**, *114*, 5149–5155.

10563

dx.doi.org/10.1021/jp206248w |*J. Phys. Chem. A* 2011, 115, 10556–10564

(47) Zhao, Y.; Truhlar, D. G. *J. Phys. Chem. A* **2004**, *108*, 6908–6918.

(48) Zhao, Y.; Truhlar, D. G. *Theor. Chem. Acc.* **2008**, *120*, 215–241.

(49) Zhao, Y.; Truhlar, D. G. *Acc. Chem. Res.* **2008**, *41*, 157–167.

(50) Møller, C.; Plesset, M. S. *Phys. Rev.* **1934**, *46*, 618–622.

(51) Matisz, G.; Fabian, W. M. F.; Kelterer, A.; Kunsági-Máté, S. *J. Mol. Struct.: THEOCHEM* **2010**, *956*, 103–109.

(52) Boys, S. F.; Bernardi, F. *Mol. Phys.* **1970**, *19*, 553–566.

(53) Martin, J. M. L. *Chem. Phys. Lett.* **1996**, *259*, 669–678.

(54) (a) Dunning, T. H. *J. Chem. Phys.* **1989**, *90*, 1007–1023. (b) Kendall, R. A.; Dunning, T. H.; Harrison, R. J. *J. Chem. Phys.* **1992**, *96*, 6796–6806.

(55) Min, S. K.; Lee, E. C.; Lee, H. M.; Kim, D. Y.; Kim, D.; Kim, K. S. *J. Comput. Chem.* **2008**, *29*, 1208–1221.

(56) (a) Molnar, L. F.; He, X.; Wang, B.; Merz, K. M. *J. Chem. Phys.* **2009**, *131*, 065102. (b) Halkier, A.; Helgaker, T.; Jørgensen, P.; Klopper, W.; Koch, H.; Olsen, J.; Wilson, A. K. *Chem. Phys. Lett.* **1998**, *286*, 243–252.

(57) Martínez, L.; Andrade, R.; Birgin, E. G.; Martínez, J. M. *J. Comput. Chem.* **2009**, *30*, 2157–2164.

(58) Aradi, B.; Hourahine, B.; Frauenheim, T. *J. Phys. Chem. A* **2007**, *111*, 5678–5684.

(59) Schmidt, M. W.; Baldridge, K. K.; Boatz, J. A.; Elbert, S. T.; Gordon, M. S.; Jensen, J. H.; Koseki, S.; Matsunaga, N.; Nguyen, K. A.; Su, S.; Windus, T. L.; Dupuis, M.; Montgomery, J. A. *J. Comput. Chem.* **1993**, *14*, 1347–1363.

(60) Frisch, M. J.; Trucks, G. W.; Schlegel, H. B.; Scuseria, G. E.; Robb, M. A.; Cheeseman, J. R.; Scalmani, G.; Barone, V.; Mennucci, B.; Petersson, G. A.; Nakatsuji, H.; Caricato, M.; Li, X.; Hratchian, H. P.; Izmaylov, A. F.; Bloino, J.; Zheng, G.; Sonnenberg, J. L.; Hada, M.; Ehara, M.; Toyota, K.; Fukuda, R.; Hasegawa, J.; Ishida, M.; Nakajima, T.; Honda, Y.; Kitao, O.; Nakai, H.; Vreven, T.; Montgomery, Jr., J. A.; Peralta, J. E.; Ogliaro, F.; Bearpark, M.; Heyd, J. J.; Brothers, E.; Kudin, K. N.; Staroverov, V. N.; Kobayashi, R.; Normand, J.; Raghavachari, K.; Rendell, A.; Burant, J. C.; Iyengar, S. S.; Tomasi, J.; Cossi, M.; Rega, N.; Millam, N. J.; Klene, M.; Knox, J. E.; Cross, J. B.; Bakken, V.; Adamo, C.; Jaramillo, J.; Gomperts, R.; Stratmann, R. E.; Yazyev, O.; Austin, A. J.; Cammi, R.; Pomelli, C.; Ochterski, J. W.; Martin, R. L.; Morokuma, K.; Zakrzewski, V. G.; Voth, G. A.; Salvador, P.; Dannenberg, J. J.; Dapprich, S.; Daniels, A. D.; Farkas, Ö.; Foresman, J. B.; Ortiz, J. V.; Cioslowski, J.; Fox, D. J. *Gaussian 09*, Revision A.02; Gaussian, Inc.: Wallingford, CT, 2009.

(61) Valiev, M.; Bylaska, E. J.; Govind, N.; Kowalski, K.; Straatsma, T. P.; Van Dam, H. J. J.; Wang, D.; Nieplocha, J.; Apra, E.; Windus, T. L.; de Jong, W. A. *Comput. Phys. Commun.* **2010**, *181*, 1477–1489.

(62) *Hyperchem(TM) Professional 7*; Hypercube, Inc.: Gainesville, Florida.

(63) Schaftenaar, G.; Noordik, J. H. *J. Comput.-Aided Mol. Des.* **2000**, *14*, 123–134.

(64) Huisken, F.; Kulcke, A.; Laush, C.; Lisy, J. M. *J. Chem. Phys.* **1991**, *95*, 3924–3929.

(65) Tarakeshwar, P.; Lee, S. J.; Lee, J. Y.; Kim, K. S. *J. Chem. Phys.* **1998**, *108*, 7217–7223.

(66) Lill, S. O. N. *J. Phys. Chem. A* **2009**, *113*, 10321–10326.

(67) Feller, D. *J. Phys. Chem. A* **1999**, *103*, 7558–7561.

(68) Molnar, L. F.; He, X.; Wang, B.; Merz, K. M. *J. Chem. Phys.* **2009**, *131*, 065102.

(69) Neves, A. R.; Fernandes, P. A.; Ramos, M. J. *J. Chem. Theory Comput.* **2011**, *7*, 2059–2067.

(70) Jurecka, P.; Sponer, J.; Cerny, J.; Hobza, P. *Phys. Chem. Chem. Phys.* **2006**, *8*, 1985–1993.

(71) Pitonak, M.; Riley, K. E.; Neogrady, P.; Hobza, P. *ChemPhysChem* **2008**, *9*, 1636–1644.

(72) Arunan, E.; Gutowsky, H. S. *J. Chem. Phys.* **1993**, *98*, 4294–4296.

(73) Scherzer, W.; Kraetzschmar, O.; Selzle, H. L.; Schlag, E. W. *Z. Naturforsch. A* **1992**, *47*, 1248–1252.

(74) Janowski, T.; Pulay, P. *Chem. Phys. Lett.* **2007**, *447*, 27–32.

(75) (a) Hobza, P.; Selzle, H. L.; Schlag, E. W. *J. Phys. Chem.* **1996**, *100*, 18790–18794. (b) Lee, E. C.; Kim, D.; Jurecka, P.; Tarakeshwar, P.; Hobza, P.; Kim, K. S. *J. Phys. Chem. A* **2007**, *111*, 3446–3457.

(76) Hill, J. G.; Platts, J. A.; Werner, H. *Phys. Chem. Chem. Phys.* **2006**, *8*, 4072–4078.

(77) Zhao, Y.; Truhlar, D. G. *J. Phys. Chem. A* **2005**, *109*, 4209–4212.